Novel formulations of chlorhexidine digluconate for application on surfaces to reduce infection and disease transmission.

A thesis submitted the University of Nottingham for the degree of
Doctor of Philosophy
In the Faculty of Science

2025

Madeline Ann Berrow, MSc, BSc

School of Pharmacy
Advanced Materials and Healthcare Technologies

Table of Contents

Abstract 7

Declaration 8

Acknowledgments 8

Rationale for submitting thesis is alternative format 8

Abbreviations 9

1.0. Chapter 1: General introduction 12

1.1. Chlorhexidine digluconate 12

1.1.1. Adverse reactions and alternative antimicrobials 12

1.1.2. Antimicrobial potency and minimum bactericidal concentration 13

1.1.3. Antimicrobial mode of action 13

1.1.4. Chlorhexidine resistance 14

1.2. Skin structure, function and native microbiome 15

1.2.1. Epidermidis and the *stratum corneum* 16

1.2.2. Dermis 17

1.2.3. Hypodermis 18

1.2.4. Skin appendages 18

1.2.5. The native skin microbiome 18

1.3. Transdermal drug transport and skin permeation pathways 19

1.3.1. Intracellular pathway 20

1.3.2. Intercellular pathway 20

1.3.3. Appendageal pathway 21

1.4. Physicochemical properties of drugs that effect transdermal permeability 21

1.4.1. Molecular size 21

1.4.2. Partition coefficient 21

1.4.3. Acid dissociation constant 21

1.4.4. Melting point 22

1.4.5. Hydrogen bonding 22

1.5. Transdermal permeation of Chlorhexidine 22

1.5.1. Chlorhexidine physicochemical properties and poor permeation 22

1.5.2. Chlorhexidine permeation pathway 23

1.6. Enhancement of chlorhexidine permeation through the skin 23

1.6.1. Formulation composition 23

1.6.2. Dendrimer-mediated permeation 26

1.6.3. Microneedle pre-treatment 26

1.7. Experimental methods to study skin permeation 27

1.7.1. *In vivo* sampling 27

1.7.2. *In vitro* sampling 28

1.8. Antimicrobial surfaces 28

1.8.1. Antimicrobial surfaces, uses and benefits 29

1.9. Antimicrobial metals and metal nanoparticles 30

1.9.1. Antimicrobial silver surfaces 30

1.9.2. Antimicrobial silver nanoparticles 31

1.9.3. Antimicrobial copper surfaces 32

1.9.4. Antimicrobial copper nanoparticles 32

1.9.5. Antimicrobial Zinc surfaces 33

1.9.6. Antimicrobial zinc nanoparticles 33

1.9.7. Antimicrobial titanium dioxide surfaces 34
1.9.8. Antimicrobial titanium dioxide nanoparticles 34

1.10. Other types of antimicrobial surfaces **35**
1.10.1. Superhydrophobic surfaces 35
1.10.2. Hydrophilic surfaces 35
1.10.3. Antimicrobial peptide-coated surfaces 36
1.10.4. Other organic antimicrobial surfaces 36
1.10.5. Mechano-bactericidal nanomaterials 37
1.10.6. Photobactricidal polymers 37

1.11. Epoxy resin paint coatings **38**
1.11.1. Epoxy resin curing and production 38
1.11.2. Epoxy resin coating uses 38

1.12. Properties of epoxy resin paint coatings **39**
1.12.1. Mechanical strength 39
1.12.2. Adhesion properties 39
1.12.3. Thermal and chemical resistance 39
1.12.4. Antimicrobial properties 40
1.12.5. Additional beneficial properties 40

1.13. Commercial antimicrobial coatings **40**
1.13.1. Antimicrobial metal-based paints 40
1.13.2. Triclosan-based antimicrobial coatings 41
1.13.3. Colophony- and Curcumin-based antimicrobial paints 42
1.13.4. Quaternary Polyethyleneimine-based antimicrobial paint 43

1.14. Antimicrobial CHX-coated materials **43**
1.14.1. Antimicrobial CHX-coated steel 43
1.14.2. Antimicrobial CHX-coated titanium 44
1.14.3. Antimicrobial CHX-coated polymers 44
1.14.4. Antimicrobial CHX-coated air filters 45

1.15. Methods to study antimicrobial efficacy of surfaces **45**
1.15.1. ISO 22196 (2011) test of antibacterial activity 45
1.15.2. Live/dead viability assay 45
1.15.3. Disc diffusion 46

1.16. Time of flight- secondary ion mass spectrometry (ToF-SIMS) **46**
1.16.1. Primary ion beam sources 47
1.16.2. Cluster ion sources 47
1.16.3. Mass analysers 48
1.16.4. Charge compensation 48
1.16.5. Secondary ion mapping and imaging 48
1.16.6. Ionisation and matrix effects 49
1.16.7. Analysis of biological tissues 49
1.16.8. Limitations of ToF-SIMS 49

1.17. High performance liquid chromatography (HPLC) **49**
1.17.1. Mobile phase 50
1.17.2. Stationary phase 51
1.17.3. Normal-phase HPLC 51
1.17.4. Reverse-phase HPLC 51
1.17.6. The theory of band broadening 52
1.17.7. Ion pairing agents 52
1.17.8. Limitations of HPLC 52

1.18. The scope of this thesis **54**

References for Chapter 1 ..... **55**

Chapter 2: Enhanced topical antimicrobial delivery for improved skin antisepsis 82
Graphical Abstract 83
Abstract 83
Keywords 84
Abbreviations 84
Introduction 84
2. Materials and Methods 86
2.1. Materials 86
2.2. Chlorhexidine Formulations 87
2.3. In Vivo Skin Permeation 87
2.4. In Vitro Skin Permeation 88
2.5. Analysis of Chlorhexidine Permeation 89
2.6. Antimicrobial Efficacy of Chlorhexidine Formulations 90
2.7. Cytotoxicity of Chlorhexidine Formulations 90
2.8. Statistical Analysis 90
3. Results and Discussion 91
3.1. Comparison of In vivo Human and In Vitro Porcine Skin Permeation of Chlorhexidine 91
3.2. Chlorhexidine Concentration and Skin Permeation 94
3.3. R6 Polyarginine to Enhance Chlorhexidine Permeation 94
3.4. Glycolic Acid to Enhance Chlorhexidine Permeation 99
3.5. Kolliphor® HS15 to Enhance Chlorhexidine Permeation 101
3.6. R6 Polyarginine is the Most Potent Permeation Enhancer of Chlorhexidine 102
4. Conclusions 102
Acknowledgements 103
Declaration of Competing Interest 103
Data Availability 103
References 104
Supplementary Information for 109
Conclusions of Chapter 2 125
Chapter 3: Development and characterisation of antimicrobial epoxy resin 127
Abstract 128
Keywords 128
Data availability statement 128
1. Introduction 129
2. Materials and Methods 130
2.1 Epoxy Resin Preparation 131
2.2 Time-of-Flight Secondary Ion Mass Spectrometry (ToF-SIMS) 131
2.3 Water Contact Angle 131
2.4 Scratch Resistance and Adhesion 132
2.5 Optical Transparency 132
2.6 Antibacterial Efficacy 132
2.7 Antifungal Efficacy 133
2.8 Antibacterial Efficacy Against Chlorhexidine-Resistant *E. coli* 133
2.9 Scanning Electron Microscopy 133

2.10 Durability of Antimicrobial Efficacy 133
2.11 HPLC analysis of CHX epoxy resin leachate 134
2.12 Stability of Chlorhexidine Epoxy Resin 134
2.13 Repeat Exposures of Chlorhexidine Epoxy Resin 134
2.14 Data Analysis 135

3. Results **135**
3.1 Surface Characterisation 135
3.2 Material Characterisation 136
3.3 Antimicrobial Efficacy 137
3.4 Surface Leaching and Durability of Efficacy 139
3.5 Stability of Chlorhexidine in Epoxy Resin 141
3.6 Repeated Exposures of Chlorhexidine Epoxy Resin to E. coli 142

4. Discussion **143**

Acknowledgments **145**

References **146**

Conclusions of chapter 3 ..... **150**

Chapter 4: Stability, durability and application of antimicrobial epoxy resin 152

Abstract **153**

Keywords **153**

1.0. Introduction **154**

2.0. Materials and methods **156**
2.1. Materials 156
2.2. Epoxy resin preparation 156
2.3. Artificially accelerated aging of epoxy resin coatings 156
2.4. 12-Month stability of antimicrobial efficacy 156
2.5. Antibiofilm efficacy 157
2.6. Visualisation of biofilms using cryo-scanning electron microscopy (Cryo-SEM) 157
2.7. Durability of antimicrobial efficacy in seawater 157
2.8. Time of flight- secondary ion mass spectrometry of post-leaching salt residue 159
2.9. Mammalian cytotoxicity of CHX epoxy resin 159
2.10. Antimicrobial efficacy on real life coated surfaces 159
2.11. Statistical analysis 160

3.0. Results and Discussion **160**
3.1. Long-term stability of antimicrobial CHX epoxy resin coatings 160
3.2. Antibiofilm efficacy of CHX epoxy resin coatings 162
3.3. Short-term durability of antimicrobial efficacy in seawater 164
3.4. Long-term durability of antimicrobial efficacy in seawater 166
3.5. Durability of antimicrobial efficacy with simulated oceanic motion 169
3.6. Salt build-up impacts the antimicrobial efficacy following seawater exposure 171
3.7. Antimicrobial efficacy of real-life coated surfaces 173
3.8. Cytotoxicity and CHX Concentration Effect on Antimicrobial Efficacy 174

Conclusions **174**

Acknowledgements **175**

References **176**

Supplementary Information for **180**

Conclusions of chapter 4 ..... **183**

Chapter 5: Conclusions and future work 184

5.1. Conclusions 184

5.2. Future work 184

5.2.1. CHX for skin sanitation 184

5.2.2. CHX epoxy resin coatings 185

References for chapter 5 186

Appendix 1: Oligoarginine peptide structure and effect on cell penetration in ocular drug delivery 188

Appendix 2: Wettability and Bactericidal Properties of Bioinspired ZnO Nanopillar Surfaces 206

Abstract

Chlorhexidine digluconate (CHX) is a very potent antimicrobial compound that demonstrates microbicidal activity against a variety of clinically relevant bacterial, fungal and some viral pathogens, including various antimicrobial-resistant strains. CHX is often used by the medical industry to eliminate the skin microbiome prior to surgery to reduce surgical site infections. Due to the skins native defence mechanisms and biocide properties, including molecular size and ability to form hydrogen bonds with components of the *stratum corneum,* CHX demonstrates poor skin permeability. This may result in ineffective clearance of skin microbes and therefore lead to the development of infections at the site. This project then evolved to utilise CHX for a novel application in epoxy resin, with the aim to produce an easy-installed, durable coating to reduce microbial reservoirs on surfaces and therefore lower disease transmission. The second chapter presents a research paper titled 'Enhanced topical antimicrobial delivery for improved skin antisepsis' which has been submitted to the Journal of Pharmaceutical Sciences. This work studies the permeation of CHX through the skin in its current clinical formulation, as well as when formulated with a series of permeation enhancer compounds, R6 polyarginine, glycolic acid and Kolliphor® HS15. An *in vitro* permeation model using *ex vivo* porcine skin was validated by comparing CHX permeation through this model to *in vivo* human skin. This allowed the effects of these compounds on the delivery of CHX through the skin to be studied. High performance liquid chromatography (HPLC) was deployed for quantification and time of flight – secondary ion mass spectrometry (ToF-SIMS) was used to understand the spatial distribution of CHX at each layer of the *stratum corneum*. The antimicrobial efficacy of these CHX-permeation enhancer formulations was analysed to determine whether the increased biocide delivery corelated with enhanced microbial elimination. In addition, the cytotoxicity profiles of these formulations were investigated against mammalian cells to determine whether they would cause damage to the skin when in used in clinical practice.

This work also discusses a novel application of CHX in the development of antimicrobial surfaces. Microorganisms that reside on inanimate surfaces can be transmitted between hosts upon contact, contributing significantly to the transmission of disease. Antimicrobial surfaces are a modern approach to eliminating environmental microbes without the need for frequent chemical sanitisation. This thesis explores the incorporation of CHX into a clear epoxy resin coating which can be applied to a variety of surfaces to reduce/eliminate microbial contamination and therefore disease transmission. The third chapter presents a research paper published in Scientific Reports titled 'Development and characterisation of antimicrobial epoxy resin', which explores the distribution of the biocide throughout the epoxy coatings, physicochemical properties such as hydrophobicity/hydrophilicity and the antimicrobial efficacy against a variety of clinically-relevant microorganisms, including *Escherichia coli, Staphylococcus aureus, Pseudomonas aeruginosa, Candida albicans* and CHX-resistant *E. coli*. This paper also looks at the scratch resistance, adhesion properties and storage stability of CHX epoxy resin. The fourth chapter is a continuation of the CHX epoxy resin work and presents a research paper submitted to Journal of Materials Chemistry B titled 'Stability, Durability and Application of Antimicrobial Epoxy Resin'. This paper explores the long-term durability of antimicrobial efficacy following curing, along with the antibiofilm efficacy against *P. aeruginosa* biofilms. Further, this paper discusses the durability of these coatings in seawater as well as their antimicrobial efficacy against environmental microbes and mammalian cytotoxicity.

Declaration

I hereby declare that no portion of the work presented in this thesis has been submitted in support of an application for any other degree or qualification of this or any University or institute of learning.

Acknowledgments

I would firstly like to acknowledge the University of Nottingham, School of Pharmacy for financially supporting the research covered by this thesis. I would like to thank my industrial collaborators from Indestructible Paints, Ltd, particularly project technician Violaine Mendez and CEO Brian Norton for making the antimicrobial paint project possible, as well as for inviting and introducing me to their manufacturing facility. It was a great opportunity to get insight into the large-scale production of the product.

I would like to thank all my colleagues from the School of Pharmacy, particularly within the Advanced Materials and Healthcare Technologies (AMHT) who have supported me and my research projects by contributing knowledge and support. I am particularly grateful for the technical support within the Boots Science Building and the Nanoscale and Microscale Research Centre, in particular, Nichola Starr, Anna Kotowska and Li Lu for technical support with the SIMS, Paul Cooling for technical support and training with the HPLC, Christopher Parmenter and Eva Simpson for support with SEM and confocal imaging and Jean Dubern for providing fluorescent bacterial strains that allowed the research to take place. I would also like to acknowledge all members from the FdC research group, in particular Sónia Pedro and Naa Dei Nikoi for all their support over the years.

I would like to thank my friends from offices D09 and A03 and the rest of Boots Science Building, in particular Reece Franklin, Alice Goode, Laura Beckett and Alexandra Thomas, who have been a continued source of encouragement and advice over the years. I could not have got through the last 3 years without them. A massive thank you to Joanne Berrow, Tyrone Berrow and Jamie Berrow, my mum, dad and brother. They have not only supported me financially through my Bachelor's and Master's degrees but have showed unwavering belief in me by continuing to provide a consistent motivational and support network throughout my PhD.

Finally, I would like to thank my two PhD supervisors, Dr Felicity de Cogan and Dr David Scurr who have pushed my development in research in more ways than I can begin to explain. I am extremely grateful for their continued support and guidance throughout this project and indebted to the effort and time that has gone into making this work possible. I am incredibly grateful to my primary supervisor Dr Felicity de Cogan for her faultless mentorship and for pushing me out of my comfort zone. I have learnt so much from her and will continue to be inspired by her enthusiasm and ambition.

Rationale for submitting thesis is alternative format

I decided to submit my thesis in an alternative format for two reasons. Firstly, in 2025, one of my papers was published in Scientific Reports, titled 'Development and characterisation of antimicrobial epoxy resin'. Secondly, I have published a research manuscript in the Journal

Pharmaceutical Sciences and have a third paper that has been submitted to Material Advances for publication.

This thesis is structured to include a general introduction into the background of the work discussed in this document. This is followed by three experimental chapters containing the original manuscripts submitted to journals. The final chapter draws conclusions from all the work in this thesis and highlights future work.

Abbreviations

CHX – chlorhexidine digluconate
SSI – surgical site infection
MRSA – methicillin-resistant *Staphylococcus aureus*
VRE – vancomycin-resistant *Enterococci*
MBC – minimum bactericidal concentration
LPS – lipopolysaccharide
ROS – reactive oxygen species
QAC – quaternary ammonium compound
ESBL – extended-spectrum β-lactamase
PACE – Proteobacterial antimicrobial compound efflux
UV – ultraviolet
m^2 – metre squared
BMZ – basement membrane zone
FA – fatty acids
cm^2 – centimetre squared
pH – potential of hydrogen
FFA – free fatty acids
DNA – deoxyribonucleic acid
ECM – extracellular matrix
pKa – acid dissociation constant
Log *P* – partition coefficient
UK – United Kingdom
NICE – National Institute for Health and Care Excellence
v/v – volume per volume
IPA – isopropyl alcohol
w/v – weight per volume
rpm – rotations per minute
G3 PAMAM-NH_2 – third generation polyamidoamine dendrimer
HEC – hydroethylcellulose
PLGA – poly(lactic-co-glycolic acid)
HPLC – high performance liquid chromatography
HAI – healthcare associated infection
MDR – multidrug resistant
MO-NP – metal oxide nanoparticles
GDP – gross domestic product
RNA – ribonucleic acid
PMF – proton motive force
Ag-NP – silver nanoparticles
ATP – adenosine triphosphate F

CuO-NP – copper oxide nanoparticles
ZnO-NP – zinc oxide nanoparticles
RND – resistance nodulation diversion
CDF – cation diffuser facilitator
TiO_2-NO – titanium dioxide nanoparticles
MIC – minimum inhibitory concentration
PFDT – perfluorodecanethiol
H_2O_2 – hydrogen peroxide
PEG – polyethylene glycol
PVP – polyvinylpyrrolidone
AMP – antimicrobial peptides
PVC – polyvinylchloride
-O- – ester group
-OH – hydroxy group
Au-NP – gold nanoparticles
NIR – near infrared
CFU – colony forming units
ENP – enoyl-acyl carrier protein reductase
SCDLP – soybean casein digest lecithin polysorbate
PBS – phosphate buffered saline
TSB – tryptic soy broth
AEP – 1-(2-aminoethylpiperazine)
PEI – polyethyleneimine
HBTU – 2-(1H-benzotriazol-1-yl)-1,1,3,3-tetramethyluronium hexafluorophosphate
DIEA – N,N-diisopropylethylamine
MALDI-ToF MS – matrix-assisted laser desorption/ionization time-of-flight mass spectrometry
LB – Luria-Bertani
BHI – brain heart infusion
SEM – scanning electron microscopy
ABS – acrylonitrile butadiene styrene
YPD – yeast peptone dextrose
FITC – fluorescein isothiocyanate
RFP – red fluorescent protein
WHO – World Health Organisation
ZOI – zone of inhibition
ToF-SIMS – time of flight secondary ion mass spectrometry
ppm – parts per million
ppb – parts per billion
GCIB – gas cluster ion beam
m/z – mass-to-charge ratio of an ion
LMIG – liquid metal ion gun
ToF – time of flight
LC – liquid chromatography
TLC – thin layer chromatography
GC – gas chromatography
NPLC – normal-phase liquid chromatography
RPLC – reverse-phase liquid chromatography
LOD – limit of detection
LOQ – limit of quantification

UV-Vis – ultraviolet-visible spectroscopy
FLD – fluorescence detection
ELSD – evaporative light scattering detection
CAD – charged aerosol detection
RID – refractive index detection
ECD – electrochemical detection
CLND – chemiluminescent nitrogen detection
HPLC-MS – high performance liquid chromatography-mass spectrometry
SPSS – Statistical Package for the Social Sciences

1.0. Chapter 1: General introduction

1.1. Chlorhexidine digluconate

Chlorhexidine digluconate (CHX) is a basic, biguanide (Figure. 1.1), crystalline compound that exhibits potent bactericidal, fungicidal and viricidal behaviours (1). It was developed by Imperial Chemical Industries (Manchester, UK) as use as an antiseptic and has been used worldwide since 1954 (2). The antimicrobial potency of CHX has been utilised throughout the medical and dental industries to provide surgical site sterilisation, surgical hand antisepsis, severe burn sterilisation, vaginal sanitisation, skin elimination of microbial populations for preoperative, intensive care and trauma patient bathing, skin cleaning prior to venipuncture, oropharyngeal decontamination for ventilator patients, development of antimicrobial medical materials such as catheters, canulae and dressings, contact lens washing, dental toothpastes and mouthwashes and treatments for gingivitis and periodontitis (1, 2, 3).

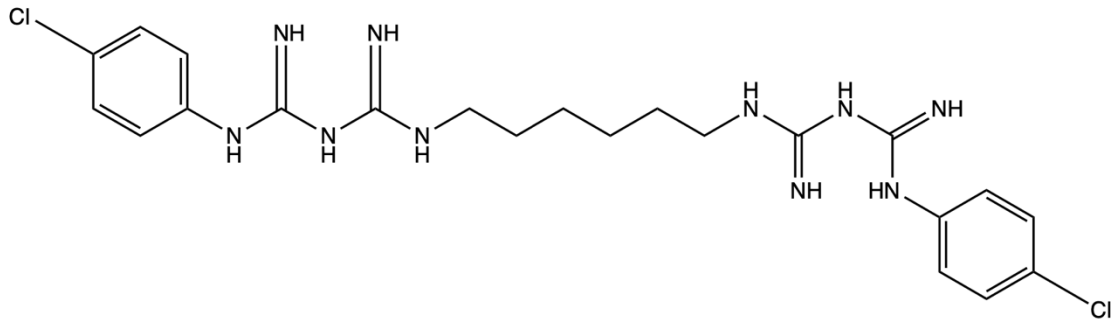


Figure 1.1. Molecular structure of chlorhexidine digluconate depicting two symmetrical biguanide and 4-chlorophenyl lineages adjoined by a central hexamethylene molecule (figure created using ChemDraw). Adapted from Opstrup *et al*., 2019 (4).

1.1.1. Adverse reactions and alternative antimicrobials

Adverse reactions following the use of CHX has been reported, ranging from mild, superficial irritant contact dermatitis to more severe and detrimental reactions, such as life-threatening anaphylaxis. The frequency of documented CHX allergic contact dermatitis has significantly increased due to elevated use of the antimicrobial, resulting in recurrent exposure to the biocide (2). Other adverse reactions of CHX have been documented, including the causation of conjunctivitis from chemical presence in contact lens solutions and xerostomia, oral numbness, taste alterations, hypogeusia, long-term tooth and tongue discolouration, parotid gland swelling, oral mucosal desquamation and paraesthesia glossodynia from formulation into dental products (2, 5).

Alternative topical skin antimicrobials have been utilised in the medical industry to eliminate the skins native microbiome to prevent surgical site infection (SSI). Povidone-iodine is a rapid acting antimicrobial consisting of elemental iodine, hydrogen iodine and povidone complexes in solution. Research suggests that iodine within the complex results in oxidation of membrane-bound lipids and interacts with membrane proteins to form salts on the microbial cell surface (6). Due to the non-specificity of the interactions, povidone-iodine demonstrates broad-spectrum antimicrobial efficacy against both gram-positive and gram-negative bacteria, acid-

fast bacteria, such as *Mycobacterium tuberculosis*, bacterial endospores, fungi, viruses and protozoa (6). However, residual antimicrobial efficacy is minimal unlike skin antisepsis using CHX formulations, which demonstrate efficacy up to 24 hours post-treatment due to binding between the biocide and proteins found on the skin's surface and mucosal membranes (1, 6). Further, antimicrobial activity of povidone-iodine is significantly reduced by the presence of body fluids, including blood, which is problematic particularly for the application of post-surgical skin sterilisation, where contact with body fluids is expected (1).

Isopropyl alcohol is one of the fastest antiseptics used to eliminate commensal microbes from the skin. It is a hydrophilic alcohol and is typically formulated in water due to enhanced antimicrobial activity in 60-90% solution compared to neat. Isopropyl alcohol denatures proteins displayed on microbial surfaces preventing metabolic processes and growth of the organism and demonstrates greater bactericidal activity against gram-positive bacteria as well as minor activity against some fungal and viral species (6). However, 2 is a mild irritant to mucosal membranes and the eyes with frequent cases of contact allergy being reported (7) as well as demonstrating cytotoxicity to mammalian cells, flammable susceptibility and a short half-life as an antiseptic (8).

1.1.2. Antimicrobial potency and minimum bactericidal concentration

CHX is mostly effective against gram-positive bacteria but exhibits strong efficacy against a variety of gram-negative bacteria, yeasts, fungi and viral pathogens (9). CHX demonstrates potent antimicrobial efficacy against many nosocomial pathogens, such as *Pseudomonas aeruginosa, Escherichia coli, Staphylococcus aureus, Acinetobacter baumannii, Klebsiella* spp*., Streptococcus* spp*., Bacillus* ssp*., Clostridium* spp*., Corynebacterium* spp. and *Proteus* spp. (1, 10), as well as some common antibacterial-resistant strains, including methicillin-resistant *S. aureus* (MRSA) (11), vancomycin-resistant *Enterococci* (VRE) (11) and carbapenem-resistant *Klebsiella pneumoniae* (12). It is also highly potent against many microorganisms found to commensally reside in the skin, including *Streptococcus pyogenes,* Viridans Streptococci, *Acinetobacter* spp*., Pseudomonas* Spp*., Actinomyces* spp*., Enterococci* spp*., Enterobacteriaceae* spp. and coagulase negative Streptococci such as *S. epidermidis, S. haemolyticus, S. lugdunensis* and *S. hominis* (13).

The minimum bactericidal concentration (MBC) is defined as the smallest concentration of an antimicrobial agent required to eliminate ≥99.9% of a bacterial species (13, 14). This concentration varies depending on the microorganism. The MBC of CHX varies between 1-30 mg/L depending on the species (13). A minimum of 2-6 mg/L is requires to eliminate common skin microorganisms such as *Escherichia coli, Staphylococcus epidermidis* and *Staphylococcus aureus* (13, 14) whilst much higher concentrations are needed to kill nosocomial pathogens such as *Enterococcus spp.* (15 μg/mL) (13)*, Klebsiella pneumoniae* (15.4 mg/L Leshem 2022, Carbapenem-resistant *K. pneumoniae* (32 mg/L) (12)*, Acinetobacter baumannii* (38.6 mg/L) (14) and *Pseudomonas aeruginosa* (12 mg/L) (13).

1.1.3. Antimicrobial mode of action

The bacterial cell wall is electronegative. Some bacteria possess teichoic acids which consist of glycerol or rubitol and phosphate repeating units bound by phosphodiester bonds. Teichoic acids are covalently bound to the peptidoglycan layer and can make up to 60% of the gram-positive bacterial cell wall (15). They provide structural stability, cell shape maintenance, regulation of cell growth and division by controlling autolytic enzyme activity, ion exchange,

charge homeostasis, antibacterial resistance and facilitate environmental interactions such as adhesion and virulence (15, 16, 17). They also play a crucial role in pharmaceutical drug targets by regulating phage binding and immunogenicity (15). Lipopolysaccharide (LPS) is a major component of the gram-negative bacterial cell wall and is also responsible for the electronegativity of this structure. LPS is highly negatively charged due to the presence of amino acids in the core oligosaccharide, phospholipids and carboxylates (18, 19). In addition, the plasma membrane is composed of protein and phospholipids which add to the cation-sequestering capabilities of the cell wall-cell membrane complex.

CHX molecules in aqueous solution are positively charged. Due to the mobility of these cations, electrostatic interactions between the CHX molecules and the electronegative bacterial cell wall-cell membrane complex occurs, facilitating passive diffusion of the antimicrobial into the cytoplasmic space. The permeation of CHX ions compromises. the integrity of the rigid, robust cell membrane, causing the cell to leak low molecular weight cytoplasmic components such as potassium ions, deactivating specific membrane-associated enzymes resulting in the inhibition of cellular respiration and supressing metabolic energy synthesis and osmoregulation of the cell (1, 5, 20). This damage is reversible if the antimicrobial concentration decreases, however, if it persists or increases, CHX demonstrates bactericidal activity by binding to phosphate-containing moieties such as adenosine triphosphate and nucleic acids causing cytoplasmic precipitation and coagulation (1, 5). In addition, the presence of CHX elevates reactive oxygen species (ROS) production, contributing to the cell membrane leakiness, lipid peroxidation and microbial cell death (21, 22, 23).

1.1.4. Chlorhexidine resistance

With the globally accelerating antibiotic resistance crisis, reduced sensitivity to clinical biocides is particularly concerning (13). Numerous nosocomial pathogens have evolved increased CHX-tolerance, including *E. coli, S. aureus, P. aeruginosa* and *K. pneumoniae*, increasing complexity of infection control (13, 14). Studies show that morphological alterations occur on the surface of susceptible cells when treated with sub-critical concentrations of CHX, unlike CHX-resistant species, which display no structural changes (21). Extensive and liberal CHX use contributed to the selective pressures applied to microbial species to evolve biocide resistant mechanisms. One study found that 86% of microorganisms that caused central-line associated bloodstream infections had demonstrated resistance to CHX following routine daily CHX bathing, whereas only 64% exhibited resistance without the bathing treatment (24).

In gram-positive bacteria, in particular *Staphylococci*, multidrug efflux pumps encoded by quaternary ammonium compound (QAC) genes such as *qacA, qacB and qacC* have evolved. Cationic biocides like CHX, are recognised by these systems as substrates and are expelled from the cell. This leads to an increase in tolerance to these antimicrobials that rely on access to the inner cellular environment to cause virulence (13, 14, 21, 25, 26, 27). For example, microorganisms that develop resistance to gentamicin, ciprofloxacin, aztreonam, cefotaxime and imipenem antibiotics have demonstrated significantly elevated resistance to CHX (28) as well as increased CHX-tolerance in carbapenem-resistant *K. pneumoniae* (12). Single nucleotide polymorphisms within chromosomal efflux genotypes, such as *norA* and *norB*, have also been described to compliment the function of QacA and QacB multidrug efflux proteins (21, 29).

Gram-negative bacteria have also evolved QacE, QacEΔ1, QacF and Mex efflux proteins to circumvent antimicrobial threats. Following exposure to sub-lethal concentrations of CHX, upregulation of these multidrug efflux systems has been described (25, 26). For example, one study in Mexico found that 24 clinical isolates of extended spectrum β-lactamase (ESBL) *Enterobacter cloacae* demonstrated a 100% resistance rate to CHX, mainly caused by the upregulation of QacEΔ1 protein (27). Further, the MexCD-OprJ is upregulated in *P. aeruginosa* following exposure to CHX, conferring resistance to the biocide (30, 31). Other families of efflux systems have evolved and are widespread across bacterial species, such as the 'Proteobacterial Antimicrobial Compound Efflux' proteins (PACE), which are becoming more abundant in gram-negative bacteria (21, 32). Other species, like *Pseudomonas*, have evolved modifications in their LPS and outer membrane protein, which aid in CHX resistance phenotypes (21). Further, intrinsic resistance to CHX is demonstrated by *Mycobacterium spp.* and bacterial endospores due to impermeable outer cell layers (9, 21).

1.2. Skin structure, function and native microbiome

The human skin is the body's largest and primary defence organ covering a surface area of 1.5-2 m^2 and accounting for approximately 15 per cent of the typical adult body mass (33, 34, 35, 36). It is a highly complex and multifunctional structure providing a physical barrier between the environment and the inner body, preventing chemical, biological, thermal and ultraviolet (UV) exposure to underlying tissues, organs and bones. The skin also helps with the retention of water and bodily fluids, thermoregulation and sensory awareness (33). The human skin is composed of three main layers, the epidermis, dermis and hypodermis, as shown in Figure 1.2, all of which vary significantly in anatomy and function (33, 37).

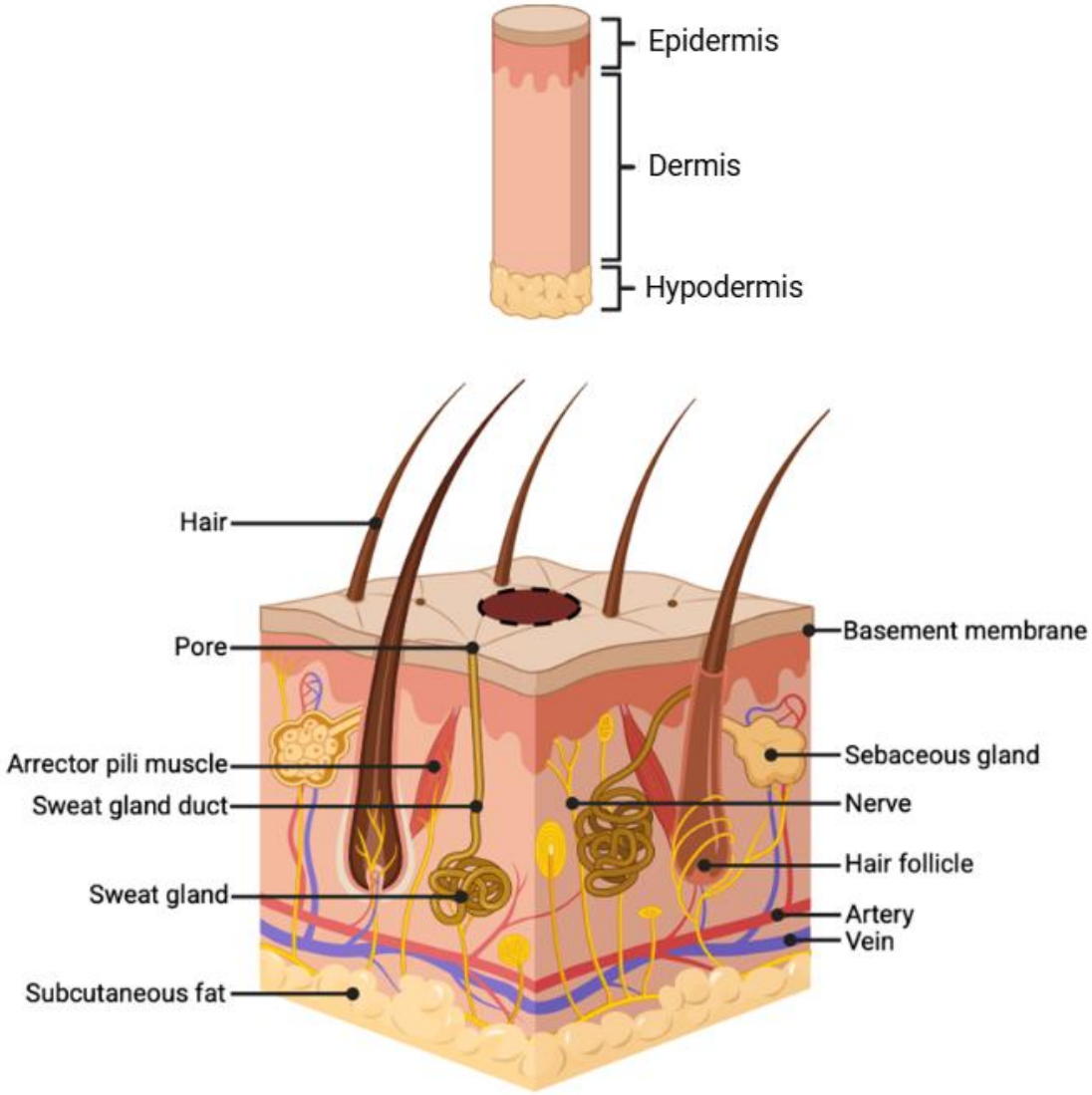


Figure 1.2. Schematic cross-section of the human skin distinguishing the three main layers, the epidermis, dermis and hypodermis and dermal structures (figure created in BioRender) Adapted from Hofmann *et al.*, 2023 (38).

1.2.1. Epidermidis and the *stratum corneum*

The epidermis is further categorised into five sub-layers, the *stratum corneum*, *stratum lucidum*, *stratum granulosum*, *stratum spinosum* and *stratum basale*. It is mainly composed of sheets of keratinocytes as well as other non-epithelial cells including Merkel cells, melanocytes and antigen-presenting dendritic Langerhans cells. Roughly every 4 weeks, fully differentiated basal keratinocytes undergo apical migration from the basement membrane, through spinous and granular layers of the epidermis to the *stratum lucidum*. This process results in the accumulation of lipids and keratin as well as the terminal differentiation of keratinocytes into corneocytes, forming the *stratum corneum* (37). Corneocytes are polygonal and organised in a highly compact and coherent arrangement to minimise skin permeability (39).

The *stratum corneum* makes up the outermost layer of the epidermis and is therefore constantly exposed to the environment. It is an essential part of the innate immune defence response

providing protection from biological threats by forming 15-20 layers (approximately 10-15 μM deep) of metabolically-inactive cells and through the secretion of defensins (37, 40). The structure of the *stratum corneum* is described by the 'bricks and mortar' hypothesis (Figure 1.3), where keratocytes (bricks) are surrounded by a hydrophobic extracellular lipid matrix (mortar) and adjoined by corneodesmosomes that provide structural rigidity and defence against the permeation of exogenous compounds and microorganisms (37, 41). The extracellular lipid matrix also plays an integral role in permeability regulation, corneocyte desquamation, antimicrobial peptide activity, toxin deactivation and chemical absorption selectivity (42).

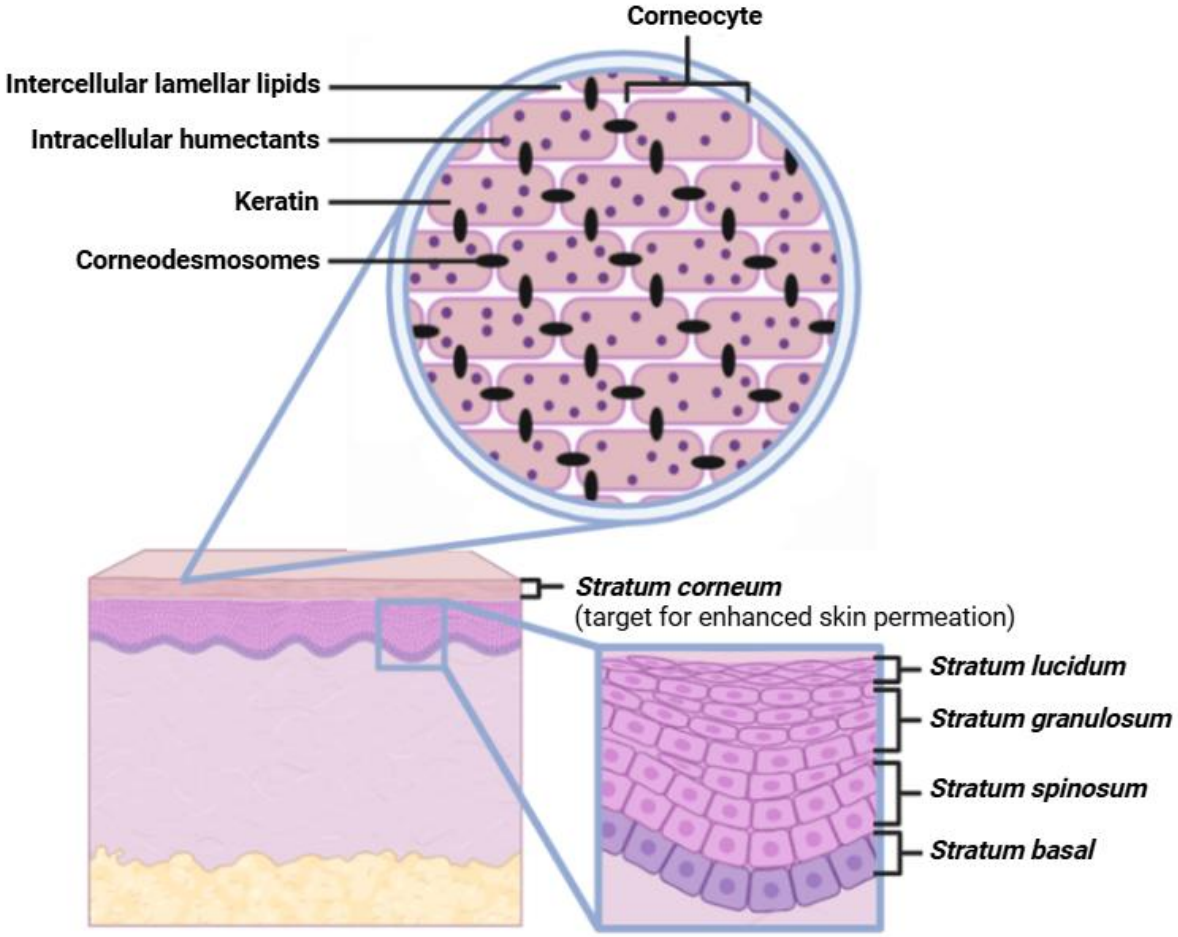


Figure 1.3. Schematic representation of the 'bricks and mortar' structure of the human *stratum corneum* and highlighting the layers of the human epidermis and target for enhanced skin permeation discussed in this thesis (figure created in BioRender). Adapted from Abdo *et al*., 2020 (37).

1.2.2. Dermis

The dermis is layer of fibrous neurovascular material and connective tissue flanked between the basement membrane of the epidermis and the subcutaneous fat layer, the hypodermis. Extracellular components such as vasculature and nerve endings, hair follicles, sweat and sebaceous glands and erector pili muscles are located here (Figure 1.2) and aid in thermoregulation and sensation (43). The dermis is mostly composed of collagen (70-80% of the skin's dry weight), particularly type I and III collagen (4:1 ratio in adult skin), which aids tissue damage repair and provides mechanical and structural integrity to the skin (43, 44, 45,

46). Collagen (type VII), in addition to other extracellular components including hyaluronic acid, help to anchor the epidermis via adhesive basement membrane zone (BMZ) components such as hemidesmosomes (43, 46). Elastic tissues such as elastin and fibrillin microfibrils provide mechanical support to the skins structure and allow flexibility of the tissue. Their biochemical arrangement facilitates the smooth movement, stretching and recoiling of these fibres (43).

The primary cell found in the dermis are fibroblasts, however other cells reside here such as mast cells, histiocytes and dermal adipocytes (43). Mast cells regulate immunological responses to microorganisms and allergens through secretion of histamine and aid in immune cell recruitment (43, 47, 48). Histiocytes are a phagocytic tissue macrophage that engulf pathogens and foreign particulate and cellular debris and initiate the immune response through antigen presentation . Mast cells and histiocytes are play key roles in the skins innate immune defence response (43). Dermal adipocytes, also aid in immune regulation by secreting various adipokines and cytokines which modulate inflammatory responses. Further, they can undergo triglyceride lipolysis to produce fatty acids (FA) which support the metabolic demands of surrounding cells and tissues. Dermal adipocytes can also transfer into myofibroblasts with aid in tissue repair as well as hair follicle regeneration (43, 49, 50).

1.2.3. Hypodermis

The hypodermis is a subcutaneous fat layer under the dermis. It is composed of areolar tissue and adipose tissue that are important for insulating the body, absorbing shock following impact, preventing damage to organs and bones and stops cohesion of the skin with the underlying muscles and bones (51, 52). It is the deepest layer of the skin and homes sensory neurones, blood vessels and less abundantly, skin appendages such as hair follicles (51).

1.2.4. Skin appendages

The human skin is abundant with epidermal and dermal-derived components known as appendages. Skin appendages include hair follicles, sweat glands, sebaceous glands and nails which all have different functions. Hairs insulate the body and protect the skin from abrasion, water, chemical and UV damage and aid in response to environmental stimuli (51, 53, 54). Sweat glands play an important role in thermoregulation (51), support of microbial growth of commensals (55), regulate human immunity and inflammatory responses (55) and secretion of pheromones (51, 56). Sebaceous glands secrete sebum that lubricates hairs and regulate microbial growth through the presence of antibacterial and antifungal triglycerides and proteolytic enzymes (51, 57).

1.2.5. The native skin microbiome

On average, three million microorganisms colonise each cm^2 of the skins surface (34). The native skin microbiome, consisting of bacterial, fungal and viral species, do not normally cause disease to their host unless the skins physical barrier becomes compromised or the balance between commensal and pathogenic species is disrupted. In fact, the relationship with their host is often symbiotic, protecting the skin from the colonisation of pathogens and breaking down natural products on the surface (58). For example, *Cutibacterium acnes* helps to maintain the skins natural acidic pH, by secreting propionic acid and cleaving sebum triglycerides into glycerol and free fatty acids (FFA), which limits colonisation of *S. aureus* and *Streptococcus pyogenes* (35, 59).

Advances in genome sequencing, from Sanger sequencing to 454 pyrosequencing, Illumina and shotgun metagenomics have enabled the resolution of different bacterial strains within a species, unlike traditional culture methods, where isolation and growth of certain strains remain challenging (58). The diversity of skin microbiota varies in anatomical location depending on physiological factors such as temperature, humidity, moisture and sebaceous (oily) environments. Species that colonises sebaceous sites, such as the face, chest and back, are predominantly lipophilic *Propionibacterium* species and auxotrophic *Malassezia* and *Corynebacterium* species that are unable to synthesise their own lipids, however, various *Staphylococci* including *S. capitis* can exist (35, 58, 60, 61). Moist and humid environments, such as the inner elbow and feet are dominated by *Staphylococcus (S. aureus, S. epidermidis, S. haemolyticus and S. homis)* and *Corynebacterium* species. The main fungal species to colonise the human skin include *Malassezia, Cryptococcus* and *Aspergillus* species (61). However, the diversity of these fungal communities in various anatomical sites doesn't vary as significantly as bacterial species, despite changes in physiology (58, 62, 63). Although bacteria are the most abundant kingdom identified to colonise the human skin, fewer fungal reference genes are known, meaning identification of these species by genome sequencing may be limited (58, 63). The colonisation of eukaryotic deoxyribonucleic acid (DNA) viruses appears to be more greatly influenced by the individual host, rather than the physiology of anatomical site (62).

Skin microbes have become tolerant to the human skin environment. For example, *Staphylococcus* species have evolved halotolerance, which allows them to withstand high salinity environments following perspiration, as well source nitrogen from the urea secreted in sweat (58). In addition, Staphylococci can adhere to the skin through the production of adherens and liberate nutrients from the *stratum corneum* by synthesising protease enzymes (58). Whilst the majority of the skin's microflora reside in superficial layers of the *stratum corneum* and upper hair follicle, anaerobic bacterial reservoirs are known to colonise the deeper epidermis, and deep hair follicle, sweat gland and sebaceous gland such as *Propionibacterium,* including *P. acnes* and *Peptostreptococci* (64, 65).

1.3. Transdermal drug transport and skin permeation pathways

The skin barrier is a challenge to the permeation of exogenous compounds and an obstacle to circumvent in the development of topical pharmaceutical drug compounds. For the majority of drug molecules, the non-viable *stratum corneum* represents the greatest challenge to transdermal permeation. The hydrophobicity of the *stratum corneum* due to the presence of intracellular and extracellular keratin proteins, as well as intercellular lamellar lipids composed of phospholipids (such as sphingomyelin), ceramides, cholesterol and FFA inhibits the permeation of hydrophilic compounds (66, 67, 68). Transdermal permeation of lipophilic drug compounds is limited by the high water content of the viable epidermis, composed of the *stratum granulosum*, *stratum spinosum* and *stratum basale* (69, 70). Other challenges to percutaneous delivery include drug metabolism within the skin, preventing actives reaching their target site (71) as well as compound binding to components of the skin preventing diffusion through the skin. For example, doxycycline binds to the intracellular keratin proteins within the *stratum corneum* corneocytes (72). Depending on their physicochemical properties, drug molecules can traverse the *stratum corneum* following three routes, the intracellular, intercellular and appendageal permeation pathways (69, 73).

1.3.1. Intracellular pathway

The intracellular permeation pathway is a discontinuous and direct route through the *stratum corneum* (Figure 1.4). Exogenous compounds must navigate through lipid plasma membranes and aqueous keratin matrices of dermal corneocytes, as well as the intercellular lamellar lipids. Due to fluctuations in hydrophilic and lipophilic environments, traversing the *stratum corneum* following this pathway is often challenging and highly relies upon the polarity of the exogenous compound (74, 75). Molecules must undergo multiple partitioning phases resulting in molecular rearrangement to allow diffusion between the aqueous and lipid environments of the *stratum corneum*, which is highly unfavourable for most drug compounds (76, 77). Intracellular permeation of compounds that exhibit high hydrophilicity are limited by the extracellular lipid lamellae and numerous lipid bilayers throughout the *stratum corneum*, whilst hydrophobic molecules are limited by the aqueous intracellular domain of the epidermal corneocytes (69).

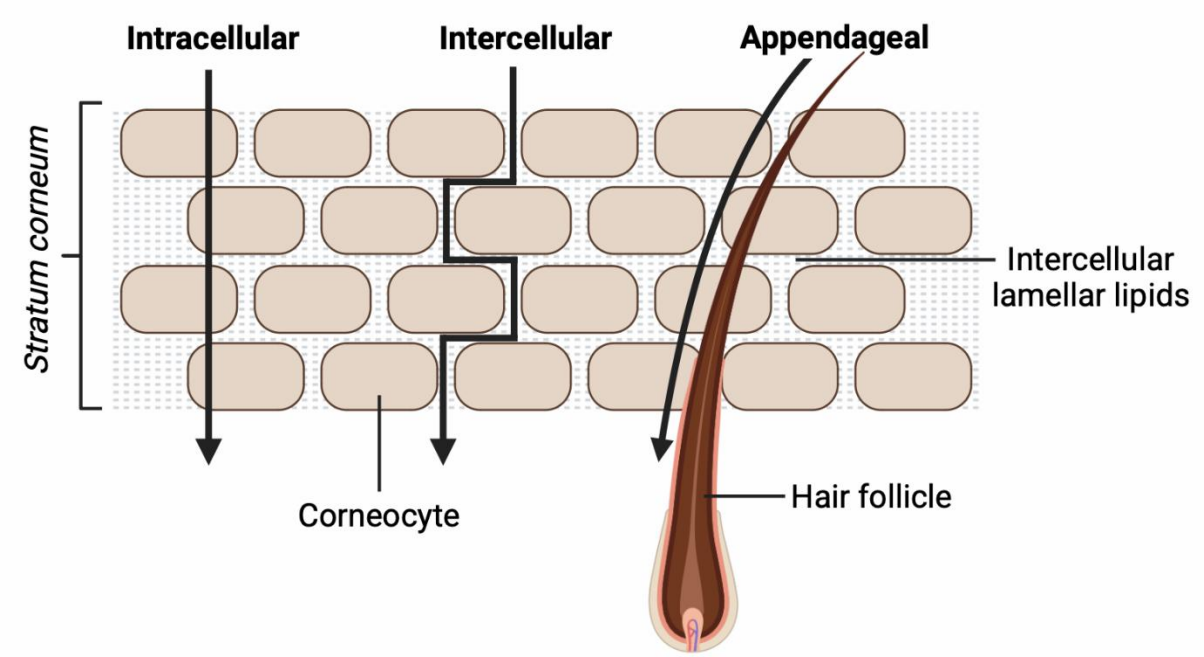


Figure 1.4. Schematic of drug permeation pathways through the *stratum corneum* (figure created in BioRender). Adapted from Bolzinger *et al*., 2012 (69).

1.3.2. Intercellular pathway

The intercellular permeation pathway allows diffusion of drug molecules to occur through the extracellular matrix (ECM) surrounding keratinocytes in a tortuous pattern (Figure 1.4). This pathway is most favoured by small lipophilic molecules, typically below 500 Da, that can navigate through the tight lipid junctions and traverse the *stratum corneum* (74, 78, 79). The ECM is composed of lipid lamellar bilayers that form a significant proportion (approximately 10%) of the *stratum corneum's* volume (80) and form a barrier to water preventing permeation of aqueous formulations (81). Further, corneodesmosome degradation appears to result in the development of aqueous pores in the *stratum corneum* which may be exploited by drug molecules that embody some hydrophobic properties (80). Whilst the intercellular pathway is the most dominant route for topical drug absorption and delivery, it is dependent on the drug molecule's balance between lipid and aqueous solubility (79, 82).

1.3.3. Appendageal pathway

The appendageal permeation pathway allows passage of exogenous compounds by exploitation of skin appendages such as hair follicles, sebaceous glands and sweat ducts (Figure 1.4). Due to reduced barrier properties of these appendages, small molecules and atypical penetrants can bypass the *stratum corneum* and rapidly access the deeper, viable skin layers and the bloodstream (78, 83). However, as skin appendages account for 0.1% of the total skins surface area, drug permeation via this pathway is not typically substantial for delivery of an efficacious dose (78).

1.4. Physicochemical properties of drugs that effect transdermal permeability

There are many drug molecule characteristics that can impact their effectiveness and rate of permeation through the skin. These properties are important to consider when delivering active ingredients percutaneously. Drug physicochemical properties that can affect skin permeation include its molecular size, lipophilicity, aqueous solubility, the acid dissociation constant (pKa), melting point and hydrogen bonding.

1.4.1. Molecular size

The molecular weight of the permeating compound plays a significant role in its ability to traverse the skin. The inverse relationship between molecular weight and transdermal flux explains that larger molecules permeate through the skin much slower and less effectively than smaller molecules (84). Optimal transdermal delivery is achieved when the molecular weight is 500 Da (84, 85, 86).

1.4.2. Partition coefficient

The partition coefficient (log *P*) is a parameter that measures equilibrium partitioning of a solute between two liquid phases, typically an aqueous phase and an organic lipid phase (often octanol). Log *P* values indicate whether a compound has equal affinity to the two phases (log $P = 0$), or favours either aqueous (log $P < 0$) or lipid (log $P > 0$) environments (87). The partition coefficient helps to determine what permeation pathways drug molecules will exploit to traverse the *stratum corneum*. Typically, drug molecules with a higher affinity to lipid environments will preferentially partition into the intercellular lamellar lipid bilayers of the extracellular cavity and hence utilise the intercellular permeation pathway (74). However, compounds with a stronger affinity for an aqueous phase, may favour partitioning into the hydrated, keratin-rich intra-keratinocyte environment and exploit the intracellular permeation pathway through the *stratum corneum* (74). Typically, for optimal transdermal drug delivery, molecules should be lipophilic and therefore have a low partition coefficient value (74). However, it is preferable that these drug molecules have sufficient aqueous partitioning properties to ensure effective delivery through the remaining aqueous viable epidermis and dermis and ensure clearance through blood capillaries at the epidermal-dermal junction (76).

1.4.3. Acid dissociation constant

The pKa is a physicochemical parameter used to understand how pharmaceutical compounds will behave when introduced into biological systems (88). It defines the relative strength of an acid or base by determining when a drug compound will equilibrate between becoming dissociated and undissociated (50% ionised) in water (89). The dissociation of drug molecules will impact its solubility in lipid and aqueous environments. Most pharmaceutical drug compounds are either weakly acidic or weakly basic (90). This is because only small fluctuations in pH are required to shift the compound between its uncharged (lipid-soluble) and charged (water-soluble) states, and vice versa (89). Lipid-soluble compounds will diffuse through lipid membranes and therefore navigate through the intercellular lamellar lipid bilayers and surpass the *stratum corneum* more easily (89).

1.4.4. Melting point

Typically, compounds with a high melting point exhibit poor aqueous solubility (91). Further, compounds that possess a high degree of symmetry correlate with high melting points, hence symmetrical drug molecules typically display low aqueous solubility and therefore poor transdermal permeation (91). Ideal drug candidates should have a melting point below 200°C to ensure sufficient water solubility and therefore absorption through the viable epidermis and clearance through capillaries at the epidermal-dermal junction (92).

1.4.5. Hydrogen bonding

80% of the ceramides, triglycerides, cholesterol and FFA that make up the *stratum corneum* intercellular lipids are nonpolar and slightly hydrophilic due to the presence of hydrophilic groups. These groups can form hydrogen bonds with drug molecules, reducing the number of free molecules available for transdermal permeation (93, 94). Hydrogen bonds most frequently occur between nitrogen, oxygen and fluorine (95), hence transdermal permeation of drug molecules that contain carboxyl, hydroxyl, amine and alcohol, functional groups are most likely to be limited by interactions with the skin (96, 97).

1.5. Transdermal permeation of Chlorhexidine

CHX formulations have been listed as the first-choice surgical skin antiseptic in the United Kingdom (UK) by the National Institute for Health and Care excellence (NICE) and subsequently is widely used to prevent SSI. However, recent research has highlighted that CHX exhibits poor transdermal permeation. Studies into permeation depth of the antimicrobial have concluded that sub-optimal penetration through full-thickness human skin occurs following exposure for 30 minutes or less (98). Significant elevation in CHX permeation through human skin can be observed following 24 hours exposure, with the greatest delivery to the upper 100 μM of the skin (98). It is recommended that CHX formulations are in contact with the skin for a minimum of 2 minutes prior to surgery (98, 99, 100) however, poor permeation of the antimicrobial occurs after short time exposures.

1.5.1. Chlorhexidine physicochemical properties and poor permeation

Some physicochemical properties of CHX, including its partition coefficient (log $P = 0.037$ in octanol/water) (101) and acid dissociation constant (pKa = 10.45) (102) suggest that CHX should demonstrate effective transdermal permeation. Whilst demonstrating high aqueous

solubility (103) CHX has a low log *P* value, suggesting that the drug is moderately favourable to lipid environments. This suggests that CHX will partition and permeate through the lamellar lipid bilayers of the intercellular matrix, whilst having sufficient aqueous solubility to pass through water-containing environments such as the viable epidermis and dermis. Further, the pKa value suggests that CHX is a weak base and is therefore desirable as small fluctuations in pH are required to shift the drug from its uncharged, lipid-soluble state to its charged, water-soluble state (89).Further, CHX has a relatively low melting point (134°C) and therefore displays good aqueous solubility (104). The drug is not limited by its high molecular symmetry, which typically increases the melting point and therefore reduces aqueous solubility (91). The melting point of CHX is within the desirable range for topical pharmaceutical candidates (92).

Despite these desirable properties, CHX demonstrates poor transdermal permeation which may be attributable to its relatively high molecular weight (11). Under physiological pH, CHX (897.8 g/mol) dissociates into its base moiety, $C_{22}H_{30}Cl_2N_2^+$ (505.4 g/mol) (11, 105). This, along with the 2 large chlorophenylbiguanide groups may hinder the permeation of the molecule (105) as bigger molecules generally exhibit poor transdermal permeation (84). In addition, CHX contains 4 imine groups (C=NH) and 6 secondary amine groups (C-NH) throughout its molecular structure. These functional groups can form 8 hydrogen bonds (6 hydrogen donor, 2 hydrogen acceptor) with the lipid components of the *stratum corneum* therefore reducing the effectiveness of transdermal drug delivery (106, 96, 93). This would justify why CHX provides prolonged surface antimicrobial activity, as bactericidal and fungicidal concentrations of CHX can be detected on the skin's surface following >24 hours post-exposure (107). However, in clinical applications where CHX is used to provide rapid and effective skin antisepsis, poor drug permeation may result in limited efficacy of the antiseptic formulation and therefore insufficient clearance of microorganisms which pose a risk of SSI following procedures (98).

1.5.2. Chlorhexidine permeation pathway

CHX is highly water soluble meaning that it is possible for drug molecules to penetrate through the corneocytes and crosses the *stratum corneum* via the intracellular route (11). In addition, the polar head groups of the intercellular lamellar lipids are 10-fold less hydrated than typical cellular phospholipid bilayers, with approximately 1-2 water molecules forming hydrogen bonds with each head group (108, 109). It is hypothesised that CHX exploits this thin aqueous pathway to permeate the *stratum corneum*, avoiding repeat partitioning that is required by traversing the lipid and aqueous phases of the intracellular pathway (11). Further, CHX is lipophilic hence may traverse the *stratum corneum* through the intercellular lamellar lipids (110). However, it has been reported that CHX binds to extracellular lipids such as cholesterol in the *stratum corneum* which may limit the effectiveness of transdermal delivery (111).

1.6. Enhancement of chlorhexidine permeation through the skin

1.6.1. Formulation composition

Karpanen *et al*, 2009 (112) studied the effect of alcohol on the permeation of CHX through full-thickness excised human skin after 2 and 30 minutes exposures. When formulated with 70% *(v/v)* isopropyl alcohol (IPA), CHX permeation was limited throughout the skin after both time points, with <0.0008 μg/mg tissue being recovered between 300 - 1500 μm depth of the

skin. After 2 minutes exposure, significantly more CHX was recovered from the upper 100 µM when formulated with IPA compared to CHX alone (Figure 1.5A). The addition of IPA to the formulation did not significantly enhance the delivery of CHX through the skin after 30 minutes exposure (Figure 1.5B). No CHX permeated through the full thickness skin occurred with either treatment (112).

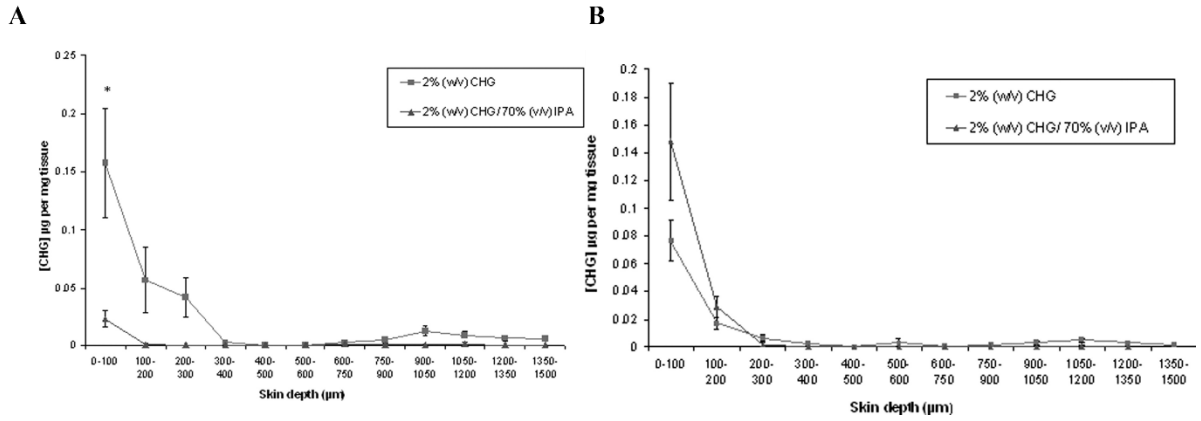


Figure 1.5. Permeation of alcoholic and aqueous CHX formulations through full thickness excised human skin determined by HPLC. (A) CHX concentration recovered from skin sections when treated with 2% CHX formulated with either 70% *(v/v)* IPA or CHX after 2 minutes. (B) CHX concentration recovered from skin sections when treated with the same formulations after 30 minutes. Figures from Karpanen *et al,* 2009 (112).

Karpanen *et al,* 2010 also studied the permeation effect of formulating eucalyptus oil with CHX through excised human skin after 2 and 30 minutes (213). After 2 minutes, between 0.019 - 0.043 µg/mL CHX was recovered at depths of 300 – 1500 µm (Figure 1.6A), which is greater than CHX formulated alone or with IPA as demonstrated by Karpanen *et al,* 2009. Enhanced CHX delivery through human skin was also achieved by increasing the concentration of eucalyptus oil from 5% *(v/v)* to 10%, 20% and 50% (Figure 1.6B). Further, by combining 10% *(v/v)* eucalyptus and 70% *(v/v)* IPA into the CHX formulation, bioavailability of the biocide was enhanced throughout the skin (Figure 1.6C) (113).

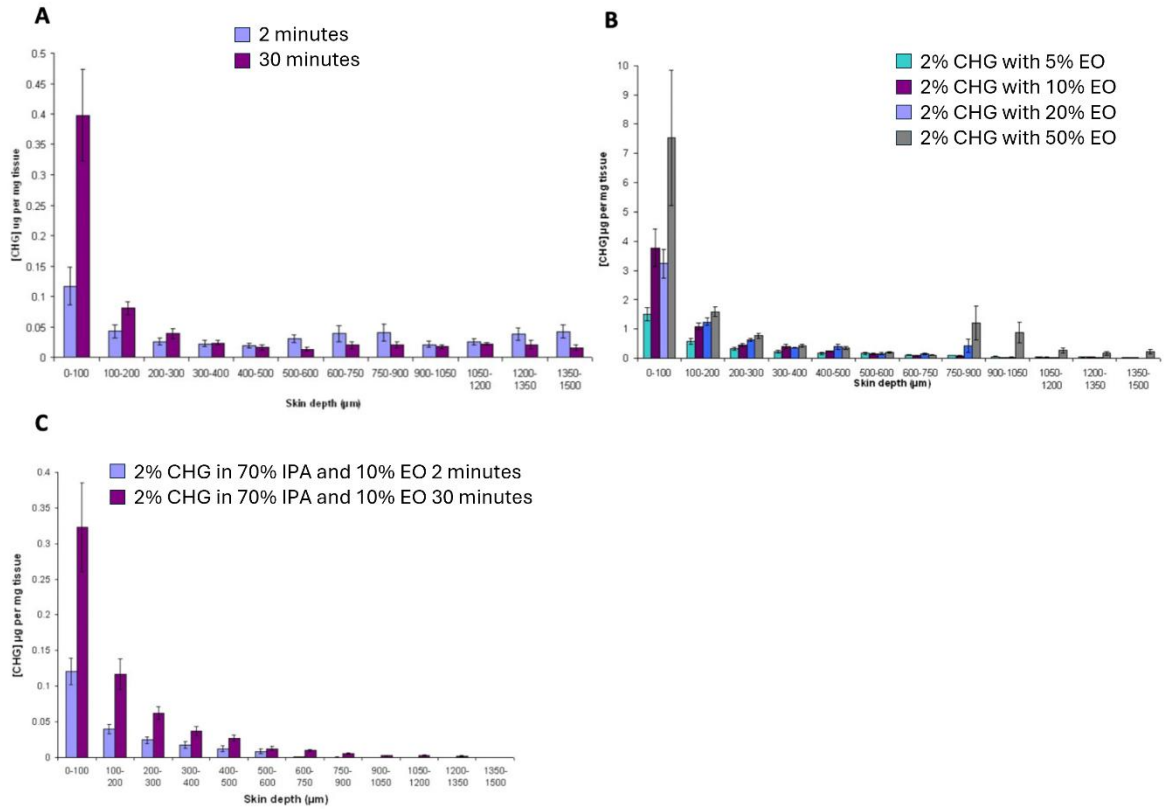


Figure 1.6. Permeation of CHX when formulated with eucalyptus oil through full thickness excised human skin determined by HPLC. (A) Concentration of CHX throughout the skin when treated with 2% *(w/v)* CHX with 50% *(v/v)* eucalyptus oil. (B) CHX concentration at different skin layers after 24 hours when treated with 2% *(w/v)* CHX formulated with either 5%, 10%, 20% or 50% *(v/v)* eucalyptus oil. (C) CHX concentration throughout the skin when treated with 2% *(w/v)* CHX combined with 70% *(v/v)* IPA and 10% *(v/v)* eucalyptus oil after 2 and 30 minutes. Figures from Karpanen *et al,* 2010 (Karpanen *et al.*, 2010) (113).

The enhancement of CHX permeation though full-thickness excised human skin using the terpene, 1,8-cineole was attempted by Casey *et al*, 2017 (114). They concluded that when formulations containing 2% *(w/v)* CHX and 70% *(v/v)* IPA were combined with 2% *(v/v)* 1,8-cineole, on average, significantly more CHX was delivered through the skin, with 33.3% (Figure 1.7) more CHX being recovered from skin samples containing the terpene compared to without (114). Further, synergistic activity between 1,8-cineole and CHX has been demonstrated with a greater antimicrobial efficacy against clinically relevant microorganisms including *S. aureus,* MRSA*, Klebsiella pneumoniae, E. coli, Enterococcus faecalis* and *Candida albicans.* No change in efficacy was demonstrated against *P. aeruginosa* (115).

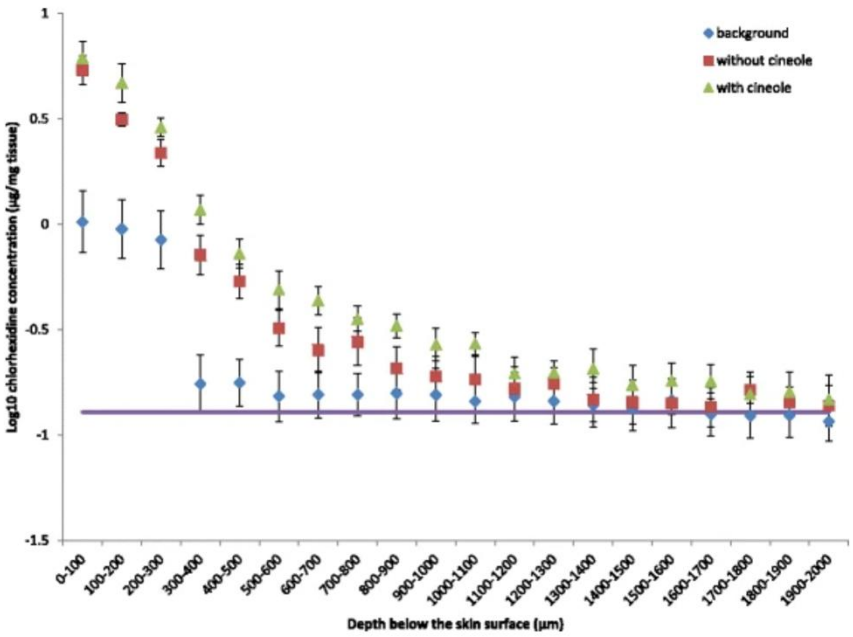


Figure 1.7. Permeation of CHX when formulated with 70% *(v/v)* IPA and 2% *(v/v)* 1,8-cineole determined by HPLC. Figure from Casey *et al,* 2017 (114).

1.6.2. Dendrimer-mediated permeation

Kirkby *et al,* 2021 studied the effect of third generation polyamidoamine dendrimers (G3 PAMAM-NH_2) on the permeation of CHX (11). 4% *(w/v)* CHX was formulated with 0.5 mM or 1 mM G3 PAMAM-NH_2 and applied to *ex vivo* porcine skin for 24 hours using an *in vitro* Franz-type diffusion cell. Compared to treatment with 4% CHX alone, the 1 mM dendrimer co-formulation resulted in a 2.7-fold and 1.8-fold increase in CHX delivery to the upper and lower *stratum corneum*, respectively. Limited enhancement of CHX permeation was observed when treated with the 0.5 mM PAMAM-NH_2 formulation compared to the 4% CHX treatment alone, however, both PAMAM-NH_2 formulations exhibited enhanced CHX delivery compared to the commercial benchmark, Hibiscrub. No CHX was quantified in the receptor fluid for any treatment therefore permeation through full thickness skin did not occur (11).

1.6.3. Microneedle pre-treatment

Kirkby *et al*, 2022 investigated the effect of a microneedle pre-treatment on the effect of CHX permeation enhancement (116). *Ex vivo* porcine skin experienced either a 12-array or 36-array stainless steel microneedle pre-treatment for 10 seconds with 8000 rpm before being assembled into a Franz-type diffusion cell and treated with a 2-hydroethylcellulose (HEC) gel containing 1% or 4% *(w/v)* CHX or the clinical formulation Hibiscrub (4% *w/v* CHX) for 24 hours. Generally, CHX permeation into the *stratum corneum* was much more effective following microneedle pre-treatment prior to formulation application. The 36-array microneedle pre-treatment resulted in a significant enhancement of CHX delivery compared to the 12-array microneedles for 1% CHX, 4% CHX and HibiScrub formulations (116). Further, the fabrication of CHX-loaded poly(lactic-co-glycolic acid) (PLGA) microneedles for the treatment of oral diseases is being investigated. They have demonstrated sustained drug release and antibacterial activity against *Streptococcus mutans* for up to 8 days. Further, they exhibited weak antibiofilm and anti-metabolic activity on established biofilms making them potentially promising for oral treatments (117).

1.7. Experimental methods to study skin permeation

1.7.1. *In vivo* sampling

In vivo tape stripping is a method of analysing *in vivo* skin permeation. It involves applying adhesive tape to the skin, applying pressure to ensure sufficient contact with the skin is achieved, followed by sequential removal the tape strip to harvest consecutive layers of the *stratum corneum* (Figure 1.8). This method has been in various avenues of dermatology research including understanding the epidermal barrier function (118, 119), dermatopathology and gene expression (120), profiling the *stratum corneum* pH and lipid content (121), topical drug delivery (122), wound healing (123, 124) and epidermal microbiome analysis (125). Tape stripping is a simple, non-invasive and relatively painless procedure as it involves the removal of dead cells and the lipid matrix that they are embedded in. Further, the integrity of the skin's barrier function is rapidly restored following the removal of corneocytes due to the body's innate homeostatic repair response (119).

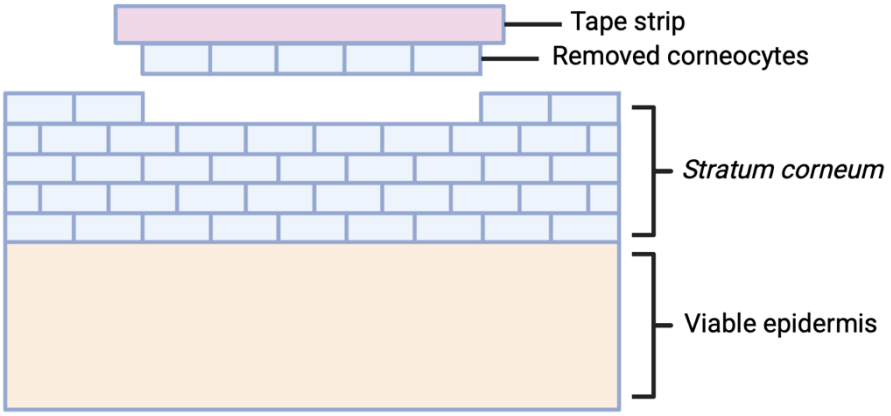


Figure 1.8. Schematic representation of the *in vivo* tape stripping process (figure created in BioRender). Adapted from Nair *et al.*, 2013 (126).

In drug delivery experiments, methodologies include topical drug application followed by corneocyte removal via tape stripping, an extraction process that involves recovering the tape strip contents into solvent and quantitative analysis, typically chromatographic methods such as high performance liquid chromatography (HPLC) are used. Normally, the first tape strip is discarded as it represents the unabsorbed drug (127). Although tape stripping is generally perceived as a simple and efficient method for sampling the *stratum corneum*, it is limited by several intrinsic and extrinsic factors (127). Intrinsic limitations include the size of corneocytes, which is affected by the anatomical sampling location, age and geographical season, transepithelial water loss, which is impacted by race, skin type and season, and the presence of skin furrows (127). Extrinsic factors that cause variations in tape stripping include the type of tape used, duration and weight of applied pressure, velocity of tape strip removal and the topical application of substances (127). These factors should be taken into consideration what developing experimental methodologies to minimise variability.

The Human Tissue Act 2004 regulates the removal, storage, use and disposal of human tissues, in England, Wales and Northern Ireland (128). The collection human corneocytes by tape stripping is covered by this legislation, meaning that licencing and approval, code of practice and consent must be considered before undergoing research.

1.7.2. *In vitro* sampling

In vitro permeation experiments to study transdermal drug delivery are normally performed using Franz-cell diffusion models. As schematically represented by Figure 1.9, this technique involves monitoring the permeation of compounds from a donor chamber, through excised skin and into the receptor chamber typically filled with a physiological buffer solution (74, 129, 130). Franz-cell permeation models are widely used to investigate drug delivery through membranes as they require no continuous sample collection, minimal tissue handling and only small quantities of drug are needed for analysis (130). Further, they can provide quick information for primary investigations regarding permeation efficacy of topical drug formulations whilst circumventing limitations such as participant recruitment and consent and ethical and legal legislation that accompanies *in vivo* human tissue sampling.

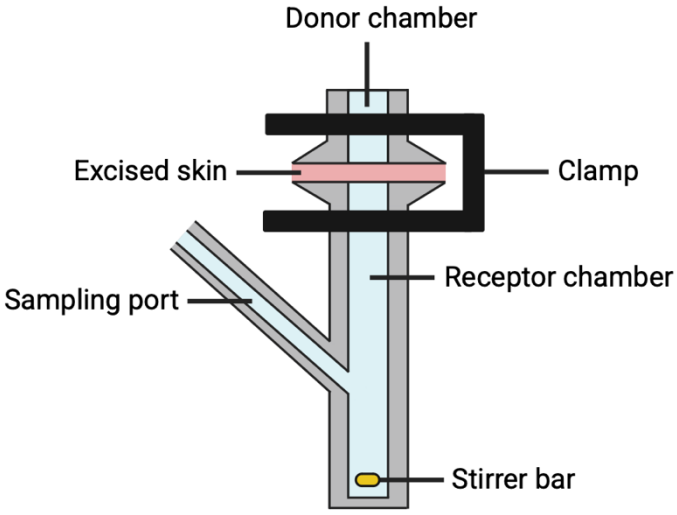


Figure 1.9. Schematic representation of a Franz-cell diffusion model (figure created in BioRender). Adapted from Supe et al., 2020 (74).

In vitro tape stripping experiments can provide information regarding the permeation of exogenous compounds to understand how permeation may occur across human skin (131). *In vitro* drug delivery experiments using Franz-cell diffusion models are frequently followed by *in vitro* tape stripping to collect layers of the *stratum corneum*. These tape strips are analysed to determine the bioavailability of drug throughout the *stratum corneum*, giving insight into the permeation of various topical formulations (116, 132, 133).

1.8. Antimicrobial surfaces

Every year, healthcare-associated infections (HAI) account for 37,000 deaths in Europe and 99,000 deaths in the United States of America, costing €7 billion and $6.5 billion, respectively (134). A significant proportion of these HAI are attributable to multiple drug-resistant (MDR) pathogens that develop as an evolutionary response to the overuse and misuse of antibiotics. Historically, MDR pathogens were considered nosocomial; however, since the early 2000s, these complicated infections could be community-acquired, with species such as MRSA being identified in public areas, including in airports, day-care facilities and on public transport (134).

Pathogens can persist upon inanimate surfaces for extended periods of time, sometimes months (Table 1.1). The rapid transmission of these bacterial, fungal and viral pathogens is an increasing concern that can lead to the outbreaks of seasonal epidemics (e.g. influenza) or even pandemics (e.g. 2019 SARS-Cov-2). The most common transmission route of microbes is through contact with contaminated public and household surfaces, such as door handles, switches, television remotes and hand railings (135). To circumvent disease transmission caused by this route, it is essential to understand how microorganisms interact with these surfaces allowing them to attach and grow in hospital and community environments.

Table 1.1. Bacterial and viral persistence on dry inanimate surfaces. Table adapted from Cassidy, 2020 (134).

	Species	Period of detectability	Disease
Bacterial pathogens	*Clostridium difficile*	5 months	Bowel infection, diarrhoea
	Escherichia coli	36 days	Kidney failure, bloody diarrhoea, vomiting
	Klebsiella spp.	32 days	Pneumonia, septicaemia, meningitis
	Staphylococcus aureus	>90 days	Pneumonia, septicaemia
Viral pathogens	Influenza	2 days	Influenza
	Norovirus	7 days	Gastroenteritis
	Rhinovirus	4 days	Common cold
	SARS-CoV-2	3 days	COVID-19

1.8.1. Antimicrobial surfaces, uses and benefits

Antimicrobial surfaces are becoming a more recognised and applied approach to tackle the spread of microorganisms, particularly within industries related to healthcare, food preparation, public transport, household hygiene and sportswear. Antimicrobial surfaces are an effective and sustainable method to prevent biofouling of a broad spectrum of microorganisms by one of two approaches, microbicidal or static activity. Surfaces that exhibit microbicidal activity prevent disease transmission by killing the microbes when they come into contact with the interface, whilst static activity targets their ability to attach, survive or grow (135).

The most common strategy to eliminate microorganisms from contaminated surface is the use of chemical sanitisers such as chlorine, hydrogen peroxide, sodium hypochlorite and alcohol. However, cleaning surfaces with chemicals can be practically and economically challenging, particularly for large areas (135). Further, effective cleaning of surfaces is heavily reliant upon cleaning staff being thorough and meticulous in their work. One study used a fluorescent tracer to analyse cleaning regimens across 27 surfaces within an intensive care unit. They concluded that only 48.1% of surfaces were disinfected appropriately with frequently touched surfaces such as door handles and bathroom light switches receiving less cleaning, 25% and 26%, respectively (134, 136). In addition, routine exposure to cleaning chemicals is extremely harmful to health and has been associated with long-term heart and lung diseases, respiratory complications, skin irritation/dryness and alcohol poisoning. The use of UV to decontaminate surfaces can also lead to skin burns and cancer (135).

Antimicrobial surfaces are highly practical and economical as once installed as they do not require any treatment such as routine cleaning. This means that when applied correctly, all surfaces will exhibit uniform antimicrobial efficacy ensuring all areas are effectively decontaminated without reliance upon the thoroughness of cleaning staff. Further, they

circumvent health risks associated with cleaning chemicals (135). There are numerous types of antimicrobial surfaces on the market and being developed including polymers, mechano-bactericidal nanomaterials, superhydrophobic coatings and antimicrobial peptide-coated surfaces. Surfaces may contain materials such as silver, silver nanoparticles, copper, copper oxide nanoparticles, zinc, zinc oxide nanoparticles, titanium dioxide and titanium dioxide nanoparticles, which will be discussed in this chapter.

1.9. Antimicrobial metals and metal nanoparticles

Certain metal surfaces demonstrate contact-killing antimicrobial activity through the release of free metal ions which can either cause microbial cell death or prevent cellular growth and/or division, as well as interfere with genetic material (137, 138). In 1893, Carl Nägeli named this process the oligodynamic effect. Metal surfaces including silver, copper, zinc and titanium exhibit the ability to reduce microbial survival, thereby reducing the spread of disease (139). For example, it was identified that using copper materials to replace stainless steel railings, shopping carts and lighting fixtures contributed to infection control on these high-touch surfaces (140).

There is also a growing interest in the use of metal oxide nanoparticles (MO-NP) as a potential strategy to circumvent antimicrobial resistance. The use of nanobiotechnology is growing exponentially with a variety of industries already successfully implementing their use, such as medicine, cancer therapy, drug delivery, food preparation and production, agriculture, wastewater treatment and environmental science. The global production of nanoproducts in 2016 was $12.7 billion which contributed to 0.01% of the global gross domestic product (GDP). It is predicted that the percentage of these nanoproducts in GDP will reach 40% by 2035 (141). MO-NP are semiconductive materials that are between 1 and 100 nm in at least one dimension (142, 143). The main properties that are important for the function and microbicidal activity of MO-NP include their size, shape, surface energy and valence state (143, 144).

The size of MO-NP is essential for its antimicrobial activity with smaller particles exhibiting greater toxicity than larger particles. Park *et al*., 2011 demonstrated that 20 nm silver nanoparticles significantly elevated the production of ROS compared to 80 nm and 113 nm particles, however, also lead to increased mammalian cytotoxicity in murine L929 fibroblasts (145). The shape of MO-NP are also crucial for their function and purpose and can influence their ability to penetrate cells (143). Chithrani *et al.,* 2006 showed that nanospheres more readily enter cells compared to nanorods (146). However, the shape of MO-NP can also impact their cytotoxicity profile in human cells, as demonstrated by Hsiao & Huang., 2011, who concluded that zinc oxide nanoparticles were significantly more cytotoxic to human lung epithelial cells than nanospheres (147). Common metal and MO-NP include silver, copper, copper oxide, zinc oxide, titanium oxide and nickel oxide, all of which exhibit broad-spectrum microbicidal activity (148).

1.9.1. Antimicrobial silver surfaces

Ionic silver (Ag^{+}) displays high antimicrobial efficacy and has been used for wound healing for centuries. It has been utilised on hospital surfaces to reduce the rate of nosocomial disease transmission and in water cleaning systems to eliminate contamination (149). More, recently,

silver-coated materials have been used for the development of antimicrobial medical devices, including orthopaedic implants, which have significantly reduced implant-associated infections, as well as urinary tract and central venous catheters (150). Silver surfaces display antimicrobial properties through numerous ways. They work by causing disruptions to the bacterial cell membrane, as well as impairing protein and enzyme metabolism through ionic interactions with the silver ions (150). In addition, they can inactivate or denature specific molecules and cause DNA damage directly (150).

Silver ions cause microbial toxicity by binding strongly to DNA and can form complexes with DNA and ribonucleic acid (RNA), with a high affinity for guanine (149). *In vitro* microscopy experiments have demonstrated that silver ions cause DNA modifications which can lead to mutation or termination of microbial replication processes (149). In addition, silver targets and binds to the sulphur in sulfhydryl groups present in lateral cysteine chains (149). Cysteine is a frequent ligand for metals and cofactors in metalloproteins which play an important role in cellular respiration (149). Bragg and Rainnie, 1974 were able to show that silver ions modified the respiratory processes in *E. coli* which was due to the inhibition of protein motive force (PMF) (151). Other studies have demonstrated that silver ions can cause proton leakage in *Vibrio cholerae*, which is possibly associated with PMF inhibition. Ag^{+} also interact with thiol containing cytoplasmic proteins such as OxyR, which senses H_2O_2 and activates transcription. Interference with such proteins can lead to protein production (149).

1.9.2. Antimicrobial silver nanoparticles

Many commercial antimicrobial surfaces are nanocomposites, meaning that they incorporate nanoscale materials such as silver nanoparticles (AgNP). They display broad-spectrum antimicrobial activity against a variety of gram-positive and gram-negative bacteria, viral species and MDR strains (134)**.** These AgNP-based antimicrobial surfaces are commercially available and work by releasing AgNP into the environment which have a strong affinity for sulphur proteins present on the bacterial cell wall and cell membranes (152). AgNP become internalised, disrupting the cell wall and cell membrane integrity. They cause deactivation of respiratory enzymes leading to the production of ROS which interrupts adenosine trisphosphate (ATP) generation and damages DNA, interfering with DNA replication and cell reproduction (152, 153). Further, can denature cytoplasmic ribosomes which causes inhibition of protein synthesis (152).

Despite the growing market, the use of AgNP-based antimicrobial surfaces is limited. As silver is released into the environment by these surfaces, they are finite and have a limited shelf-life. In addition, silver is an expensive raw material making regular replacement of these surfaces' undesirable. Further, AgNP can cause cytotoxicity, genotoxicity and the activation of immunological responses within mammalian cells, even in low doses (154, 155). AgNP have demonstrated an ability to permeate into animal cells (156). Research has shown that AgNP internalisation causes oxidative stress though the production of ROS causing DNA damage and the activation of antioxidant enzymes (154, 155, 156)**.** This leads to the depletion of antioxidant molecules such as glutathione (156), which is heavily involved in the support of cellular processes, redox homeostasis, organelle function and cell protection from DNA damage (157). One study demonstrated that the accumulation of AgNP within the nucleus leads to DNA damage, chromosomal aberrations and cell cycle arrest, halted in G2/Mitosis interphase, inhibiting cell proliferation (155). With the increased application of AgNP in the development of antimicrobial materials, there is growing concern that exposure to these materials may cause log-term health implications to biological systems.

1.9.3. Antimicrobial copper surfaces

The earliest documented use of copper for its antimicrobial properties dated back between 2600 and 2200 B.C in Egypt, where the metal was used to sterilise chest infections and drinking water. Since then, it has been used to treat headaches, burns, infections, intestinal parasites, and for general hygiene. Awareness of copper's antimicrobial properties were highlighted in 1832 when copper workers demonstrated immunity to the cholera outbreak. As a result, its use has become widespread in the medical industry (158). Microbial toxicity of copper has led to the development of antimicrobial copper surfaces which result in rapid and effective microbial elimination. Grass *et al,* 2010 reported that contact killing with copper surfaces results in at least a 7-8 log microbial reduction per hour, with no recovery of microbes after prolonged exposure. It has also been reported that as little as 1 minute is necessary to kill certain strains of *E. coli* (159), 30 minutes for *Clostridoides difficile* (160), 45 minutes for MRSA (161) and 60 minutes for *Candida albicans* (162).

The U.S Environmental Protection Agency listed copper and copper alloys as the first solid antimicrobial material and since has been used to reduce nosocomial and community infection on high-touch surfaces such as door handles, bathroom fixtures and bed rails (158). Copper ions undergo redox-cycles and fluctuate between Cu(I) and Cu(II). This causes ROS which in turn, cause lipid peroxidation, protein oxidation and DNA damage (163). Cu(I) has a strong affinity for thiolates that are present in cysteine, glutathione and other proteins involved with catalysis, cell signalling and antioxidant defence mechanisms (163). Further, it has been reported that the presence of copper ions reduces the iron-sulphur cluster stability leading to increased iron and sulphur accumulation in *E. coli* and *Bacillus subtilis* (163). In *E. coli,* copper ions deactivate components within the amino-acid synthesis pathway, Krebs cycle and pentose phosphate pathway. This is lethal due to inhibition of essential processes including protein production, energy generation, DNA replication and NADPH production essential for anabolic reactions, antioxidant defence and signalling (163).

1.9.4. Antimicrobial copper nanoparticles

Copper oxide nanoparticles (CuO-NP) are also used for their broad-spectrum bacterial and antifungal properties. They exploit a variety of mechanisms to exhibit microbicidal effects including direct interaction with the cell membrane (164). CuO-NP can electrostatically adhere to the surface of the cell by targeting LPS, teichoic acids, lipo-teichoic acids and sulphur-containing compounds (164). This increases the permeability of the cell, disrupting the osmotic balance and causing cell lysis (164). CuO-NP can also become internalised by microbial cells. The nanoparticles can release copper cations (Cu^{2+}) which can interact with DNA and protein structures and functions (164). In addition, CuO-NP have photocatalytic properties which cause the generation of ROS. ROS can cause membrane oxidation further contributing to the reduction in membrane barrier function, as well as damage proteins and DNA directly (164). CuO-NP have displayed potent antimicrobial activity against a variety of clinically relevant pathogens including *Enterococcus faecalis, B. subtilis, E. coli, P. aeruginosa, K. pneumoniae, Bacillus cereus, S. aureus* and *C. albicans* (164).

Despite this, the use of these nanoparticles is limited by its cytotoxicity profile to human cells. Research suggests that CuO-NP cause oxidative stress, increased lipid peroxidation and ROS production in human cell lines *in vitro*, including human epithelial (A549), human cardiac microvascular endothelial, kidney and neuronal cells (165). However, CuO-NP have

demonstrated anticancer effects against human breast cancer cell line (MCF-7) and lung cancer cell line (A549) whilst causing minimal fibroblast toxicity (164, 166).

1.9.5. Antimicrobial Zinc surfaces

Zinc is a crucial trace element found within all living things and is essential for growth, metabolism and the function of proteins, enzymes and cells (167). It is a highly versatile element that displays biocompatibility and improves the mechanical and electrochemical properties of coatings when incorporated (168). Zinc also demonstrates antibacterial properties against a variety of gram-positive and gram-negative bacteria, including species belonging to *Staphylococcus, Streptococcus, Pseudomonas, Bacillus, Enterobacter, Klebsiella* and *Escherichia* genera (167). Further, zinc demonstrates antimicrobial activity against various fungal and viral pathogens (167, 169). Zinc ions (Zn^{2+}) cause microbial toxicity by causing disruptions in the bacterial cell membrane. This causes inhibition of various cellular metabolic processes as well as reduces the formation of biofilm (168).

In addition to effective microbial killing, zinc plays a crucial role in the proliferation and differentiation of osteoblasts making them an excellent candidate for bone-regenerating medical materials (168). Further, evidence suggests that zinc surfaces may promote the adsorption of proteins (168). Increased protein adsorption is important for the modulation of biological processes such as blood clotting, inflammation and immune activation (including complement activation), highlighting the benefits of zinc surfaces in the development of implantable medical devices such as catheters, canulae and heart valves (170). However, there have been questions surrounding the scalability of zinc surfaces due to the long manufacturing methods and lack of electrolyte stability in solution which complicates production (168).

1.9.6. Antimicrobial zinc nanoparticles

Zinc oxide nanoparticles (ZnO-NP) are also biocompatible materials that exhibit wide-spectrum antimicrobial activity against a variety of bacterial species. Several studies have reported that ZnO-NP do not cause toxicity to human cells and have therefore been exploited within medical and food hygiene industries (171). Nanoscale zinc oxide is significantly more antimicrobial than microscale formulations and therefore is a very attractive material for the development of antimicrobial medical materials (171). ZnO-NP are bactericidal to both gram-positive and gram-negative bacteria through various mechanisms (172). Direct contact of the nanoparticle with the bacterial cell wall can damage the integrity of the structure, disturb the osmotic balance of the cell and cause cell death (171). It is also reported that ZnO-NP liberate Zn^{2+} ions which are inherently antimicrobial (171). Zn^{2+} ions cause electronic excitation that can rupture the bacterial cell membrane by destabilising charges within the membrane itself. These metallic ions also have a high affinity for sulphur groups, particularly thiolates present within cysteine residues or glutathione peptides. Binding to these molecules can lead to alterations and inhibitions of protein structure, function and cellular regulation (173). Finally, ZnO-NP can cause the generation of ROS such as hydroxy, superoxide and hydroperoxide radicals which causes oxidative stress, DNA and protein damage and inhibition of protein synthesis (171, 172).

Despite the wide-spectrum antimicrobial efficacy of ZnO-NP, bacterial resistance to zinc is commonly reported. Mechanisms including efflux, chelation, sequestration and uptake have evolved across both gram-positive and gram-negative bacteria. Resistance nodulation diversion (RND) efflux pumps, P-type ATPase pumps and cation diffuser facilitator (CDF) proteins are

all zinc exporter mechanisms that bacteria use to expel zinc from the cell, contributing to resistance towards these antimicrobial formulations (167). Examples of these include the ZitB and YiiP CDF proteins in *E. coli*, the ZntA ATPase pump in *S. aureus* and the CadA P-type ATPase efflux pump in *B. subtilis*, which all mediate the expulsion of Zn^{2+} from the cell (167). Furthermore, it has been reported that extended exposure to zinc can lead to multidrug resistance. Rihacek *et al.,* 2023 demonstrated that prolonged exposure to ZnO promoted resistance to aminoglycosides, cephalosporins and sulphonamides, and exposure to ZnO-NP resulted in increased resistance to chloramphenicol in *E. coli* (174).

1.9.7. Antimicrobial titanium dioxide surfaces

Titanium dioxide (TiO_2) is a broad-spectrum antibacterial and antimycotic compound with self-sterilising properties. It can oxidise organic contaminants and eliminate bacterial and fungal pathogens (175). In addition to this, its relatively low-cost, non-reactivity, stability, durability, biocompatibility, reusability and corrosion resistance make TiO_2 a frequently used material for dental and orthopaedic implants, medical and hospital devices such as catheters and pharmaceutical coatings to deliver anticancer and antibiotic drugs (176, 177).

TiO_2 surfaces exhibit photocatalytic activity and have been reported to significantly reduce microbial adhesion through the alteration of the surface free energy and therefore the wettability (176). Photo-generated ROS including hydroxyl and superoxide radicals, singlet oxygen and hydrogen peroxide create damage to cells and cell growth. ROS can damage the integrity of LPS and lipid layers in gram-negative bacteria which may increase the permeability of the cell and reduce the bacterial viability. Although gram-positive are inherently less susceptible to extracellular threats due to the presence of a thick peptidoglycan cell wall, ROS can passage through the peptidoglycan pores into the cytoplasm and cause damage to crucial microbial enzymes and respiratory mechanisms (176). The ROS generated by TiO_2 surfaces can also interfere with communication mechanisms within biofilms. They can supress autoinducer signalling molecules produced by communities within biofilms, inhibit their receptor binding, prevent biofilm gene expression and transcription and deactivate quorum sensing signalling pathways (176).

1.9.8. Antimicrobial titanium dioxide nanoparticles

The use of titanium dioxide nanoparticles (TiO_2-NP) for antimicrobial materials or medical applications has drastically increased since 2005, with almost 40% of TiO_2-NP research in 2023 focusing on their antimicrobial activity (178). TiO_2-NP display low cytotoxicity to mammalian cells and therefore demonstrate high biocompatibility (178). They also exhibit broad-spectrum antibacterial and antifungal activity against many clinically relevant pathogens including *E. coli, P. aeruginosa, K. pneumoniae, B., subtilis, S, aureus, Vibrio cholerae, Salmonella typhimurium* and *C. albicans,* although a greater minimum inhibitory concentration (MIC) is observed in gram-negative bacteria (178). Data suggests that TiO_2-NP are highly effective against gram-negative bacteria, which due to the presence of the LPS outer membrane, frequently contribute to aggressive and drug-resistant infections. Further, emerging research highlights the antiviral properties of TiO_2-NP, particularly against the HCoV-NL63 human coronavirus (179) and H_3N_2 influenza virus (178).

TiO_2-NP cause microbicidal effects through numerous mechanisms. When in extracellular environments, they have the potential to depolarise the outer membrane of gram-negative bacteria by targeting membrane proteins and LPS, damaging the integrity of its barrier function

(178). Further, in gram-positive bacteria, they target lipoteichoic acids also contributing to the breakdown of the membrane. In both mechanisms, this causes osmotic stress and can lead to cellular rupture (178). Further, TiO_2-NP are photocatalytic and have a strong oxidising power (178, 180). Light interacts with the nanoparticles causing ROS generation, including hydroxyl and superoxide anion radicles which further contribute to the oxidative stress on the microbial cell (178). This causes alterations to DNA and protein chemistries, inactivation of enzymes, genotoxicity and therefore inhibition of DNA replication cycles, and further damages the cell wall integrity TiO_2-NP (178)**.** TiO_2-NP have also displayed antimicrobial activity against biofilm communities (178). In addition, research shows that TiO_2-NP enhance the efficacy of other antimicrobial agents including antibiotics and have therefore been used in pharmaceutical drug delivery systems (178, 181, 182). Khashan *et al.,* 2021 highlighted the synergy between TiO_2-NP and amoxicillin against *E. coli* and *S. aureus* (183).

1.10. Other types of antimicrobial surfaces

1.10.1. Superhydrophobic surfaces

Superhydrophobic coatings are biomimetic surfaces that have undergone surface modifications to alter their topography, to create an extremely low surface energy. They are largely inspired by naturally bacteria-resistant surfaces such as the lotus leaf (184, 185), gecko skin (186) and insect wings (184). These water-repellent properties of superhydrophobic surfaces resist bacterial adhesion and biofilm formation (187)**.** Zhang *et al*., 2019 developed a mussel-inspired polydopamine coating to anchor silver nanoparticles with hydrophobic modifications through treatment with 1*H*,1*H*,2*H*,2*H*-perfluorodecanethiol (PFDT), to reduce medical device-associated infections from catheters (188). The authors reported that these surfaces exhibited excellent superhydrophobicity and prolonged antimicrobial efficacy against *E. coli* and *Proteus mirabilis*. Further, they note that these coatings significantly decrease static and dynamic biofilm growth, whilst reducing bacterial migration on the outer surfaces of the catheter compared to silicone or silver-alloy-hydrogel catheters. They also demonstrate good biocompatibility with mammalian cells suggesting that they may be an excellent material for use with medical devices such as catheters and canulae, to reduce urinary tract and biofilm infections (188).

1.10.2. Hydrophilic surfaces

The physiological environment is always aqueous (189). Hydrophilic antimicrobial surfaces are another strategy to eliminate contaminating microorganisms. These surfaces attract and bind to water molecules creating a hydration layer between the surface and the environment. This layer is a physical barrier that prevents microbial attachment and can be used to prevent biofouling in water-based environments such as around biomedical implants, biological fluids, diagnostic devices and coatings for marine and fresh-water locations (189). Common hydrophilic antimicrobial coatings include polyethylene glycol (PEG)-based polymers, zwitterionic polymers and cationic polymers (189). Lai *et al*., 2024 have developed PEG- and polyvinylpyrrolidone (PVP)-based thermoplastic polyurethane for the application of medical devices, in particular catheters. These coatings display excellent biocompatibility with blood and exhibit a good mammalian cytotoxicity profile (190).

1.10.3. Antimicrobial peptide-coated surfaces

Antimicrobial peptide-coated surfaces are engineered to display bound antimicrobial peptides (AMP) which can either interact with microorganisms upon contact or be released into the environment. One study investigated the effect of melamine and Mel4 peptides covalently integrated onto glass surfaces. These AMP-coated surfaces displayed high biocompatibility in animal models as well as passing phase I, II and III human clinical trial testing. Both coatings caused interactions with LPS, membrane depolarisation and decreased membrane integrity leading to the leakiness of ATP and nucleic acids. Melamine and Mel4 AMP coatings have exhibited an ability to reduce bacterial cell viability by 82% and 63%, respectively. Further, these surfaces demonstrated an ability to neutralise bacterial endotoxins (191). Another study by Salvagni *et al*., 2020 showed that soft commercial contact lenses anchored with short and ultrashort AMP's, named 'LK' and 'IR', inhibit over 99% bacterial attachment of *P. aeruginosa* and up to 100%attachment by *S. aureus* (192). In addition, these contact lenses exhibited no cytotoxicity towards human corneal epithelial or human retinal epithelial cells and could be used to reduce the risk of eye infections that accompanies contact lens usage (192). In addition, Riordan *et al*., 2019 have developed an antimicrobial metal surface by incorporating AMP RRRRRRGALAGRRRRRRGALAG/5(6)-RRRRRRGALAGRRRRRRGALAG onto steal surfaces by plasma nitriding (193). These surfaces were tested against MSRA, *S. aureus, E. coli, S. epidermidis, Enterococcus spp.* and *P. aeruginosa* isolated from patient wounds/infections from the Queen Elizabeth Hospital, Birmingham, UK (193). The authors concluded that these surfaces demonstrated highly effective antimicrobial activity against both gram-positive and gram-negative bacteria. Further, these AMP-steel surfaces displayed greater antimicrobial efficacy than current commercially available technologies during clinical trial (193).

1.10.4. Other organic antimicrobial surfaces

Organic antimicrobial surfaces include both naturally derived antimicrobial surfaces and surfaces that have been modified with organic compounds, often inspired by biological systems. One example of this are chitosan-modified surfaces. Chitosan is a natural fibrous, biopolymer derived from the deacetylation chitin found within mushrooms and the shells of crustaceans (i.e. crabs and shrimps). Chitosan is cationic and exhibits antimicrobial activity, is biocompatible, biodegradable and non-toxic highlighting its usefulness in the production of antimicrobial medical materials. Chitosan cations form electrostatic interactions with the bacterial cell wall/membrane causing destabilisation, in particular gram negative bacteria due to their hydrophilicity and greater degree of surface negative charge compared to gram positives (194). Clinically, chitosan wound dressings (produced by wet spinning) has demonstrated protective effects against pathogenic species including *Staphylococci, Enterococcus* spp., *Enterobacter* spp., and *Parabacteroides,* 8 days post-surgery (195). In addition, these dressings promoted probiotic microbes including *Prevotella, Lactobacillus* and *Oscillibacter* species which are reported to support skin defence and injury recovery mechanisms (195). Chitosan also promotes mucosal adhesion, blood coagulation and clotting, fibroblast proliferation, collagen synthesis and deposition and wound healing, as well as having anticancer and antigenotoxicity activity, making it attractive for use in medical materials and coatings (194). Other research shows that combining chitosan with other antimicrobials, may promote synergised antimicrobial efficacy. Colistin nanoliposomes demonstrate a decreased MIC against multidrug resistant *Pseudomonas aeruginosa* with the addition of chitosan, which is possibly due to increased microbial cell membrane destabilisation of chitosan (196).

Another example of organic antimicrobial surfaces includes the incorporation of polyphenols into the material. Polyphenols are biosynthesised from natural sources such as plants and marine organisms. They contain numerous hydrophilic groups including phenolic rings, carboxyl groups and hydroxyl groups which are able to cross-link with biopolymers through hydrogen bonding. Tannic acid is a polyphenolic acid widely studied in biomedicine and displays a broad spectrum of antiviral and antibacterial activity against Influenza A virus, Papilloma viruses, Human Immunodeficiency virus, Noroviruses, Herpes Simplex type 1 and 2, *S. aureus, E. coli. S. pyogenes, E. faecalis, P. aeruginosa, Yersinia enterocolitica* and *Listeria innocula* (197). In addition, tannic acid demonstrates tissue regeneration, wound healing and cell proliferation enhancement properties making it a promising component to biomaterials. Tannic acid has been incorporated into a variety of polymers such as collagen, chitosan, agarose, starch, hyaluronic acid and silk for purposes such as wound dressings (197, 198, 199), tissue regenerative materials (200, 197), anticancer biomaterials (197, 201, 202) and antimicrobial coatings (197, 203).

1.10.5. Mechano-bactericidal nanomaterials

Mechano-bactericidal nanomaterials are defined as natural or synthetic surfaces that apply physical forces to the bacterial cell, inducing cell death (204). Structures such as nanopillars exhibit a nanotopography that demonstrates bactericidal activity against gram-positive and gram-negative bacteria, as well as endospores (135). However, these surfaces are frequently manufactured using expensive techniques such as reactive-ion beam etching therefore commercial viability is questionable due to high production costs and time, particularly for large surface areas (135). One study fabricated silicon nanopillars with a 35 nm diameter and height of 360 nm which demonstrated good bactericidal activity against *P. aeruginosa* and *S. aureus*, resulting in 95% and 83% cell death, respectively (205).

1.10.6. Photobactricidal polymers

Photobactericidal polymers are materials that encapsulate photoantimicrobials into polymers. These surfaces require light to activate the photoantimicrobial and elicit an antimicrobial effect. When exposed to light of a specific wavelength, the photosensitiser will produce ROS that exhibit microbicidal effects on bacterial, fungal and viral species (206). One example of photobactericidal polymers was developed by Gavara *et al*., 2021. They immobilised Rose Bengal into cationic polystyrene as well as a gel-type resin to produce two types of antimicrobial surfaces (207). Rose Bengal is an organic compound and synthetic dye frequently used for ophthalmic diagnostics to detect corneal and conjunctiva damage (208). The authors tested the antimicrobial efficacy of these surfaces against *P. aeruginosa, E. coli, E. faecalis, S. aureus* and *C. albicans* following exposure to 515 ± 10 nm (the excitation wavelength of Rose Bengal). Each surface was expose to a total light does of 200 J/cm^2 with samples taken intermittently and cultured onto blood agar. Antimicrobial efficacy was determined by CFU counts. The authors concluded that these surfaces were effective at reducing microbial growth again both gram positive and negative bacteria and fungi. They reported an 8-log reduction in *E. faecalis* and *P. aeruginosa*, 7-log in *S. aureus*, 5.5-log in *E. coli* and 3-log in *C. albicans* (207).

Other types of photobactericidal polymers include silicone-photosensitiser composites separately encapsulating crystal violet and methylene blue dyes, which exhibited antimicrobial efficacy against *E. coli* and *S. aureus* following light exposure (209). In addition,

poly(caprolactone) polymers have been prepared with phloxine B (a photoactive dye) which has demonstrated reductions in *S. aureus* biofilm formation following light treatment (210).

1.11. Epoxy resin paint coatings

Epoxy resin was first discovery by Russian organic chemist Nikolai Prileschajew in 1909 (211, 212). They are reactive intermediates that produce thermosetting polymers that can be used for an extraordinarily wide range of commercial applications. Epoxy resins contain at least one 3-membered cyclic ether group, often referred to as an epoxy, oxirane, epoxide or ethoxyline group. Strictly, epoxy resins are defined as uncross-linked monomers or oligomers that contain the characteristic epoxy group, however in practice, the term is loosely used to describe cured epoxy materials (213).

1.11.1. Epoxy resin curing and production

Epoxy resin is manufactured by forming chemical reactions between epoxy compounds and curing agents/hardeners. Epoxy groups are highly reactive with numerous functional groups making them extremely attractive to chemists and chemical engineers. This reaction forms three-dimensional cross-linking between epoxy monomers (214, 215). When epoxy curing agents are combined with epoxy compounds, irreversible changes occur. Dependent on their chemical composition, curing agents can be categorised into amine type, alkali, anhydride and catalytic curing agents (214).

The use of amine type curing agents is a basic curing method. They can either be classified as aliphatic, aromatic or cycloaliphatic amine cuing agents, each with differing reactivity profiles. Amine-containing agents react with epoxide rings by nucleophilic addition, causing the opening of the ring structure and the formation of a new carbon bond and hydroxyl functional group (214, 216). The epoxy resin discussed in this thesis uses an epoxy resin provided by Indestructible Paints Ltd. This epoxy resin uses an amine type curing agent to cure the coating to break open the epoxide ring as shown in Figure 1.10.

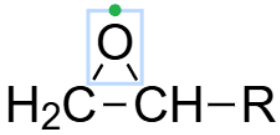


Figure 1.10. Epoxide functional group. Figure made using ChemDraw. Adapted from Jin *et al*, 2015 (211).

1.11.2. Epoxy resin coating uses

The mechanical strength and thermal resilience properties of epoxy resins have made the material highly attractive for use in many industries including chemistry, engineering, aerospace, automotive, electrical, marine and leisure fields (214). They are highly versatile and have been used for protective surface coatings, adhesives, insulating materials, modelling compounds, high-performance composites and packaging materials, amongst other things (212, 214, 215). The most common epoxy resins on the market are bisphenol A diglycidyl ether,

which account for over 75% of sales worldwide. Many of the desirable properties of epoxy resins come from the bisphenol A moiety (mechanical strength and temperature resilience), ester linkages (chemical resilience) and hydroxy and epoxy groups (high adhesive properties) (213). Epoxy resins materials are reasonably cost-effective and therefore their application can be wide throughout commercial and private sectors (213).

1.12. Properties of epoxy resin paint coatings

1.12.1. Mechanical strength

Epoxy resin is an extremely durable material characterised by a high mechanical strength. This means that the material has significant static and dynamic impact strength and is heavily resistant to wear. These properties have made epoxy resins an attractive option for protective coatings of more delicate and high-touch materials (217). A study by Wang *et al.,* 2012, reported that the impact strength of pure epoxy resin was 7.2 KJ/m^2 (217, 218) which is significantly higher that the impact of other coating materials such as acrylic resins (2.83 – 3.30 KJ/m^2) (219), or polyvinyl chloride (PVC) (5 KJ/m^2) (220).

1.12.2. Adhesion properties

Epoxy resins have great adhesion properties. They can form hydrogen bonds and/or chemically bond with the substrate forming mechanical interlocking between the two materials. Epoxy resins can adhere to a wide variety of porous materials such as metals, ceramics, concrete, wood and stone and are commonly used as glues for joining or reinforcement (221, 222, 223). However, adherence to non-porous materials may be difficult. Generally, substrates that contain ether (-O-) and hydroxy (-OH) groups exhibit high adherence to epoxy resin coatings due to their ability to act as both proton acceptors and donor-acceptors, respectively (224). Further, degreasing and sandblasting treatments can be carried out on materials to enhance their adhesion to the epoxy resin, particularly with metal substrates (222).

1.12.3. Thermal and chemical resistance

Epoxy resins are highly resistant to elevated temperatures. The glass transition temperature is a crucial property of amorphous materials and defines the temperature at which they transition from their ridged, glassy state to soft and rubbery (225). Thermoset polymers, such as epoxy resin, as well as thermoplastics are materials that undergo glass transition. Pure epoxy resin exhibits a glass transition at 122.5°C but can be increased or decreased depending on additive combined in the formulation (226).

Epoxy resins also exhibit excellent chemical resistance making them appropriate for a wide variety of applications (227). The extent of chemical resistance is influenced by the crosslinking density of the resin, the degree of cure and the chemistries of structures incorporated into the material (216). This property of epoxy resin is essential for the functionality, durability and lifespan of the material, particularly to chemicals such as acids, alkalis, organic solvents and salt water which can cause structural damage and material dissolution (228).

1.12.4. Antimicrobial properties

Unmodified epoxy resin coatings also exhibit antimicrobial activity. Rigo *et al.,* 2024 demonstrated that numerous commercially available and widely used epoxy resins significantly reduced the survival of *E. coli* ATCC8739 and *S. aureus* ATCC6538P after 24 hours incubation. No bacteria were recovered from 2 epoxy materials after incubation which was significantly ($p \leq 0.001$) less than the bacteria that grew on the control surface, polypropylene (229). In addition, these commercial epoxy resins exhibited antiviral activity against herpes simplex virus type 1 and human coronavirus OC43 (HCoV-OC43) (229).

1.12.5. Additional beneficial properties

In addition to the mechanical strength, resilience and adhesive and antimicrobial properties of the material, epoxy resin has many other characteristics that make it a highly attractive coating. Properties such as its ultra-high water resistance, displaying minimal creep under high load and long shelf life contribute to the resilience and durability of the surface (228). Further, their electrical and dielectric insulating capacity, optical transparency, low shrinkage during manufacture, easiness and versatility of production process and light weight nature make epoxy resins highly attractive for many applications including protective coatings and packaging materials (228). Cured epoxy resins are also highly stable, emit minimal odour and no volatile products are used or released during the production process making these materials safe to use (228). Finally, environmentally friendly epoxy resins are being developed which retain their high-strength characteristics whilst also being biodegradable and recyclable (230).

1.13. Commercial antimicrobial coatings

1.13.1. Antimicrobial metal-based paints

Antimicrobial metal-based coatings such as silver and copper paints have been developed and are commercially available with the aim to reduce microbial contamination on surfaces and therefore the transmission of disease. Silver-based coatings are significantly more researched and are more commercially available than other metal-based coatings, however studies show that copper-based coatings may exhibit more potent antimicrobial activity (231). Nikolav *et al.,* 2023 described the development of a novel geopolymer paint that incorporates natural zeolite clinoptilolite modified with either silver or copper supplements (232). Silver and copper zeolite formulations were prepared by ion exchange using aqueous silver nitrate ($AgNO_3$) or copper sulphate pentahydrate ($CuSO_4 \cdot 5H_2O$) solutions, respectively. Geopolymer paints also contained TiO_2 or ZnO pigments to enhance mechanical strength as suggested for other geopolymer coatings. Antimicrobial activity against *E. coli* and *S. aureus* was observed with both silver- and copper-modified geopolymer formulations containing both metal-oxide pigments. The greatest efficacy being displayed by copper-containing TiO_2 paint (232).

Hochmannova and Vytrasova., 2010 tested the antimicrobial efficacy of their interior paint containing nano ZnO and TiO_2 pigments (233). After formulating the paint, they coated filter paper twice and left the surfaces for 2 weeks to air dry under normal visible light. Antimicrobial efficacy of these coatings was tested against *E. coli* CCM 3954, *S. aureus* CCM 6188, *P. aeruginosa, Penicillium chrysogenum* and *Aspergillus niger*. They conducted agar diffusion

experiments and measured zones of inhibition. They concluded that paint containing nano ZnO displayed excellent antibacterial and antimycotic activity whilst the nano TiO_2-containing paint exhibited minimal or no efficacy (233).

Further, Jeong *et al.,* 2023 have developed an antimicrobial gold-oxide paint aimed to manage the microbial growth in humid indoor environments (234). Hollow gold-oxide nanoparticles (Au-NP) were combined with a white water-based paint and painted on to a glass plate. Once dry, the Au-NP based paint was inoculated with *E. coli* solution and exposed near-infrared (NIR) radiation for 7 cycles of set duration. After each cycle, an aliquot of bacterial solution was plated onto agar and incubated at 37°C, following which colony forming units (CFU) were counted. The authors concluded that Au-NP paint significantly reduced the growth of *E. coli* after each cycle with a 99% bacterial reduction rate following the final NIR treatment (234). However, the authors do not discuss the treatment of the control samples and therefore the causality of the Au-NP on the antimicrobial efficacy is unclear as NIR radiation may have contributed to the reduction in bacterial survival.

1.13.2. Triclosan-based antimicrobial coatings

The development of antimicrobial coatings can also be achieved by incorporating biocides into the formulations. Chen *et al.,* 2024 developed two novel coatings named 23EV and 28SC which display antimicrobial properties due to the incorporation of triclosan within the formulation (235). Triclosan is a broad-spectrum antimicrobial agent that demonstrates activity against both gram-positive and gram-negative bacteria. Triclosan has been applied to a variety of materials, including metals, polymers and textiles to reduce microbial survival and transmission of disease. They have been implemented into commercially available household appliances with large manufacturing companies such as LG and Whirlpool applying this technology to refrigerator and washing machines (235). Triclosan is a competitive inhibitor of the enoyl-acyl carrier protein reductase (ENP) enzyme by forming a non-covalent complex with NAD^+ in the active site. ENP enzymes are crucial in bacterial biosynthesis pathways of FA and is integral for cell membrane formation and cell division (235, 236). In low concentrations, triclosan is bacteriostatic, inhibiting this enzymes activity supressing growth and replication of bacteria. In high concentrations, the agent induces the leakage of potassium ions (K^+) from the cell and therefore destabilises the bacterial cell membrane. This action is rapidly bactericidal (236).

Both triclosan-based coatings developed by Chen *et al., 2024* were tested for antimicrobial efficacy against *E. coli,* ESBL-producing *E. coli, S. aureus,* MDR *S. aureus, P. aeruginosa, Acinetobacter baumannii,* MDR *A. baumannii, Salmonella spp., K. pneumoniae* and vancomycin-resistant *Enterococcus faecium* (235). They inoculated the surfaces with bacterial suspensions, incubated at 35°C for 24 hours and extracted recovered bacteria into soybean casein digest lecithin polysorbate (SCDLP) broth, which were diluted in phosphate buffered saline (PBS) and plated onto blood agar plates. CFU were counted following 48 hours incubation at 35°C. The authors concluded that both of their triclosan-based coatings caused at least a 99% reduction in bacterial survival for all pathogens tested. Both coatings were most effective against *K. pneumoniae*, reducing microbial survival by 99.999%. The authors conclude that these surfaces can be used to effectively reduce bacterial contamination, but the extent of antibacterial efficacy is highly dependent on the pathogen (235). However, triclosan is becoming more commonly detected in wastewater and sewage systems and is reported to be a public health hazard (236). Further research into whether triclosan leaches out of these coatings is crucial to determine whether they are appropriate for application.

1.13.3. Colophony- and Curcumin-based antimicrobial paints

Querido *et al.,* 2021 have developed two antimicrobial coatings by combining colophony and curcumin with a commercially available acrylic paint. Colophony is a naturally derived resin polymer extracted from coniferous trees, such as the pine (237). It is considered safe and has been used in food packaging materials and cosmetic products including shaving creams and hair dyes. It is also used commonly in the pharmaceutical industry, for both microencapsulation of drugs and as a binding agent in drug formulations. Colophony exhibits excellent antimicrobial properties as well as anticancer properties without causing cytotoxicity to normal, healthy cells (237, 238). Curcumin is extracted from the rhizome of the plant *Curcuma longa* (a.k.a. turmeric). It is well known for exhibiting strong antibacterial, antifungal, antiviral, anticancer and anti-infective properties. Curcumin is widely used in the pharmaceutical industry in the production of tablets, capsules, nanoparticles and powder formulations and is used in commercially available vitamin supplements (237). Querido *et al.,* 2021 studied the antibacterial effects of acrylic paint coatings containing either colophony or curcumin against *E. coli* (ATCC25922), *Klebsiella variicola* (ATCC31488), *S. aureus* (ATCC25923)*, E. faecalis* (NCTC775) and *B. cereus* (environmentally isolated) (237). Following ISO 22196 and JIS Z2801 protocols, they inoculated the cured paint surfaces with bacterial suspensions and incubated them at 37°C for 24 hours in high humidity. Bacteria was recovered in tryptic soy broth (TSB), diluted and combined with plate count agar. CFU's were counted following 48 hours of incubation at 37°C to calculate the number of viable bacteria. The authors concluded that both colophony- and curcumin-containing paints reduced the bacterial viability of all tested species. However, according to the antimicrobial activity (R) values, the colophony surface was only antimicrobial against *S. aureus, E. coli* and *B. cereus* and the curcumin coatings showed no efficacy towards any of the pathogens. Despite this, the curcumin coatings resulted in almost a 2-log reduction of *S. aureus, B. cereus* and *E. faecalis* compared to the control (237). The curcumin surfaces did cause yellow discolouration of the paint which may limit the usefulness of the product in certain applications. These surfaces also displayed no cytotoxicity against two human keratinocyte and alveolar epithelial cell lines, HaCaT and A549, respectively (237).

Gupta *et al*., 2024 also aimed to tackle the increase in global demand for antimicrobial coatings. They report on their development of a novel PVC that was grafted with 1-(2-aminoethly piperazine) (AEP) and formulated into a commercially available paint. They demonstrated that PVC-AEP exhibited superior antimicrobial activity against *E. coli, S. aureus, Mycobacterium smegmatis* and *C. albicans* by conducting agar diffusion assays (239). These polymers display antimicrobial activity due to the incorporation of cationic piperazine, which form electrostatic interactions with microbial cell walls and membranes. These interactions increase the fluidity and permeability of the microbial cell by forming pores in their cell wall/membrane. This results in the leakage of intracellular components such as ions and metabolites and disruptions to the osmotic balance of the cell. Further, the depletion of essential nutrients and energy inhibits crucial cellular functions and metabolic pathways and microbial growth and replication (239). The authors report that the PVC-AEP formulation retains on average, 90% of its antimicrobial efficacy against these tested pathogens when incorporated into the paint and applied to glass slides. In addition, these antimicrobial coatings displayed excellent water stability and increased porosity of the material, 5-fold, whilst maintaining its aesthetic visual appearance (239).

However, the cost of raw materials for the production of this antimicrobial paint are very expensive which may limit both small-scale and large-scale implementation of the material

(239). In addition, the National Center for Biotechnology Information reports classify AEP as a dermatotoxin, that can cause severe skin and eye burns. It is extremely destructive to mucosal membrane tissues and the upper respiratory tract. If inhaled, can cause respiratory irritation and inflammation (toxic pneumonitis) as well as long-term bronchitis and dermatitis. Further, AEP is harmful if ingested (240). The authors do not discuss whether the PVC-AEP polymers are retained within the paint or whether it leaches out of the material. This could be a significant limitation of the antimicrobial coating as frequent contact by the public or application in water purification systems or food packaging industries may lead to serious health hazards. In addition, due to the toxicity profile of AEP, strict regulations and cautious manufacturing protocols must be followed, further complicating large-scale production of this antimicrobial coating.

1.13.4. Quaternary Polyethyleneimine-based antimicrobial paint

Ghosh *et al*., 2021 have developed an organo-soluble, hydrophobic quaternary polyethyleneimine (PEI) based paint using linear PEI to help tackle community and hospital-acquired infections transmitted between high-touch surfaces (241). PEIs are polycationic molecules that exhibit enhanced antimicrobial activity by disrupting the cell membrane, particularly through the LPS displayed on the outer membrane of gram negative bacteria (242, 243). These PEI-based antimicrobial paints demonstrated complete killing of drug-resistant *E. coli*, MRSA, *P. aeruginosa* and fluconazole-resistant *C. albicans* within 45 minutes and reduced the viral burden by approximately 10,000 viruses when tested against the Influenza virus (H1N1) (241). Further, no bacterial growth was observed when inoculated with stationary MRSA and *E. coli* cells. Stationary bacterial cells are metabolically inactive and often evade antibiotic therapies, making treatment complicated, hence these paints could potentially be used to eliminate challenging bacteria from the environment (241). Despite this, linear PEIs have been reported to cause over 60% haemolysis at a polymeric concentration of 1 mg/mL (242) therefore the cytotoxicity profile of these polymers may limit their community and healthcare use.

1.14. Antimicrobial CHX-coated materials

1.14.1. Antimicrobial CHX-coated steel

Bryant *et al*., 2022 have developed an antimicrobial CHX-coated steel surface by agitating commercially-nitrided steel with CHX, along with acetonitrile, 2-(1H-benzotriazol-1-yl)-1,1,3,3-tetramethyluronium hexafluorophosphate (HBTU) and N,N-diisopropylethylamine (DIEA). The authors tested the CHX-coated surfaces for antifungal activity against *C. albicans* and *Cryptococcus neoformans* by conducting a simulates splash test (244). They inoculated each surface with 1 x 10^6 fungal cells, allowed them to incubate for up to 60 minutes. Following incubation, surviving fungi were extracted into Dey-Engley's neutralising solution and plated onto potato dextrose agar. CFU's were counted to determine antifungal efficacy of the CHX-coatings. The authors also completed live/dead staining and subsequent confocal imaging of *C. albicans* following 30 minutes exposure to these coatings (244). It was reported that within 15 minutes of exposure, both *C. albicans* and *C. neoformans* were killed and imaging confirmed that fungal cells were permeable to the 'live-or-dye' dead cell indicator within 30 minutes of inoculation on the antimicrobial-coated surfaces (244).

Further explorations of these CHX-coated steel surfaces were conducted by William *et al*., 2025 to determine their antibacterial properties (245). They aimed to test the surfaces against nosocomially isolated bacterial strains acquired from Queen Elizabeth Hospital, Brimingham. The hospital isolates were identified as MRSA, MSSA, *Enterococcus,* coagulase-negative *S. aureus, Bacillus, S. epidermidis, S. aureus, P. aeruginosa, K. pneumoniae, Enterobacter cloacae, E. coli, Moraxella catarrhalis, Citrobacter, Haemophilus influenzae* and 5 unknown bacterial strains by matrix-assisted laser desorption/ionization time-of-flight mass spectrometry (MALDI-ToF MS). A simulated splash test was conducted again which followed a 30 minute incubation period. Surviving bacteria were extracted into Dey-Engley's neutralising solution and plated onto Luria-Bertani (LB) agar. CFU's were counted to determine bacterial survival (245). The authors concluded that CHX-coated steel surfaces significantly reduced the survival of all 91 clinical isolates after 30 minutes exposure, 85% of which exhibited a 7-8 log reduction, whilst the remaining 12% exhibited a 3-4 log reduction in growth. An MIC assay also concluded that resistance to free-in-solution CHX exhibited by these clinical isolates did not correlate to resistance demonstrated against these CHX-coated surfaces (245).

1.14.2. Antimicrobial CHX-coated titanium

Matos *et al*., 2023 have developed commercially pure titanium surfaces coated with CHX-doped thin film to challenge the growing problem of peri-implantitis, a chronic inflammatory condition that occurs in response to the build-up of pathogenic bacterial biofilms surrounding dental implants (246). Titanium discs were coated in CHX-doped thin film by glow discharge plasma, resulting in coated metal surfaces that retain their function. The antibiofilm efficacy of these antimicrobial-coated surfaces was evaluated by inoculating the surface with *Fusobacterium nucleatum* grown in brain-heart infusion (BHI) broth supplemented with yeast extract, vitamin K and hemin. The authors also dosed their cultures with varying levels of nicotine, a growth promoting compound to determine whether these antimicrobial surfaces could reduce biofilm formation for cigarette smokers (246). Following 48 hours of anaerobic incubation (37°C), various methods were employed to determine biofilm formation. Titanium discs were transferred into NaCl solutions and *F. nucleatum* was extracted by sonication. Biofilm was quantified spectrophotometrically by measuring absorbance at 600 nm, as well as counting CFU's following plating onto blood agar and subsequent anaerobic incubation (48 hours; 37°C). In addition, scanning electron microscopy (SEM) imaging was conducted following inoculation and initial incubation of bacteria onto the CHX-coated surfaces. The authors concluded that CHX-doped thin film coated titanium surfaces inhibited the growth of *F. nucleatum* biofilms, even in the presence of nicotine and are therefore a promising material for multifunctional dental implant surfaces (246).

1.14.3. Antimicrobial CHX-coated polymers

Watson *et al*., 2023 have developed antimicrobial CHX-coated polymer surfaces that hope to be used to reduce the transmission of fomite infections, particularly in hospital environments (247). These surfaces were prepared by agitating nitrided acrylonitrile butadiene styrene (ABS) plastic with CHX, HBTU and DIEA and the antibacterial, antifungal and antiviral properties were measured. The authors conducted a simulated splash test assay with *E. coli, S.* aureus and *C. albicans*, as previously described in section 1.14.1 by Bryant *et al.,* 2022 and Williams *et al.,* 2025, with bacterial cultures being plated onto LB agar and fungal cultures onto Yeast peptone dextrose (YPD) agar (247). The authors concluded that no viable colonies of *E. coli, S. aureus* or *C. albicans* could be recovered from the antimicrobial CHX-coated ABS plastic

surfaces after 45 minutes. In addition, the same level of efficacy could be observed against CHX-resistant *E. coli* and *S. aureus* strains. Further, the authors concluded that no SARS-CoV-2 virions could be found after 30 minutes exposure to these surfaces highlighting their possible application into hospitals or within the community to reduce fomite infection (247).

1.14.4. Antimicrobial CHX-coated air filters

Following the COVID-19 pandemic, there has been a massive emphasis on developing new technologies to prioritise clean air and reduce the spread of air borne respiratory pathogens. Watson *et al.,* 2022 have developed antimicrobial air filters that could be implemented onto public transportation such as onboard the rail network (248). The antibacterial and antifungal efficacy of the CHX-coated filters were tested using a simulated splash test as previously described with bacterial CFU's being plated and counted on LB agar and fungal CFU's on potato dextrose agar (248). The authors concluded that the antimicrobial air filters killed *E. coli, S. aureus* and *C. albicans* pathogens within 15 minutes of inoculation. Antiviral efficacy tests also confirmed that SARS-CoV-2 virions were destroyed within 30 seconds of contact. The research also included a field trial where the CHX-coated air filters were installed onboard UK rail networks for 3 months, after which were removed and shipped in individual containers back to the authors. Sections of the filters were immersed in Dey-Engley's neutralising solution and cultured onto blood agar. CFU's were counted following 48 hours incubation (37°C). The field trial showed that the air filters displayed excellent antimicrobial efficacy and significantly reduces the microorganisms in the air conditioning systems on public transport, highlighting their usefulness at reducing the transmission of air borne pathogens (248).

1.15. Methods to study antimicrobial efficacy of surfaces

1.15.1. ISO 22196 (2011) test of antibacterial activity

ISO 22196 (2011), formally known as JIS Z 2801, describes an ISO standard protocol that determines whether plastics or other non-porous materials such as surface materials, medical devices, packaging materials and household appliances exhibit antibacterial activity. When conducting ISO 22196 testing, material samples are inoculated with a liquid bacterial culture of a known concentration and volume. Typically, 400 µL of 2.5 x 10^6 CFU/mL (total ~ 1 x 10^5 bacteria) is inoculated onto the test surface however, in methods discussed in this thesis, 9 µL of 1 x 10^9 CFU/mL (9 x 10^5 bacteria) was added. Specimens are typically incubated for a given time (i.e. 24 hours) and temperature (i.e. 37°C or room temperature), following which surviving bacteria are measured and antimicrobial efficacy is reported. Following recovery of bacteria from the sample surface, serial dilutions are frequently conducted prior to plating on a nutrient agar for CFU enumeration. The ISO 22196 test is often carried out by product manufacturers who are committed to producing antibacterial materials safely and with high quality (249). This protocol has proven to be reliable and has been used to determine the antibacterial properties of many materials including copper-coated surface treatments (249, 250, 251), silver-based coatings (253, 254) and titanium materials (255, 256).

1.15.2. Live/dead viability assay

Live/dead staining is a dual-parameter cell viability assay that differentially dyes cells depending on whether they are living or dead. Typically, a green dye such as calcein

acetoxymethyl ester is used to colour living cells. calcein acetoxymethyl ester is a non-fluorescent dye that is converted to calcein, a bright, anionic fluorescent green dye, by esterases produced by viable bacterial cells. Calcein is trapped inside bacterial cells allowing permanent labelling living cells (257). In addition, a red type is also used to identify dead cells, such as propidium iodide or ethidium homodimer-1. Such dyes are large and positively charged preventing its permeation through the membrane of healthy, viable cells. However, when a cell is dying or dead, the membrane integrity is weakened and the dye can penetrate intracellularly, binding to negatively charged nucleic acids such as DNA and RNA, staining them fluorescent red. Live/dead staining techniques are very effective as they allow quick and easy visualisation of cell viability with common microscope filters (i.e. fluorescein isothiocyanate [FITC] and red fluorescent protein [RFP]) or flow cytometry (258).

1.15.3. Disc diffusion

The disc diffusion assay is a slow but simple, reliable, and cost-effective standard method to determine whether specific bacterial species are susceptible to various antimicrobial compounds. It is recommended by the World Health Organisation (WHO) and was first standardised by Bauer *et al* in 1966 (259, 260). The method is still used for hospital formulary and antibiogram reporting to determine local resistance trends (260). The disc diffusion assay is performed by preparing and streaking bacterial suspensions onto a rich nutrient agar such as horse blood agar or LB agar to create a 'lawn'. Small discs made from absorbent filter paper are treated with the drug of interest and allowed to air dry before applying to the inoculated agar and incubating at a specific temperature and duration depending on the bacterial species (260). The zone of inhibition (ZOI) is the region surrounding each disc where the bacterial 'lawn' does not grow indicating the effectiveness of the drug and is measured as shown in Figure 1.11. However, the ZOI measurements can be if influenced by several factors including drug characteristics such as concentration, aqueous solubility, rate of diffusion and molecular size/weight, as well as experimental factors such as the microorganism used, growth media composition and incubation temperature, time and humidity (261, 262). In addition, common limitations of the disc diffusion assay include an inability to provide information on MIC or antibacterial mode of action (bactericidal or bacteriostatic). The technique is time consuming due to its long incubation period, often ≥24 hours and is subject to interpretation and human error reducing the reproducibility of the test (263). Further, diffusion variability of the drug can cause uneven ZOI which can affect the accuracy of the data (264) and may not be suitable to all fastidious bacteria or fungi such as *Campylobacter* spp. (265).

1.16. Time of flight- secondary ion mass spectrometry (ToF-SIMS)

Time of flight – secondary ion mass spectrometry (ToF-SIMS) is a surface characterisation technique developed by Alfred Benninghoven in the early 1980's (266). As schematically displayed by Figure 1.11, this ultra-high vacuum technique uses a primary ion beam to bombard the sample surface, causing a collision cascade in the top layers (266, 267, 268). Particles located from the upper two atomic layers, within a few nanometres from the primary ion impact zone are sputtered. Ionised particles are differentiated according to molecular mass, detected and analysed in the form of spectral data (268). ToF-SIMS has been utilised across the scientific community to provide information regarding surface composition, contamination and molecular conformation (269) of a diverse range of materials, including biological tissues (270, 271), cells (272), proteins (273, 274) and lipids (275, 276), polymers (277, 278) and more. It has exceptional detection limits allowing species within the part per million (ppm)/parts per

billion (ppb) concentration to be detected. Further, the instrumentation has a high spatial resolving power of <100 nm and with the development of the bas cluster ion beam (GCIB), a depth resolving power of <10 nm can be achieved (269). Although the mass resolving power of ToF-SIMS is exceeded by other surface characterisation techniques, such as the 3D OrbiSIMS (>240,000 at *m/z* = 200) (279) recent advances in the ToF mass analyser and ion reflection has improved the mass resolving power from 13,000 to 26,000 at *m/z* = 200 (280), leading to better separation of low mass peaks (269).

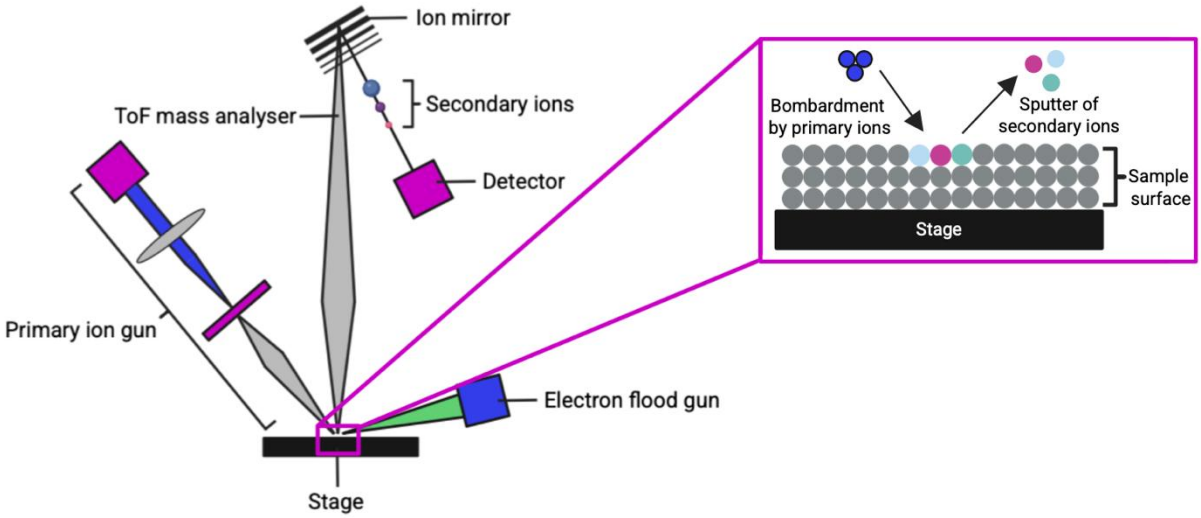


Figure 1.11. Schematic representation of Time of Flight – Secondary Ion Mass Spectrometry (figure created in BioRender). Adapted from Mazel & Richardin., 2009 (281).

1.16.1. Primary ion beam sources

Primary ion beam sources can be classified into four basic types according to their primary ion production mechanisms. These include surface ionisation, plasma, electron bombardment and field ionisation, which are all compatible and have been used with ToF-SIMS analyses (267). Field ionisation produces primary ions by utilising an ultra-high electronic field to remove electrons from a liquid metal source, such as bismuth, which flow over a tungsten tip (radius <1 μm) in close proximity to an extraction field (10 – 40 KeV). This causes a Taylor cone to form where primary ions are stripped away. Field ionisation sources are typically referred to as a liquid metal ion gun (LMIG) and produce focusable ion beams with high current densities and spatial resolution preferable for static SIMS (267). The ToF-SIMS work discussed in this thesis was analysed by a field ionisation primary ion beam acquisition.

1.16.2. Cluster ion sources

Cluster ion beams such as Bi_3^+, Ar_n^+, C_{60}^+, $(H_2O)_n^+$ and $(CO_2)^+$ are frequently used in ToF-SIMS systems. These lower energy (per atom) cluster ion beams minimise damage to biological molecules, which consequently increases the production efficiency of secondary molecular ions at high *m/z* ranges, unlike early ToF-SIMS analysis, which use monoatomic metals such as Ga^+, Cs^+ and In^+ to generate small, high energy ion beams (280, 282). Cluster ion beams result in increased surface ion desorption therefore a greater yield of secondary ions are detected (283). Bombardment of the sample surface with a cluster ion beam is reported to elevate secondary ion yield by up to 100-fold, which is preferable for the analysis of organic

and biological material where ionisation is less efficient than inorganic material (284). Further, a greater yield of intact molecular species and high *m/z* molecular fragments from biological materials (i.e. peptides and lipids) can be achieved using cluster ion beams, as opposed to monoatomic beams, optimising spatial resolving power of the instrument (280).

1.16.3. Mass analysers

The time of flight (ToF) mass analyser functions on the principle that ions with equal kinetic energy but vary in *m/z* will move at different velocities through a constant electric field (285). In ToF-SIMS, desorbed secondary molecules are ionised and pulled into a detector system using a pulsed extractor voltage (negative or positive charge depending on polarity required). Once secondary ions are pulled into the ToF analyser, they are accelerated to a constant energy much higher (~2000 KeV) than typical secondary ions (~20 KeV). After acceleration through the ToF analyser, ions are reflected off an ion mirror and into a detector where their impact will send a signal to the software converting information into spectral data (269). Larger, heavier ions travel slower than smaller, lighter ions, hence will hit the detector first (269). There are many advantages of using the ToF analyser over other mass analysers such as the quadrupole, including the ability to analyse all ions together rather that sequentially, allowing up to 500 spectra to be generated per second. This rapid analysis of the ToF improves productivity, reduces sample waste and allows the detection of transient events. Further, the ToF has better sensitivity and a greater mass range and mass resolving power for analysis compared to other mass analysers such as the quadrupole (266).

1.16.4. Charge compensation

The use of positively charged ion beams for the bombardment of a sample surface increases the surface potential, particularly for electrical insulators such as biological materials. This is due to the elevation in positively charged ions and the expulsion of negatively charged secondary ions from the surface. The elevation in surface potential can result in the loss of negative polarity data as the interaction between itself and negative ions reduces ion repulsion from the surface into the mass analyser. Further, positive polarity data can be lost due to over-acceleration of positive ions, resulting in them surpassing the acceptance window of the mass analyser (267). To counteract the increase in surface potential, an electron flood gun is commonly used to flood the sample surface with low-energy electrons, neutralising positively charged regions (286). However, the use of electron flood guns has been reported to cause sample surface damage, hence it is recommended to limit the flood gun to 6×10^{18} electrons/m^2 (287, 288, 289).

1.16.5. Secondary ion mapping and imaging

ToF-SIMS is a powerful imaging technique that allows the spatial distribution of secondary ions to be mapped out in X and Y coordinates in accordance with its *m/z* value. Every pixel of a two-dimensional ToF-SIMS secondary ion image contains a full spectrum, meaning that information regarding ion *m/z* ratios and intensities can be extrapolated from any given region of the analysed sample surface (290). Exceptional spatial resolving power, as little as 50 nm (compared to 3D OrbiSIMS [<2 μm for biomolecules][279])], can be achieved when conducting ToF-SIMS imaging using an LMIG source as described in section 1.7.2, however is very dependent on the type of primary cluster ion source. For example, a Bi_3^+ ion beam can have exceptional spatial resolving power of 200 nm when analysing biological tissues or cells

(280, 291), compared to Au_n^+ (~500 nm [280]), C_{60}^+ (2 – 5 μm [292, 293]), $(H_2O)_n^+$ (<1 μm [280]), $(CO_2)^+$ (5 – 10 μm [294]) and Ar_n^+ (4 – 15 μm) cluster ion beams (295).

1.16.6. Ionisation and matrix effects

The physics behind the ionisation and expulsion of secondary ions following primary ion bombardment is a complex process and is still largely unknown. This lack of knowledge prevents the development of generalised models which would allow quantitative interpretation of the spectra. Therefore, the composition of a given molecule may not directly be proportional to its yield/intensity in the detected secondary ion spectra (269). The term 'matrix effect' refers to the phenomenon where the secondary ion yield is affected by interactions or interferences with the sample surface (269). The ionisation efficiency is strongly affected by presence and interactions of secondary material with the remaining sample surface; hence it is possible for significant variation in secondary ion formation and intensity to occur for the same ionic species within different samples of varying materials.

1.16.7. Analysis of biological tissues

ToF-SIMS has been widely used to analyse and image a variety of biological material, included but not limited to tissues, individual cells, bacteria, proteins and lipids (299). In recent years, ToF-SIMS has been used to analyse skin samples to contribute to knowledge regarding lipid composition (296), dermal pathology (297) and drug delivery (298). The excellent spatial resolving power attainable by this technology allows variances to be detected and imaged across nanoscale structures. Further, sample preparation of biological materials does not require an extraction process, which is often the case for analysis by chromatography techniques (299). In addition, compounds can be mapped through biological materials with high sensitivity and chemical specificity without the need for fluorescent or radioactive tagging, reducing the sample handling required (299).

1.16.8. Limitations of ToF-SIMS

The biggest limitation of ToF-SIMS is the inability to acquire quantitative date due to the matrix effects. As only ionised particles will be analysed by the detector, and 0.01 – 10% of sputtered material becomes ionised (268, 300), the yield of detected secondary ions may not be proportional to the composition within the sample (269). Further, in order to acquire ToF-SIMS data, samples must be analysed under ultra-high vacuum. This limits the use of this technique for *in vivo* real-time samples, meaning biological tissues will have to be analysed in the form of biopsies, rather than directly from the organism. Analysing intact proteins is also a limitation of this technique as fragmentation of amino acids reduces chemical specificity (300). Further, ToF-SIMS is an expensive instrument restricting its availability for wide-scale use (301).

1.17. High performance liquid chromatography (HPLC)

Chromatography is an analytical technique that functions on the principle that when a mixture is solubilised into a mobile phase and passed over a stationary phase, the components within the mixture will separate according to their differing affinities for the mobile or stationary phases. Eluents can then be detected using UV absorption and fluorescence. Chromatography

was first used by Mikhail Tswett in 1906 using a calcium carbonate mobile phase to analyse plant pigments. Since then, advancements in technology have driven the evolution of chromatography into the modern technique HPLC, as well as other forms of liquid chromatography (LC) such as thin-layer chromatography (TLC), gas chromatography (GC) and more recently, ultra-HPLC (302). High efficiency, specificity, resolution and sensitivity to small quantities of analyte make HPLC an extremely powerful tool utilised for multidisciplinary applications (302, 303). HPLC is currently used in clinical laboratories for vitamin, hormone and metabolite detection and quantification, disease diagnostics and xenobiotic detection in body fluids. Further, the technique is widely used to aid with pharmaceutical, molecular biology, food and environmental science and forensic studies, giving valuable insight into relevant research topics such as environmental pollution and contamination, purity and potency of pharmaceuticals and discovery of novel biomolecules and disease mechanisms (302).

1.17.1. Mobile phase

For HPLC, the mobile phase consists of a liquid that flushes the sample mixture through the stationary phase resulting in compound separation (Figure 1.12). The mobile phase must not cause damage or dissolvement to the stationary phase or instrument (304). Its composition is important as analyte affinity to this phase is crucial for effective separation and therefore good peak formation the chromatogram output. The mobile phase can contain either polar or non-polar solvents and can be isocratic or gradient, depending on the nature of the target analyte (302). The most commonly used mobile phases include water, buffers, acetonitrile and/or methanol, and typically, polar mobile phases are used with non-polar stationary phases to optimise compound separation. Multiple types of solvents can be combined to form the mobile phase; however, combinations must be completely miscible with each other (304). The use of buffers into the mobile phase is often used to stabilise the pH of the solvent when target compounds are sensitive to pH fluctuations (305). Finally, degassing the mobile phase is essential to remove dissolved gas such as oxygen that can cause bubbles and therefore inconsistencies with solvent flow, impacting the reliability and reproducibility of compound separation. This can be achieved by either inert gas bubbling (i.e. helium sparging), vacuum degassing, sonication or refluxing, all which have varying advantages and limitations (306). Filtration of the mobile phase is essential to remove contaminating particulate matter which may clog the column and cause damage to the instrument as well as induce leaks and increase back pressure of the system (307).

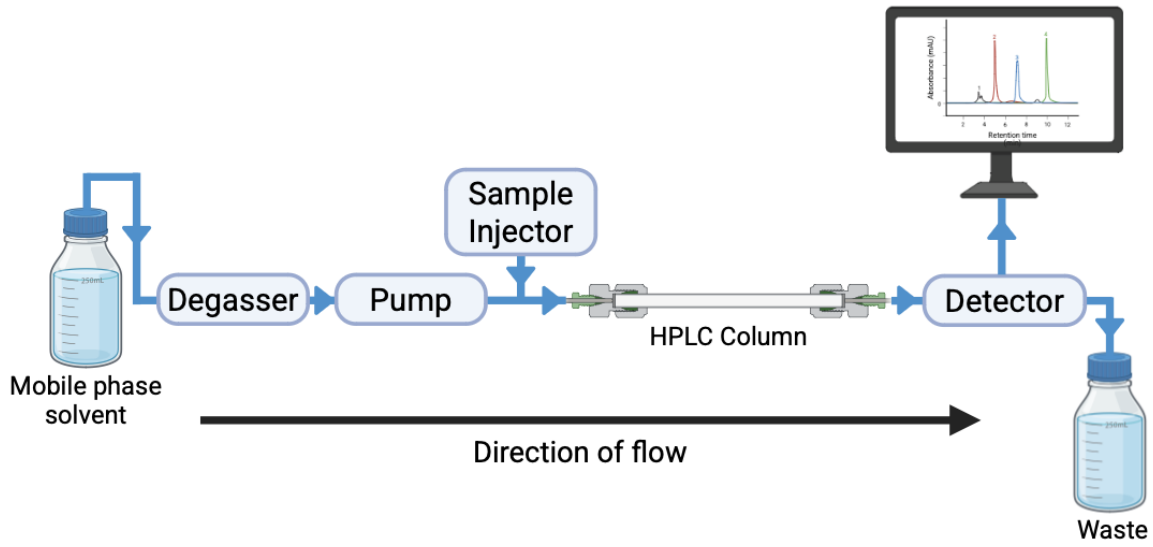


Figure 1.12. Schematic representation of the HPLC components (figure created in BioRender). Adapted from Czaplicki., 2013 (308).

1.17.2. Stationary phase

The stationary phase is also a crucial component of HPLC, which is present within the column. The mobile phase delivers the solubilised sample mixture through the stationary phase in order to achieve separation (302). Different molecules within the sample mixture interact with the stationary phase based on their size, affinity, charge and polarity (302). This leads to variation in the retention time, elution profiles and therefore peak separation of these components. Column chromatography is the most frequently used type of chromatography, which utilises stationary phase consisting of a fibreglass or steal column packed with silica beads (302).

1.17.3. Normal-phase HPLC

Normal-phase liquid chromatography (NPLC) is conducted using a column containing a polar stationary phase and a non-polar or moderately polar mobile phase to separate solutes. NPLC is particularly useful when samples exhibit limited water solubility. Further, better separation of samples that are variable in number and type of functional groups can be achieved (309). NPLC has been widely used in the research of isomers, lipids, plant extracts and petroleum (309, 310).

1.17.4. Reverse-phase HPLC

Reverse-phase liquid chromatography (RPLC) uses a non-polar, hydrophobic stationary phase and a polar mobile phase. In RPLC, organo-silanes are covalently bonded to the silanol groups present on the surface of the spherical silica particles that make up the stationary phase. Typically, increased carbon bound to the silica leads to longer alkyl chains in the stationary phase, resulting in increased retention of solutes (311). RPLC is the preferred separation technique for complex samples containing components that differ in molecular weight and water solubility (309).

1.17.6. The theory of band broadening

Following separation, LC should produce highly efficient chromatograms with thin, defined peaks. Following injection into the mobile phase stream, analytes separate into bands as they travel through the system. The thickness of these bands directly affects the peak shape leading to reduced peak separation efficiency and peak resolution within the chromatogram therefore hindering quantification of analytes (312). This phenomenon is known as band broadening and is caused by several factors including longitudinal diffusion, eddy diffusion, mass transfer limitations and dead volume (313, 314, 315, 316).

1.17.7. Ion pairing agents

In HPLC, particularly RPLC, ion-pairing agents are added to the mobile phase to interact with charged analytes in the sample mixture, forming ion pairs. Ion-pairing agents are frequently used with the analysis of biomolecules, pharmaceuticals and ionic compounds. They alter the physicochemical properties of the analyte and therefore its interaction with the stationary phase, allowing efficient resolution and detection of solutes that otherwise may elute too quickly or fail to result in sufficient separation (316). Commonly used agents include triethylamine (317), trifluoracetic acid (318), quaternary ammonium salts such as tetramethylammonium hydroxide (319) and tetrabutylammonium hydroxide (320), and sulphonic acid derivatives including hexane- (321), heptane- (322), octane-sulphonic acid (323).

1.17.8. Limitations of HPLC

Although HPLC is a highly sensitive technique, the methodology has a limit of detection (LOD) and a limit of quantification (LOQ). The term LOD is used to define the smallest concentrations of an analyte required for detection but cannot be accurately quantified by the method, whist the LOQ is the smallest concentration necessary to reliably quantify the analyte. For the work carried out in this thesis, the LOD and LOQ of HPLC analysis was 0.2 $\mu g/mL^{-1}$ and 1 $\mu g/mL^{-1}$, respectively, as discussed by Cardoso *et al*, 2011 (324). Further, in RPLC, the silanol (Si-OH) groups present on the surface of the stationary phase silica particles are bound to organo-silane molecules. However, more than 50% of these silanol groups are unreacted which can lead to polar or ionic interactions with the with polar solutes, in particular basic compounds. This can affect retention times and cause poor separation of peaks leading to peak shape distortion and/or tailing (310).

Another limitation of HPLC is that there are no true universal detectors that can analyse all compounds within the mobile phase without the need for calibration or standards. Firstly, this requires knowing the target compound so the parameters of the methodology can be tuned accordingly to the chemistry of the analyte, hence untargeted quantification is challenging. Secondly, consideration when selecting an appropriate detector for quantification of the analyte must be taken as there are advantages and disadvantages to each. The most commonly used detector for HPLC analysis is the ultraviolet-visible spectroscopy (UV-Vis) due to its simplicity, high precision, low cost, linearity and compatibility with gradient mobile phases methods. However, the UV-Vis detector can only be used for the quantification of analytes with moderate to strong chromophores (325). Table 1.2 discusses alternative HPLC detection strategies and their advantages and limitations.

Table 1.2. HPLC detection strategies and their advantages and limitations of use in research.

Detection	Advantages	Limitations
Ultraviolet-visible spectroscopy (UV-Vis)	– Simple method (325) – High precision (325) – Low cost (325) – Linear signal-concentration relationship (325) – Compatible with gradient mobile phase methods (325)	– Cannot be used to quantify molecules with weak chromophores (325)
Fluorescence detection (FLD)	– High sensitivity (326) – High selectivity (326) – Lower detection limit than UV-Vis (326) – Linear relationship between analyte concentration and signal (326)	– Only used with fluorescent molecules (326) – More expensive than UV-Vis (326) – Incompatible with certain mobile and stationary phases (326) – Most common lamp, Xenon, has short lifetime, high energy consumption, high replacement costs and low light intensity stability (326)
Evaporative light scattering detection (ELSD)	– Can be used to quantify molecules with weak/no chromophore (325)	– Signal dependent on volatility of mobile phase (325) – Limited dynamic range (325) – Limited sensitivity (325)
Charged aerosol detection (CAD)	– Can be used to quantify molecules with weak chromophores (327)	– Signal dependent on volatility of mobile phase (325)
Refractive index detection (RID)	– Can be used to quantify molecules with weak/no chromophore (328) – Non-destructive detection allowing downstream analysis (328) – Technically a universal detector that can detect anything with a refractive index different to the mobile phase (328)	– Limited sensitivity (325) – Not compatible with gradient mobile phase methods (325) – Sensitive to thermal changes (328) – Small dynamic range (328)
Electrochemical detection (ECD)	– High sensitivity (325) – High selectivity (325) – Can be used to quantify molecules with weak/no chromophore (329) – Can detect either oxidation or reduction modes (325)	– Effected by changes in mobile phase composition and pump pulsations (gradient mobile phase methods challenging) (325)
Chemiluminescent nitrogen detection (CLND)	– High sensitivity (325) – High selectivity for nitrogen-containing compounds (325) – Universal detector for nitrogen-containing compounds (325) – Can be used to quantify molecules with weak/no chromophore (330)	– Incompatible with nitrogen-containing solvents such as acetonitrile (325)

HPLC mass spectrometry (HPLC-MS)	– One of the most sensitive and selective analytical techniques (325) – Can be used to quantify molecules with weak/no chromophore (329)	– Expensive to analyse samples (325)

1.18. The scope of this thesis

This thesis investigates how novel formulations of CHX can be applied to various surfaces to reduce infection and disease transmission. This work addresses current issues surrounding CHX permeation though the *stratum corneum*, to reduce SSIs following surgical interventions. This work investigates the representability of an *in vitro* porcine skin permeation model using a Franz-type diffusion cell to study CHX permeation through human skin. Comparisons were made between this *in vitro* model and permeation through *in vivo* human skin using HPLC to quantify the antimicrobial at each layer of the *stratum corneum* and ToF-SIMS surface imaging to determine spatial distribution of the antimicrobial. After confirmation of model representability, the *in vitro* porcine model was used to investigate permeation enhancement of CHX when formulated with a variety of permeation enhancer compounds, including R6 polyarginine, glycolic acid and Kolliphor® HS15. The antimicrobial efficacy and cytotoxicity profiles of these novel formulations was explored to determine whether they are appropriate for clinical use.

This thesis also explores the use of CHX as the active agent for the development of an antimicrobial epoxy resin coatings to eliminate microbial reservoirs on public surfaces, in particular, hospitals, public transport and public toilet facilities. These coatings are highly versatile, commercially affordable, easily installed and transparent when cured. This work investigates the antimicrobial efficacy, physicochemical properties, long-term stability and durability of these surfaces in a variety of different environments.

This thesis is composed of 3 experimental chapter composed of manuscripts published or submitted for publishing in peer-reviewed journals. The first experimental chapter reports on the permeation enhancement of CHX through skin to increase microbial clearance and reduce surgical site infection. This paper was published in the Journal of Pharmaceutical Sciences in 2026. The second experimental chapter discusses the physicochemical properties and distribution of CHX throughout the epoxy resin surfaces, as well as the efficacy of these coatings against a variety of clinically-relevant pathogens. This paper was published in Scientific Reports journal in 2025. The third experimental chapter addresses the long-term durability of these surfaces using UV and time aging methods. This chapter also explores the durability and antibiofilm/antibiofouling efficacy for application in marine environments. This paper was submitted to Materials Advances . In addition, 2 published manuscripts are included in Appendix 1 (Title: Oligoarginine peptide structure and effect on cell penetration in ocular drug delivery) and Appendix 2 (Title: Wettability and Bactericidal Properties of Bioinspired ZnO Nanopillar Surfaces) that I contributed to.

References for Chapter 1

1. Lim KS, Kam PC. Chlorhexidine-pharmacology and clinical applications. Anaesthesia and intensive care. 2008 Jul;36(4):502-12.

2. Silvestri DL, McEnery-Stonelake M. Chlorhexidine: uses and adverse reactions. Dermatitis. 2013 Jun 1;24(3):112-8.

3. Varoni E, Tarce M, Lodi G, Carrassi A. Chlorhexidine (CHX) in dentistry: state of the art. Minerva Stomatol. 2012 Sep 1;61(9):399-419.

4. Opstrup MS, Jemec GB, Garvey LH. Chlorhexidine allergy: on the rise and often overlooked. Current Allergy and Asthma Reports. 2019 May;19(5):23.

5. Deus FP, Ouanounou A. Chlorhexidine in dentistry: pharmacology, uses, and adverse effects. International dental journal. 2022 Jun 1;72(3):269-77.

6. Bednarek RS, Nassereddin A, Ramsey ML. Skin antiseptics. 2018.

7. García-Gavín J, Lissens R, Timmermans A, Goossens A. Allergic contact dermatitis caused by isopropyl alcohol: a missed allergen?. Contact dermatitis. 2011 Aug;65(2):101-6.

8. Alajlan AA, Mukhtar LE, Almussallam AS, Alnuqaydan AM, Albakiri NS, Almutari TF, Bin Shehail KM, Aldawsari FS, Alajel SM. Assessment of disinfectant efficacy in reducing microbial growth. Plos one. 2022 Jun 27;17(6):e0269850.

9. Horner C, Mawer D, Wilcox M. Reduced susceptibility to chlorhexidine in staphylococci: is it increasing and does it matter?. Journal of Antimicrobial Chemotherapy. 2012 Nov 1;67(11):2547-59.

10. Anderson MJ, Horn ME, Lin YC, Parks PJ, Peterson ML. Efficacy of concurrent application of chlorhexidine gluconate and povidone iodine against six nosocomial pathogens. American journal of infection control. 2010 Dec 1;38(10):826-31.

11. Kirkby M, Sabri AB, Scurr DJ, Moss GP. Dendrimer-mediated permeation enhancement of chlorhexidine digluconate: Determination of in vitro skin permeability and visualisation of dermal distribution. European journal of pharmaceutics and biopharmaceutics. 2021 Feb 1;159:77-87.

12. Stein C, Vincze S, Kipp F, Makarewicz O, Al Dahouk S, Pletz MW. Carbapenem-resistant Klebsiella pneumoniae with low chlorhexidine susceptibility. The Lancet Infectious Diseases. 2019 Sep 1;19(9):932-3.

13. Aftab R, Dodhia VH, Jeanes C, Wade RG. Bacterial sensitivity to chlorhexidine and povidone-iodine antiseptics over time: a systematic review and meta-analysis of human-derived data. Scientific reports. 2023 Jan 7;13(1):347.

14. Leshem T, Gilron S, Azrad M, Peretz A. Characterization of reduced susceptibility to chlorhexidine among Gram-negative bacteria. Microbes and Infection. 2022 Mar 1;24(2):104891.

15. Naumova IB, Shashkov AS, Tul'skaya EM, Streshinskaya GM, Kozlova YI, Potekhina NV, Evtushenko LI, Stackebrandt E. Cell wall teichoic acids: structural diversity, species specificity in the genus Nocardiopsis, and chemotaxonomic perspective. FEMS microbiology reviews. 2001 May 1;25(3):269-83.

16. Brown S, Santa Maria Jr JP, Walker S. Wall teichoic acids of gram-positive bacteria. Annual review of microbiology. 2013 Sep 8;67(1):313-36.

17. Pasquina LW, Santa Maria JP, Walker S. Teichoic acid biosynthesis as an antibiotic target. Current opinion in microbiology. 2013 Oct 1;16(5):531-7.

18. Gong Z, Guo J, Li Q, Xie H. Molecular mechanism of lipopolysaccharide (LPS) in promoting biomineralization on bacterial surface. Biochimica et Biophysica Acta (BBA)-General Subjects. 2023 Mar 1;1867(3):130305.

19. Adams PG, Lamoureux L, Swingle KL, Mukundan H, Montaño GA. Lipopolysaccharide-induced dynamic lipid membrane reorganization: tubules, perforations, and stacks. Biophysical journal. 2014 Jun 3;106(11):2395-407.

20. Milani ES, Hasani A, Varschochi M, Sadeghi J, Memar MY. Biocide resistance in Acinetobacter baumannii: Appraising the mechanisms. Journal of Hospital Infection. 2021 Nov 1;117:135-46.

21. Cieplik F, Jakubovics NS, Buchalla W, Maisch T, Hellwig E, Al-Ahmad A. Resistance toward chlorhexidine in oral bacteria–is there cause for concern?. Frontiers in microbiology. 2019 Mar 22;10:587.

22. Biswas D, Tiwari M, Tiwari V. Molecular mechanism of antimicrobial activity of chlorhexidine against carbapenem-resistant Acinetobacter baumannii. PloS one. 2019 Oct 29;14(10):e0224107.

23. Cheung HY, Wong MM, Cheung SH, Liang LY, Lam YW, Chiu SK. Differential actions of chlorhexidine on the cell wall of Bacillus subtilis and Escherichia coli. PLoS One. 2012 May 11;7(5):e36659.

24. Suwantarat N, Carroll KC, Tekle T, Ross T, Maragakis LL, Cosgrove SE, Milstone AM. High prevalence of reduced chlorhexidine susceptibility in organisms causing central line–associated bloodstream infections. Infection Control & Hospital Epidemiology. 2014 Sep;35(9):1183-6.

25. Poole K. Efflux pumps as antimicrobial resistance mechanisms. Annals of medicine. 2007 Jan 1;39(3):162-76.

26. Liu Q, Zhao H, Han L, Shu W, Wu Q, Ni Y. Frequency of biocide-resistant genes and susceptibility to chlorhexidine in high-level mupirocin-resistant, methicillin-resistant

Staphylococcus aureus (MuH MRSA). Diagnostic microbiology and infectious disease. 2015 Aug 1;82(4):278-83.

27. Kampf G. Acquired resistance to chlorhexidine–is it time to establish an 'antiseptic stewardship'initiative?. Journal of Hospital Infection. 2016 Nov 1;94(3):213-27.

28. Koljalg S, Naaber P, Mikelsaar M. Antibiotic resistance as an indicator of bacterial chlorhexidine susceptibility. Journal of Hospital Infection. 2002 Jun 1;51(2):106-13.

29. Hardy K, Sunnucks K, Gil H, Shabir S, Trampari E, Hawkey P, Webber M. Increased usage of antiseptics is associated with reduced susceptibility in clinical isolates of Staphylococcus aureus. MBio. 2018 Jul 5;9(3):10-128.

30. Morita Y, Tomida J, Kawamura Y. Responses of Pseudomonas aeruginosa to antimicrobials. Frontiers in microbiology. 2014 Jan 8;4:422.

31. Fraud S, Campigotto AJ, Chen Z, Poole K. MexCD-OprJ multidrug efflux system of Pseudomonas aeruginosa: involvement in chlorhexidine resistance and induction by membrane-damaging agents dependent upon the AlgU stress response sigma factor. Antimicrobial agents and chemotherapy. 2008 Dec;52(12):4478-82.

32. Hassan KA, Liu Q, Elbourne LD, Ahmad I, Sharples D, Naidu V, Chan CL, Li L, Harborne SP, Pokhrel A, Postis VL. Pacing across the membrane: the novel PACE family of efflux pumps is widespread in Gram-negative pathogens. Research in microbiology. 2018 Sep 1;169(7-8):450-4.

33. Lopez-Ojeda W, Pandey A, Alhajj M, Oakley AM. Anatomy, skin (integument). StatPearls Publishing 2022 Oct 17.

34. Richardson M. Understanding the structure and function of the skin. Nursing times. 2003 Aug 1;99(31):46-8.

35. Grice EA, Segre JA. The skin microbiome. Nature reviews microbiology. 2011 Apr;9(4):244-53.

36. Wong DJ, Chang HY. Skin tissue engineering. StemBook [Internet]. 2009 Mar 31.

37. Abdo JM, Sopko NA, Milner SM. The applied anatomy of human skin: A model for regeneration. Wound Medicine. 2020 Mar 1;28:100179.

38. Hofmann E, Schwarz A, Fink J, Kamolz LP, Kotzbeck P. Modelling the complexity of human skin in vitro. Biomedicines. 2023 Mar 6;11(3):794.

39. Bozkurt A, Kose K, Alessi-Fox C, Dy JG, Brooks DH, Rajadhyaksha M. Unsupervised delineation of stratum corneum using reflectance confocal microscopy and spectral clustering. Skin Research and Technology. 2017 May;23(2):176-85.

40. Zsikó S, Csányi E, Kovács A, Budai-Szűcs M, Gácsi A, Berkó S. Methods to evaluate skin penetration in vitro. Scientia Pharmaceutica. 2019;87(3):19.

41. Haftek M. Epidermal barrier disorders and corneodesmosome defects. Cell and tissue research. 2015 Jun;360(3):483-90.

42. Murphrey MB, Miao JH, Zito PM. Histology, stratum corneum. 2018.

43. Brown TM, Krishnamurthy K. Histology, dermis. 2018.

44. Tzaphlidou M. The role of collagen and elastin in aged skin: an image processing approach. Micron. 2004 Apr 1;35(3):173-7.

45. Rippa AL, Kalabusheva EP, Vorotelyak EA. Regeneration of dermis: scarring and cells involved. Cells. 2019 Jun 18;8(6):607.

46. Conradt G, Hausser I, Nyström A. Epidermal or dermal collagen VII is sufficient for skin integrity: insights to anchoring fibril homeostasis. Journal of Investigative Dermatology. 2024 Jun 1;144(6):1301-10.

47. Wilgus TA, Wulff BC. The importance of mast cells in dermal scarring. Advances in wound care. 2014 Apr 1;3(4):356-65.

48. Numata T, Harada K, Nakae S. Roles of mast cells in cutaneous diseases. Frontiers in immunology. 2022 Jul 6;13:923495.

49. Shook BA, Wasko RR, Mano O, Rutenberg-Schoenberg M, Rudolph MC, Zirak B, Rivera-Gonzalez GC, López-Giráldez F, Zarini S, Rezza A, Clark DA. Dermal adipocyte lipolysis and myofibroblast conversion are required for efficient skin repair. Cell Stem Cell. 2020 Jun 4;26(6):880-95.

50. Zhang Z, Shao M, Hepler C, Zi Z, Zhao S, An YA, Zhu Y, Ghaben AL, Wang MY, Li N, Onodera T. Dermal adipose tissue has high plasticity and undergoes reversible dedifferentiation in mice. The Journal of clinical investigation. 2019 Dec 2;129(12):5327-42.

51. Yousef H, Alhajj M, Sharma S. Anatomy, skin (integument), epidermis. 2017.

52. Kim JY, Dao H. Physiology, integument. StatPearls Publishing. 2023 May 1.

53. Lai-Cheong JE, McGrath JA. Structure and function of skin, hair and nails. Medicine. 2013 Jun 1;41(6):317-20.

54. Ezure T. Vellus hair condition is related to dermal elasticity and facial sagging severity. Skin Research and Technology. 2023 Feb;29(2):e13287.

55. Cui CY, Schlessinger D. Eccrine sweat gland development and sweat secretion. Experimental dermatology. 2015 Sep;24(9):644-50.

56. Hodge BD, Sanvictores T, Brodell RT. Anatomy, skin sweat glands. 2018.

57. Lovászi M, Szegedi A, Zouboulis CC, Törőcsik D. Sebaceous-immunobiology is orchestrated by sebum lipids. Dermato-endocrinology. 2017 Jan 1;9(1):e1375636.

58. Byrd AL, Belkaid Y, Segre JA. The human skin microbiome. Nature Reviews Microbiology. 2018 Mar;16(3):143-55.

59. Flowers L, Grice EA. The skin microbiota: balancing risk and reward. Cell host & microbe. 2020 Aug 12;28(2):190-200.

60. Scharschmidt TC, Fischbach MA. What lives on our skin: ecology, genomics and therapeutic opportunities of the skin microbiome. Drug Discovery Today: Disease Mechanisms. 2013 Dec 1;10(3-4):e83-9.

61. Becker K, Heilmann C, Peters G. Coagulase-negative staphylococci. Clinical microbiology reviews. 2014 Oct;27(4):870-926.

62. Oh J, Byrd AL, Deming C, Conlan S, Kong HH, Segre JA. Biogeography and individuality shape function in the human skin metagenome. Nature. 2014 Oct 2;514(7520):59-64.

63. Findley K, Oh J, Yang J, Conlan S, Deming C, Meyer JA, Schoenfeld D, NomicosF E, Park M, Kong HH. Topographic diversity of fungal and bacterial communities in human skin. Nature. 2013 Jun 20;498(7454):367-70.

64. Guarch-Pérez C, Riool M, De Boer L, Kloen P, Zaat SA. Bacterial reservoir in deeper skin is a potential source for surgical site and biomaterial-associated infections. Journal of Hospital Infection. 2023 Oct 1;140:62-71.

65. Cohen-Poradosu R, Kasper DL. Anaerobic Infections. Mandell, Douglas, and Bennett's Principles and Practice of Infectious Diseases. 2015:2736-43.

66. Feingold KR. Lamellar bodies: the key to cutaneous barrier function. Journal of Investigative Dermatology. 2012 Aug 1;132(8):1951-3.

67. Phatale V, Vaiphei KK, Jha S, Patil D, Agrawal M, Alexander A. Overcoming skin barriers through advanced transdermal drug delivery approaches. Journal of controlled release. 2022 Nov 1;351:361-80.

68. Lazarus BS, Chadha C, Velasco-Hogan A, Barbosa JD, Jasiuk I, Meyers MA. Engineering with keratin: A functional material and a source of bioinspiration. iscience. 2021 Aug 20;24(8).

69. Bolzinger MA, Briançon S, Pelletier J, Chevalier Y. Penetration of drugs through skin, a complex rate-controlling membrane. Current opinion in colloid & interface science. 2012 Jun 1;17(3):156-65.

70. Smijs TG, Pavel S. Titanium dioxide and zinc oxide nanoparticles in sunscreens: focus on their safety and effectiveness. Nanotechnology, science and applications. 2011 Oct 13:95-112.

71. Ahmad N, Mukhtar H. Cytochrome p450: a target for drug development for skin diseases. Journal of investigative dermatology. 2004 Sep 1;123(3):417-25.

72. Banning TP, Heard CM. Binding of doxycycline to keratin, melanin and human epidermal tissue. International journal of pharmaceutics. 2002 Mar 20;235(1-2):219-27.

73. Chen Q, Yi S, Yang L, Zhu L. Penetration pathways, influencing factors and predictive models for dermal absorption of exobiotic molecules: A critical review. Science of The Total Environment. 2024 Jun 1;927:172390.

74. Supe S, Takudage P. Methods for evaluating penetration of drug into the skin: A review. Skin Research and Technology. 2021 May;27(3):299-308.

75. Jakobsen ND, Kaiser K, Ebbesen MF, Lauritsen L, Gjerstorff MF, Kuntsche J, Brewer JR. The ROC skin model: A robust skin equivalent for permeation and live cell imaging studies. European Journal of Pharmaceutical Sciences. 2022 Nov 1;178:106282.

76. Benson HA, Watkinson AC, editors. Topical and transdermal drug delivery: principles and practice. John Wiley & Sons; 2012 Feb 3.

77. Goel A, Pendlington R, Glavin S, Chen T, Belsey NA. Characterisation of skin penetration pathways using stimulated Raman scattering microscopy. European Journal of Pharmaceutics and Biopharmaceutics. 2024 Nov 1;204:114518.

78. Zoabi A, Touitou E, Margulis K. Recent advances in nanomaterials for dermal and transdermal applications. Colloids and Interfaces. 2021 Mar 18;5(1):18.

79. Ramadon D, McCrudden MT, Courtenay AJ, Donnelly RF. Enhancement strategies for transdermal drug delivery systems: Current trends and applications. Drug delivery and translational research. 2022 Apr;12(4):758-91.

80. Elias PM. Structure and function of the stratum corneum extracellular matrix. Journal of investigative dermatology. 2012 Sep 1;132(9):2131-3.

81. Swartzendruber DC, Wertz PW, Kitko DJ, Madison KC, Downing DT. Molecular models of the intercellular lipid lamellae in mammalian stratum corneum. Journal of Investigative Dermatology. 1989 Feb 1;92(2):251-7.

82. N'Da DD. Prodrug strategies for enhancing the percutaneous absorption of drugs. Molecules. 2014 Dec 12;19(12):20780-807.

83. Patzelt A, Lademann J. The increasing importance of the hair follicle route in dermal and transdermal drug delivery. InPercutaneous Penetration Enhancers Chemical Methods in Penetration Enhancement: Drug Manipulation Strategies and Vehicle Effects 2015 Apr 4 (pp. 43-53). Berlin, Heidelberg: Springer Berlin Heidelberg.

84. Bos JD, Meinardi MM. The 500 Dalton rule for the skin penetration of chemical compounds and drugs. Experimental Dermatology: Viewpoint. 2000 Jun;9(3):165-9.

85. Singpanna K, Suriyaamporn P, Pornpitchanarong C, Ngawhirunpat T, Li SK, Opanasopit P. Chitosan-gold nanoparticles: A trend of skin permeation enhancement effect in animal and human skin model. Journal of Drug Delivery Science and Technology. 2025 Mar 1;105:106598.

86. Yu YQ, Yang X, Wu XF, Fan YB. Enhancing permeation of drug molecules across the skin via delivery in nanocarriers: novel strategies for effective transdermal applications. Frontiers in bioengineering and biotechnology. 2021 Mar 29;9:646554.

87. Işık M, Levorse D, Mobley DL, Rhodes T, Chodera JD. Octanol–water partition coefficient measurements for the SAMPL6 blind prediction challenge. Journal of computer-aided molecular design. 2020 Apr;34(4):405-20.

88. Reijenga J, Van Hoof A, Van Loon A, Teunissen B. Development of methods for the determination of pKa values. Analytical chemistry insights. 2013 Jan;8:ACI-S12304.

89. Forrester JV, Dick AD, McMenamin PG, Roberts F, Pearlman E. General and ocular pharmacology. The Eye. 2016 Jan 1:338-69.

90. Manallack DT. The p K a distribution of drugs: application to drug discovery. Perspectives in medicinal chemistry. 2007 Jan;1:1177391X0700100003.

91. Morimoto J, Miyamoto K, Ichikawa Y, Uchiyama M, Makishima M, Hashimoto Y, Ishikawa M. Improvement in aqueous solubility of achiral symmetric cyclofenil by modification to a chiral asymmetric analog. Scientific reports. 2021 Jun 16;11(1):12697.

92. Golla S, Neely BJ, Whitebay E, Madihally S, Robinson Jr RL, Gasem KA. Virtual design of chemical penetration enhancers for transdermal drug delivery. Chemical biology & drug design. 2012 Apr;79(4):478-87.

93. Souto EB, Fangueiro JF, Fernandes AR, Cano A, Sanchez-Lopez E, Garcia ML, Severino P, Paganelli MO, Chaud MV, Silva AM. Physicochemical and biopharmaceutical aspects influencing skin permeation and role of SLN and NLC for skin drug delivery. Heliyon. 2022 Feb 1;8(2).

94. Das C, Olmsted PD. The physics of stratum corneum lipid membranes. Philosophical Transactions of the Royal Society A: Mathematical, Physical and Engineering Sciences. 2016 Jul 28;374(2072):20150126.

95. Wan Q, Thompson BC. Control of properties through hydrogen bonding interactions in conjugated polymers. Advanced Science. 2024 Feb;11(8):2305356.

96. Petukhov M, Rychkov G, Firsov L, Serrano L. H-bonding in protein hydration revisited. Protein science. 2004 Aug;13(8):2120-9.

97. Thode AB, Kruse SW, Nix JC, Jones DN. The role of multiple hydrogen-bonding groups in specific alcohol binding sites in proteins: insights from structural studies of LUSH. Journal of molecular biology. 2008 Mar 7;376(5):1360-76.

98. Karpanen TJ, Worthington T, Conway BR, Hilton AC, Elliott TS, Lambert PA. Penetration of chlorhexidine into human skin. Antimicrobial agents and chemotherapy. 2008 Oct;52(10):3633-6.

99. Boonwittaya N, Yurayart C, Udomkusonsri P, Kaewmanee S, Sompaisarnsilp S, Thengchaisri N, Duangurai T. Comparative evaluation of chlorhexidine gluconate with alcohol and polyhexamethylene biguanide with Tris-EDTA as antiseptic solutions for pre-operative skin preparation in dogs. Veterinary World. 2024 Nov 5;17(11):2451.

100. Stinner DJ, Krueger CA, Masini BD, Wenke JC. Time-dependent effect of chlorhexidine surgical prep. Journal of Hospital Infection. 2011 Dec 1;79(4):313-6.

101. Farkas E, Kiss D, Zelkó R. Study on the release of chlorhexidine base and salts from different liquid crystalline structures. International journal of pharmaceutics. 2007 Aug 1;340(1-2):71-5.

102. chEMBL. Chlorhexidine. Available at: https://www.ebi.ac.uk/chembl/explore/compound/CHEMBL790

103. Mohammadi Z. Chlorhexidine gluconate, its properties and applications in endodontics. Iranian endodontic journal. 2008 Jan 10;2(4):113.

104. National Library of Medicine. Available at: https://pubchem.ncbi.nlm.nih.gov/compound/Chlorhexidine

105. Carrijo-Carvalho LC, Sant'ana VP, Foronda AS, de Freitas D, de Souza Carvalho FR. Therapeutic agents and biocides for ocular infections by free-living amoebae of Acanthamoeba genus. survey of ophthalmology. 2017 Mar 1;62(2):203-18.

106. Agarwal A, Nelson TB, Kierski PR, Schurr MJ, Murphy CJ, Czuprynski CJ, McAnulty JF, Abbott NL. Polymeric multilayers that localize the release of chlorhexidine from biologic wound dressings. Biomaterials. 2012 Oct 1;33(28):6783-92.

107. Bashir MH, Hollingsworth A, Schwab D, Prinsen KS, Paulson JE, Morse DJ, Bernatchez SF. Ex vivo and in vivo evaluation of residual chlorhexidine gluconate on skin following repetitive exposure to saline and wiping with 2% chlorhexidine gluconate/70% isopropyl alcohol pre-operative skin preparations. Journal of Hospital Infection. 2019 Jul 1;102(3):256-61.

108. Boncheva M. The physical chemistry of the stratum corneum lipids. International journal of cosmetic science. 2014 Dec;36(6):505-15.

109. Wertz PW. Stratum corneum lipids and water. Exogenous Dermatology. 2005 Jul 20;3(2):53-6.

110. Abbood HM, Hijazi K, Gould IM. Chlorhexidine resistance or cross-resistance, that is the question. Antibiotics. 2023 Apr 22;12(5):798.

111. Aki H, Kawasaki Y. Thermodynamic clarification of interaction between antiseptic compounds and lipids consisting of stratum corneum. Thermochemical acta. 2004 Jun 24;416(1-2):113-9.

112. Karpanen TJ, Worthington T, Conway BR, Hilton AC, Elliott TS, Lambert PA. Permeation of chlorhexidine from alcoholic and aqueous solutions within excised human skin. Antimicrobial agents and chemotherapy. 2009 Apr;53(4):1717-9.

113. Karpanen TJ, Conway BR, Worthington T, Hilton AC, Elliott TS, Lambert PA. Enhanced chlorhexidine skin penetration with eucalyptus oil. BMC Infectious Diseases. 2010 Sep 22;10(1):278.

114. Casey AL, Karpanen TJ, Conway BR, Worthington T, Nightingale P, Waters R, Elliott TS. Enhanced chlorhexidine skin penetration with 1, 8-cineole. BMC Infectious Diseases. 2017 May 17;17(1):350.

115. Şimşek M, Duman R. Investigation of effect of 1, 8-cineole on antimicrobial activity of chlorhexidine gluconate. Pharmacognosy research. 2017 Jul;9(3):234.

116. Kirkby M, Sabri AB, Scurr D, Moss G. Microneedle-mediated permeation enhancement of chlorhexidine digluconate: mechanistic insights through imaging mass spectrometry. Pharmaceutical Research. 2022 Aug;39(8):1945-58.

117. Salaymeh EA, Steinberg D, Ammar AA. Chlorhexidine-loaded microneedles for treatment of oral diseases. International Journal of Pharmaceutics. 2025 Feb 10;670:125143.

118. Keurentjes, A.J., Jakasa, I. and Kezic, S., 2021. Research techniques made simple: stratum corneum tape stripping. *Journal of Investigative Dermatology*, *141*(5), pp.1129-1133.

119. Herkenne C, Alberti I, Naik A, Kalia YN, Mathy FX, Préat V, Guy RH. In vivo methods for the assessment of topical drug bioavailability. Pharmaceutical research. 2008 Jan;25(1):87-103.

120. Fritz B, Halling AS, Cort ID, Christensen MO, Rønnstad AT, Olesen CM, Knudgaard MH, Zachariae C, Heegaard S, Thyssen JP, Bjarnsholt T. RNA-sequencing of paired tape-strips and skin biopsies in atopic dermatitis reveals key differences. Allergy. 2024 Jun;79(6):1548-59.

121. Weerheim A, Ponec M. Determination of stratum corneum lipid profile by tape stripping in combination with high-performance thin-layer chromatography. Archives of dermatological research. 2001 Apr;293(4):191-9.

122. Escobar-Chavez JJ, Merino-Sanjuán V, López-Cervantes M, Urban-Morlan Z, Piñón-Segundo E, Quintanar-Guerrero D, Ganem-Quintanar A. The tape-stripping technique as a method for drug quantification in skin. Journal of pharmacy & pharmaceutical sciences. 2008 Mar 26;11(1):104-30.

123. Robinson H, Ravikulan A, Nater UM, Skoluda N, Jarrett P, Broadbent E. The role of social closeness during tape stripping to facilitate skin barrier recovery: Preliminary findings. Health Psychology. 2017 Jul;36(7):619.

124. Barber C, Boiko S. Tape stripping: investigational, diagnostic, and therapeutic uses in dermatology. Clinics in Dermatology. 2022 Jul 1;40(4):355-62.

125. Soga N, Nagura R, Nakamura R, Kohda K, Motoyama Y, Ito M, Nakagawa I, Nakajima S, Ikeuchi A. Simple tape-stripping method for highly reliable and quantitative analysis of skin microbiome. Experimental Dermatology. 2024 Aug;33(8):e15154.

126. Nair A, Jacob S, Al-Dhubiab B, Attimarad M, Harsha S. Basic considerations in the dermatokinetics of topical formulations. Brazilian journal of pharmaceutical sciences. 2013;49:423-34.

127. Lademann J, Jacobi U, Surber C, Weigmann HJ, Fluhr JW. The tape stripping procedure–evaluation of some critical parameters. European Journal of Pharmaceutics and Biopharmaceutics. 2009 Jun 1;72(2):317-23.

128. Taylor SJ, Wilson DJ. The Human Tissue Act (2004), anatomical examination and the importance of body donation in Northern Ireland. The Ulster medical journal. 2007 Sep;76(3):124.

129. Pulsoni I, Lubda M, Aiello M, Fedi A, Marzagalli M, von Hagen J, Scaglione S. Comparison between Franz diffusion cell and a novel micro-physiological system for

in vitro penetration assay using different skin models. SLAS technology. 2022 Jun 1;27(3):161-71.

130. Salamanca CH, Barrera-Ocampo A, Lasso JC, Camacho N, Yarce CJ. Franz diffusion cell approach for pre-formulation characterisation of ketoprofen semi-solid dosage forms. Pharmaceutics. 2018 Sep 5;10(3):148.

131. Trebilcock K, Heylings JR, Wilks MF. In vitro tape stripping as a model for in vivo skin stripping. Toxicology in vitro. 1994 Aug 1;8(4):665-7.

132. Jonsdottir F, Snorradottir BS, Gunnarsson S, Georgsdottir E, Sigurdsson S. Transdermal drug delivery: determining permeation parameters using tape stripping and numerical modeling. Pharmaceutics. 2022 Sep 6;14(9):1880.

133. Simon K, Oberender G, Roloff A. Continuous removal of single cell layers by tape stripping the stratum corneum–a histological study. European Journal of Pharmaceutics and Biopharmaceutics. 2023 Jul 1;188:48-53.

134. Cassidy SS, Sanders DJ, Wade J, Parkin IP, Carmalt CJ, Smith AM, Allan E. Antimicrobial surfaces: A need for stewardship?. PLoS Pathogens. 2020 Oct 15;16(10):e1008880.

135. Mahanta U, Khandelwal M, Deshpande AS. Antimicrobial surfaces: a review of synthetic approaches, applicability and outlook. Journal of Materials Science. 2021 Nov;56(32):17915-41.

136. Carling PC, Parry MF, Bruno-Murtha LA, Dick B. Improving environmental hygiene in 27 intensive care units to decrease multidrug-resistant bacterial transmission. Critical care medicine. 2010 Apr 1;38(4):1054-9.

137. Vincent M, Duval RE, Hartemann P, Engels-Deutsch M. Contact killing and antimicrobial properties of copper. Journal of applied microbiology. 2018 May 1;124(5):1032-46.

138. Chang T, Babu RP, Zhao W, Johnson CM, Hedstrom P, Odnevall I, Leygraf C. High-resolution microscopical studies of contact killing mechanisms on copper-based surfaces. ACS applied materials & interfaces. 2021 Oct 7;13(41):49402-13.

139. Turner RJ. The good, the bad, and the ugly of metals as antimicrobials. Biometals. 2024 Jun;37(3):545-59.

140. Salgado CD, Sepkowitz KA, John JF, Cantey JR, Attaway HH, Freeman KD, Sharpe PA, Michels HT, Schmidt MG. Copper surfaces reduce the rate of healthcare-acquired infections in the intensive care unit. Infection Control & Hospital Epidemiology. 2013 May;34(5):479-86.

141. Serov DA, Gritsaeva AV, Yanbaev FM, Simakin AV, Gudkov SV. Review of antimicrobial properties of titanium dioxide nanoparticles. International Journal of Molecular Sciences. 2024 Sep 29;25(19):10519.

142. Chavali MS, Nikolova MP. Metal oxide nanoparticles and their applications in nanotechnology. SN applied sciences. 2019 Jun;1(6):607.

143. Dunnick K. Metal oxide nanoparticles: The importance of size, shape, chemical composition, and valence state in determining toxicity. 2015.

144. Sánchez-López E, Gomes D, Esteruelas G, Bonilla L, Lopez-Machado AL, Galindo R, Cano A, Espina M, Ettcheto M, Camins A, Silva AM. Metal-based nanoparticles as antimicrobial agents: an overview. Nanomaterials. 2020 Feb 9;10(2):292.

145. Park MV, Neigh AM, Vermeulen JP, de la Fonteyne LJ, Verharen HW, Briedé JJ, van Loveren H, de Jong WH. The effect of particle size on the cytotoxicity, inflammation, developmental toxicity and genotoxicity of silver nanoparticles. Biomaterials. 2011 Dec 1;32(36):9810-7.

146. Chithrani BD, Ghazani AA, Chan WC. Determining the size and shape dependence of gold nanoparticle uptake into mammalian cells. Nano letters. 2006 Apr 12;6(4):662-8.

147. Hsiao IL, Huang YJ. Effects of various physicochemical characteristics on the toxicities of ZnO and TiO2 nanoparticles toward human lung epithelial cells. Science of the total environment. 2011 Mar 1;409(7):1219-28.

148. Correa MG, Martínez FB, Vidal CP, Streitt C, Escrig J, de Dicastillo CL. Antimicrobial metal-based nanoparticles: A review on their synthesis, types and antimicrobial action. Beilstein journal of nanotechnology. 2020 Sep 25;11(1):1450-69.

149. Barras F, Aussel L, Ezraty B. Silver and antibiotic, new facts to an old story. Antibiotics. 2018 Aug 22;7(3):79.

150. Weber J, Henssler L, Zeman F, Pfeifer C, Alt V, Nerlich M, Huber M, Herbst T, Koller M, Schneider-Brachert W, Kerschbaum M. Nanosilver/DCOIT-containing surface coating effectively and constantly reduces microbial load in emergency room surfaces. Journal of Hospital Infection. 2023 May 1;135:90-7.

151. Bragg PD, Rainnie DJ. The effect of silver ions on the respiratory chain of Escherichia coli. Canadian journal of microbiology. 1974 Jun 1;20(6):883-9.

152. Yin IX, Zhang J, Zhao IS, Mei ML, Li Q, Chu CH. The antibacterial mechanism of silver nanoparticles and its application in dentistry. International journal of nanomedicine. 2020 Apr 17:2555-62.

153. Sharma P, Fialho L, Figueiredo NM, Serra R, Cavaleiro A, Carvalho S. Antimicrobial polymeric surfaces using embedded silver nanoparticles. Antibiotics. 2023 Jan 18;12(2):207.

154. Flores-López LZ, Espinoza-Gómez H, Somanathan R. Silver nanoparticles: Electron transfer, reactive oxygen species, oxidative stress, beneficial and toxicological effects. Mini review. Journal of Applied Toxicology. 2019 Jan;39(1):16-26.

155. Zhang T, Wang L, Chen Q, Chen C. Cytotoxic potential of silver nanoparticles. Yonsei medical journal. 2014 Feb 10;55(2):283.

156. McShan D, Ray PC, Yu H. Molecular toxicity mechanism of nanosilver. Journal of food and drug analysis. 2014 Mar 1;22(1):116-27.

157. Jeong EM, Yoon JH, Lim J, Shin JW, Cho AY, Heo J, Lee KB, Lee JH, Lee WJ, Kim HJ, Son YH. Real-time monitoring of glutathione in living cells reveals that high glutathione levels are required to maintain stem cell function. Stem cell reports. 2018 Feb 13;10(2):600-14.

158. Grass G, Rensing C, Solioz M. Metallic copper as an antimicrobial surface. Applied and environmental microbiology. 2011 Mar 1;77(5):1541-7.

159. Santo CE, Lam EW, Elowsky CG, Quaranta D, Domaille DW, Chang CJ, Grass G. Bacterial killing by dry metallic copper surfaces. Applied and environmental microbiology. 2011 Feb 1;77(3):794-802.

160. Wheeldon LJ, Worthington T, Lambert PA, Hilton AC, Lowden CJ, Elliott TS. Antimicrobial efficacy of copper surfaces against spores and vegetative cells of Clostridium difficile: the germination theory. Journal of Antimicrobial Chemotherapy. 2008 Sep 1;62(3):522-5.

161. Noyce JO, Michels H, Keevil CW. Potential use of copper surfaces to reduce survival of epidemic meticillin-resistant Staphylococcus aureus in the healthcare environment. Journal of Hospital Infection. 2006 Jul 1;63(3):289-97.

162. Mehtar S, Wiid I, Todorov SD. The antimicrobial activity of copper and copper alloys against nosocomial pathogens and Mycobacterium tuberculosis isolated from healthcare facilities in the Western Cape: an in-vitro study. Journal of Hospital Infection. 2008 Jan 1;68(1):45-51.

163. Dupont CL, Grass G, Rensing C. Copper toxicity and the origin of bacterial resistance—new insights and applications. Metallomics. 2011 Nov;3(11):1109-18.

164. Gudkov SV, Burmistrov DE, Fomina PA, Validov SZ, Kozlov VA. Antibacterial properties of copper oxide nanoparticles. International Journal of Molecular Sciences. 2024 Oct 28;25(21):11563.

165. Naz S, Gul A, Zia M. Toxicity of copper oxide nanoparticles: a review study. IET nanobiotechnology. 2020 Feb;14(1):1-3.

166. Rajamma R, Gopalakrishnan Nair S, Abdul Khadar F, Baskaran B. Antibacterial and anticancer activity of biosynthesised CuO nanoparticles. IET nanobiotechnology. 2020 Dec;14(9):833-8.

167. Hussain S, Khan M, Sheikh TM, Mumtaz MZ, Chohan TA, Shamim S, Liu Y. Zinc essentiality, toxicity, and its bacterial bioremediation: A comprehensive insight. Frontiers in microbiology. 2022 May 31;13:900740.

168. Malheiros SS, Borges MH, Rangel EC, Fortulan CA, da Cruz NC, Barao VA, Nagay BE. Zinc-Doped Antibacterial Coating as a Single Approach to Unlock Multifunctional and Highly Resistant Titanium Implant Surfaces. ACS Applied Materials & Interfaces. 2025 Mar 18;17(12):18022-45.

169. Pasquet J, Chevalier Y, Pelletier J, Couval E, Bouvier D, Bolzinger MA. The contribution of zinc ions to the antimicrobial activity of zinc oxide. Colloids and Surfaces A: Physicochemical and Engineering Aspects. 2014 Sep 5;457:263-74.

170. Hlady V, Buijs J. Protein adsorption on solid surfaces. Current opinion in biotechnology. 1996 Feb 1;7(1):72-7.

171. Sirelkhatim A, Mahmud S, Seeni A, Kaus NH, Ann LC, Bakhori SK, Hasan H, Mohamad D. Review on zinc oxide nanoparticles: antibacterial activity and toxicity mechanism. Nano-micro letters. 2015 Jul;7(3):219-42.

172. Mendes CR, Dilarri G, Forsan CF, Sapata VD, Lopes PR, de Moraes PB, Montagnolli RN, Ferreira H, Bidoia ED. Antibacterial action and target mechanisms of zinc oxide nanoparticles against bacterial pathogens. Scientific reports. 2022 Feb 16;12(1):2658.

173. Pace NJ, Weerapana E. Zinc-binding cysteines: diverse functions and structural motifs. Biomolecules. 2014 Apr 17;4(2):419-34.

174. Rihacek M, Kosaristanova L, Fialova T, Kuthanova M, Eichmeier A, Hakalova E, Cerny M, Berka M, Palkovicova J, Dolejska M, Svec P. Zinc effects on bacteria: insights from Escherichia coli by multi-omics approach. Msystems. 2023 Dec 21;8(6):e00733-23.

175. De Matteis V, Cascione M, Rinaldi R. Titanium dioxide: Antimicrobial surfaces and toxicity assessment. InTitanium Dioxide (Tio_2) and Its Applications 2021 Jan 1 (pp. 373-393). Elsevier.

176. Kumaravel J, Lalitha K, Arunthirumeni M, Shivakumar MS. Mycosynthesis of bimetallic zinc oxide and titanium dioxide nanoparticles for control of Spodoptera frugiperda. Pesticide Biochemistry and Physiology. 2021 Oct 1;178:104910.

177. Jafari S, Mahyad B, Hashemzadeh H, Janfaza S, Gholikhani T, Tayebi L. Biomedical applications of TiO2 nanostructures: recent advances. International journal of nanomedicine. 2020 May 14:3447-70.

178. Serov DA, Gritsaeva AV, Yanbaev FM, Simakin AV, Gudkov SV. Review of antimicrobial properties of titanium dioxide nanoparticles. International Journal of Molecular Sciences. 2024 Sep 29;25(19):10519.

179. Khaiboullina S, Uppal T, Dhabarde N, Subramanian VR, Verma SC. Inactivation of human coronavirus by titania nanoparticle coatings and UVC radiation: throwing light on SARS-CoV-2. Viruses. 2020 Dec 24;13(1):19.

180. Chandoliya R, Sharma S, Sharma V, Joshi R, Sivanesan I. Titanium dioxide nanoparticle: A comprehensive review on synthesis, applications and toxicity. Plants. 2024 Oct 23;13(21):2964.

181. Ion R, Necula MG, Mazare A, Mitran V, Neacsu P, Schmuki P, Cimpean A. Drug delivery systems based on titania nanotubes and active agents for enhanced osseointegration of bone implants. Current Medicinal Chemistry. 2020 Feb 1;27(6):854-902.

182. Pulit-Prociak J, Długosz O, Staroń A, Radomski P, Domagała D, Banach M. In vitro studies of titanium dioxide nanoparticles modified with glutathione as a potential drug delivery system. Nanotechnology Reviews. 2023 Nov 6;12(1):20230126.

183. Khashan KS, Sulaiman GM, Abdulameer FA, Albukhaty S, Ibrahem MA, Al-Muhimeed T, AlObaid AA. Antibacterial activity of TiO2 nanoparticles prepared by one-step laser ablation in liquid. Applied Sciences. 2021 May 19;11(10):4623.

184. Lee MS, Hussein HR, Chang SW, Chang CY, Lin YY, Chien Y, Yang YP, Kiew LV, Chen CY, Chiou SH, Chang CC. Nature-inspired surface structures design for antimicrobial applications. International journal of molecular sciences. 2023 Jan 10;24(2):1348.

185. Zhang D, Ji J, Yan C, Zhang J, An Z, Shen Y. Research advances in bio-inspired superhydrophobic surface: Bridging nature to practical applications. Journal of Industrial and Engineering Chemistry. 2024 Dec 25;140:20-46.

186. Watson GS, Green DW, Schwarzkopf L, Li X, Cribb BW, Myhra S, Watson JA. A gecko skin micro/nano structure–A low adhesion, superhydrophobic, anti-wetting, self-cleaning, biocompatible, antibacterial surface. Acta biomaterialia. 2015 Jul 15;21:109-22.

187. Ashok D, Cheeseman S, Wang Y, Funnell B, Leung SF, Tricoli A, Nisbet D. Superhydrophobic surfaces to combat bacterial surface colonization. Advanced Materials Interfaces. 2023 Aug;10(24):2300324.

188. Zhang S, Liang X, Gadd GM, Zhao Q. Superhydrophobic coatings for urinary catheters to delay bacterial biofilm formation and catheter-associated urinary tract infection. ACS Applied Bio Materials. 2019 Dec 3;3(1):282-91.

189. Xie Z, Zhang P, Zhang Z, Chen C, Wang X. The choice of antimicrobial polymers: Hydrophilic or hydrophobic?. Chinese Chemical Letters. 2024 Sep 1;35(9):109768.

190. Lai C, Wang S, Zhong P, Chen Y, Xu J, Li X, Liu W. A low-friction and high-stability hydrophilic PVP/PEG coated TPU for interventional catheter applications. Tribology International. 2024 Oct 1;198:109859.

191. Yasir M, Dutta D, Hossain KR, Chen R, Ho KK, Kuppusamy R, Clarke RJ, Kumar N, Willcox MD. Mechanism of action of surface immobilized antimicrobial peptides against Pseudomonas aeruginosa. Frontiers in microbiology. 2020 Jan 22;10:3053.

192. Salvagni E, García C, Manresa À, Müller-Sánchez C, Reina M, Rodríguez-Abreu C, García-Celma MJ, Esquena J. Short and ultrashort antimicrobial peptides anchored onto soft commercial contact lenses inhibit bacterial adhesion. Colloids and Surfaces B: Biointerfaces. 2020 Dec 1;196:111283.

193. Riordan L, Smith EF, Mills S, Hudson J, Stapley S, Nikoi ND, Edmondson S, Blair J, Peacock AF, Scurr D, Forster G. Directly bonding antimicrobial peptide mimics to steel and the real world applications of these materials. Materials Science and Engineering *: C*. 2019; *102*, 299-304.

194. Suba RB, Raj RD, Keerthika K, Vinothini V. Chitosan-based biomaterial in wound healing: a review. Cureus. 2024;16(2).

195. Wang CH, Cherng JH, Liu CC, Fang TJ, Hong ZJ, Chang SJ, Fan GY, Hsu SD. Procoagulant and antimicrobial effects of chitosan in wound healing. International Journal of Molecular Sciences. 2021 Jun 30;22(13):7067.

196. Laverde-Rojas V, Liscano Y, Rivera-Sánchez SP, Ocampo-Ibáñez ID, Betancourt Y, Alhajj MJ, Yarce CJ, Salamanca CH, Oñate-Garzón J. Antimicrobial contribution of chitosan surface-modified nanoliposomes combined with colistin against sensitive and colistin-resistant clinical Pseudomonas aeruginosa. Pharmaceutics. 2020 Dec 30;13(1):41.

197. Kaczmarek B. Tannic acid with antiviral and antibacterial activity as a promising component of biomaterials—A minireview. Materials. 2020 Jul 20;13(14):3224.

198. Brazdaru L, Micutz M, Staicu T, Albu M, Sulea D, Leca M. Structural and rheological properties of collagen hydrogels containing tannic acid and chlorhexidine digluconate intended for topical applications. Comptes Rendus. Chimie. 2015;18(2):160-9.

199. Kumorek M, Minisy IM, Krunclová T, Voršiláková M, Venclíková K, Chánová EM, Janoušková O, Kubies D. pH-responsive and antibacterial properties of self-assembled multilayer films based on chitosan and tannic acid. Materials Science and Engineering: C. 2020 Apr 1;109:110493.

200. Lee J, Yeo M, Kim W, Koo Y, Kim GH. Development of a tannic acid cross-linking process for obtaining 3D porous cell-laden collagen structure. International journal of biological macromolecules. 2018 Apr 15;110:497-503.

201. Sun H, Choi D, Heo J, Jung SY, Hong J. Studies on the drug loading and release profiles of degradable chitosan-based multilayer films for anticancer treatment. Cancers. 2020 Mar 5;12(3):593.

202. Bridgeman CJ, Nguyen TU, Kishore V. Anticancer efficacy of tannic acid is dependent on the stiffness of the underlying matrix. Journal of Biomaterials science, Polymer edition. 2018 Mar 4;29(4):412-27.

203. Xu L, Pranantyo D, Neoh KG, Kang ET. Tea stains-inspired antifouling coatings based on tannic acid-functionalized agarose. ACS Sustainable Chemistry & Engineering. 2017 Apr 3;5(4):3055-62.

204. Linklater DP, Ivanova EP. Nanostructured antibacterial surfaces–what can be achieved?. Nano Today. 2022 Apr 1;43:101404.

205. Ivanova EP, Linklater DP, Werner M, Baulin VA, Xu X, Vrancken N, Rubanov S, Hanssen E, Wandiyanto J, Truong VK, Elbourne A. The multi-faceted mechano-bactericidal mechanism of nanostructured surfaces. Proceedings of the National Academy of Sciences. 2020 Jun 9;117(23):12598-605.

206. Wainwright M, Amaral L. Photobactericides—a local option against multi-drug resistant bacteria. Antibiotics. 2013 Mar 27;2(2):182-90.

207. Gavara R, De Llanos R, Pérez-Laguna V, Arnau del Valle C, Miravet JF, Rezusta A, Galindo F. Broad-spectrum photo-antimicrobial polymers based on cationic polystyrene and rose bengal. Frontiers in Medicine. 2021 May 24;8:641646.

208. Ghosh S, Carter KA, Lovell JF. Liposomal formulations of photosensitizers. Biomaterials. 2019 Oct 1;218:119341.

209. Patir A, Hwang GB, Nair SP, Allan E, Parkin IP. Photobactericidal activity of dual dyes encapsulated in silicone enhanced by silver nanoparticles. ACS omega. 2018 Jun 22;3(6):6779-86.

210. Skoura E, Boháč P, Barlog M, Palkova H, Mautner A, Bugyna L, Bujdakova H, Bujdak J. Structure, photoactivity, and antimicrobial properties of phloxine B/poly (caprolactone) nanocomposite thin films. Applied Clay Science. 2023 Sep 15;242:107037.

211. Jin FL, Li X, Park SJ. Synthesis and application of epoxy resins: A review. Journal of industrial and engineering chemistry. 2015 Sep 25;29:1-1.

212. Kouznetsov VV, Vargas Méndez LY. Synthesis of eugenol-based monomers for sustainable epoxy thermoplastic polymers. Journal of applied polymer science. 2022 Jun 10;139(22):52237.

213. Pham HQ, Marks MJ. Epoxy resins. Ullmann's Encyclopedia of Industrial Chemistry. 2000 Jun 15.

214. Shundo A, Yamamoto S, Tanaka K. Network formation and physical properties of epoxy resins for future practical applications. Jacs Au. 2022 Jun 9;2(7):1522-42.

215. Bray PG. Epoxy resins. Occupational medicine (Philadelphia, Pa.). 1999 Oct 1;14(4):743-58.

216. Tofanica BM, Ungureanu E, Awaja F. Surface Chemistry and Molecular Dynamics of Epoxy Resin: Insights from Analysis During Curing and Post-Curing Processes. Polymers. 2025 Apr 18;17(8):1094.

217. Alsuwait RB, Souiyah M, Momohjimoh I, Ganiyu SA, Bakare AO. Recent development in the processing, properties, and applications of epoxy-based natural fiber polymer biocomposites. Polymers. 2022 Dec 28;15(1):145.

218. Wang Y, Wang Y. Toughening Modification of Epoxy Resin with Different Core-Shell Particles. Polym. Mater. Sci. Eng. 2012;28:23-7.

219. Srivastava R, Khandelwal S, Makker R, Razdan R, Bhogisetty C, Albar NH, Alamoudi A, Panta P. Impact strength of various types of acrylic resin: An in vitro study. The Journal of Contemporary Dental Practice. 2023 May 4;24(1).

220. Kakhk SH, Rad JK, Abedini H, Mahdavian AR. Thermomechanical study on toughened PVC with an impact modifier based on the acrylonitrile-styrene-acrylate core-shell particles. Polymer. 2024 Jan 5;290:126545.

221. Hao J, Yang K, Wu J, Wu M, Li Y. Overview of Recent Developments in Composite Epoxy Resin in Organic Coating on Steel (2020–2024). Materials. 2025 Mar 28;18(7):1531.

222. Schmidt RG, Bell JP. Investigation of steel/epoxy adhesion durability using polymeric coupling agents. II. Factors affecting adhesion durability. the Journal of Adhesion. 1988 Apr 1;25(2):85-107.

223. Szewczak A, Łagód G. Adhesion of modified epoxy resin to a concrete surface. Materials. 2022 Dec 15;15(24):8961.

224. Nakamura S, Tsuji Y, Yoshizawa K. Role of hydrogen-bonding and OH− π interactions in the adhesion of epoxy resin on hydrophilic surfaces. ACS omega. 2020 Oct 1;5(40):26211-9.

225. Suter JL, Muller WA, Vassaux M, Anastasiou A, Simmons M, Tilbrook D, Coveney PV. Rapid, Accurate and Reproducible Prediction of the Glass Transition Temperature Using Ensemble-Based Molecular Dynamics Simulation. Journal of Chemical Theory and Computation. 2025 Jan 29;21(3):1405-21.

226. Wang Y, Mertiny P. Mechanical and Thermal Properties of Epoxy Resin upon Addition of Low-Viscosity Modifier. Polymers. 2024 Aug 24;16(17):2403.

227. Tazi A, Dagdag O, El Amri A, Rafik M, Azogagh M, Haidara H, Kim H, El Bachiri A, Berisha A, Berdimurodov E, Tursunqulov J. New epoxy resin as a high-performance corrosion inhibitor for steel: experimental and theoretical investigations. Journal of Materials Science. 2025 Sep 13:1-21.

228. Dallaev R, Pisarenko T, Papež N, Sadovský P, Holcman V. A brief overview on epoxies in electronics: properties, applications, and modifications. Polymers. 2023 Sep 30;15(19):3964.

229. Rigo M, Khatami H, Mansi A, Marcelloni AM, Proietto AR, Chiominto A, Amori I, Bargellini A, Marchesi I, Frezza G, Lipani F. Revealing Commercial Epoxy Resins' Antimicrobial Activity: A Combined Chemical–Physical, Mechanical, and Biological Study. Polymers. 2024 Sep 11;16(18):2571.

230. Jiang G, Xiao Y, Qian Z, Yang Y, Jia P, Song L, Hu Y, Ma C, Gui Z. A novel phosphorus-, nitrogen-and sulfur-containing macromolecule flame retardant for

constructing high-performance epoxy resin composites. Chemical Engineering Journal. 2023 Jan 1;451:137823.

231. Pereira-Silva P, Borges J, Sampaio P. Recent advances in metal-based antimicrobial coatings. Advances in Colloid and Interface Science. 2025 Jun 29:103590.

232. Nikolov A, Dobreva L, Danova S, Miteva-Staleva J, Krumova E, Rashev V, Vilhelmova-Ilieva N, Tsvetanova L, Barbov B. Antimicrobial geopolymer paints based on modified natural zeolite. Case Studies in Construction Materials. 2023 Dec 1;19:e02642.

233. Hochmannova L, Vytrasova J. Photocatalytic and antimicrobial effects of interior paints. Progress in Organic Coatings. 2010 Jan 1;67(1):1-5.

234. Jeong S, Park JY, Kim JM, Kim Y. Photothermally enhanced hollow gold nanopigment for water evaporation and sterilization achieved via a photothermal effect. Building and Environment. 2023 Feb 1;229:109970.

235. Chen WC, Ho MH, Yuan SH, Chou HW, Chang CC, Chen CH, Lin YE. The Evaluation of Antibacterial Coatings Against Commonly Found Pathogenic Bacteria in the Environment—Implications for Environmental Safety and Infection Prevention. Pathogens. 2024 Dec 30;14(1):13.

236. Yueh MF, Tukey RH. Triclosan: a widespread environmental toxicant with many biological effects. Annual review of pharmacology and toxicology. 2016 Jan 6;56(1):251-72.

237. Querido MM, Paulo I, Hariharakrishnan S, Rocha D, Barbosa N, Galhano dos Santos R, Bordado JM, Teixeira JP, Pereira CC. Self-disinfecting paints with the natural antimicrobial substances: Colophony and curcumin. Antibiotics. 2021 Nov 5;10(11):1351.

238. Ke Z, Yu J, Liao L, Rao X. Application progress of rosin in food packaging: A review. International Journal of Biological Macromolecules. 2024 Nov 1;280:135900.

239. Gupta S, Puttaiahgowda YM, Kulal A. Development and evaluation of antimicrobial PVC-grafted polymer for enhanced paint applications. RSC advances. 2024;14(35):25669-77.

240. National Center for Biotechnology Information. "PubChem Compound Summary for CID 8795, Aminoethylpiperazine" *PubChem*, https://pubchem.ncbi.nlm.nih.gov/compound/Aminoethylpiperazine. Accessed 6 January, 2026.

241. Ghosh S, Jolly L, Haldar J. Polymeric paint coated common-touch surfaces that can kill bacteria, fungi and influenza virus. MRS communications. 2021 Oct;11(5):610-8.

242. Akif FA, Mahmoud M, Prasad B, Richter P, Azizullah A, Qasim M, Anees M, Krüger M, Gastiger S, Burkovski A, Strauch SM. Polyethylenimine increases antibacterial efficiency of chlorophyllin. Antibiotics. 2022 Oct 7;11(10):1371.

243. Gibney KA, Sovadinova I, Lopez AI, Urban M, Ridgway Z, Caputo GA, Kuroda K. Poly (ethylene imine) s as antimicrobial agents with selective activity. Macromolecular bioscience. 2012 Sep;12(9):1279-89.

244. Bryant JA, Riordan L, Watson R, Nikoi ND, Trzaska W, Slope L, Tibbatts C, Alexander MR, Scurr DJ, May RC, De Cogan F. Developing Novel Biointerfaces: Using Chlorhexidine Surface Attachment as a Method for Creating Anti-Fungal Surfaces. Global Challenges. 2022 May;6(5):2100138.

245. Williams G, Alao M, Brooks A, Doherty HM, Moynihan PJ, Moradigaravand D, Banzhaf M, de Cogan F, Bryant JA. Antimicrobial efficacy of chlorhexidine-treated surfaces against clinical isolates implicated in nosocomial infections. Journal of Medical Microbiology. 2025 Jun 24;74(6):002025.

246. Matos AO, Rangel EC, Barão VA, Gregory RL. Antimicrobial behavior of titanium coating with chlorhexidine-doped thin film exposed to a biofilm supplemented with nicotine. Dental materials journal. 2023 Mar 25;42(2):228-35.

247. Watson R, Maxwell M, Dunn S, Brooks A, Jiang L, Hill HJ, Williams G, Kotowska A, Nikoi ND, Stamataki Z, Banzhaf M. Development of biocide coated polymers and their antimicrobial efficacy. Nano Select. 2023 Jul;4(7):442-53.

248. Watson R, Oldfield M, Bryant JA, Riordan L, Hill HJ, Watts JA, Alexander MR, Cox MJ, Stamataki Z, Scurr DJ, de Cogan F. Efficacy of antimicrobial and anti-viral coated air filters to prevent the spread of airborne pathogens. Scientific Reports. 2022 Mar 9;12(1):2803.

249. Bento de Carvalho T, Barbosa JB, Teixeira P. Assessing antimicrobial efficacy on plastics and other non-porous surfaces: a closer look at studies using the ISO 22196: 2011 standard. Biology. 2024 Jan 20;13(1):59.

250. Seo B, Kanematsu H, Nakamoto M, Miyabayashi Y, Tanaka T. Copper surface treatment method with antibacterial performance using “super-spread wetting” properties. Materials. 2022 Jan 5;15(1):392.

251. Rosenberg M, Vija H, Kahru A, Keevil CW, Ivask A. Rapid in situ assessment of Cu-ion mediated effects and antibacterial efficacy of copper surfaces. Scientific reports. 2018 May 25;8(1):8172.

252. Kanasugi K, Nakajima T, Hirakuri K. Antibacterial and Film Characteristics of Copper-Doped Diamond-like Carbon Films via Sputtering Using a Mixed Target of Copper and Graphite. Coatings. 2025 May 7;15(5):559.

253. Varghese S, Elfakhri S, Sheel DW, Sheel P, Bolton FJ, Foster HA. Novel antibacterial silver-silica surface coatings prepared by chemical vapour deposition for infection control. Journal of applied microbiology. 2013 Nov 1;115(5):1107-16.

254. Thokala N, Kealey C, Kennedy J, Brady DB, Farrell J. Comparative activity of silver-based antimicrobial composites for urinary catheters. International journal of antimicrobial agents. 2018 Aug 1;52(2):166-71.

255. Kasperkiewicz K, Major R, Sypien A, Kot M, Dyner M, Major Ł, Byrski A, Kopernik M, Lackner JM. Antibacterial optimization of highly deformed titanium alloys for spinal Implants. Molecules. 2021 May 24;26(11):3145.

256. van Hengel IA, Tierolf MW, Fratila-Apachitei LE, Apachitei I, Zadpoor AA. Antibacterial titanium implants biofunctionalized by plasma electrolytic oxidation with silver, zinc, and copper: A systematic review. International journal of molecular sciences. 2021 Apr 6;22(7):3800.

257. Uggeri J, Gatti R, Belletti S, Scandroglio R, Corradini R, Rotoli BM, Orlandini G. Calcein-AM is a detector of intracellular oxidative activity. Histochemistry and cell biology. 2000 Nov;122(5):499-505.

258. Perfetto SP, Chattopadhyay PK, Lamoreaux L, Nguyen R, Ambrozak D, Koup RA, Roederer M. Amine-reactive dyes for dead cell discrimination in fixed samples. Current protocols in cytometry. 2010 Jul;53(1):9-34.

259. Bauer AW, Kirby WM, Sherris JC, Turck M. Antibiotic susceptibility testing by a standardized single disk method. American journal of clinical pathology. 1966 Apr 1;45(4_ts):493-6.

260. Webber DM, Wallace MA, Burnham CA. Stop waiting for tomorrow: Disk diffusion performed on early growth is an accurate method for antimicrobial susceptibility testing with reduced turnaround time. Journal of clinical microbiology. 2022 May 18;60(5):e03007-20.

261. Bubonja-Šonje M, Knežević S, Abram M. Challenges to antimicrobial susceptibility testing of plantderived polyphenolic compounds. Arhiv za higijenu rada i toksikologiju. 2020 Dec 23;71(4):300-11.

262. Hossain TJ. Methods for screening and evaluation of antimicrobial activity: A review of protocols, advantages, and limitations. European Journal of Microbiology and Immunology. 2024 May 14;14(2):97-115.

263. Callebaut K, Stoefs A, Emmerechts K, Vandoorslaer K, Wybo I, De Geyter D, Demuyser T, Piérard D, Muyldermans A. Evaluation of Automated Disk Diffusion Antimicrobial Susceptibility Testing Using Radian® In-Line Carousel. Current microbiology. 2024 Jul;81(7):196.

264. Hombach M, Ochoa C, Maurer FP, Pfiffner T, Böttger EC, Furrer R. Relative contribution of biological variation and technical variables to zone diameter variations of disc diffusion susceptibility testing. Journal of Antimicrobial Chemotherapy. 2016 Jan 1;71(1):141-51.

265. Lehtopolku M, Kotilainen P, Puukka P, Nakari UM, Siitonen A, Eerola E, Huovinen P, Hakanen AJ. Inaccuracy of the disk diffusion method compared with the agar

dilution method for susceptibility testing of Campylobacter spp. Journal of Clinical Microbiology. 2012 Jan;50(1):52-6.

266. Benninghoven A. The development of SIMS and international SIMS conferences: a personal retrospective view. Surface and Interface Analysis. 2011 Jan;43(1-2):2-11.

267. Gilmore IS, Vickerman JC. Surface analysis: the principal techniques. John Wiley & Sons; 2009.

268. Henkel T, Gilmour J, Holland HD, Turekian KK. 15.22-Time-of-Flight Secondary Ion Mass Spectrometry, Secondary Neutral Mass Spectrometry, and Resonance Ionization Mass Spectrometry. InTreatise on Geochemistry (Second Edition) 2014 Aug 21 (pp. 411-424). Elsevier BV.

269. Graham DJ, Gamble LJ. Back to the basics of time-of-flight secondary ion mass spectrometry of bio-related samples. I. Instrumentation and data collection. Biointerphases. 2023 Mar 1;18(2).

270. Van Nuffel S, Brunelle A. TOF-SIMS imaging of biological tissue sections and structural determination using tandem MS. InMass Spectrometry Imaging of Small Molecules: Methods and Protocols 2021 Dec 14 (pp. 77-86). New York, NY: Springer US.

271. Yoon S, Lee TG. Biological tissue sample preparation for time-of-flight secondary ion mass spectrometry (ToF–SIMS) imaging. Nano Convergence. 2018 Sep 25;5(1):24.

272. Noun M, Akoumeh R, Abbas I. Cell and tissue imaging by TOF-SIMS and MALDI-TOF: an overview for biological and pharmaceutical analysis. Microscopy and Microanalysis. 2022 Feb 1;28(1):1-26.

273. Muramoto S, Graham DJ, Wagner MS, Lee TG, Moon DW, Castner DG. ToF-SIMS analysis of adsorbed proteins: principal component analysis of the primary ion species effect on the protein fragmentation patterns. The Journal of Physical Chemistry C. 2011 Dec 15;115(49):24247-55.

274. Neunzehn J, Draude F, Golla-Schindler U, Arlinghaus HF, Wiesmann HP. Detection of protein coatings on nanoparticles surfaces by ToF-SIMS and advanced electron microscopy. Surface and interface analysis. 2013 Sep;45(9):1340-6.

275. Passarelli MK, Winograd N. Lipid imaging with time-of-flight secondary ion mass spectrometry (ToF-SIMS). Biochimica et Biophysica Acta (BBA)-Molecular and Cell Biology of Lipids. 2011 Nov 1;1811(11):976-90.

276. Denbigh JL, Lockyer NP. ToF-SIMS as a tool for profiling lipids in cancer and other diseases. Materials Science and Technology. 2015 Jan;31(2):137-47.

277. Berrow M, Brooks A, Kotowska AM, Watts J, Riordan L, Kidger L, Scurr DJ, Nikoi ND, Banzhaf M, Bryant JA, Greenway S. Development and characterisation of antimicrobial epoxy resin. Scientific Reports. 2025 Apr 23;15(1):12463.

278. Mei H, Laws TS, Terlier T, Verduzco R, Stein GE. Characterization of polymeric surfaces and interfaces using time-of-flight secondary ion mass spectrometry. Journal of Polymer Science. 2022 Apr 1;60(7):1174-98.

279. Passarelli MK, Pirkl A, Moellers R, Grinfeld D, Kollmer F, Havelund R, Newman CF, Marshall PS, Arlinghaus H, Alexander MR, West A. The 3D OrbiSIMS—label-free metabolic imaging with subcellular lateral resolution and high mass-resolving power. Nature methods. 2017 Dec 1;14(12):1175-83.

280. Jia F, Zhao X, Zhao Y. Advancements in ToF-SIMS imaging for life sciences. Frontiers in Chemistry. 2023 Aug 24;11:1237408.

281. Mazel V, Richardin P. ToF-SIMS study of organic materials in cultural heritage: Identification and chemical imaging. Wiley; 2009 Jul 28.

282. Postawa Z, Czerwinski B, Szewczyk M, Smiley EJ, Winograd N, Garrison BJ. Microscopic insights into the sputtering of Ag {111} induced by C60 and Ga bombardment. The Journal of Physical Chemistry B. 2004 Jun 10;108(23):7831-8.

283. Jones EA, Fletcher JS, Thompson CE, Jackson DA, Lockyer NP, Vickerman JC. ToF-SIMS analysis of bio-systems: Are polyatomic primary ions the solution?. Applied surface science. 2006 Jul 30;252(19):6844-54.

284. Weibel DE, Lockyer N, Vickerman JC. C60 cluster ion bombardment of organic surfaces. Applied surface science. 2004 Jun 15;231:146-52.

285. Rockwood AL, Kushnir MM, Clarke NJ. Principles and Applications of Clinical Mass Spectrometry. 2018.

286. Hong A, Lee SJ, Choi CM, Baek JY, Choi MC. Neutral gas effect on the surface potential and charge compensation of an insulating sample. Applied Surface Science. 2022 Jan 15;572:151338.

287. Havelund R, Seah MP, Shard AG, Gilmore IS. Electron flood gun damage effects in 3D secondary ion mass spectrometry imaging of organics. Journal of The American Society for Mass Spectrometry. 2014 Jun 10;25(9):1565-71.

288. Gilmore IS, Seah MP. Electron flood gun damage in the analysis of polymers and organics in time-of-flight SIMS. Applied surface science. 2002 Feb 14;187(1-2):89-100.

289. Gilmore IS, Seah MP. Investigating the difficulty of eliminating flood gun damage in TOF-SIMS. Applied surface science. 2003 Jan 15;203:600-4.

290. Tyler BJ, Rayal G, Castner DG. Multivariate analysis strategies for processing ToF-SIMS images of biomaterials. Biomaterials. 2007 May 1;28(15):2412-23.

291. Touboul D, Kollmer F, Niehuis E, Brunelle A, Laprévote O. Improvement of biological time-of-flight-secondary ion mass spectrometry imaging with a bismuth

cluster ion source. Journal of the American Society for Mass Spectrometry. 2005 Oct;16(10):1608-18.

292. Fletcher JS, Lockyer NP, Vaidyanathan S, Vickerman JC. TOF-SIMS 3D biomolecular imaging of Xenopus laevis oocytes using buckminsterfullerene (C60) primary ions. Analytical Chemistry. 2007 Mar 15;79(6):2199-206.

293. Fletcher JS, Sämfors S, Vallin J, Svanström A, Grantham J. Correlated fluorescence microscopy and multi-ion beam secondary ion mass spectrometry imaging reveals phosphatidylethanolamine increases in the membrane of cancer cells over-expressing the molecular chaperone subunit CCTδ. Analytical and Bioanalytical Chemistry. 2021 Jan;413(2):445-53.

294. Tian H, Sparvero LJ, Amoscato AA, Bloom A, Bayır H, Kagan VE, Winograd N. Gas cluster ion beam time-of-flight secondary ion mass spectrometry high-resolution imaging of cardiolipin speciation in the brain: identification of molecular losses after traumatic injury. Analytical chemistry. 2017 Apr 18;89(8):4611-9.

295. Rabbani S, Barber AM, Fletcher JS, Lockyer NP, Vickerman JC. TOF-SIMS with argon gas cluster ion beams: a comparison with C60+. Analytical chemistry. 2011 May 15;83(10):3793-800.

296. Sjövall P, Skedung L, Gregoire S, Biganska O, Clément F, Luengo GS. Imaging the distribution of skin lipids and topically applied compounds in human skin using mass spectrometry. Scientific reports. 2018 Nov 12;8(1):16683.

297. Neittaanmäki N, Zaar O, Cehajic KS, Nilsson KD, Katsarelias D, Bagge RO, Paoli J, Fletcher JS. ToF-SIMS imaging reveals changes in tumor cell lipids during metastatic progression of melanoma. Pigment Cell & Melanoma Research. 2024 Nov;37(6):793-800.

298. Belsey NA, Dexter A, Vorng JL, Tsikritsis D, Nikula CJ, Murta T, Tiddia MV, Zhang J, Gurdak E, Trindade GF, Gilmore IS. Visualisation of drug distribution in skin using correlative optical spectroscopy and mass spectrometry imaging. Journal of Controlled Release. 2023 Dec 1;364:79-89.

299. Al-Mayahy MH, Marlow M, Scurr DJ. The Complementary Role of ToF-SIMS in the Assessment of Imiquimod Permeated into the Skin from a Microemulsion Dosage Form. Al Mustansiriyah Journal of Pharmaceutical Sciences. 2019 Dec 1;19(4):196-210.

300. Graham DJ, Castner DG. Image and spectral processing for ToF-SIMS analysis of biological materials. Mass Spectrometry. 2013 Apr 15;2(Special_Issue):S0014-.

301. Bich C, Touboul D, Brunelle A. Biomedical studies by TOF-SIMS imaging. Biointerphases. 2015 Mar 1;10(1).

302. Premnath SM, Zubair M. Chromatography. StatPearls. 2024 Jan 11.

303. Mahdi G, Alamdary A, Kaghazian H, Ahmadi N, Mardani R, Gholami A. Biopharmaceutical Analysis by HPLC: Practices and Challenges. Chonnam Medical Journal. 2025 Jan 24;61(1):19.

304. Rusli H, Putri RM, Alni A. Recent developments of liquid chromatography stationary phases for compound separation: from proteins to small organic compounds. Molecules. 2022 Jan 28;27(3):907.

305. Graceffa O, Kim E, Broweleit R, Rawle RJ. Choice of buffer in mobile phase can substantially alter peak areas in quantification of lipids by HPLC-ELSD. Journal of Chromatography B. 2022 Oct 15;1209:123417.

306. Park D, Won SM, Lee H. Enhanced Deoxygenation of Solvents via an Improved Inert Gas Bubbling Method with a Ventilation Pathway. ACS omega. 2024 Oct 12;9(42):42915-22.

307. Zapata A, Chefer VI, Shippenberg TS, Denoroy L. Detection and quantification of neurotransmitters in dialysates. Current protocols in neuroscience. 2009 Jul;48(1):7-4.

308. Czaplicki S. Chromatography in bioactivity analysis of compounds. Column chromatography. 2013 Apr 10:99-122.

309. Cooper WT. Normal-Phase Liquid Chromatography. Encyclopedia of analytical chemistry: applications, theory and instrumentation. 2006 Sep 15.

310. Jiang P, Lucy CA. Coupling normal phase liquid chromatography with electrospray ionization mass spectrometry: strategies and applications. Analytical Methods. 2016;8(35):6478-88.

311. Jandera P, Hájek T. Dual-mode hydrophilic interaction normal phase and reversed phase liquid chromatography of polar compounds on a single column. Journal of Separation Science. 2020 Jan;43(1):70-86.

312. Berthod A. Band broadening inside the chromatographic column: the interest of a liquid stationary phase. Journal of Chromatography a. 2006 Sep 8;1126(1-2):347-56.

313. Striegel AM. Longitudinal diffusion in size-exclusion chromatography: a stop-flow size-exclusion chromatography study. Journal of Chromatography A. 2001 Oct 12;932(1-2):21-31.

314. Sun K, Huang Y, Cao H, Mei X, Feng T, Chen Z, Zhang X, Wang X, Zhang B. A Complementary Type of Zero Dead Volume Connection for Capillary Column Liquid Chromatography. Analytical Chemistry. 2025 May 1;97(19):10149-54.

315. Heeter GA, Liapis AI. Frontal chromatography of proteins: Effect of axial dispersion on column performance. Journal of Chromatography A. 1998 Feb 13;796(1):157-64.

316. Gritti F, Guiochon G. Measurement of the eddy diffusion term in chromatographic columns. I. Application to the first generation of 4.6 mm ID monolithic columns. Journal of Chromatography A. 2011 Aug 5;1218(31):5216-27.

317. Levin DS, Shepperd BT, Gruenloh CJ. Combining ion pairing agents for enhanced analysis of oligonucleotide therapeutics by reversed phase-ion pairing ultra performance liquid chromatography (UPLC). Journal of Chromatography B. 2011 Jun 1;879(19):1587-95.

318. Cai B, Li J. Evaluation of trifluoroacetic acid as an ion-pair reagent in the separation of small ionizable molecules by reversed-phase liquid chromatography. Analytica chimica acta. 1999 Nov 15;399(3):249-58.

319. Sadi BB, Vonderheide AP, Gong JM, Schroeder JI, Shann JR, Caruso JA. An HPLC-ICP-MS technique for determination of cadmium–phytochelatins in genetically modified Arabidopsis thaliana. Journal of Chromatography B. 2008 Jan 1;861(1):123-9.

320. Zhang J, Raglione T, Wang Q, Kleintop B, Tomasella F, Liang X. Regeneration of tetrabutylammonium ion-pairing reagent distribution in a gradient elution of reversed phase ion-pair chromatography. Journal of chromatographic science. 2011 Nov 1;49(10):825-31.

321. Ivanović D, Popović A, Radulović D, Medenica M. Reversed-phase ion-pair HPLC determination of some water-soluble vitamins in pharmaceuticals. Journal of pharmaceutical and biomedical analysis. 1999 Jan 1;18(6):999-1004.

322. Mikšık I, Charvatova J, Eckhardt A, Cserhati T, Forgacs E, Deyl Z. Capillary electrophoretic separation of proteins and peptides by ion-pairing with heptanesulfonic acid. Journal of Chromatography B. 2004 Feb 5;800(1-2):161-7.

323. Baheti KG, Shah N, Shaikh S. Ion-pairing reverse-phase high performance liquid chromatography method for simultaneous estimation of atenolol and indapamide in bulk and combined dosage form. Indian Journal of Pharmaceutical Sciences. 2012 May;74(3):271.

324. Cardoso MA, Favero ML, Gasparetto JC, Hess BS, Stremel DP, Pontarolo R. Development and validation of an RP-HPLC method for the determination of chlorhexidine and p-chloroaniline in various pharmaceutical formulations. Journal of liquid chromatography & related technologies. 2011 Sep 1;34(15):1556-67.

325. Sobolewska E, Biesaga M. High-performance liquid chromatography methods for determining the purity of drugs with weak UV chromophores–A review. Critical Reviews in Analytical Chemistry. 2025 Apr 3;55(3):419-33.

326. Shamsaei D, Hsieh SA, Ocaña-Rios I, Ryan SJ, Anderson JL. Smartphone as a fluorescence detector for high-performance liquid chromatography. Analytica Chimica Acta. 2023 Nov 1;1280:341863.

327. Barnhart WW, Farooq MQ, Ahmad IA. A simplified tutorial on charged aerosol detection: Understanding the basics, optimization, and troubleshooting. Journal of Chromatography Open. 2024 Nov 1;6:100181.

328. Wade JH, Bailey RC. Refractive index-based detection of gradient elution liquid chromatography using chip-integrated microring resonator arrays. Analytical chemistry. 2014 Jan 7;86(1):913-9.

329. Özcan S, Geven A, Kozanli M, Can NÖ. The Development and Full Validation of a Novel Liquid Chromatography Electrochemical Detection Method for Simultaneous Determination of Nine Catecholamines in Rat Brain. Turkish Journal of Pharmaceutical Sciences. 2023 Nov 7;20(5):318.

330. Fujinari EM. High performance liquid chromatography-chemiluminescent nitrogen detection: HPLC-CLND. InDevelopments in Food Science 1998 Jan 1 (Vol. 39, pp. 431-466). Elsevier.

Chapter 2: Enhanced topical antimicrobial delivery for improved skin antisepsis

This chapter shows the final manuscript published by the Journal of Pharmaceutical Sciences. It discusses investigations on the permeation enhancement of CHX though human skin using an *in vitro* porcine skin permeation model. This work looks at the effects of formulating the clinical CHX-containing product, Hibiscrub with permeation enhancer compounds R6 polyarginine, glycolic acid and Kolliphor® HS15 to determine their impact on CHX delivery through the *stratum corneum* to improve microbial clearance through epidermis and reduce infection following surgery. As microbes reside throughout the entire *stratum corneum* and in deeper tissues such as the dermis, it is essential that skin antiseptics such as CHX permeate deep enough to these layers to prevent contamination and infection following surgical procedures. Hibiscrub is a clinical and commercially available hand soap formulation containing 4% *(w/v)* CHX, and poloxamer 237, isopropyl alcohol, lauryl dimethyl amine oxide, glycerol, macrogol 7 glycerol cocoate, gluconolactone, citrus perfume, ponceau 4R (E124), sodium hydroxide and purified water excipients. This paper also explores the antimicrobial efficacy of these permeation enhancer formulations when combined with CHX as well as their mammalian cytotoxicity profiles to determine their effectivity and suitability for use in clinic.

R6 polyarginine was selected due to its well established drug delivery power. As discussed in this paper, previous research has demonstrated that that R6 polyarginine has an ability to deliver macromolecules such as Insulin through the skin, in addition to ocular drug delivery which is notoriously challenging. Glycolic acid was selected due to its wide use in commercially available cosmetic skin products and its well-recognised ability to open keratinocyte tight junctions and promote desquamation of skin cells. Kolliphor® HS15 was used as it has been experimentally used for corneal drug delivery as well as increase the skins absorptive properties through interactions with P-glycoprotein, as reported in chapter 2.

My contributions to this manuscript include method development, sample analysis including ToF-SIMS, HPLC, microbial and cytotoxicity assays. I was also responsible for data collection, analysis and figure creation. The manuscript was written and reviewed by myself.

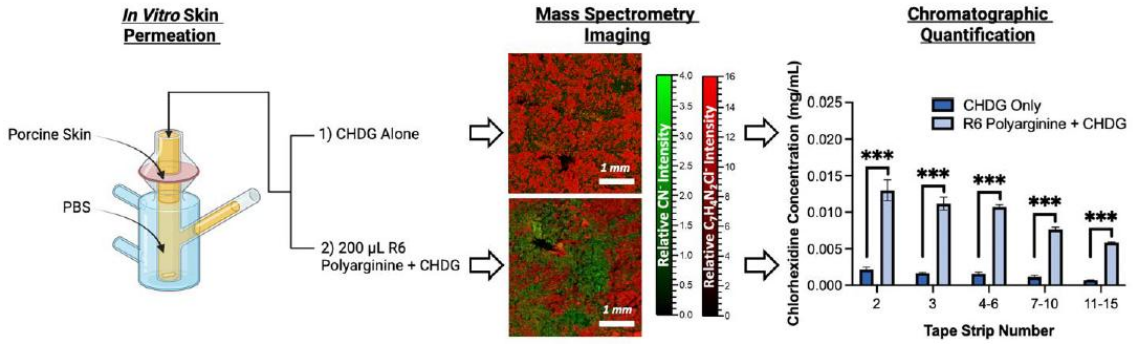
Enhanced topical antimicrobial delivery for improved skin antisepsis

Madeline Berrow [a], Nichola J Starr [a], David J Scurr [a], Felicity de Cogan [a]

[a] School of Pharmacy, University of Nottingham, University Park, Nottingham, NG7 2RD, United Kingdom

Corresponding author: Felicity de Cogan
Email: felicity.decogan@nottingham.ac.uk

Graphical Abstract



Abstract

The National Institute for Health and Care Excellence recommend the routine use of topically applied chlorhexidine digluconate (CHX) formulations to eliminate skin microorganisms prior to incision to prevent surgical site infections (SSI). However, CHX exhibits poor permeation through the *stratum corneum* and consequently is not effective in eliminating all skin microbes, resulting in an increased chance of patients acquiring infection. This study validates an *in vitro* porcine permeation model (Franz-type diffusion cell) by comparing CHX permeation through the porcine *stratum corneum* to *in vivo* human *stratum corneum.* Tape strips were sampled from the epidermis of both models and CHX distribution and abundance was analysed using time-of-flight secondary ion mass spectrometry (ToF-SIMS) and high performance liquid chromatography (HPLC). Once validated, the *in vitro* porcine model was used to determine the CHX permeation enhancement abilities of a series of experimental compounds, including R6 polyarginine, glycolic acid and Kolliphor® HS15. The porcine *stratum corneum* was tape stripped following treatment with these compounds and ToF-SIMS and HPLC was used to analyse permeation enhancement. This research demonstrated the similarity in CHX permeation through *in vivo* human skin and the *in vitro* porcine skin permeation model. Using the porcine model, we determined that R6 polyarginine, glycolic acid and Kolliphor® HS15 significantly increased CHX delivery through the entire epidermis. Finally, we demonstrate that our permeation enhancer formulations improve skin antisepsis throughout the *stratum corneum* whilst causing

no additional cytotoxicity to mammalian cells compared to clinical formulations. This research highlights three potential novel CHX formulation strategies for reducing SSI occurrence.

Keywords

chlorhexidine digluconate; skin permeation; topical antimicrobial; surgical site infection

Abbreviations

SSI – surgical site infection
CHX – chlorhexidine digluconate
ToF-SIMS – time-of-flight secondary ion mass spectrometry
HPLC – high performance liquid chromatography
DMEM – Dulbecco's Modified Eagle Medium
PBS – phosphate buffered saline
ATCC – American Type Culture Collection
NHS – National Health Service
LOD – limit of detection
LOQ – limit of quantification
MBC – minimum bacterial concentration
MRSA – methicillin-resistant *Staphylococcus aureus*

Introduction

Surgical interventions result in the incision through the skin and therefore improper skin antisepsis can lead to complications such as surgical site infections (SSI). Of the 5 million annual NHS hospital administrations, up to 150,000 patients encounter postoperative wound infections which often results in a 7-11 day prolonged hospitalisation, re-operation and up to 3.5% chance in mortality.[1,2,3,4] Amongst the implemented interventions to decrease SSI's, preoperative skin antisepsis strategies are routinely carried out to eliminate residing microflora.[2] The human skin harbours many species of microorganisms, including *Staphylococcus aureus,* coagulase-negative *Staphylococcus* (including *Staphylococcus haemolyticus* and *Staphylococcus hominis*), *Escherichia coli* and *Enterococcus spp.*[5,6] The native skin microbiome normally presents no threat to health until the skins physical barrier becomes compromised, and these microorganisms are free to infect sterile tissues and the bloodstream.

Chlorhexidine digluconate (CHX) is a highly potent, cationic bisbiguanide that exhibits broad-spectrum bactericidal, fungicidal and viricidal activity.[7] Due to its low mammalian cytotoxicity and ability to adsorb to skin and mucosal membranes,[8] CHX is routinely used in the medical industry for preoperative skin and hand antisepsis, intensive care and trauma patient bathing, skin antisepsis prior to medical device insertion (such as catheters and canulae) and for dental infection treatment.[7] For effective skin antisepsis and therefore the reduced risk of SSI, the permeation of CHX through the *stratum corneum* is essential to ensure that the microorganisms colonising the skin are eliminated[9] as it is well understood that bacteria reside deep within the epidermis and are constantly found within the dermis.[10] However, CHX, like many other antimicrobials, exhibits limited skin permeation (predominantly the upper 100 mm of the epidermis)[8,10,11] due to its high molecular weight, hydrophilicity and ionisation state.[10] This, coupled with the innate defence mechanisms of the *stratum corneum* prevents CHX from accessing deeper sites such as the hair follicle and sebaceous gland, particularly after short-term exposure, which is essential for effective skin antisepsis.[12,13,14]

In vivo human skin permeation studies are the preferred approach to monitoring transdermal drug delivery, followed by biopsy studies. However, due to limitations regarding availability, cost, regulations surrounding use and ethical considerations, along with the unpredictability of testing experimental compounds, these approaches are often substituted for *in vitro* permeation models, such as the Franz cell.[15,16] Analysing tape strips collected from *in vitro* porcine skin permeation models is a common approach to studying drug permeation as it is cheap, readily available and allows the study of unapproved formulations.[17] Validation of the model is essential before comparing results to *in vivo* drug permeation due to inconsistencies denoted in the literature. Starr *et al*., 2022 demonstrated the homogeneity in palmitoyl oligopeptide permeation between *in vitro* human skin and *in vivo* human skin models.[18] However, Simon *et al*., 2016 emphasises that the variability between *in vivo* human skin and *ex vivo* human and animal skin models can affect drug permeability.[19]

Porcine skin is the generally preferred animal model to study permeation through human skin due to similarities in histology, skin thickness, hair density and lipid composition.[20] The lipid abundancy is relatively poor in the human and porcine *stratum corneum* compared to other animal models like mice, rats and guinea pigs.[20] Inconsistencies between lipid compositions and architecture may affect barrier permeability making rodents an unsuitable model to study human skin permeation. Further, human and porcine skin contain similar metabolising enzymes including esterases and amidases, as well as phase II enzymes which form conjugation reactions and improve aqueous solubility of exogenous compounds, potentially altering their permeation profile through the skin.[20]

Various analytical approaches have been utilised to study drug permeation through the skin including chromatographic and secondary ion mass spectrometry techniques. High performance liquid chromatography (HPLC) is a powerful analytical tool with high resolution, sensitivity, versatility and accuracy. It has been used extensively to quantify drug compounds through different layers of the skin to determine permeation profiles, including adefovir (antiviral medication),[21] metformin (antidiabetic medication)[22] and caffeine.[23] Time-of-flight secondary ion mass spectrometry (ToF-SIMS) is an emerging analytical technique and has enabled the spatial distribution of permeating exogenous compounds to be acquired my mapping out corresponding ion distributions, including diclofenac (anti-inflammatory drug),[24] metallic salts[25] and vitamin C.[26] Both HPLC and ToF-SIMS have been deployed to study CHX permeation through the skin[27] as well CHX permeation enhancement by dendrimer[10,28] and microneedle[29] treatments.

This research paper utilised HPLC and ToF-SIMS analytical approaches to investigate the representability of our described *in vitro* porcine skin permeation model when studying CHX permeation through *in vivo* human skin. Further, we demonstrate the effect of increasing the concentration of CHX on the permeation depth and distribution of the antimicrobial through the *stratum corneum* using 2% and 4% *w/v* CHX formulations. HPLC and ToF-SIMS were also deployed to assess the improvement in permeation depth and spatial distribution of CHX throughout the *stratum corneum* when co-formulated with known permeation enhancers R6 polyarginine, a cell-penetrating peptide commonly used in ocular drug delivery mechanisms,[31] glycolic acid, a natural exfoliator that loosens epidermal tight junctions and promotes epithelial desquamation,[32] and Kolliphor® HS15 (polyoxyl 15 hydroxystearate), a surfactant previously used to improve corneal and transdermal drug bioavailability.[33]

2. Materials and Methods

2.1. Materials

Fresh porcine flank skin was collected from gilts reared at the University of Nottingham, Sutton Bonington, School of Veterinary Medicine and Science abattoir. Hibiscrub (4% w/v CHX) was purchased from Mölnlyckeâ, Gothenburg, Sweden. HPLC grade acetonitrile (>99.9%), triethylamine (99%) and syringe filters (0.2 mm, 33 mm diameter) were obtained from Fisher Scientific, Loughborough, UK. Sodium phosphate monobasic monohydrate (molecular weight 119.98 g/mol), phosphoric acid (85%), glycolic acid (99%), Luria-Bertoni broth and agar were acquired from Sigma Aldrich, Dorset, UK. D-Squame medical grade tape strips were purchased from CuDerm corporation. Franz-type diffusion cells were acquired from Soham Scientific (Soham, Cambridgeshire, UK). R6 polyarginine was purchased from GenScript, New Jersey, US. Kolliphor® HS15 was acquired from BASF, Ludwigshafen, Germany. 2 mL amber robotic 9 mm thread vials and 9 mm screw caps with white silicon/red polytetrafluoroethylene septa were acquired from Chromatography Direct, Wellingborough, UK. An ACE HPLC column (C_{18} dimension, 150 x 4.6 mm, 5 mm) was purchased from Hichrom Limited, Reading, UK. The ToF-SIMS IV instrument used for this research was purchased from IONTOF, GmbH, Münster, Germany and the HPLC 1260 Infinity II Liquid Chromatography System was acquired from Agilent, Santa Clara, US. Dulbecco's Modified Eagle Medium (DMEM), 0.25% trypsin-EDTA, newborn calf serum (heat inactivated), Pen Strep (10,000 units/mL Penicillin, 10,000 mg/mL Streptomycin), HEPES buffer solution, GlutaMAX™, phosphate buffered saline (PBS) (with Ca^{2+}/Mg^{2+}) and

PBS (without Ca^{2+}/Mg^{2+}), trypan blue 0.4%, Invitrogen cell counting chambers, Invitrogen Countess Automated cell counter and T75 cell culture flasks were all acquired from Thermo Fisher Scientific, US. Alamar Blue® solution was procured from Merck, UK and Murine 3T3 Fibroblasts were acquired from the American Type Culture Collection (ATCC).

2.2. Chlorhexidine Formulations

4% w/v CHX was acquired in the form of Hibiscrub® (4% w/v CHX [40 mg/mL]). 2% w/v CHX was produced by mixing Hibiscrub and deionised water (50:50). CHX formulations were stored in foil-wrapped scintillation vials at room temperature until used.

2.3. In Vivo Skin Permeation

2.3.1. Participant Criteria and Obtaining Consent

Following ethical approval (FMHS-1711122) granted from the University of Nottingham Faculty of Medicine and Health Sciences Research Committee, 6 Caucasian females (same sex from birth) aged between 20-30 years old were provided with a detailed information sheet about the research and procedure (experimental design to exclude male sex was done to reduce sample variability, which was previously studied). All were informed about the inclusion/exclusion criteria which ensured that participants had no current or previous skin condition (such as eczema or contact dermatitis), an allergy to CHX or soaps, involvement in research studies within the last month, applied cosmetic, skin or perfume products to the forearm within a day prior to sample collection or shaved their forearm within a week prior to sample collection. Signed participant consent forms were encrypted and uploaded to a secure online platform.

2.3.2. Preparation and Treatment of Human Skin

A 2 x 2 cm patch was marked out on each participant's forearm, approximately 10 cm up from the wrist to maximise corneocyte removal, which may be hindered by skin folds around the wrist joint and to prevent any possible contamination from previously applied cosmetics. Skin was washed with deionised water and absorbent paper towel to remove skin oils and dirt before 200 mL of 2% w/v CHX was pipetted onto the skins surface (Supplementary information, Figure 1). The CHX formulation was evenly spread over the skin, ensuring good skin coverage was achieved as recommended by the National Health Service (NHS)[34] and left on the skin for 2 minutes. Excess formulation was removed with absorbent tissue, washed with deionised water and dried using tissue (Teepol, which was used to wash the skin in the in vitro studies [section 2.4.2], was not applied to human skin due to the conditions of our ethical approval). 15 tape strips were immediately collected to sample the entire thickness of the stratum corneum so that CHX distribution through the skin could be determined after short-term exposure. This was achieved by applying a D-Squame® tape stripping disc to the skin, rolling the disc onto the skin using equal pressure and number of rolls, and a smooth, fast removal. Consecutive tape strips were applied and removed from the skin with an increasing 90° orientation from the previous, to maximise corneocyte removal. The process was repeated using 4% w/v CHX (Hibiscrub®) on a separate patch of skin in close proximity to the sampling location treated with 2% CHX . 15 tape strips were collected from untreated skin in close proximity to the CHX-treated sample sites, to provide a native skin

profile. Tape strip samples were stored in 1.5 mL Eppendorf tubes and frozen at -20°C until analysed using ToF-SIMS and HPLC.

2.4. In Vitro Skin Permeation

2.4.1. Preparation of Porcine Skin

Skin was collected prior to scolding treatment of the carcass, to preserve epidermal integrity. The subcutaneous fat was removed, and skin was washed in deionised water to remove blood and dirt. Porcine skin was cut into small pieces, approximately 10 cm^2, wrapped in aluminium foil and frozen at -20°C until used.

2.4.2. Franz-Type Diffusion Model Using Porcine Skin

Porcine skin was removed from the freezer and thawed at room temperature. The skin was cut into 2 x 2 cm sections and using micro scissors, the hair removed as close to the *stratum corneum* as possible without causing damage to the skin surface. Finally, the skin was washed with deionised water and an absorbent sponge to remove excess hair, dirt and oils before being clamped into a Franz-type diffusion cell. The Franz-type diffusion model experiment was conducted under non-occlusive conditions due to the short exposure times, and the circular permeation area of the Franz cell has a 12 mm diameter.

The receptor domain of each Franz-type diffusion cell was filled with PBS until the chamber was overflowing (approx. 3 mL). Prepared porcine skin was clamped between the receptor and donor chambers and incubated in a 37°C water bath with stirring for 20 minutes to allow equilibration of the cell. Following this, 200 mL of CHX formulation was added to the donor chamber to ensure good skin coverage was achieved, as advised by the NHS (National Health Service 2021). The assembled Franz-cell was incubated in a water bath for 2 minutes (Supplementary information, Figure 2). After treatment, the Franz-cell was disassembled, excess CHX formulation was wiped away and the skin was washed with 3% v/v Teepol detergent and deionised water to remove excess formulation oils and dirt and make corneocyte removal by tape stripping more successful. Porcine skin was then dried using absorbent tissue, similarly to *in vivo* sampling (section 2.3.2) and 15 tape strips were collected to sample the *stratum corneum*.

2.4.3. Formulating Permeation Enhancers for In Vitro Permeation Studies

Porcine skin was treated with 200 µL of our permeation enhancer formulations, which contained 2% *(w/v)* CHX co-formulated with either 200 µM R6 polyarginine, 1.307 M glycolic acid or 5 mM Kolliphor® HS15.

2.4.4. Full Thickness Skin Permeation Studies

Franz-type diffusion cells were prepared as previously described and treated with 200 mL of 2% *(w/v)* CHX alone or combined with 200 mM R6 polyarginine, 1.307 M glycolic acid or 5 mM Kolliphor® HS15 for 2 minutes (Supplementary information, Figure 3). Following skin treatment, Franz-cells were disassembled, excess CHX formulations were wiped away and the skin was cleaned using 3% Teepol detergent and deionised water. Prior to removal of the *stratum corneum* by tape stripping, numerous intersecting deep lesions were

made in the remaining skin which was then submerged in 3 mL HPLC mobile phase (32:68 acetonitrile: phosphate buffer solution). The remaining skin samples were vortex-mixed (20 seconds), refrigerated (4°C, 24 hours), vortex-mixed again (20 seconds), sonicated (10 minutes) and centrifuged (10,000 rpm, 5 minutes) to extract remaining CHX from the sample and separate proteinaceous debris. 1 mL aliquot of receptor fluid was also sampled to determine permeation through full thickness skin. Samples were 0.22 mm filter sterilised before transferring to amber HPLC vials for chromatographic analysis.

2.5. Analysis of Chlorhexidine Permeation

2.5.1. ToF-SIMS Analysis

ToF-SIMS analysis of tape strips 2, 4, 6, 8, 10 and 12 of CHX and permeation enhancer studies was conducted using a ToF-SIMS IV instrument (IONTOF, GmbH). A liquid metal ion gun, which deployed Bi_3^+ ion clusters with a primary ion energy of 25 KeV, a ≤1× ions/cm ion density and a 0.8 μA emission was used. Imaging analysis was acquired over a 4.0 x 4.0 mm area consisting of 100 individual 0.4 x 0.4 mm patches with 15 scans per patch. Scans were conducted in negative polarity with a 100 pixel/mm resolution. Charge compensation was applied and optimised to each sample (ranging between 16.3-158.0 V) using a low-energy (<20 Kev) electron flood gun. The CHX fragment ion $C_7H_4N_2Cl^-$ (*m/z* = 151) [29] was mapped through the skin and 4 separate 1.0 × 1.0 mm regions of interest (ROI) were captured. Secondary ion intensity data representing the $C_7H_4N_2Cl^-$ (spectra on human and porcine skin shown in Supplementary information, Figure 4 and 5) were exported from each ROI and normalised to the total ion intensity of the spectra using SurfaceLab 7 software (IONTOF, GmbH).

2.5.2. HPLC Analysis

The limit of detection (LOD) and the limit of quantification (LOQ) of the HPLC method was determined by analysing the concentration of a series of standards containing known concentration of CHX. Standard concentrations included 1.0, 0.8, 0.6, 0.4, 0.2, 0.1 and 0.01 mg/mL CHX (Hibiscrub) diluted in deionised water. A regression analysis was conducted in Microsoft Excel to determine the standard deviation of the y-intercept and the slope of the curve and the LOD/LOQ was determined using the following calculations:

$$\mathrm{LOD} = \frac{3.3 \times \text{Standard Deviation of y} - \text{intercept}}{\text{Slope of the curve}}$$

$$\mathrm{LOQ} = \frac{10 \times \text{Standard Deviation of y} - \text{intercept}}{\text{Slope of the curve}}$$

For HPLC analysis, tape strips 1, 2 and 3 from human and porcine skin were analysed individually, whilst tape strips 4-6, 7-10 and 11-15 were pooled together to maximise chromatographic detection and quantification of CHX. HPLC mobile phase was added to each tape strip sample (1 mL to individual samples, 3 mL to pooled samples). CHX extraction protocol was conducted as previously described for full thickness permeation studies (section 2.4.4).

Chromatographic separation was achieved using a methodology developed and validated by Cardoso et al., 2011[35] and an Agilent 1260 liquid chromatography system, consisting of a G7111B quaternary pump, G7115A diode array detector, G7129A vial sampler and the OpenLab, Agilent Technologies software version 3.5 (3.5.0.654). An ACE C18 (150 x 4.6 mm I.D., 5mm) column was deployed using an isocratic mobile phase consisting of 32:68 *(v/v)* acetonitrile and phosphate buffer solution (0.05 M monobasic sodium phosphate solution including 0.5% triethylamine, which was adjusted to pH 3.0 using 85% phosphoric acid). A CHX-spiked sample was used to identify the retention time of the CHX which can be seen at approximately 2.3 minutes (Supplementary information, Figure 6). A series of CHX standards varying from 0.1-1.0 mg ml^{-1} were used to develop a calibration curve for the quantification of CHX present in the skin samples.

2.6. Antimicrobial Efficacy of Chlorhexidine Formulations

Fresh porcine skin was collected from a local abattoir prior to routine scalding treatment. Muscular tissue, subcutaneous fat and hair was removed from the skin, before washing with water to remove excess dirt and blood. Skin was cut into approximately 1.5 x 1.5 cm sections and allowed to equilibrate at room temperature for 30 minutes. 200 µL of each permeation enhancer formulation (as described in section 2.4.3), along with 2% *w/v* CHX alone (Hibiscrub), was applied to the surface of the *ex vivo* porcine skin for 2 minutes before removing and cleaning the skin with deionised water. Each treated porcine skin sample was left to dry for 5 minutes to maximise corneocyte removal when skin sampling. 15 tape strips were collected, and microorganisms present on the sample were cultured onto blood agar by pressing the tape strip onto the culture media. Agar plates were wrapped in parafilm for containment and incubated at 37°C for 24 hours. Colonies were counted for each sample.

2.7. Cytotoxicity of Chlorhexidine Formulations

Murine 3T3 fibroblasts (cultured in DMEM supplemented with 10% newborn calf serum, 4 mM GlutaMAX™, 100 IU/mL penicillin, 100 µg/mL streptomycin and 20 mM HEPES) were seeded into a 96 well plate with a seeding density of 4 x 10^3 cells/well. Cells were treated with 50 µL of each permeation enhancer formulation (section 2.4.3), in triplicate. A 2% CHX only and cell culture media control was set up per plate. Treatments were left on cells for 24 hours, which were then washed with PBS (with Ca^{2+}/Mg^{2+}). 100 µL Alamar Blue® solution (0.1 mg/mL) prepared in cell culture media, was added to the cells and incubated for 2 hours before measuring fluorescence with excitation and emission wavelengths at 550 – 590 nm. Fluorescence was normalised to the number of cells per well.

2.8. Statistical Analysis

Statistical analysis was carried out using IBM SPSS Statistics version 29.0.1.0 (171). Datasets were tested for normal distribution using the Shapiro-Wilk test and log transformation was attempted on datasets where normal distribution was not achieved (Shapiro-Wilk, $p < 0.05$). Experiments comparing *in vivo* and *in vitro* permeation models, concentrations of antimicrobial (2% and 4% CHX) and antimicrobial efficacy and cytotoxicity of permeation enhancer formulations were analysed by independent samples T-Test (parametric) or Mann Whitney U

(non-parametric). Experiments comparing CHX delivery when using permeation enhancers was analysed by ANOVA (parametric) or Kruskal Wallis test (non-parametric).

3. Results and Discussion

3.1. Comparison of In vivo Human and In Vitro Porcine Skin Permeation of Chlorhexidine

In order to evaluate any variation in the permeation behaviour of CHX between *in vivo* human skin and our *in vitro* porcine skin permeation model, HPLC and ToF-SIMS analysis was conducted on sampled tape strips (shown schematically in Supplementary information, Figure 1 and 2).

The secondary ion intensities for $C_7H_4N_2Cl^-$ (*m/z* = 151), which represents a diagnostic CHX fragment obtained from ToF-SIMS analysis of *in vivo* human and *in vitro* porcine skin, are shown in Figure 1A. The data for both studies demonstrates delivery of CHX in the upper *stratum corneum* (layers 2 - 6), despite reduced permeation as depth from the surface increases (Figure 1A), which is supported by previous findings by Judd et al., 2013, Karpanen et al., 2008 and Kirkby et al., 2022.[11,27,29] ToF-SIMS analysis showed that minimal CHX permeation occurred past the 6th layer of human corneocytes when treated with either 2% or 4% *(w/v)* CHX, compared to trace CHX detected in the lower *stratum corneum* (layers 8 - 12) of *in vitro* porcine skin (Figure 1A). Nevertheless, no significant difference was identified between *in vivo* human or *in vitro* porcine skin, emphasising the 2 models are highly comparable.

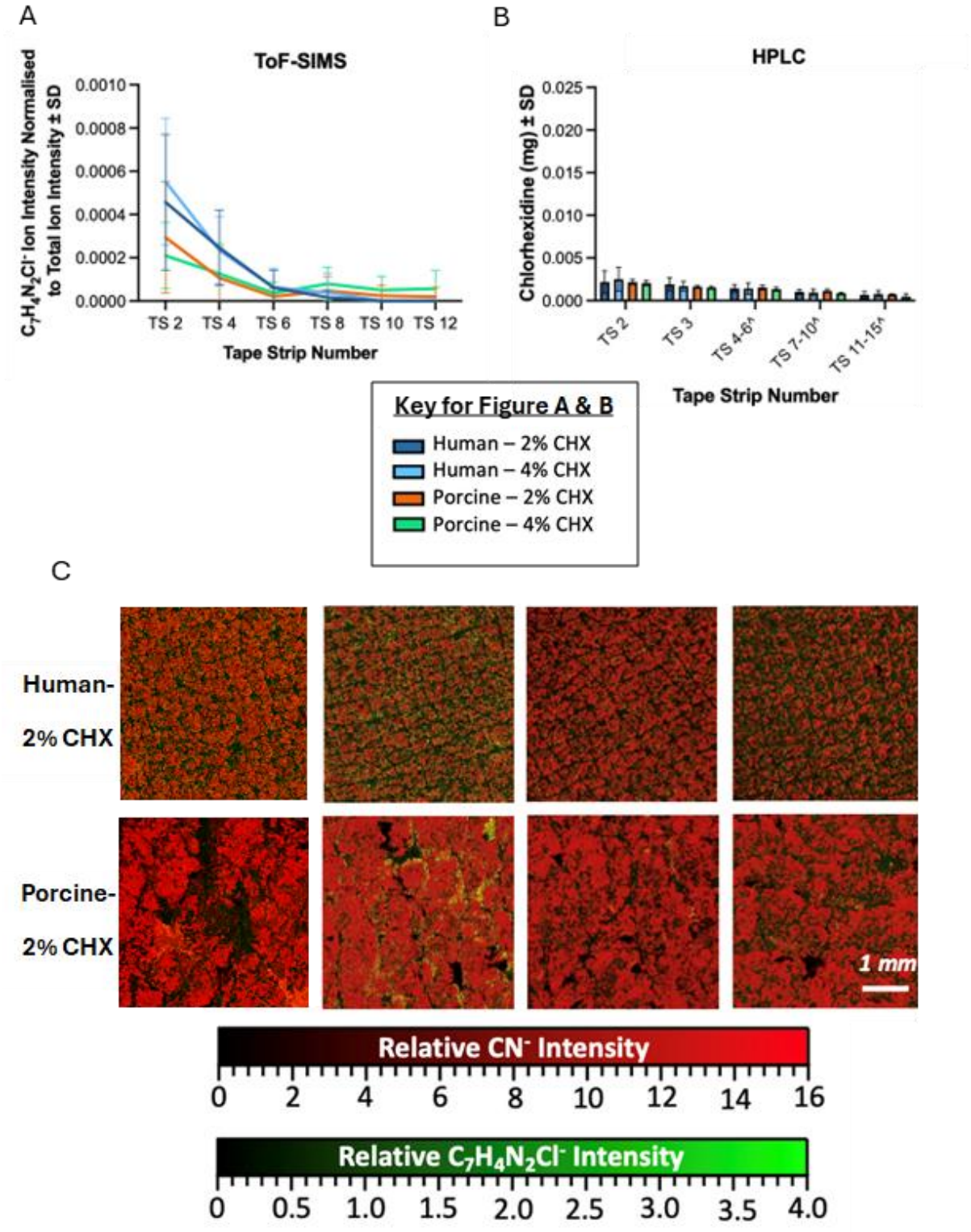


Figure 1. 2% and 4% *w/v* CHX permeation through *in vivo* human skin and *in vitro* porcine skin permeation model over 2 minutes. Tape strips sampled from human and porcine skin were (A) semi-quantified by ToF-SIMS to determine the relative $C_7H_4N_2Cl^-$ (*m/z* = 151) ion intensity normalised to total ion intensity (n = 12) as well as (B) HPLC quantification to determine the concentration of CHX extracted from each tape strip (n = 9). ^ symbolizes pooled tape strips which were normalised to the number of tape strips in the sample. (C) ToF-SIMS ion maps of CN^- (*m/z* = 26) was overlayed with the $C_7H_4N_2Cl^-$ diagnostic CHX ion to visualize spatial distribution of CHX permeation on tape strip 2, 8 and 12. The human and porcine

control overlay was taken from tape strip 8 of untreated skin and is representative of all tape strips from the native skin profiles (n = 12, displayed ion maps are representative of all repeats).

HPLC analysis confirms this trend for both systems, showing CHX delivery appears greatest to the upper *stratum corneum* and declines through the lower layers (Figure 1B), aligning with the findings of the ToF-SIMS analysis. However, regression analysis of the HPLC standards showed that the LOD and LOQ for this method was 0.00737 mg/mL and 0.02235 mg/mL, respectively (Supplementary information, Table 1). Despite the trend in findings, the data recorded for CHX delivery through the porcine and human *stratum corneum* was below the LOD and LOQ and therefore could not be accurately quantified, highlighting the poor delivery of the antimicrobial through the upper epidermis.

The minimum bactericidal concentration (MBC) is defined as the smallest concentration of an antimicrobial agent required to kill a specific bacterial species and varies depending on the microorganism.[36] The MBC of CHX varies from 0.001 – 0.03 mg/mL depending on the species (Aftab et al. 2023). To eliminate the most common skin microflora, such as *S. aureus* and coagulase-negative *Staphylococci*, a minimum CHX concentration of 0.002 – 0.004 mg/mL is required.[36] Whilst this HPLC method may lack sensitivity to detect such small doses of CHX extracted from individual tape strips, it is able to show that the concentration of CHX throughout the *stratum corneum* when treated with Hibiscrub alone is not sufficient to eliminate the native microbiome (Figure 1B).

Ex vivo skin models generally demonstrate poorer permeation of exogenous compounds compared to *in vivo* models due to the cessation of circulation and subsequent stiffening of tissues.[37] Despite this, the trace detection of CHX in the *ex vivo* skin samples may be attributable the effects of freezing storage of porcine skin, which is commonly reported throughout the literature[38] and may account for the minimal fluctuations in the trend observed in Figure 1B. Although current clinical CHX formulations provide excellent skin surface sterilisation, these findings suggest that ineffective skin antisepsis may occur due to insufficient antimicrobial delivery to the lower two thirds of the *stratum corneum,* which is limited by the innate impermeability of the skin.[13,14]

An even antimicrobial distribution throughout *stratum corneum* is desirable to ensure effective antimicrobial elimination and prevent sublethal concentrations that promote biocide resistance amongst microorganisms.[39] Secondary ion distribution maps for CN^- and $C_7H_4N_2Cl^-$, which represent skin tissue and CHX chemistries respectively, are shown in red/green colour overlays in Figure 1C. These secondary ion images show that the spatial distribution of CHX is inhomogeneous in all tape strips for human and porcine skin. Both human and porcine secondary ion distribution maps show that CHX is most abundant in tape strip 2 compared to tape strip 8 and 12, demonstrating poorer permeation to the lower *stratum corneum*. *In vivo* validation of the *in vitro* permeation model was accomplished by these similarities in CHX permeation depth and distribution between the two systems. Human and porcine native skin profiles (Supplementary information, Figure 11) show a relatively high background noise at m/z = 151, suggesting that the majority of the $C_7H_4N_2Cl^-$ signal observed from CHX-treated samples (Supplementary information, Figures 7-10) was background noise, and not the target secondary ion, reiterating poor permeation depth and spatial distribution of the antimicrobial. Further, when tape stripping porcine skin (Supplementary information, Figure 7 - 8), a lack of uniformity when removing corneocytes was observed compared to *in vivo* human tape stripping (Supplementary information, Figure 9 - 10), which may account for inconsistencies

in the CN^- and $C_7H_4N_2Cl^-$ maps between the two models. It is apparent from this data that topical CHX delivery is insufficient past the superficial layers of the *stratum corneum*, suggesting that native microorganisms in the deeper *stratum cornuem* are exposed to sublethal concentrations of CHX, if any at all, challenging the efficacy of current CHX skin antisepsis formulations.

The comparability between the human and porcine skin models allows confidence in our *in vitro* porcine skin permeation model when studying the topical application of novel, less-studied compounds and their effects on CHX permeation, without the concern of acquiring ethical approval and possibly causing cytotoxicity following *in vivo* human skin treatment and sampling.

3.2. Chlorhexidine Concentration and Skin Permeation

ToF-SIMS analysis of *in vivo* human and *in vitro* porcine skin tape strips showed that no significant enhancement in antimicrobial delivery was accomplished when treated with 2% or 4% CHX formulations. Both formulations resulted in sufficient CHX delivery to the upper *stratum corneum* (layers 2 - 6) but poor delivery to lower regions was observed (Figure 1A). Secondary $C_7H_4N_2Cl^-$ ion distribution maps from both *in vivo* human and *in vitro* porcine skin samples depict no significant improvement in CHX distribution uniformity when treated with the greater antimicrobial concentration (Supplementary information, Figure 7 - 10). The similarity in CHX permeation depth through *in vivo* human and *in vitro* porcine skin when treated with 2% and 4% formulations was confirmed by HPLC analysis (Figure 1B). Despite, this trend, the concentration of CHX extracted from the analysed tape strips was below the LOD and LOQ (Supplementary information, Table 1) for the HPLC method and therefore could not be accurately quantified.

Kirkby *et al*., 2022 demonstrated that sufficient delivery of CHX up to and past the 15th layer of corneocytes in the *stratum corneum* was possible after 24 hours exposure to the skin.[29] However, in clinical applications, rapid biocide delivery is essential to ensure thorough skin antisepsis. These findings highlight that effective CHX delivery to the entire *stratum cornuem* requires a more complex delivery system than increasing the antimicrobial concentration.

3.3. R6 Polyarginine to Enhance Chlorhexidine Permeation

HPLC analysis of *in vitro* porcine skin demonstrated significantly increased CHX permeation *($p<0.001$)* to all layers of the *stratum corneum* when treated with a Hibiscrub-R6 polyarginine co-formulation compared to Hibiscrub alone (Figure 2A).

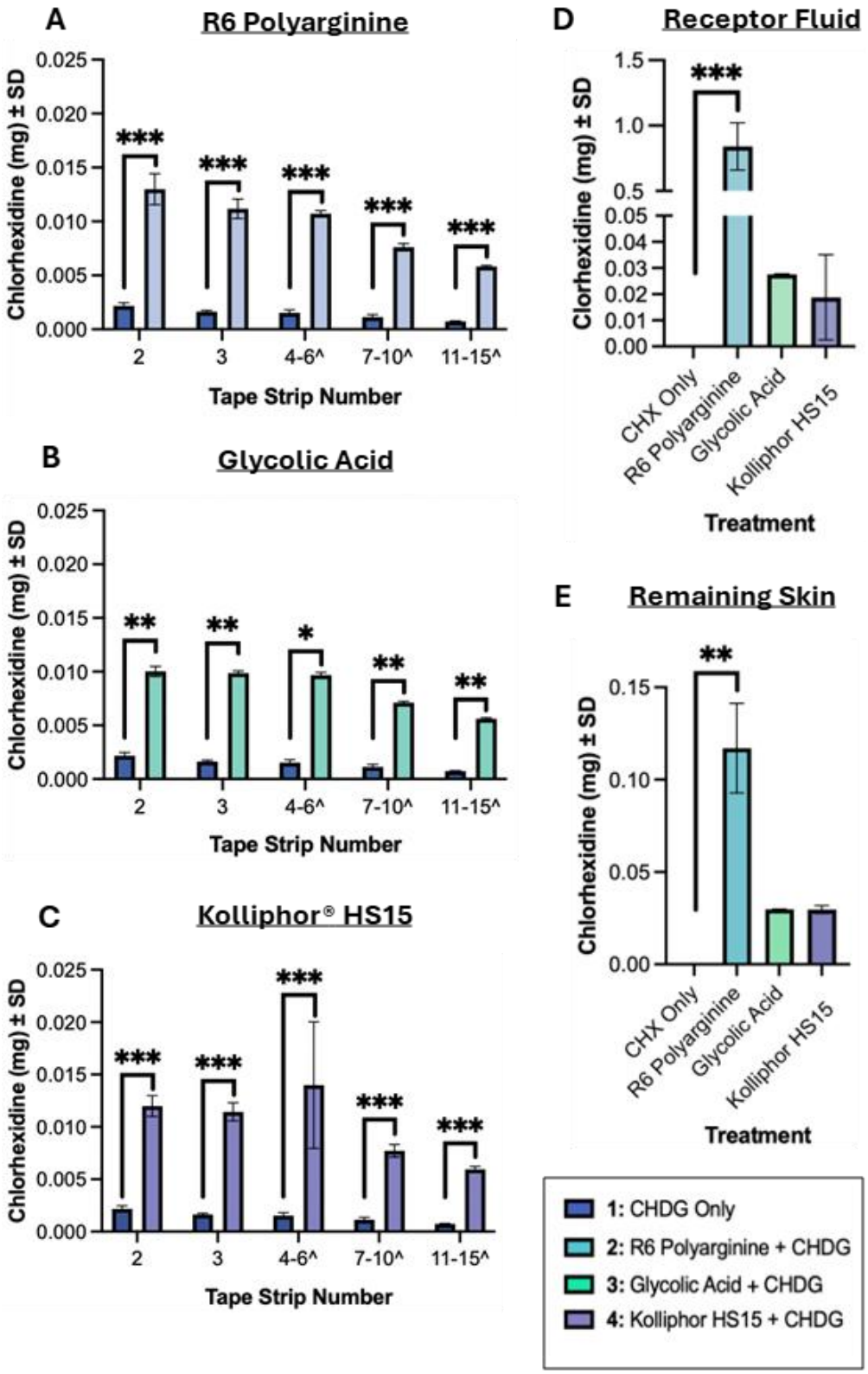


Figure 2. HPLC analysis of permeation enhancement of CHX with the addition of either R6 polyarginine, glycolic acid or Kolliphor® HS15 compared to CHX alone (Hibiscrub) following 2 minutes exposure on the skin. Formulations were applied to our *in vitro* porcine skin permeation model. HPLC quantification of CHX extracted from each tape strip following treatment with (A) R6 polyarginine, (B) glycolic acid and (C) Kolliphor® HS15 permeation enhancers. CHX quantified from (D) the receptor fluid and (E) remaining

skin was acquired following the full thickness skin permeation study. n = 9 for figures A-C, n = 3 for figures D-E). ^ resembles pooled tape strips which were normalised to the amount of tape strips in the sample. *** resembles statistical significance *p<0.001,* ** *p<0.01* and * *p<0.05.* Error bars show standard deviation of the mean.

With addition of R6 polyarginine in the formulation, 0.01298 ± 0.00144 mg/mL was delivered to the second layer of corneocytes and 0.00583 ± 0.0001 mg/mL to the lower *stratum corneum* (tape strips 11-15). It is evident from Figure 2A that there was an increase in CHX delivery to layers 11-15 when R6 polyarginine was formulated into the Hibiscrub, however this was below the LOD (Supplementary information, Table 1) and cannot be quantified accurately. It is also important to note that the concentration of CHX measured from the tape strips from R6 polyarginine-treated skin was below the LOQ (Supplementary information, Table 1), therefore the accuracy of the readings is questionable. Despite this, it is clear that the addition of R6 polyarginine enhances CHX permeation through the entire *stratum cornuem* as CHX extracted from skin treated with Hibiscrub alone was below the LOD and the CHX extracted from tape strips 1, 2, 3, 4-6, 7-10 and 11-15 was significantly greater when treated with Hibiscrub with R6 polyarginine than alone *(p<0.001* for all samples).

Full thickness skin permeation studies showed that 0.280 ± 0.060 mg/mL CHX was delivered through full thickness porcine skin into the receptor fluid (Figure 2D) and 0.090 ± 0.008 mg/mL CHX was extracted from the remaining porcine skin when formulated with the Hibiscrub-R6 polyarginine formulation (Figure 2E), which was significantly greater (*p = 0.003* and *0.002,* respectively) than when treated with alone Hibiscrub, where CHX was undetected past the sampled *stratum corneum.* This suggests that the concentration of CHX that has passed through the full thickness of the skin is great enough to eliminate skin pathogens such as *Enterococci*, Enterobacteriales, *S. aureus* (including Methicillin-resistant *Staphylococcus aureus* [MRSA]), *Pseudomonas, Acinetobacter, Actinomyces, Streptococcus pyogenes*, coagulase negative Staphylococci and anaerobic species, which require CHX concentrations between 0.002 and 0.02 mg/mL for microbial elimination.[36]

ToF-SIMS analysis agreed that when co-formulated with R6 polyarginine, CHX permeation is significantly enhanced to all layers of the porcine *stratum corneum* (*p<0.001* for all tape strips except 2 and 6 where *p=0.021* and *0.014,* respectively) compared to CHX treatment alone (Hibiscrub) (Figure 3A and Supplementary information, Figure 12). The lack of uniformity in CHX distribution is possibly an effect observed when using *ex vivo* porcine skin (seen in Figure 1C).

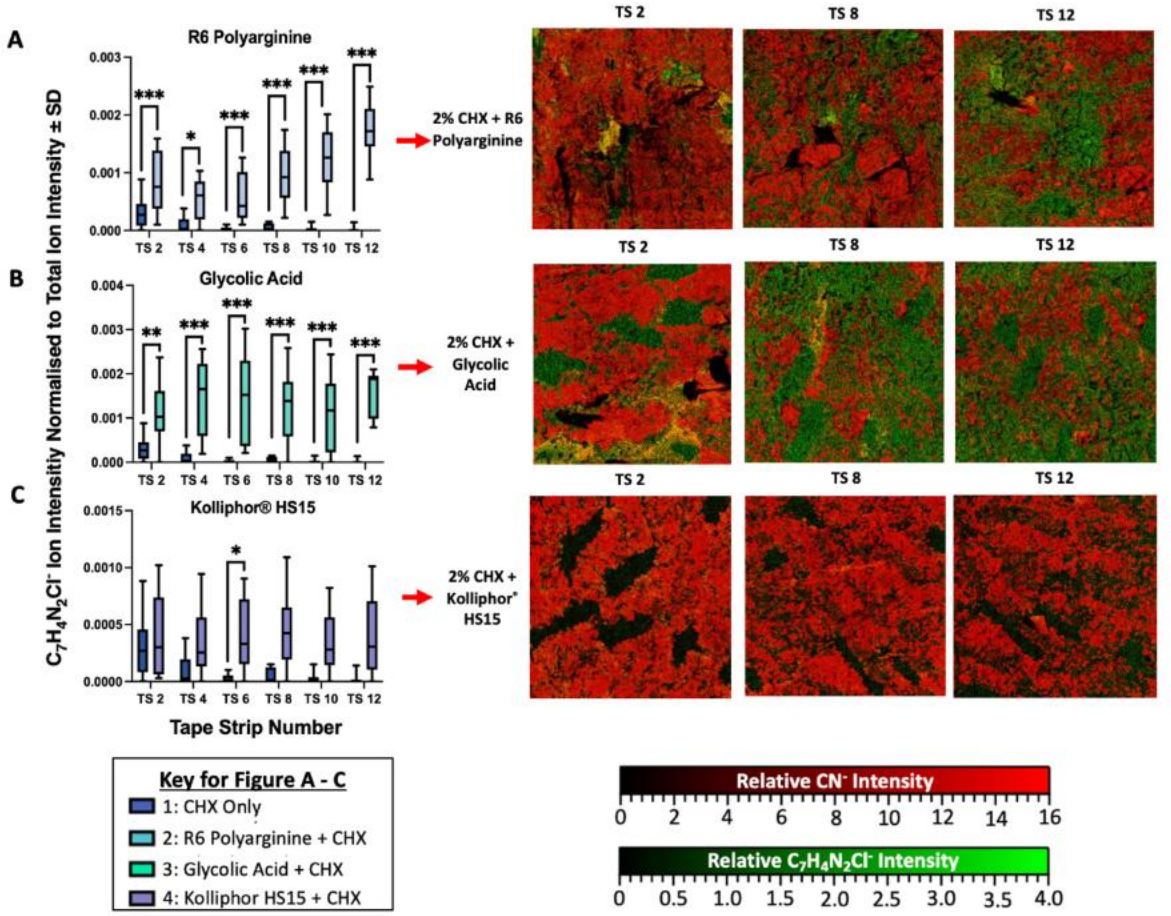


Figure 3. ToF-SIMS analysis of CHX permeation depth and spatial distribution when treated with CHX formulated with either (A) R6 polyarginine, (B) glycolic acid or (C) Kolliphor® HS15 for 2 minutes. Relative $C_7H_4N_2Cl^-$ (*m/z* = 151) ion intensity normalised to total ion intensity following treatment with permeation enhancer formulations compared to CHX alone (Hibiscrub). $C_7H_4N_2Cl^-$ ion overlayed with CN^- (*m/z* = 26) ion depicting the spatial distribution of CHX on tape strip 2, 8 and 12 (n = 12, displayed ion maps are representative of all repeats). Error bars show standard deviation of the mean. *** resembles statistical significance $p<0.001$, ** $p<0.01$ and * $p<0.05$.

Significantly fewer microbes were cultured from tape strips 1, 2, 3, 4, 5, 6, 8, 9, 11 and 12 ($p = 0.003, 0.005, 0.004, 0.027, 0.004, 0.043, 0.006, 0.009, 0.036, 0.041$, respectively) collected from porcine skin treated R6 polyarginine formulations, compared to untreated skin (Figure 4B). Microbial elimination was greater with the addition of R6 polyarginine compared to treatment with CHX alone (Hibiscrub), which only resulted in significant microbial elimination on tape strips 1, 2, 3, 5, 8 and 9 ($p = 0.004, 0.007, 0.008, 0.006, 0.026$, respectively) compared to untreated skin (Figure 4A). No significant difference was observed in microbial culture between porcine treated with CHX formulated alone or with R6 polyarginine on tape strips 7, 10, 13, 14 or 15, despite a clear trend in reduced microbial growth when treated with R6 polyarginine (Supplementary information, Figure 15). However, it is difficult to distinguish whether enhanced *stratum corneum* permeation was achieved by overcoming the lipid barrier or increased appendageal delivery in this assay. The high abundancy in cultured microbes from tape strip 10 – 15 when treated with CHX alone (Hibiscrub) supports previous findings that current clinical formulations result in poor antimicrobial delivery to the lower *stratum corneum* (Figure 1).

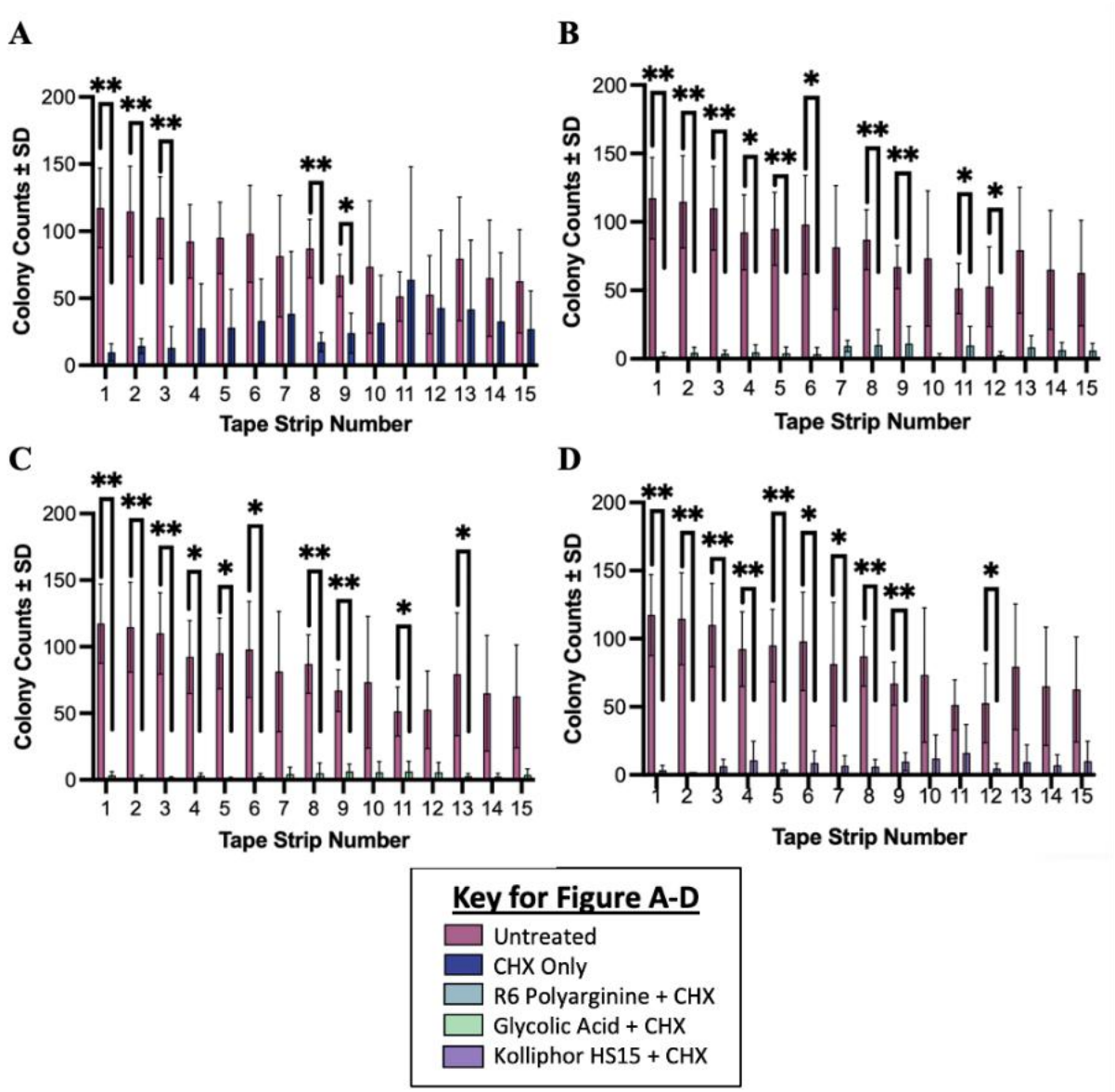


Figure 4. Skin microbes cultured from tape strips 1-15 when treated for 2 minutes with of (A) CHX -alone (Hibiscrub) or co-formulation with (B) R6 polyarginine, (C) glycolic acid or (D) Kolliphor® HS15, compared to skin microflora cultured from untreated porcine skin (n = 3 for all figures). *** resembles statistical significance *p<0.001,* ** *p<0.01* and * *p<0.05.* Error bars show standard deviation of the mean.

No significant difference was observed in mammalian cell cytotoxicity of our CHX-R6 polyarginine formulation compared to CHX alone (Hibiscrub) (Figure 5).

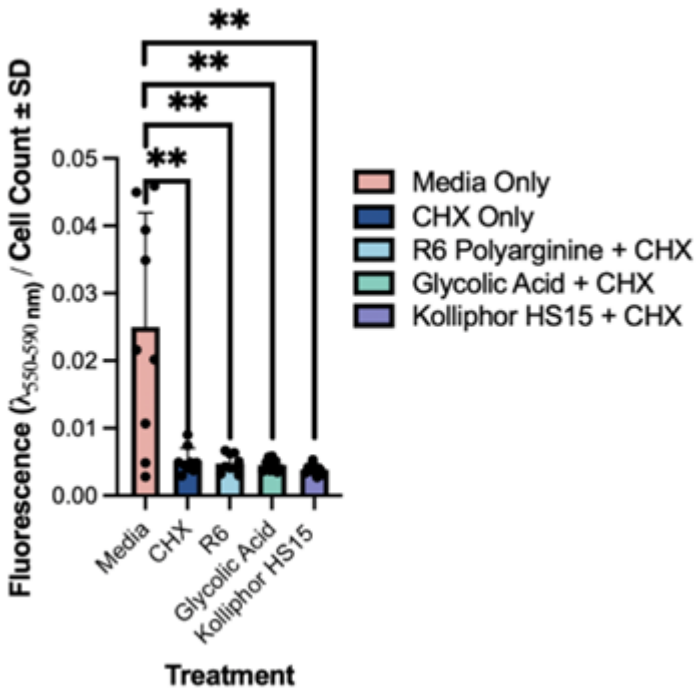


Figure 5. Cytotoxicity of CHX formulations containing either R6 polyarginine, glycolic acid or Kolliphor® HS15 compared to chlorhexidine alone (Hibiscrub) and cell culture media control treatments (n = 9). ** resembles statistical significance where $p<0.01$.

R6 polyarginine is used as a non-injectable alternative drug delivery system. It is highly effective in facilitating transcutaneous delivery of macromolecules such as insulin across the *stratum corneum*.[30] Studies by de Cogan et al, 2017 show that large quantities of anti-VEGF cargo can be delivered into the rat eye *in vivo*, with less than 1 minute exposure.[40] R6 polyarginine contains guanidinium side groups which give the peptide a high degree of positive charge. This allows bidentate binding as the *stratum corneum* carries a net negative charged[41] due to negatively charged entities embedded throughout the plasma membrane, such as glycosaminoglycans and sialic acids.[31] Components within the keratinocytes of the *stratum granulosum*, such as lamellar bodies and keratohyalin granules consist of negatively charged phospholipids and glycosphingolipids, which are secreted via exocytosis, into the extracellular matrix surrounding the *stratum corneum* and *granulosum*.[42] It is possible that R6 polyarginine enhances the permeation of CHX through the *stratum corneum* by binding with these negatively charged components of the *stratum corneum*, altering the organisation of the lipid structures which may consequently reduce the efficiency of the skin's natural barrier, although a conclusive mechanism of action has not yet been identified.

3.4. Glycolic Acid to Enhance Chlorhexidine Permeation

HPLC analysis of *in vitro* porcine skin demonstrated significantly increased CHX permeation to all layers of the *stratum corneum* when treated with a Hibiscrub-glycolic acid co-formulation compared to Hibiscrub alone (Figure 2B).

Figure 2B shows that the addition of glycolic acid into the Hibiscrub formulation significantly enhanced the CHX permeation through the entire stratum cornuem with 0.01003 ± 0.00047 mg/mL being extracted from the second layer of corneocytes (tape strip 2) and 0.00562 ±

0.00011 mg/mL from the lower *stratum corneum* (tape strips 11-15). CHX extracted from skin treated with Hibiscrub only was below the LOD and therefore could not be accurately quantified. Further, the concentration of CHX extracted from Hibiscrub-glycolic acid treated skin was below the LOQ, and therefore the accuracy of these measurements are uncertain. However, these results showed a statistical significance in CHX delivery between the two formulations with significantly more CHX being extracted from tape strips 1, 2, 3, 4-6, 7-10 and 11-15 *(p=0.009*, *0.009, 0.009, 0.022, 0.009* and *0.003,* respectively) when treated with the Hibiscrub-glycolic acid co-formulation.

Full thickness skin permeation studies showed that 0.009 ± 0.000 mg/mL CHX was delivered through full thickness porcine skin into the receptor fluid (Figure 2D) whilst 0.010 ± 0.000 mg/mL CHX was extracted from the remaining porcine skin (Figure 2E) when treated with the Hibiscrub-glycolic acid formulation. Although these measurements were below the LOQ for the HPLC method (Supplementary information, Table 1), no CHX was detected in the receptor fluid or remaining skin when skin was treated with Hibiscrub alone. Whilst this comparison was not statistically significant, there was a clear trend in Figure 2D and 2E, that the addition of glycolic acid enhanced permeation through the full thickness skin. These findings suggest that the concentration of CHX that has passed through the full thickness of the skin when treated with this permeation enhancer is great enough to eliminate skin microbes such as *S. aureus* (including MRSA)*, Actinomyces*, coagulase negative Staphylococci and anaerobic species, which require CHX concentrations between 0.002 and 0.02 mg/mL for microbial elimination.[36]

ToF-SIMS analysis showed that our CHX-glycolic acid formulation significantly enhanced CHX permeation through the entire porcine *stratum corneum* (*p<0.001* for all tape strips except 2, where *p=0.007*) (Figure 3B and Supplementary information*,* Figure 13). The spatial distribution of CHX appeared relatively even towards the lower *stratum corneum*, however, the lack of uniformity in CHX distribution observed on tape strip 2 may be due to masking of signal by strong CN^- readings. Glycolic acid formulations resulted in significantly fewer skin microbes being cultured from tape strip 1, 2, 3, 4, 5, 6, 8, 9, 11 and 13 (*p = 0.003, 0.004, 0.004, 0.029, 0.026, 0.044, 0.004, 0.003, 0.017* and *0.045,* respectively) compared to untreated skin (Figure 4C), unlike CHX alone (Hibiscrub), which demonstrated poorer skin antisepsis (discussed in section 3.3) (Figure 4A). No significant difference was observed in microbial culture between porcine treated with CHX formulated alone (Hibiscrub) or with glycolic acid, except cultures from tape strip 2 (*p = 0.018*) (Supplementary information, Figure 15). No significant difference in mammalian cell cytotoxicity was observed between our CHX-glycolic acid formulation and CHX-only (Hibiscrub) treatment (Figure 5).

Glycolic acid promotes the desquamation of the *stratum corneum* by interacting with the desmosomes in the *stratum cornuem,* causing the loosening of tight junctions between living and dead corneocytes, removing dead cells and stimulating cellular regeneration.[32,43] It is possible that after short-term exposure with glycolic acid (2 minutes), this initial interaction with desmosomes could loosen the tight junctions enough to facilitate increased intercellular CHX permeation. Further, elevated CHX permeation may be a result of transient skin acidification caused by the addition of glycolic acid as disruptions to the skins pH is well known to cause damage to barrier integrity.[44]

3.5. Kolliphor® HS15 to Enhance Chlorhexidine Permeation

HPLC analysis of *in vitro* porcine skin demonstrated significantly increased CHX permeation *(p<0.001)* to all layers of the *stratum corneum* when treated with the Hibiscrub-Kolliphor® HS15 co-formulation compared to Hibiscrub alone (Figure 2C).

HPLC analysis determined that co-formulation with Kolliphor® HS15 significantly *(p<0.001)* increased CHX permeation to all layers of the *stratum corneum* (Figure 2C). When treated with the Hibiscrub-Kolliphor® HS15 formulation, 0.01197 ± 0.00100 mg/mL, was extracted from tape strip 2, whilst 0.00593 ± 0.00026 mg/mL CHX was extracted from the lower *stratum corneum* (tape strips 11-15). Although these measurements were below the LOQ for the HPLC method used (Supplementary information, Table 1) and therefore could not be accurately quantified, the CHX concentration measured from skin samples treated with Hibiscrub alone were below the LOD. In addition, the concentration of CHX extracted from all tape strip samples was significantly higher when treated with Hibiscrub and Kolliphor® HS15 compared (*P<0.001* for all tape strip samples) to Hibiscrub alone.

Full thickness skin permeation studies showed that 0.006 ± 0.005 mg/mL CHX was delivered through full thickness porcine skin into the receptor fluid (Figure 2D) and 0.010 ± 0.001 mg/mL remained in the skin (Figure 2E) when treated with the Hibiscrub-Kolliphor® HS15 co-formulate. Although the amount of CHX remaining in the skin following 2 minute treatment and tape stripping was detected but below the LOQ for the HPLC method (Supplementary information, Table 1), no CHX was detected in the remaining skin following treatment with Hibiscrub alone, showing a significant enhancement in antimicrobial permeation. The amount of CHX in the receptor fluid when treated with Hibiscrub alone and in combination with Kolliphor® HS15 was below the LOD. This data suggests that the amount of CHX that has permeated past the *stratum corneum* to deeper within the skin when treated with this permeation enhancer is great enough to eliminate skin microbes including Viridans Streptococci, *S. aureus* (including MRSA)*, Actinomyces*, coagulase negative Staphylococci and anaerobic species, which require CHX concentrations between 0.002 and 0.01 mg/mL for microbial elimination.[36]

This suggests that skin microbes, including *S. aureus* (including MRSA), *Acinetobacter spp., Actinomyces spp., Pseudomonas spp., S. pyogenes,* coagulase-negative Staphylococci, anaerobic bacteria and *Enterococci spp.,* may be eliminated. Whilst the CHX concentration extracted from CHX-only (Hibiscrub) tape strips were below the LOQ (Supplementary information, Table 1) and could therefore be accurately quantified, the CHX concentration extracted from Kolliphor® HS15 tape strips was either above or around the estimated LOQ and therefore there is confidence that the formulation promotes CHX delivery through the skin.

Full thickness skin permeation studies showed that 0.006 ± 0.005 mg/mL CHX was delivered through full thickness porcine skin (Figure 2D) and 0.010 ± 0.001 mg/mL remained in the skin (Figure 2E) when co-formulated with Kolliphor® HS15, indicating that CHX permeated through the dermis and hypodermis with minimal quantities passing through full thickness skin. Although no significant difference in CHX extracted from the receptor fluid or remaining skin was observed when compared to the control, zero CHX was detected past the *stratum cornuem* when treated with CHX alone, suggesting enhanced antimicrobial permeation was achieved using Kolliphor® HS15.

ToF-SIMS analysis showed no significant CHX permeation enhancement when co-formulated with Kolliphor® HS15, except tape strip 6 *(p=0.039)* (Figure 3C and Supplementary information, Figure 14). These inconsistencies with HPLC analysis suggest that analysis of Kolliphor® HS15-containing samples using ToF-SIMS may be limited by 'the matrix effect', where co-eluting compounds in the sample effect the ionisation of the target analyte, therefore rendering quantitative analysis difficult.[45,46] SIMS analytical techniques rely upon the ionisation of the target analyte for successful detection, hence, are vulnerable to this phenomenon.[47] Treatment with our CHX-Kolliphor® HS15 formulation resulted in significant microbial elimination at tape strip 1, 2, 3, 4, 5, 6, 7, 8, 9 and 12 (*p = 0.003, 0.004, 0.004, 0.01, 0.004, 0.014, 0.048, 0.003, 0.004* and *0.047,* respectively) compared to untreated porcine skin (Figure 4D), unlike treatment with CHX alone (Hibiscrub), which demonstrated poorer skin antisepsis (discussed in section 3.3) (Figure 4A). No significant difference was observed in microbial culture from porcine skin treated with CHX alone (Hibiscrub) compared to formulation with Kolliphor® HS15, expect for cultures from tape strip 2 (*p = 0.018*) (Supplementary information, Figure 15). No significant difference in mammalian cell cytotoxicity was observed when treated with our CHX and Kolliphor® HS15 co-formulation compared to CHX alone (Hibiscrub) (Figure 5).

Kolliphor® HS15 has previously been used for corneal drug delivery and improving transdermal drug bioavailability.[33,48] Whilst no mechanism of permeation enhancement has been described, it has been reported that Kolliphor® HS15 interacts with and inhibits P-glycoprotein, a protein present in the human skin and plays an important role in the skin's absorptive properties[48] as well as notoriously increasing the aqueous solubility of compounds.[49]

3.6. R6 Polyarginine is the Most Potent Permeation Enhancer of Chlorhexidine

Despite all three permeation enhancer formulations significantly enhancing permeation through and past the *stratum corneum*, along with evidential improvements in skin antisepsis with no elevated level of mammalian cell cytotoxicity, R6 polyarginine appears to improve CHX permeation the most significantly. The amount of CHX delivered to the lower *stratum corneum* resulted in the elimination of more skin microbes from deeper sites within the epidermis, which is challenging with Hibiscrub alone. Further, R6 polyarginine facilitates the permeation of CHX through the dermis and hypodermis and may result in drug delivery into the bloodstream. Although evidence suggests minimal systemic CHX indicates no health risk,[50] the powerful penetrating capabilities of R6 polyarginine may deliver undesirable quantities of CHX into the bloodstream. Formulation with Kolliphor® HS15 CHX appears to elevate CHX permeation slightly more than glycolic acid formulations, however, similarities in permeation patterns through full thickness skin and cytotoxicity profiles suggest that neither one enhancer is significantly better than the other.

4. Conclusions

Current clinical CHX formulations exhibit poor permeation through the *stratum corneum*. CHX permeates to the 6-8th layer of corneocytes when applied to *in vivo* human skin or our *in vitro* porcine permeation model. Co-formulation with R6 polyarginine, glycolic acid or Kolliphor® HS15 significantly improves CHX permeation to all layers of the *stratum*

cornuem and potentially into the dermis and hypodermis. Current clinical CHX -only formulations, along with the addition of our permeation enhancers results in excellent skin surface decontamination, however, only when co-formulated with R6 polyarginine, glycolic acid or Kolliphor® HS15 do we observe thorough microbial elimination throughout the lower *stratum cornuem*. Our permeation enhancer formulations exhibit no additional cytotoxicity compared to current clinical CHX formulations. This research suggests that increased CHX permeation and skin antisepsis, along with minimal cytotoxicity can be achieved by the addition of R6 polyarginine, glycolic acid or Kolliphor® HS15. However, our R6 polyarginine formulation appears to be the strongest permeation enhancer, delivering CHX past the hypodermis and possibly, into the bloodstream.

Acknowledgements

This research was financially supported by the EP/P029868/1 Engineering and Physical Sciences Research Council (EPSRC) grant.

Declaration of Competing Interest

The authors declare no conflict of interest.

Data Availability

Data is available in the University of Nottingham's Data Repository.

References

[1] Guest JF, Keating T, Gould D, Wigglesworth N. Modelling the annual NHS costs and outcomes attributable to healthcare-associated infections in England. 2020. *BMJ Open.* doi: 10.1136/bmjopen-2019-033367

[2] Dobbs TD, Gibson JAG, Fowler AJ, Abbott TE, Shahid T, Torabi F, et al. Surgical activity in England and Wales during the COVID-19 pandemic: a nationwide observational cohort study. *British Journal of Anaesthesia*. 2021;127, 196-204. doi: 10.1016/j.bja.2021.05.001

[3] Atumanyire J, Muhumuza J, Talemwa N, Molen SF, Kithinji SM, Kagenderezo BP, et al. Incidence and outcomes of surgical site infection following emergency laparotomy during the COVID-19 pandemic in a low resource setting: A retrospective cohort. *International Journal Surgery Open.* 2023;56. doi: 10.1016/j.ijso.2023.100641

[4] Seidelman JL, Mantyh CR, Anderson DJ. Surgical Site Infection Prevention: A Review. *JAMA*. 2023;329. 244-252. doi: 10.1001/jama.2022.24075

[5] Becker K, Heilmann C, Peters G. Coagulase-negative staphylococci. *Clinical Microbiology Reviews*. 2014;27:870-926. doi: 10.1128/cmr.00109-13

[6] Zabaglo M, Sharman, T. *Postoperative Wound Infection*. StatPearls. 2024.

[7] Silvestri DL, McEnery-Stonelake M. Chlorhexidine: Uses and Adverse Reactions. *Dermatitis*. 2013;24:112-8. doi: 10.1097/DER.0b013e3182905561

[8] Kakadia PG, Conway BR. Nanoemulsions for enhanced skin permeation and controlled delivery of chlorohexidine digluconate. *Journal of Microencapsulation*. 2022;39:110-24. doi: 10.1080/02652048.2022.2050318

[9] Jalalzadeh H, Groenen H, Buis DR, Dreissen YE, Goosen JH, Ijpma FF, et al. Efficacy of different preoperative skin antiseptics on the incidence of surgical site infections: a systematic review, GRADE assessment, and network meta-analysis. *The Lancet Microbe*. 2019;3:762-71. doi: 10.1016/S2666-5247(22)00187-2

[10] Kirkby M, Sabri AB, Scurr DJ, Moss GP. Dendrimer-mediated permeation enhancement of chlorhexidine digluconate: Determination of in vitro skin permeability and visualisation of dermal distribution. *European Journal of Pharmaceutics and Biopharmaceutics*. 2021;159:77-87. doi: 10.1016/j.ejpb.2020.12.014

[11] Karpanen TJ, Worthington T, Conway BR, Hilton AC, Elliott TS, Lambert PA. Penetration of chlorhexidine into human skin. *Antimicrobial agents and chemotherapy*, 2008;52:3633-3636. doi: 10.1128/aac.00637-08

[12] Poppolo Deus F, Ouanounou A. Chlorhexidine in Dentistry: Pharmacology, Uses, and Adverse Effects. *International Dental Journal*, 2022;72:269-77. doi: 10.1016/j.identj.2022.01.005

[13] Phatale V, Vaiphei KK, Jha S, Patil D, Agrawal M, Alexander A. Overcoming skin barriers through advanced transdermal drug delivery approaches. *Journal of Controlled Release*, 2022;351:361-80. doi: 10.1016/j.jconrel.2022.09.025

[14] Supe S, Takudage, P. Methods for evaluating penetration of drug into the skin: A review. *Skin Research and Technology*, 2021;27:299-308. doi: org/10.1111/srt.12968

[15] Summerfield A, Meurens F, Ricklin ME. The immunology of the porcine skin and its value as a model for human skin. *Molecular Immunology*, 2025;66:14-21. doi: 10.1016/j.molimm.2014.10.023

[16] Todo H. Transdermal Permeation of Drugs in Various Animal Species. *Pharmaceutics*, 2017;9:33. doi: 10.3390/pharmaceutics9030033

[17] Hamilton DW, Walker JT, Tinney D, Grynyshyn M, El-Warrak A, Truscott E, et al. The pig as a model system for investigating the recruitment and contribution of myofibroblasts in skin healing. *Wound Repair and Regeneration*, 2022;30:45-63. doi: 10.1111/wrr.12981

[18] Starr NJ, Khan MH, Edney MK, Trindade GF, Kern S, Pirkl A, Kleine-Boymann M, Elms C, O'Mahony MM, Bell M, Alexander MR. Elucidating the molecular landscape of the stratum corneum. *Proceedings of the National Academy of Sciences*. 2022. doi: 10.1073/pnas.2114380119

[19] Simon A, Amaro MI, Healy AM, Cabral LM, de Sousa VP. Comparative evaluation of rivastigmine permeation from a transdermal system in the Franz cell using synthetic membranes and pig ear skin with in vivo-in vitro correlation. *International Journal of Pharmaceutics*, 2016;512:234-241. doi: 10.1016/j.ijpharm.2016.08.052

[20] Pirmohamed M. Drug metabolism. *Medicine*, 2008;36:355-359. doi.org/10.1016/j.mpmed.2008.04.002

[21] Vávrová K, Lorencová K, Klimentová J, Novotný J, Hrabálek A. HPLC method for determination of in vitro delivery through and into porcine skin of adefovir (PMEA). *Journal of Chromatography A*, 2007;853:198-203. doi: 10.1016/j.jchromb.2007.03.012

[22] Maloney DJ, Zhang J, Bhargava S, Hogan MV, Wang JH. Quantifying skin permeation of a novel metformin lotion using modified hydrophilic interaction

liquid chromatography. *Bioanalysis*. 2024;16:1115-1124. doi: 10.1080/17576180.2024.2412438

[23] Mansour RS, Hamdan II, Salem MS, Khalil EA, Sallam AA. HPLC method development/validation and skin diffusion study of caffeine, methyl paraben and butyl paraben as skin–diffusing model drugs. *PLoS One*. 2021 doi: 10.1371/journal.pone.0247879

[24] Belsey NA, Dexter A, Vorng JL, Tsikritsis D, Nikula CJ, Murta T, Tiddia MV, Zhang J. Gurdak E, Trindade GF, Gilmore IS. Visualisation of drug distribution in skin using correlative optical spectroscopy and mass spectrometry imaging. *Journal of Controlled Release*, 2023;364:79-89. doi: 10.1016/j.jconrel.2023.10.026

[25] Hagvall L, Pour MD, Feng J, Karma M, Hedberg Y, Malmberg P. Skin permeation of nickel, cobalt and chromium salts in ex vivo human skin, visualized using mass spectrometry imaging. *Toxicology In Vitro*, 2021;76. doi: 10.1016/j.tiv.2021.105232

[26] Starr NJ, Hamid KA, Wibawa J, Marlow I, Bell M, Perez-Garcia L, Barrett DA, Scurr DJ. Enhanced vitamin C skin permeation from supramolecular hydrogels, illustrated using in situ ToF-SIMS 3D chemical profiling. *International Journal of Pharmaceutics*, 2019;563: 21-29. doi: 10.1016/j.ijpharm.2019.03.028

[27] Judd AM, Scurr DJ, Heylings JR, Wan KW, Moss GP. Distribution and Visualisation of Chlorhexidine Within the Skin Using ToF-SIMS: A Potential Platform for the Design of More Efficacious Skin Antiseptic Formulations. *Pharmaceutical Research*, 2013;30: 1896-905. doi: 10.1007/s11095-013-1032-5

[28] Holmes AM, Scurr DJ, Heylings JR, Wan KW, Moss GP. Dendrimer pre-treatment enhances the skin permeation of chlorhexidine digluconate: characterisation by in vitro percutaneous absorption studies and time-of-flight secondary ion mass spectrometry. *European Journal of Pharmaceutical Sciences*, 2017;104:90-101. doi: 10.1016/j.ejps.2017.03.034

[29] Kirkby M, Sabri AB, Scurr DJ, Moss G. Microneedle-Mediated Permeation Enhancement of Chlorhexidine Digluconate: Mechanistic Insights Through Imaging Mass Spectrometry. *Pharmaceutical Research*, 2022;39:1945-58. doi: 10.1007/s11095-022-03309-8

[30] Kitaoka M, Imamura K, Hirakawa Y, Tahara Y, Kamiya N, Goto M. Needle-free immunization using a solid-in-oil nanodispersion enhanced by a skin-permeable oligoarginine peptide. *International Journal of Pharmaceutics*, 2013;*458*;334-339. doi: 10.1016/j.ijpharm.2013.10.0065

[31] Kristensen M, Nielsen HM. Cell-penetrating peptides as tools to enhance non-injectable delivery of biopharmaceuticals. *Tissue Barriers*. 2016. doi: 10.1080/21688370.2016.1178369

[32] Puricelli C, Gigliotti CL, Stoppa I, Sacchetti S, Pantham D, Scomparin A, et al. Use of Poly Lactic-co-glycolic Acid Nano and Micro Particles in the Delivery of Drugs Modulating Different Phases of Inflammation. *Pharmaceutics*, 2023;15:1772. doi: 10.3390/pharmaceutics15061772

[33] Younes NF, Abdel-Halim SA, Elassasy AI. Solutol HS15 based binary mixed micelles with penetration enhancers for augmented corneal delivery of sertaconazole nitrate: optimization, in vitro, ex vivo and in vivo characterization. *Drug Delivery*, 2018;25:1706-17. doi: 10.1080/10717544.2018.1497107

[34] National Health Service. 2022 Preparing your skin before orthopaedic surgery using chlorhexidine gluconate skin cleanser. Available at: https://www.evelinalondon.nhs.uk/resources/patient-information/preparing-your-skin-for-surgery.pdf. Accessed June 20, 2025.

[35] Cardoso MA, Favero ML, Gasparetto JC, Hess BS, Stremel DP, Pontarolo R. Development and validation of an RP-HPLC method for the determination of chlorhexidine and p-chloroaniline in various pharmaceutical formulations. *Journal of liquid chromatography & related technologies*, 2011;34:1556-1567. doi: 10.1080/10826076.2011.575979

[36] Aftab R, Dodhia VH, Jeanes C, Wade RG. Bacterial sensitivity to chlorhexidine and povidone-iodine antiseptics over time: a systematic review and meta-analysis of human-derived data. *Scientific Reports,* 2023;13:347. doi: 10.1038/s41598-022-26658-1

[37] Wei JC, Cartmill ID, Kendall MA, Crichton ML. In vivo, in situ and ex vivo comparison of porcine skin for microprojection array penetration depth, delivery efficiency and elastic modulus assessment. *Journal of the Mechanical Behaviour of Biomedical Materials*, 2022;130. doi: 10.1016/j.jmbbm.2022.105187

[38] Morin M, Runnsjö A, Ruzgas T, Engblom J, Björklund S. Effects of storage conditions on permeability and electrical impedance properties of the skin barrier. *International Journal of Pharmaceutics*, 2023;637. doi: 10.1016/j.ijpharm.2023.122891

[39] Laumen JGE, Van Dijck C, Manoharan-Basil, SS, Abdellati S, De Baetselier I, Cuylaerts V, et al. Sub-Inhibitory Concentrations of Chlorhexidine Induce Resistance to Chlorhexidine and Decrease Antibiotic Susceptibility in Neisseria gonorrhoeae. *Frontiers in Microbiology*, 2021;12. doi: 10.3389/fmicb.2021.776909

[40] De Cogan F, Hill LJ, Lynch A, Morgan-Warren PJ, Lechner J, Berwick MR, Peacock AF, Chen M, Scott RA, Xu H, Logan A. Topical delivery of anti-VEGF drugs to the ocular posterior segment using cell-penetrating peptides. *Investigative ophthalmology & visual science*, 2017;*58*:2578-2590. doi: 10.1167/iovs.16-20072

[41] Baspinar Y, Borchert HH. Penetration and release studies of positively and negatively charged nanoemulsions-is there a benefit of the positive charge? *International Journal of Pharmaceutics*, 2012;430:247-52. doi: 10.1016/j.ijpharm.2012.03.040

[42] Yousef H, Alhajj M, Sharma S. *Anatomy, Skin (Integument), Epidermis*. StatPearls. 2022

[43] Narda M, Trullas C, Brown A, Piquero-Casals J, Granger C, Fabbrocini G. Glycolic acid adjusted to pH 4 stimulates collagen production and epidermal renewal without affecting levels of proinflammatory TNF-alpha in human skin explants. *Journal of Cosmetic Dermatology*, 2021;20:513-21. doi: 10.1111/jocd.13570

[44] Brooks SG, Mahmoud RH, Lin RR, Fluhr JW, Yosipovitch G. The skin acid mantle: an update on skin pH. *Journal of Investigative Dermatology*, 2025;145:509-521. doi: 10.1016/j.jid.2024.07.009

[45] Panuwet P, Hunter Jr RE, D'Souza PE, Chen X, Radford SA, Cohen JR, et al. Biological Matrix Effects in Quantitative Tandem Mass Spectrometry-Based Analytical Methods: Advancing Biomonitoring. *Critical Reviews in Analytical Chemistry,* 2016;46:93-105. doi: 10.1080/10408347.2014.980775

[46] Kasel B, Wirtz T. Reduction of the SIMS matrix effect using the storing matter technique: a case study on Ti in different matrices. *Analytical Chemistry*, 2014;86:3750-3755. doi: 10.1021/ac4030472

[47] Nakano S, Yamagishi T, Aoyagi S, Portz A, Durr M, Iwai H, et al. Evaluation of matrix effects on TOF-SIMS data of leu-enkephalin and 1,2-dioleoyl-sn-glycero-3-phosphocholine mixed samples. *Biointerphases*, 2018;13. doi: 10.1116/1.5013219

[48] El-Tokhy FS, Abdel-Mottaleb MMA, Abdel Mageed SS, Mahmoud AMA, El-Ghany EA, Geneidi AS. Boosting the In Vivo Transdermal Bioavailability of Asenapine Maleate Using Novel Lavender Oil-Based Lipid Nanocapsules for Management of Schizophrenia. *Pharmaceutics*, 2023;15. doi: 10.3390/pharmaceutics15020490

[49] Bajza A, Kocsis D, Berezvai O, Laki AJ, Lukacs B, Imre T, et al. Verification of P-Glycoprotein Function at the Dermal Barrier in Diffusion Cells and Dynamic "Skin-On-A-Chip" Microfluidic Device. *Pharmaceutics*, 2020;12. doi: 10.3390/pharmaceutics12090804

[50] Mullany LC, Darmstadt GL, Tielsch JM. Safety and impact of chlorhexidine antisepsis interventions for improving neonatal health in developing countries. *The Pediatric Infectious Disease Journal*, 2006;25:665-675. doi: 10.1097/01.inf.0000223489.02791.70

Supplementary Information for

Enhanced Topical Antimicrobial Delivery for Improved Skin Antisepsis

Madeline Berrow [a], Nichola J Starr [a], David J Scurr [a], Felicity de Cogan [a*]

[a] School of Pharmacy, University of Nottingham, University Park, Nottingham, NG7 2RD, United Kingdom

[*]Corresponding author: Felicity de Cogan
Email: pazfd@exmail.nottingham.ac.uk

This PDF includes:

Methodology Schematic Figures: S1-S3
Figures: S4-S15

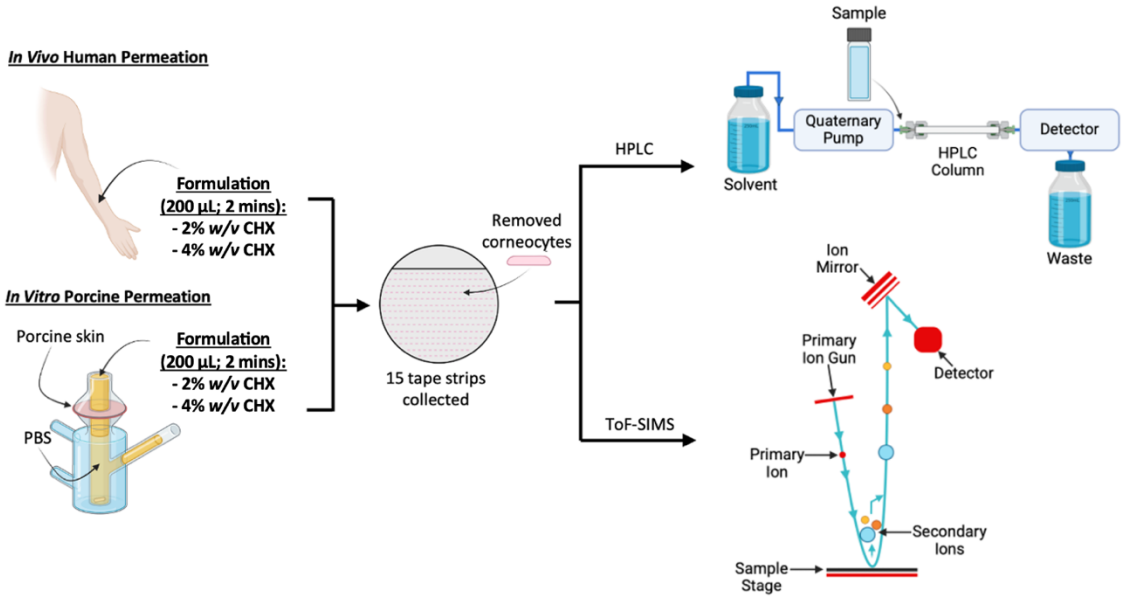


Figure 1. Workflow diagram depicting sample treatment, collection and analyses methods of *in vivo* human skin treated with 2% *w/v* CHX (figure designed using BioRender).

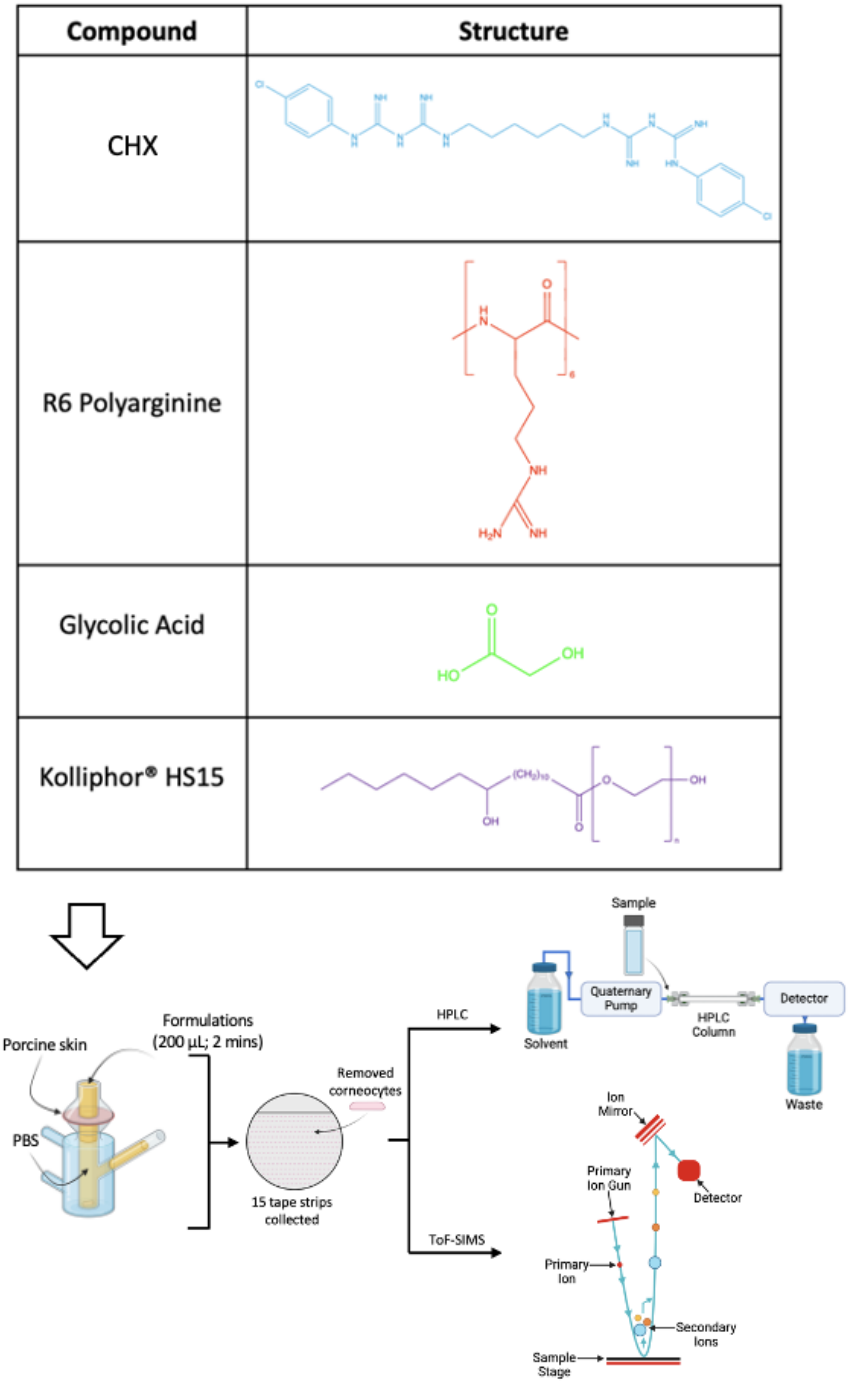


Figure 2. Workflow overview of sample treatment, collection and analyses of our *in vitro* porcine skin permeation model using CHX only formulations (blue) and CHX co-formulations with permeation enhancers R6 polyarginine (red), glycolic acid (green) and Kolliphor® HS15 (purple) (figure designed using BioRender).

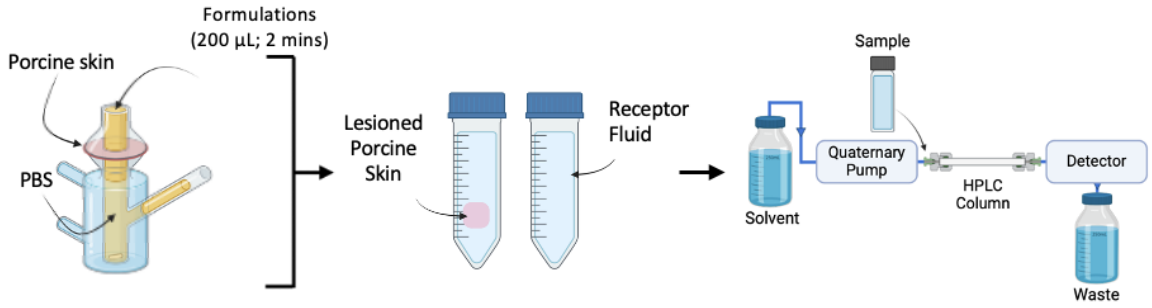


Figure 3. Workflow diagram of *in vitro* porcine skin full recovery permeation studies using CHX co-formulated with R6 polyarginine, glycolic acid and Kolliphor® HS15 permeation enhancers (figure designed using BioRender).

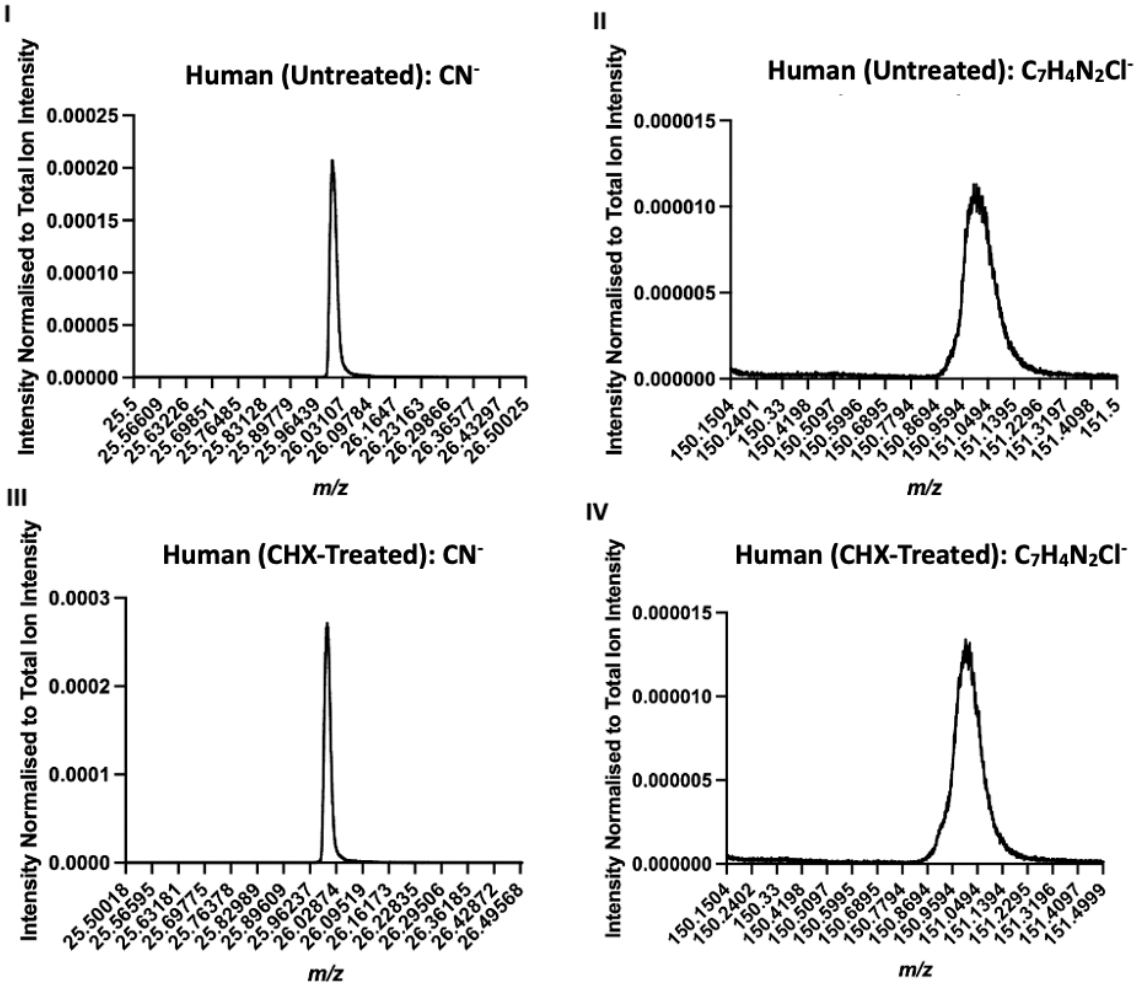


Figure 4. ToF-SIMS spectra obtained from CN^- and $C_7H_4N_2Cl^-$ scans of untreated *in vivo* human skin (I and II, respectively), and CN^- and $C_7H_4N_2Cl^-$ scans of CHX-treated *in vivo* human skin (III and IV, respectively). Intensities were normalised to the total ion intensity of that sample.

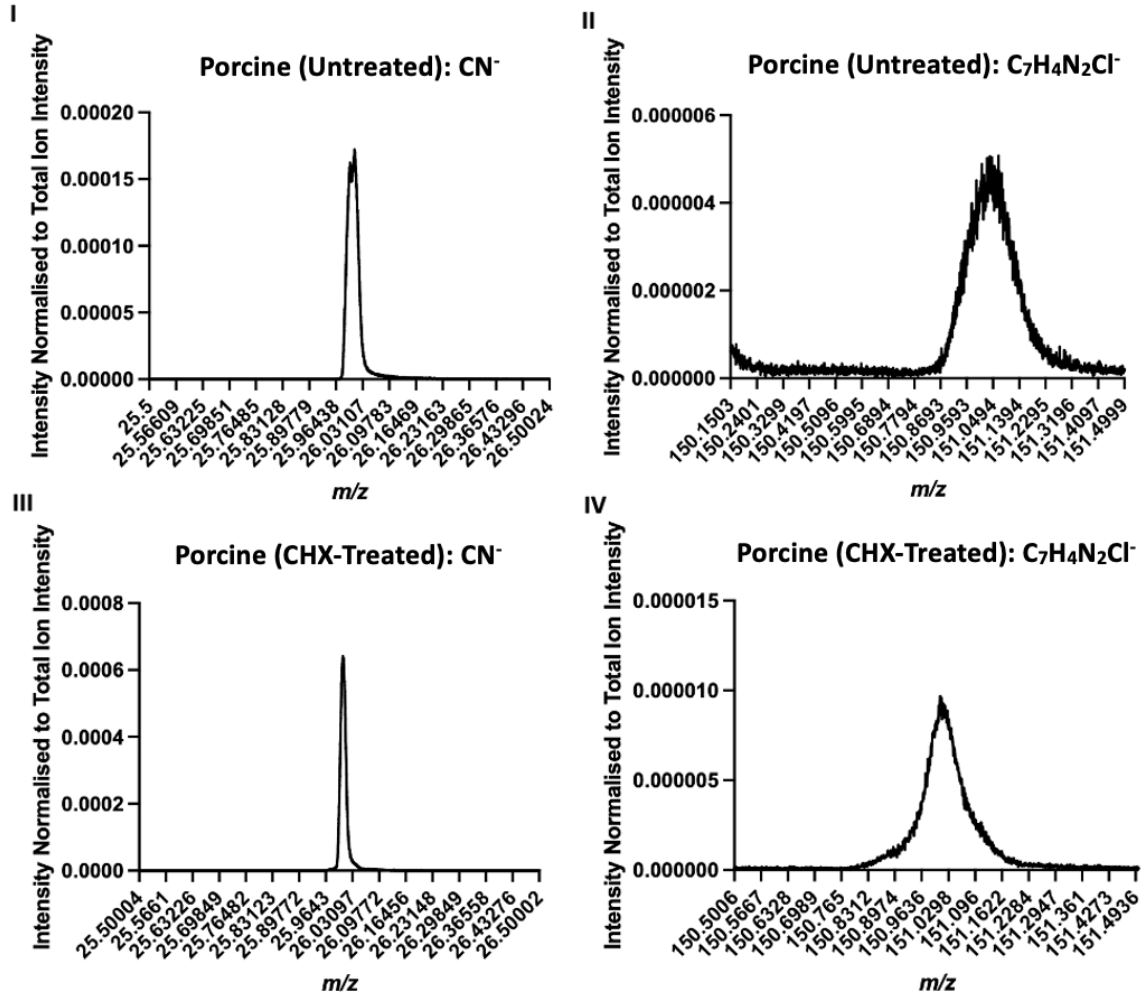


Figure 5. ToF-SIMS spectra obtained from CN^- and $C_7H_4N_2Cl^-$ scans of untreated porcine skin (I and II, respectively), and CN^- and $C_7H_4N_2Cl^-$ scans of CHX-treated porcine skin (III and IV, respectively), using our described *in vitro* permeation model. Intensities were normalised to the total ion intensity of that sample.

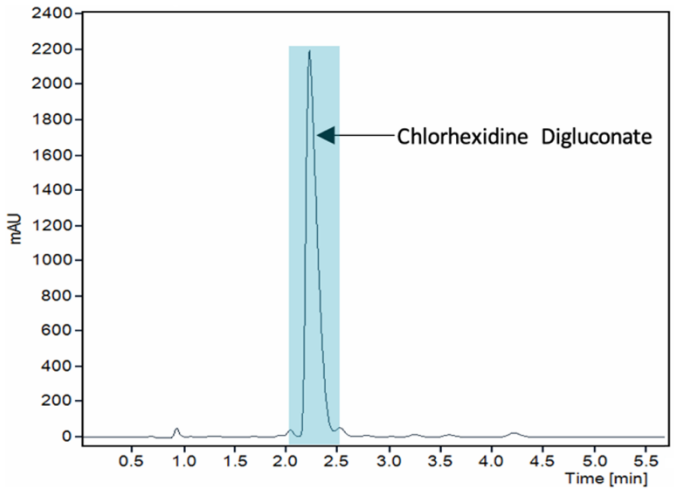


Figure 6. HPLC spectra of CHX-spiked sample depicting the corresponding peak (retention time ~ 2.25 minutes)

Table 1. Limit of detection (LOD) and limit of quantification (LOQ) of HPLC method.

Limit Type	Limit Concentration (mg/mL)
Detection (LOD)	0.00737
Quantification (LOQ)	0.02235

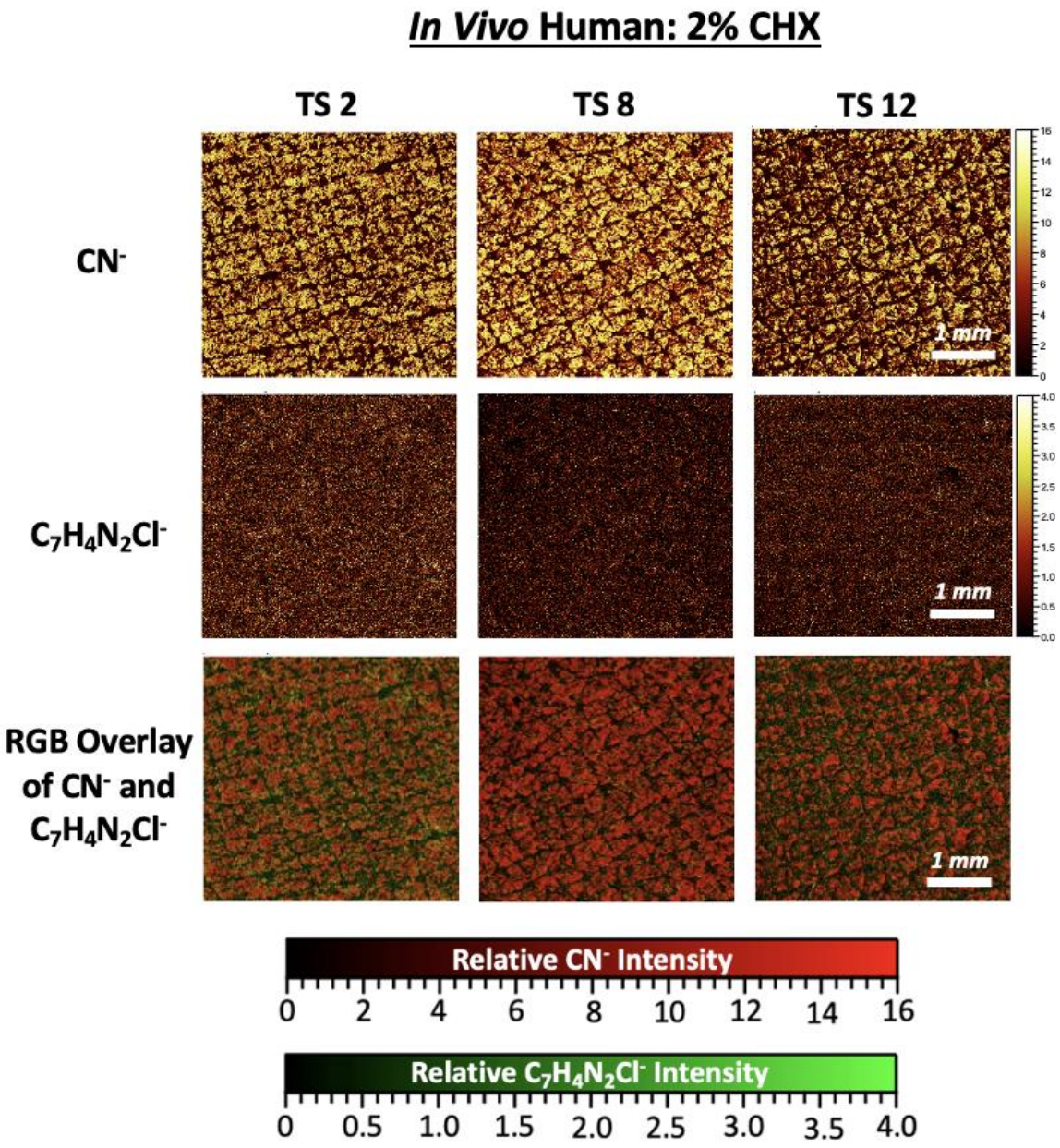


Figure 7. ToF-SIMS ion maps imaged from tape strip 2, 8 and 12 of 2% *w/v* CHX-treated *in vivo* human skin, depicting the spatial distribution of CN^- (skin marker) and $C_7H_4N_2Cl^-$ (chlorhexidine fragment), including overlayed images of the ions.

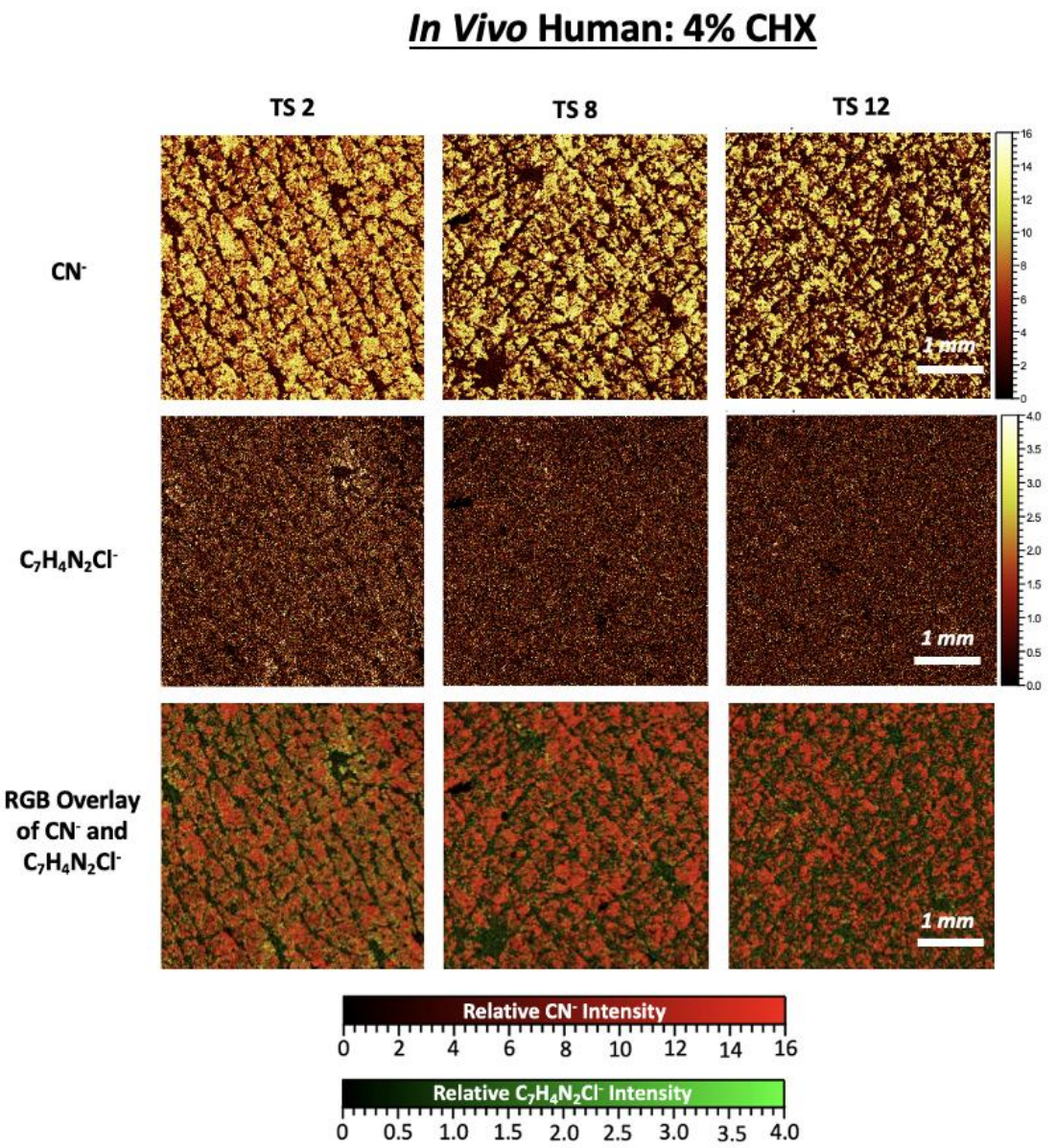


Figure 8. ToF-SIMS ion map images of tape strip 2, 8 and 12 of 4% *w/v* CHX-treated *in vivo* human skin. Images depicting the spatial distribution of the skin marker, CN^- and chlorhexidine fragment $C_7H_4N_2Cl^-$, including overlayed images of the ions.

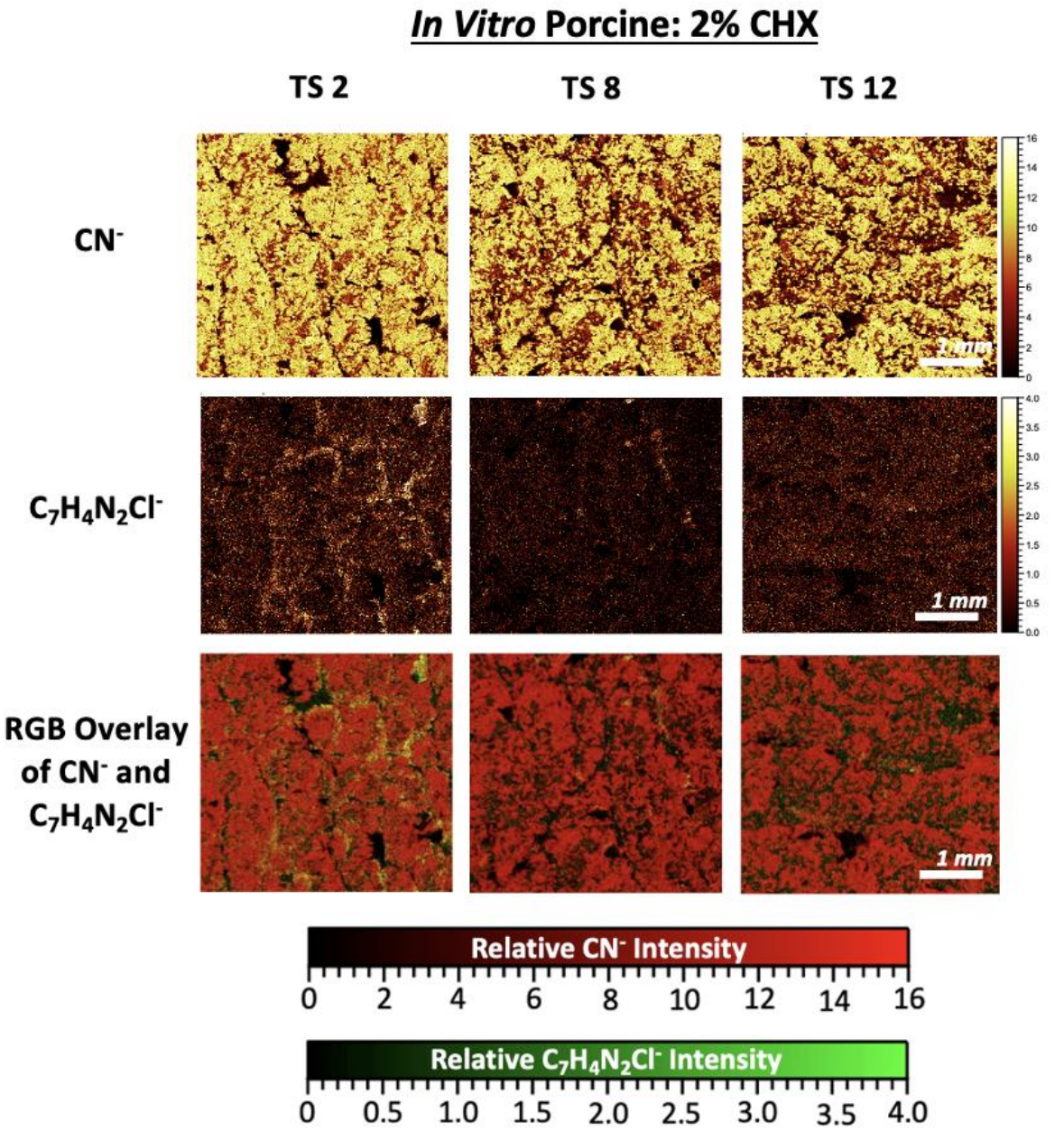


Figure 9. ToF-SIMS CN^- (skin marker) and $C_7H_4N_2Cl^-$ (CHX fragment) ion maps imaged from tape strip 2, 8 and 12 of 2% *w/v* CHX-treated porcine skin using our *in vitro* permeation model, including overlayed images of the ions.

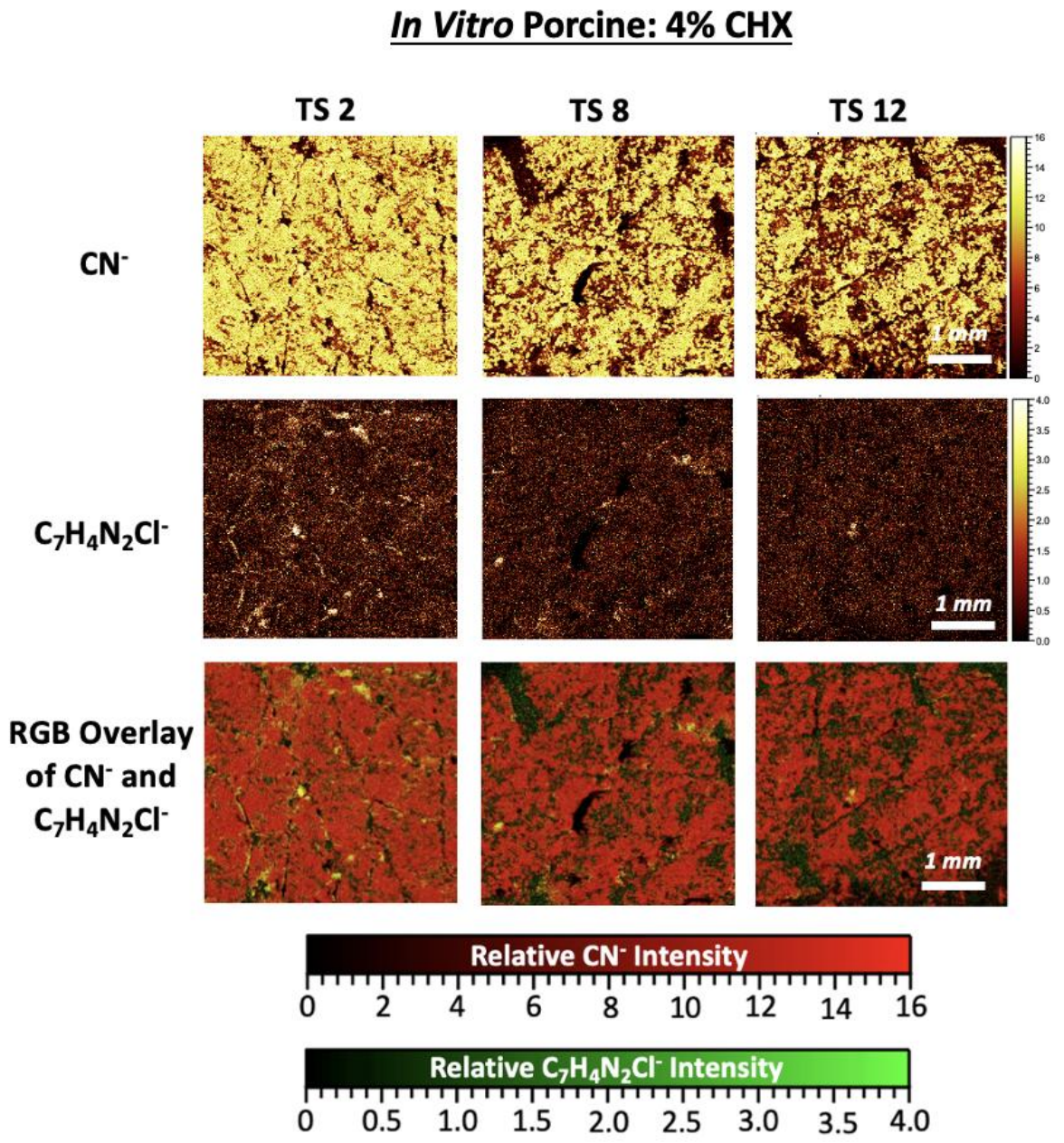


Figure 10. ToF-SIMS ion maps displaying the CN^- skin marker and $C_7H_4N_2Cl^-$ CHX fragment ion imaged from tape strip 2, 8 and 12 of 4% *w/v* CHX-treated porcine skin using our described *in vitro* permeation model, including overlayed images of the two ions.

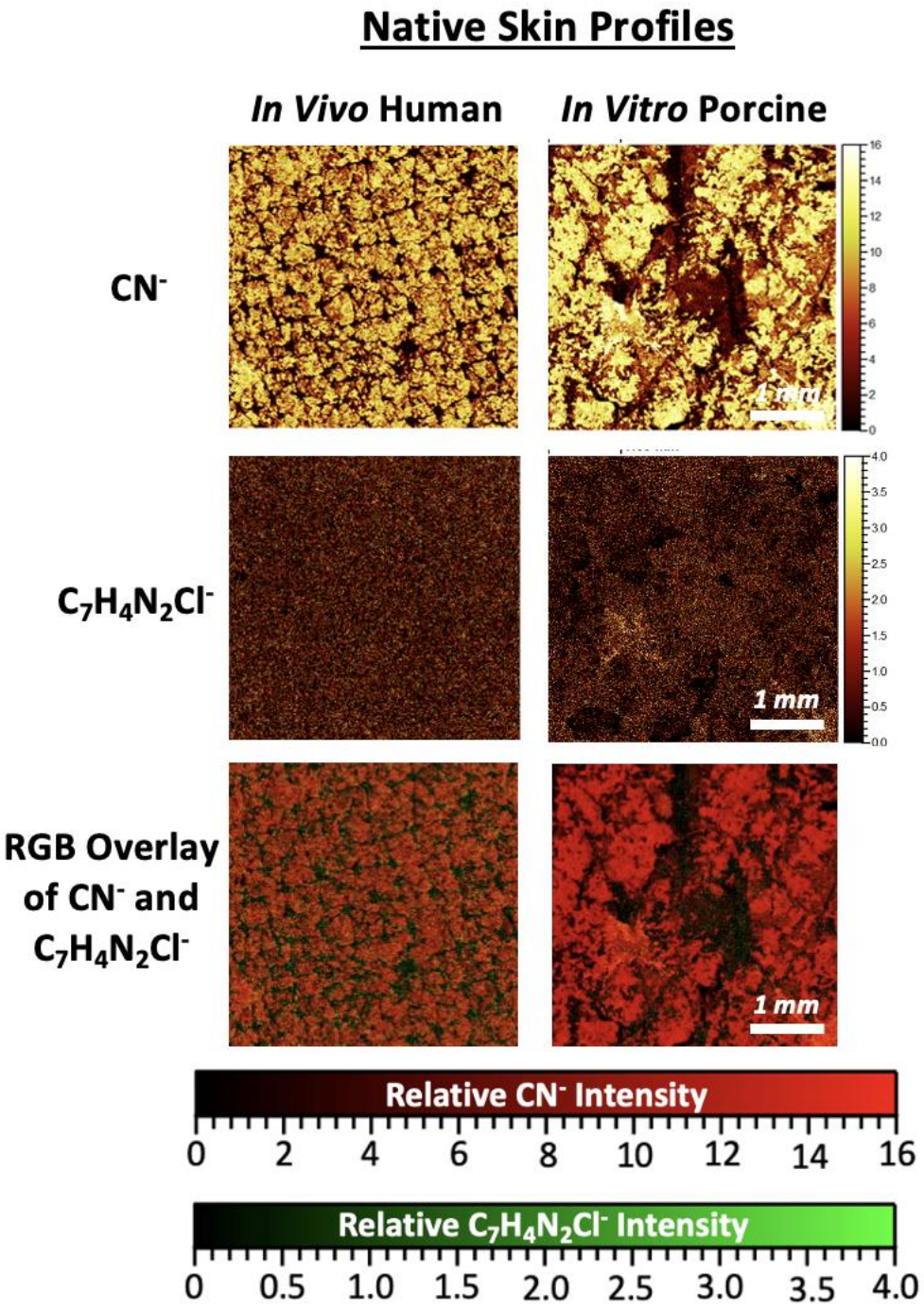


Figure 11. ToF-SIS ion maps depicting the CN^- skin marker and background $C_7H_4N_2Cl^-$ signal imaged from tape strip 8 of *in vivo* human and *in vitro* porcine skin models.

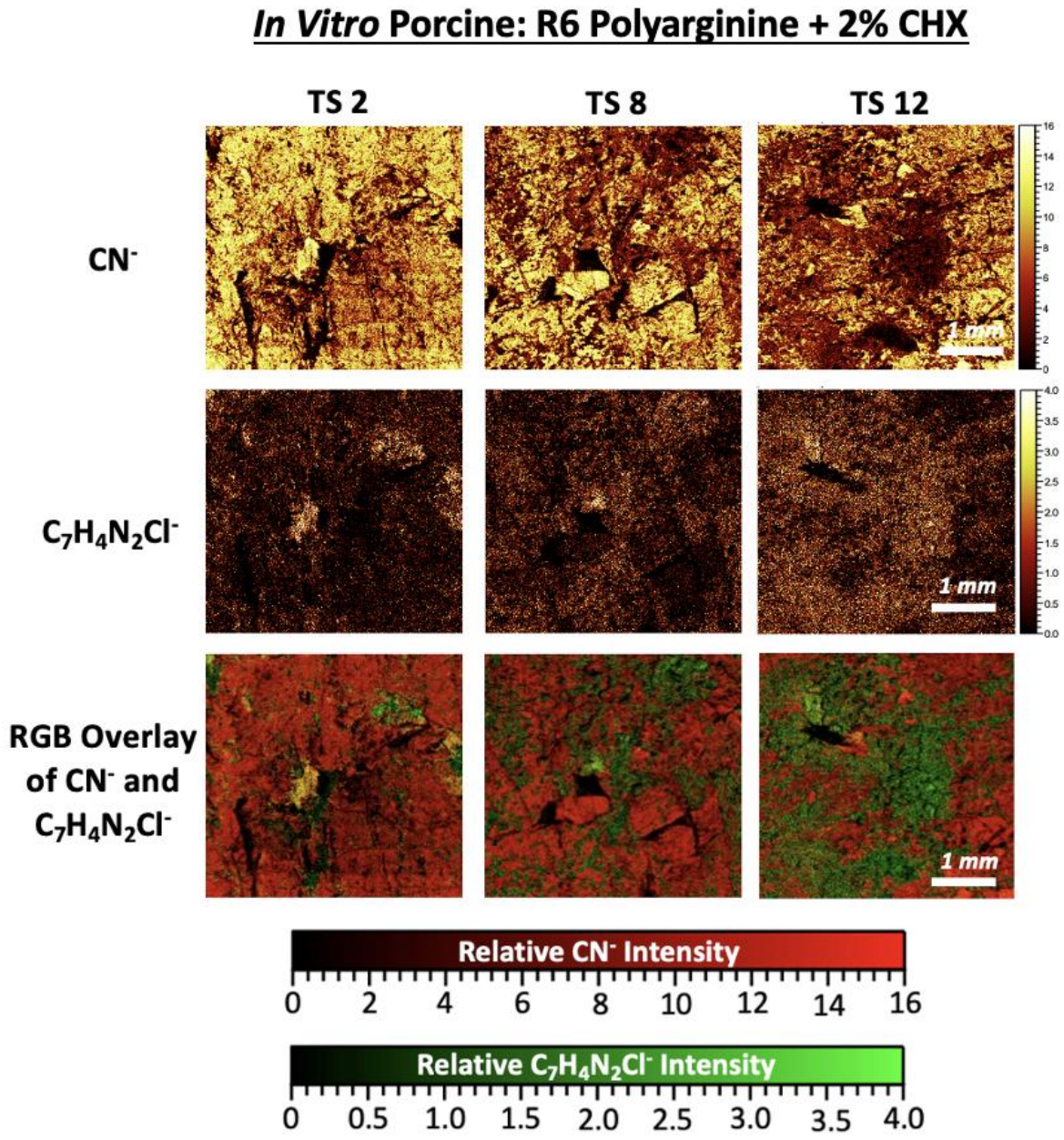


Figure 12. ToF-SIMS ion maps imaged from tape strip 2, 8 and 12 of *in vitro* porcine skin treated with CHX co-formulated with R6 polyarginine. Images depict the CN^- skin marker and $C_7H_4N_2Cl^-$ CHX fragment ions, including an overlayed map of the two ions.

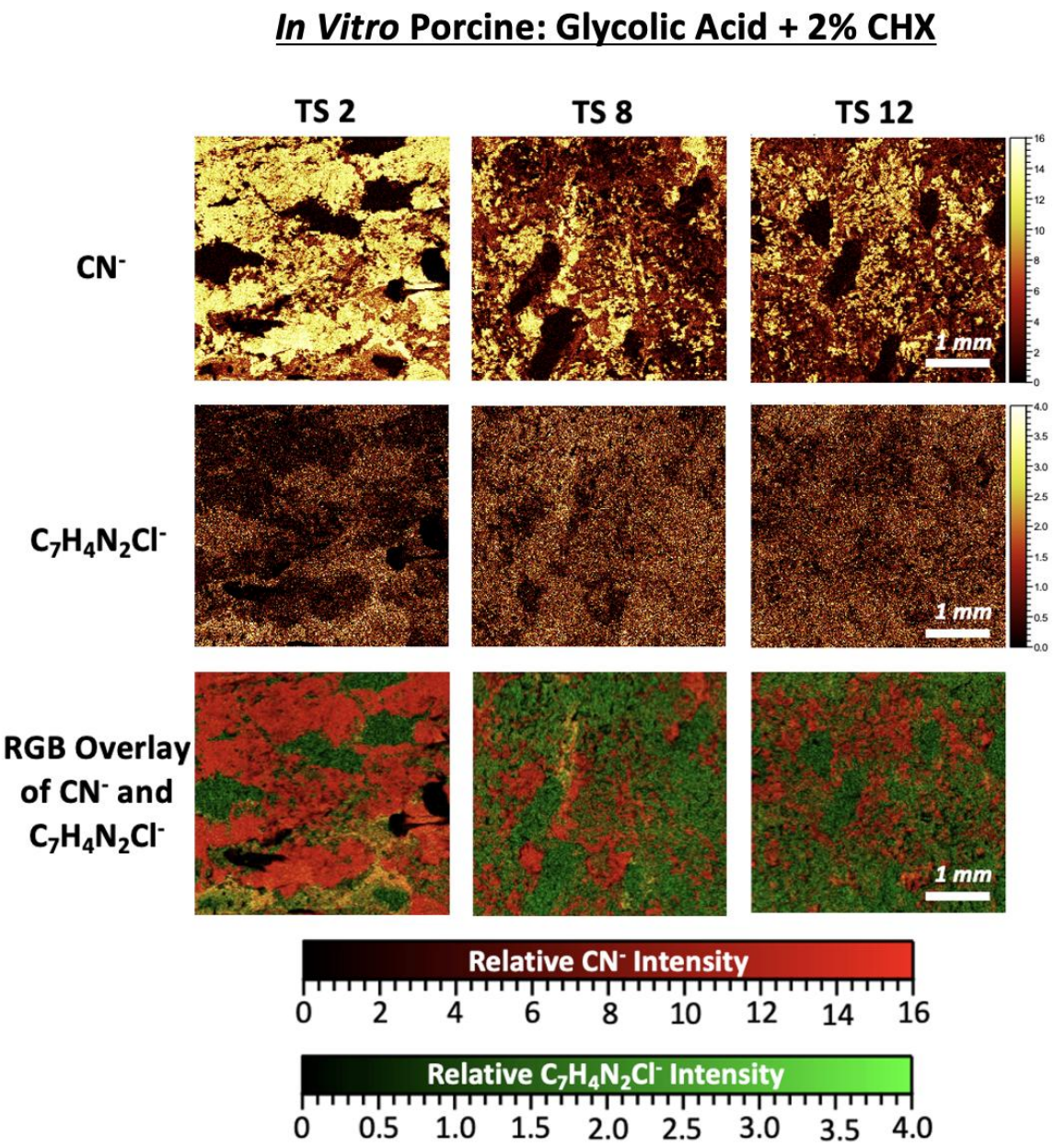


Figure 13. ToF-SIMS CN^- skin marker and $C_7H_4N_2Cl^-$ CHX fragment ion maps imaged from *in vitro* porcine skin treated with CHX formulated with glycolic acid. Overlayed images show where the two ions overlap.

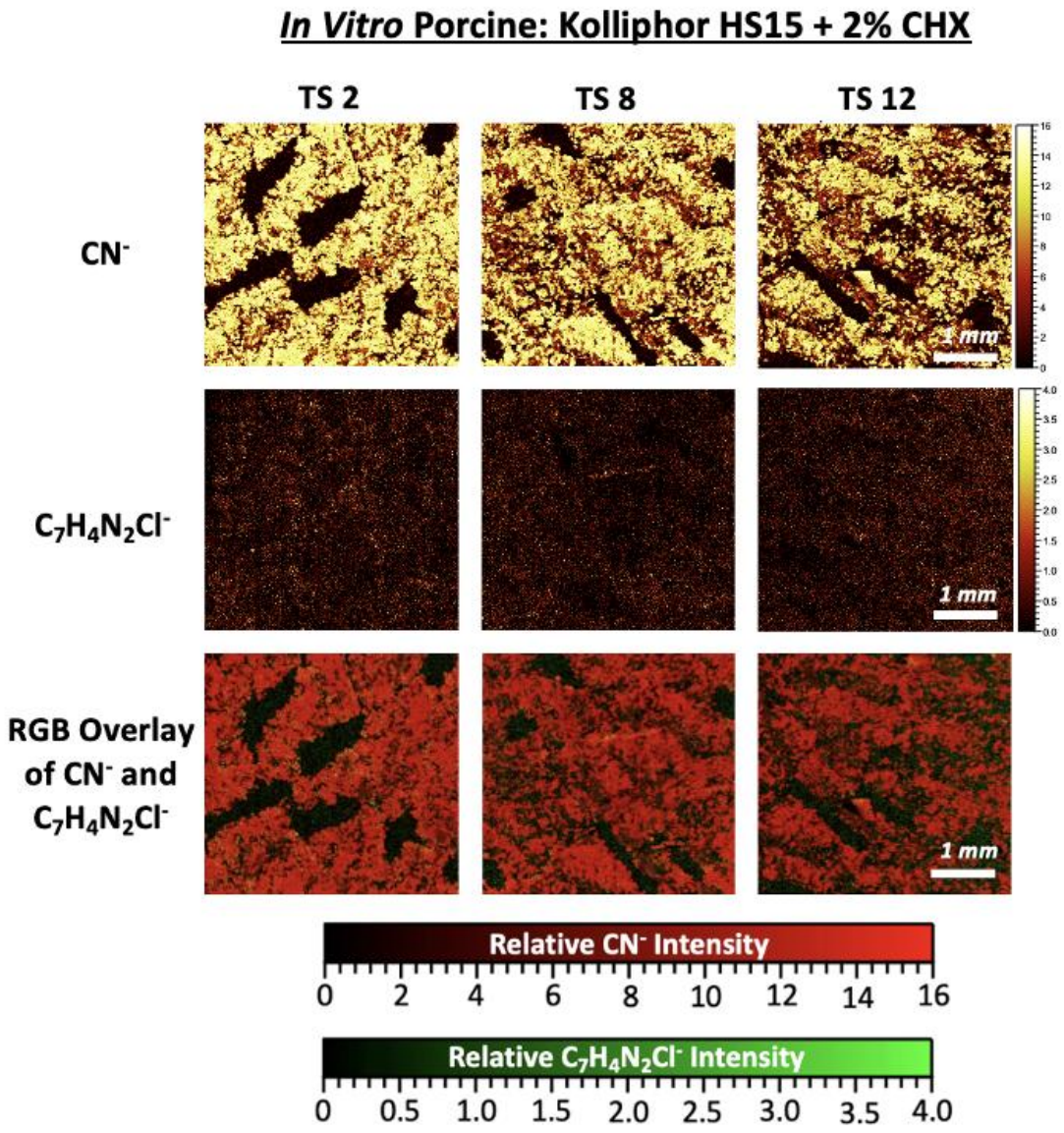


Figure 14. ToF-SIMS ion maps depicting the spatial distribution of the CN^- skin marker and $C_7H_4N_2Cl^-$ CHX fragment ion imaged from tape strip 2, 8 and 12 of *in vitro* porcine skin treated with CHX formulated with Kolliphor® HS15. Overlayed images show where the two ions overlap.

Conclusions of Chapter 2

This paper highlights that CHX permeates poorly through the human *stratum corneum* which may contribute to the occurrence of surgical site infections following incision through improper sanitised skin. This paper concludes that CHX delivery can be significantly enhanced through the porcine *stratum corneum* by formulating the biocide with glycolic acid, Kolliphor® HS15 and mostly, R6 polyarginine. This work also concludes that the addition of these permeation enhancer compounds improves the microbial clearance, which if applied to clinical skin sanitiser formulations, may significantly reduce the risk of infection following surgery. Further, these formulations cause no significant difference in mammalian cell viability and therefore cause no damage to murine 3T3 fibroblasts compared to the formulation currently used in clinic.

Chapter 3: Development and characterisation of antimicrobial epoxy resin

The previous chapter discusses the optimisation of a current clinical CHX formulation to improve microbial clearance through the skin and therefore prevent infections following surgery. The next chapter aims to utilise the broad-spectrum antimicrobial potency of CHX for the development of antimicrobial surfaces to eliminate environmental pathogens and reduce disease transmission.

This chapter shows a research paper that was published in Scientific Reports in 2025. This work discusses the development of a CHX epoxy resin coating which can be applied to pre-existing materials and surfaces, eliminating contaminating microorganisms. The paper explores the surface characterisation, antimicrobial efficacy, physicochemical properties, durability and stability of the CHX epoxy resin coatings to determine their efficacy and appropriateness for use as an antimicrobial surface.

My contributions to this manuscript include method development, particularly with ToF-SIMS and HPLC analysis. I was responsible for experimentation, and collection/presentation and analysis of data regarding antimicrobial efficacy of epoxy resin coatings against *E. coli* and *P. aeruginosa* species. In addition, I conducted experiments to determine the durability of these surfaces when immersed in PBS for 14 days. I analysed the leachate during the immersion period using absorbance and HPLC. In addition, I tested the scratch resistance and adhesion of the epoxy coatings following immersion. I also contributed to the write up of this manuscript, in particular the methodology of the experimentation, as well as post-review editing.

Development and characterisation of antimicrobial

Madeline Berrow[1#], Alexander Brooks[1#], Anna M. Kotowska[1], Julie Watts[1], Lily Riordan[1], Luke Kidger[1], David J. Scurr[1], Naa Dei Nikoi[1], Manuel Banzhaf[2], Jack Alfred Bryant[2], Simon Greenway[3], Violaine Mendez[3], Brian Norton[3], Felicity de Cogan[1*]

1. School of Pharmacy, University of Nottingham, UK
2. Institute of Microbiology and Infection, University of Birmingham, UK
3. Indestructible Paint Ltd, 16-25 Pentos Drive, Birmingham, UK

* Corresponding author

\# These authors contributed equally

Abstract

Surface contamination is an important, if under-discussed, route of infection transmission. In this study, we suspended chlorhexidine digluconate (CHX) in epoxy resin. CHX was found to be stably incorporated into the material, and its addition to epoxy resin was found to have minimal effects on the optical transparency of the material. After application of the epoxy resin to steel surfaces, time-of-flight secondary ion mass spectrometry revealed that CHX was uniformly present over the surface. Surfaces painted with CHX-resin were found to have significant, reproducible antimicrobial efficacy against *E. coli*, *S. aureus*, and *C. albicans*. We have shown that the addition of CHX has minimal effects on the adhesion of the epoxy resin to surfaces, as well as a high durability of the antimicrobial efficacy. We believe that this material has a wide array of applications, and could be utilised to confer significant, low-cost antimicrobial efficacy to existing surfaces, to prevent surface contamination, and to stop the transmission of infectious disease.

Keywords

chlorhexidine; $C_7H_4N_2Cl^-$; antimicrobial; polymer; epoxy resin; biocidal; paint

Data availability statement

Data will be made available by the authors upon reasonable request.

1. Introduction

Contamination of surfaces by pathogenic microorganisms is an important route of infection with this being especially important in healthcare settings. Research has suggested that healthcare professionals frequently encounter pathogenic microorganisms through contact with contaminated surfaces—one study suggested that 52% of healthcare personnel acquired vancomycin-resistant *Enterococci* through contact with surfaces,[1] whilst another study claimed that 40% of healthcare personnel who touched contaminated surfaces acquired methicillin-resistant *Staphylococcus aureus* on their hands.[2,3] Recent studies have suggested that SARS-CoV-2 can persist on stainless steel for 48 hours and can remain viable on plastic for up to 72 hours.[4,5] This is also observed with bacterial species, as *Escherichia coli* can survive for more than 28 days on stainless steel,[6] and *S. aureus* has been found to persist on stainless steel for six weeks,[7] and can persist on polyethylene for over 90 days.[8] The pathogenic bacteria *Acinetobacter baumannii*, which can cause nosocomial infections, has been found to be able to survive for seven days on glass, and for more than 25 days on cotton,[9] although other studies have found that strains associated with hospital outbreaks can survive for up to 33 days on glass surfaces.[10] *Klebsiella pneumoniae*, another frequent cause of nosocomial infections, can survive for seven days on stainless steel and polycarbonate surfaces, and can remain viable on aluminium for more than 15 days.[11] The pathogenic fungus *Candida albicans* has been found to survive for three days on both glass and steel surfaces, and could survive on fabric surfaces for 14 weeks,[12] whilst *Aspergillus fumigatus* has been found to remain viable on plastic surfaces for up to a month.[13]

Despite the clear prevalence of pathogenic microorganisms in hospital settings, and the ability of these microorganisms to persist on hard surfaces, the role of contaminated surfaces in the transmission of these pathogenic species has frequently been under-discussed. In a clinical setting, where healthcare professionals are working alongside vulnerable patients, the elimination of virulent microorganisms is essential; despite this, many such microorganisms can be resistant to enhanced, deep-cleaning regimes.[14] Furthermore, another major issue is the development of antimicrobial resistance in the clinical environment. Levels of antimicrobial resistance have increased in recent years, and the potential for resistant strains to colonise hard surfaces, evade deep cleaning regimes, and continue to infect the most vulnerable patients is of ever-increasing concern.[15] In clinical settings, resistance is not just confined to antimicrobial agents – resistance has begun to emerge against biocidal agents, such as chlorhexidine and triclosan. Resistance to these biocides is frequently correlated with resistance to other antibiotics; for example, extensively-drug resistant *K. pneumoniae* and multidrug-resistant *Enterobacter* have been found to exhibit resistance to chlorhexidine.[16,17] As such, the development of novel antimicrobial technologies is vitally important, to prevent the colonisation of abiotic surfaces by pathogenic microorganisms, including those that are resistant to antimicrobial therapies, and to prevent patient infections by eliminating this mode of transmission.

One of the major issues around surface coatings as a method to prevent colonisation of abiotic surfaces, regardless of the materials used to produce them, is that they require synthesis in a factory or laboratory setting, often requiring specialised equipment and reagents.[18] This increases the costs of producing the materials, which in turn increases the costs of purchasing these antimicrobial technologies.[19] Due to the high costs, this restricts their widespread implementation, with the materials being reserved for specialist applications. As such, there is a need to develop alternative antimicrobial materials that can be applied to a pre-existing surface by the consumer. These types of materials will have lower production costs, which will

make the purchasing costs lower; this will lead to more widespread applications of the material, including those that will benefit the general public.

With the need for intrinsically antimicrobial surfaces well documented, research has been carried out into the development of antimicrobial paints. Resins and paints containing silver nanoparticles appear to have potent antimicrobial efficacy against *E. coli* and *S. aureus*, although this activity was not quantified.[20] Other approaches have utilised copper nanoparticles to develop appliable antimicrobial materials, however the reduction in microbial burden was inconsistent across microbial species and application environment.[21] Recently, researchers have attempted to develop antimicrobial paints containing the plant-based compounds colophony and curcumin, which were found to provide a two-log reduction in the concentration of *S. aureus*, and a one-log reduction of *E. coli*, that could be recovered from painted surfaces; these values were not found to be statistically significant.[22] Other approaches have been based on cationic polymers, which were found to possess variable antimicrobial activity, with large quantities of highly concentrated polymeric paint being required to eliminate *E. coli* from surfaces. It was also found that the polymeric paints struggled to eliminate drug-resistant bacteria, including *K. pneumoniae*.[23] The ability to suspend the antiseptic agents chloroxylenol and terpineol in paint has also been investigated, with it being found that the antimicrobial activity of these paints is reduced when painted surfaces are exposed to deep cleaning techniques.[24] Despite these positive developments, many of these materials are still expensive to manufacture and purchase, with limited antimicrobial efficacy, and questions surrounding the durability of this efficacy. As such, it is crucial that antimicrobial paints continue to be developed, due to their greater affordability, but it is important that these paints possess significant, reproducible, and durable antimicrobial efficacy against a broad range of pathogenic microorganisms, including drug-resistant strains.

In this study, we demonstrate the development and characterisation of an industrial epoxy resin containing chlorhexidine digluconate (CHX). CHX is a broad-spectrum biocidal agent that exerts its effects by destabilising microbial membranes through the generation of reactive oxygen species, causing oxidative stress, lipid peroxidation, and leakage of metabolites from the cytoplasm, resulting in cell death. [25,26,27] Previous work has demonstrated the possibility of coating steel,[28] air filters,[29] and polymers,[30] with CHX, resulting in antimicrobial surfaces that possess strong antimicrobial efficacy, without altering the physical characteristics of the material. Previously, the coatings were all successfully characterised using time of flight secondary ion mass spectrometry (ToF-SIMS), specifically using the $C_7H_4N_2Cl^-$ (m/z 151.03) diagnostic secondary ion.[31] In this study, we aim to investigate the antimicrobial activity of CHX epoxy resin against clinically relevant pathogens *Staphylococcus aureus*, *Escherichia coli*, *Pseudomonas aeruginosa*, and *Candida albicans*. The effects of the addition of CHX to the physical properties of the paint, such as optical transparency and paint strength, will be investigated. We will also determine the durability of the antimicrobial efficacy of the paint and tested the efficacy of the paint against repeated bacterial exposures. Lastly, we will also examine if the paint remains biocidal against bacterial strains that have evolved resistance to CHX. This study represents an exciting development in the field of antimicrobial technologies, that could provide highly efficacious, durable, but low-cost, antimicrobial efficacy to pre-existing surfaces and materials.

2. Materials and Methods

All paint was provided by Indestructible Paint Ltd. All reagents were purchased from Sigma Aldrich UK, unless stated otherwise.

2.1 Epoxy Resin Preparation

To prepare epoxy clear gloss resin, clear gloss base and epoxy catalyst were mixed in an equal ratio, and the chemicals were allowed to react together for 15 minutes. The resin was then applied in a thin layer (50 μm) to 1cm × 1cm steel samples, and the resin was allowed to cure until hard in a 60˚C incubator for 90 minutes.

To prepare chlorhexidine epoxy resin, CHX solution was added at a 1 in 10 dilution, to make a 2% CHX concentration (v/v). The reaction was allowed to proceed for 15 minutes as described above, and the resin was applied to steel samples for antimicrobial testing and aluminium samples for analytical testing and cured as previously described (60 ºC, 90 minutes).

2.2 Time-of-Flight Secondary Ion Mass Spectrometry (ToF-SIMS)

All ToF-SIMS spectra of epoxy resin deposited on aluminium substrate were acquired using a ToF V (IONTOF GmbH) instrument. A 30 keV Bi_3^+ primary beam was used to acquire liquid metal ion gun (LMIG) ToF-SIMS images. The LMIG current was 0.05 pA, and the ToF image was run on an area of 300μm × 300μm using random raster mode with a 256 × 256-pixel density. The cycle time was set to 200 μs. The optimal target potential was set to -57.5 V. Four separate surface areas were analysed on each sample, and each measurement lasted 15 scans; the total ion dose per measurement was 9.44×10^{10} ions/cm^2.

Depth profile measurement on the control resin sample and on chlorhexidine resin sample was carried out to determine chlorhexidine presence throughout the paint until the substrate is reached and the total ion dose was 3.59×10^{16} ions/cm^2, which is approximated to be a 90μm depth based on sputtering of irganox 1010 in similar conditions, which is commonly used as an analogous material to estimate the sputter yield of organic samples[i]. The depth profile analysis was carried out by using a 20 keV Ar_{2072}^+ gas cluster ion beam (GCIB) with a current of 4 nA as a sputter beam. An area of 300μm × 300μm was imaged during depth profiling, and the crater size was set to 500μm × 500μm. ToF-SIMS was also performed on post-leaching steel samples, with preparation of these samples described in the section below. The depth profile of the post-leaching samples was run until a total ion dose of 3.26×10^{13} ions/cm^2.

Detection of the $C_7H_4N_2Cl^-$ ion using ToF-SIMS is used to confirm the presence of CHX on the surface, as this ion is a diagnostic fragment of the molecule of interest, CHX, as established in Judd, *et al*..[31]

2.3 Water Contact Angle

Epoxy resin deposited on aluminium substrate was prepared as described previously, and applied to steel surfaces and cured (60 ºC, 90 minutes). The water contact angle was measured using the CAM 200 Goniometer (Krüss Scientific) using the sessile drop technique. 10 μL droplets of distilled, deionised water were used for the measurements, which were taken from

20 locations (five locations on each sample). The values for the water contact angle were obtained through application of Young-Laplace fitting to raw data.

2.4 Scratch Resistance and Adhesion

To test the scratch resistance and adhesion strength of the paint, aluminium panels were shot blasted, before control and chlorhexidine epoxy resin was prepared as described above. Aluminium panels were painted with either type of epoxy resin using a 50 μm spiral wire bar coater (TQC Sheen) to obtain a thin, uniform paint layer. The painted sheets were then force cured at 121˚C for 60 minutes.

For scratch resistance, painted aluminium panels were placed in a manual scratch testing machine (TQC Sheen), and followed the assay according to ISO 1518 [33]. In brief, weights were added to the apparatus, before being run across the painted surface until a scratch developed; the weight was increased in 100 g increments. The point at which to end the test was determined through examination with a magnifying glass, when it was observed that the integrity of the painted layer had been compromised.

For adhesion testing, a cross-cut test was performed. A 10 × 10 square pattern was scored into the painted aluminium steel using a template and a utility knife. A layer of tape was applied over the scored area, and was pulled to remove any paint that had not bonded to the aluminium sheet. The integrity of the paint was graded following the test according to ISO 2409:2007.[33]

2.5 Optical Transparency

Following preparation of control and chlorhexidine epoxy resin as described above, a thin layer (50 μm) of each type of resin was applied to the individual wells of a 96-well culture plate (Greiner Bio-One). The resin was cured as described previously. Once the resin was fully cured, 100 μL of phosphate buffered saline (PBS) was added to each well, and an absorbance spectrum reading taken using the BMG LabTech ClarioStar plate reader, scanning from 220nm to 1000nm.

2.6 Antibacterial Efficacy

Escherichia coli ATCC25922, *Staphylococcus aureus* ATCC6538 and *Pseudomonas aeruginosa* PA14 were cultured in 5 mL lysogeny broth (LB) for 18 hours at 37˚C, 180 rpm, before being adjusted to 1×10^9 CFU/mL. Steel samples that were painted with either control or antimicrobial epoxy resin were placed into a 12-well culture plate (Starlab). The cultures were pipetted onto the painted surfaces in 9 × 1 μL drops, in a simulated splash test. The cultures were allowed to dry onto the painted surfaces and were incubated on the surfaces for 18 hours at room temperature, following the ISO standard 22196 [33]. Following incubation, the surfaces were transferred into 10 mL Dey-Engley Neutralising Broth with 7-10 sterile zirconium beads (Thistle Scientific), and were vortex mixed for 1 minute each to recover the bacteria from the surfaces. The neutralising broth suspension was serially diluted 1:3 in sterile PBS, and bacterial survival was determined by counting colony forming units (CFU) following incubation at 37 ˚C for 18 hours on LB agar. Efficacy testing was performed in triplicate both for surfaces painted with control and antimicrobial epoxy resin, and for both *E. coli* and *S. aureus*.

2.7 Antifungal Efficacy

Candida albicans SC5314 was cultured in 5 mL yeast peptone dextrose (YPD) broth (1% yeast extract, 2% peptone, 2% glucose) for 18 hours at 30˚C with shaking set to 180 rpm, before being adjusted to 1×10^9 CFU/mL. Antimicrobial efficacy was then tested as described previously in **2.6**, replacing LB agar with YPD agar.

2.8 Antibacterial Efficacy Against Chlorhexidine-Resistant *E. coli*

As detailed in Watson et. al. (2023), *E. coli* BW25113 was serially passaged in Mueller-Hinton Broth (MHB) containing increasing concentrations of CHX to elevate the minimum inhibitory concentration (MIC) of the strain to 32 μM [30]. Chlorhexidine-resistant *E. coli* BW25113 was cultured overnight in 5 mL LB broth for 18 hours at 37˚C, 180 rpm, before being adjusted to 1×10^9 CFU/mL. Antibacterial efficacy was then tested as described previously in **2.6**.

2.9 Scanning Electron Microscopy

Steel surfaces painted with control or chlorhexidine epoxy resin were prepared as described previously. *E. coli* and *S. aureus* were cultured in 5 mL LB for 18 hours at 37˚C, 180rpm, and then adjusted to 1×10^9 CFU/mL. The samples were then placed into a 12-well culture plate (Starlab), with the cultures being pipetted onto the painted surfaces in 9 × 1 μL drops. The cultures were allowed to dry onto the painted surfaces and were incubated on the surfaces for 18 hours at room temperature. Following this incubation, the surfaces were covered in 4% paraformaldehyde (Fisher Scientific) for one hour, before being washed with sterile PBS. The inoculated surfaces were then serially dried using solutions containing increasing concentrations of ethanol, up to 100% ethanol, and then underwent critical point drying. Samples were mounted using conductive carbon tape onto SEM support stubs and coated with Iridium (Quorum G 150T ES, East Sussex UK). Scanning electron microscopy was performed at an operating voltage of 5 kV, nominal working distance 5mm, SESI detector, using a field emission SEM (Zeiss CrossBeam 550, Oberkochen, Germany).

2.10 Durability of Antimicrobial Efficacy

The durability of the antimicrobial efficacy of the paint was investigated by conducting a leaching study. Painted steel samples were prepared and cured as described previously. Following curing, the samples were immersed in 10 mL sterile PBS. All samples were stored in the dark, at room temperature. At 24-hour intervals, 200 μL of the PBS solution was removed, and was plated in a black-bottomed, black-walled 96-well cell culture plate (Corning). After 14 days, the absorbance was read at 280 nm. The painted surfaces were removed from the leachate, and were dried and retained for future work. The leachate was also retained for future work, remaining in dark conditions.

To assess if there was any leaching of CHX from the painted surface, the antimicrobial efficacy of the leachate was assessed. The leachate was serially diluted 1:10 in sterile PBS, to a 10^{-9}

concentration. 9 µL of *E. coli* at 1×10^9 CFU/mL was added to 100 µL of each leachate dilution, and incubated at room temperature for one hour; fresh sterile PBS was used as a control, and was also inoculated with the bacterial suspension. The inoculated leachate solution was serially diluted 1:3 in sterile PBS, and bacterial survival was determined by counting CFU following incubation at 37˚C for 18 hours on LB agar. Furthermore, to determine if the painted surfaces retained antimicrobial efficacy, *E. coli* was added to the surface as per **2.6**. The antimicrobial efficacy testing for both the leachate and the post-leaching painted surfaces was performed in triplicate.

2.11 HPLC analysis of CHX epoxy resin leachate

Leachates from **2.10** were 0.22 µL filter sterilised into 2 mL amber robotic 9 mm thread vials for HPLC analysis. Chromatographic separation was achieved using an Agilent 1260 liquid chromatography system , consisting of a G7111B quaternary pump, G7115A diode array detector, G7129A vial sampler and the OpenLab, Agilent Technologies software version 3.5 (3.5.0.654). An ACE C18 (150 × 4.6 mm I.D.,5 µM) column was deployed using an isocratic mobile phase consisting o f 32:68 (v/v) acetonitrile and phosphate buffer solution (0.05 M monobasic sodium phosphate solution including 0.5% triethylamine, which was adjusted to pH 3.0 using 85% phosphoric acid). A flow rate of 2.0 mL min-1 was consistent throughout the analysis, along with UV detection of 239 nm, a column oven temperature of 40 ºC and an injection volume of 20 µL. A series of CHX standards varying from 0.1-1.0 mg mL^{-1} were used to develop a calibration curve for quantification of the CHX peak at retention 2.3 minutes.

2.12 Stability of Chlorhexidine Epoxy Resin

To determine the stability of chlorhexidine epoxy resin in shelf storage conditions, 20% (w/v) CHX solution was added to the clear gloss base to a concentration of 20% in a 15 mL centrifuge tube (Eppendorf), and mixed thoroughly. The tube was closed and wrapped in aluminium foil, to mimic shelf storage conditions, and the chlorhexidine epoxy base was stored at room temperature for one month. After this, the chlorhexidine epoxy base was mixed in an equal ratio with the epoxy catalyst, and the chemicals were allowed to react together for 15 minutes. The paint was applied to steel surfaces, and cured at 60˚C for 90 minutes. After this, the painted surfaces were investigated for antimicrobial efficacy. *E. coli* was cultured in 5mL LB for 18 hours at 37˚C, 180 rpm. The culture was adjusted to 1×10^9 CFU/mL, and was applied to the painted surfaces in a 9 × 1 µL simulated splash pattern. The culture was allowed to dry onto the painted surfaces, and the surfaces were incubated overnight for 18 hours at room temperature. Following this incubation period, antibacterial testing was performed as per 2.6, and bacterial survival was assessed by calculating CFU following incubation at 37˚C for 18 hours on LB agar. Antibacterial testing for aged chlorhexidine resin was performed in triplicate.

This protocol was also performed for chlorhexidine epoxy base that had been stored at room temperature in the shelf-storage conditions described above for three months.

2.13 Repeat Exposures of Chlorhexidine Epoxy Resin

Steel surfaces were painted with control or chlorhexidine epoxy resin, and cured as described previously. After this, the painted surfaces were investigated for the ability to retain

antimicrobial efficacy upon repeat exposures to microorganisms. As such, *E. coli* was cultured in 5mL LB for 18 hours at 37˚C, 180 rpm. The culture was adjusted to 1×10^9 CFU/mL, and was applied to the painted surfaces in a 9 × 1 μL simulated splash pattern. The culture was allowed to dry onto the painted surfaces, and the surfaces were incubated overnight for 18 hours at room temperature. Following this incubation period, the painted steel samples were transferred to 10 mL sterile distilled water with 7-10 sterile zirconium beads (Thistle Scientific), and vortex mixed for 1 minute to recover the bacteria from the surface. The bacterial suspension was serially diluted 1:3 in sterile PBS, and bacterial survival was assessed by calculating CFU following incubation for 18 hours on LB agar. The painted steel pieces were removed from the bacterial suspension and washed in sterile distilled water, before being dried using an airline. After drying, the washed steel was inoculated again with a normalised culture of *E. coli*, and the bacterial recovery and washing stages were performed again, to a total of three exposures. Antibacterial testing was performed in triplicate for all three exposures.

2.14 Data Analysis

All statistical analysis was performed using SPSS (Version 28.0.1.1 (14); IBM). All data obtained was analysed by performing an Independent Samples t-test, with α set to 0.01. Image analysis was performed using ImageJ (Version 1.53t; NIH). All graphs were generated in Prism (Version 10.0.0 (131); GraphPad). All data is presented as the mean plus/minus the standard error of the mean.

3. Results

3.1 Surface Characterisation

ToF-SIMS was performed to detect the presence of CHX on the surface and throughout the epoxy resin (**figure 1**). Scans of the surfaces revealed uniformity of the presence of CHX ions across the surfaces painted with chlorhexidine epoxy resin (**figure 1A**), whilst these ions could not be detected on surfaces painted with control epoxy resin (**figure 1B**). The average ion intensity for surfaces painted with chlorhexidine epoxy resin was 0.035 ± 0.00073, which is significantly higher ($p < 0.001$) than the average ion intensity recorded for surfaces painted with control epoxy resin, which had a mean of 0.001 ± 0.00016 (**figure 1C**). In addition, ToF-SIMS depth profile was carried out on the control resin sample and on chlorhexidine resin sample to determine chlorhexidine ($C_7H_4N_2Cl^-$ ion) presence throughout the paint. Depth profiling through samples painted with chlorhexidine epoxy resin revealed that CHX ion was most prevalent at the uppermost layer, although it could be detected throughout the depth profile until the substrate was reached after delivering primary ion dose of approximately 2.7×10^{16} ions/cm^2 (70μm depth based on sputtering of irganox 1010 in similar conditions)[32]. (**figure 1D**). Lastly, the surface water contact angle was measured to determine if the addition of CHX to the epoxy resin altered the hydrophobicity of the material. Following curing, the addition of CHX to the epoxy resin decreased the water contact angle from 88.74 ± 1.97˚ to 79.83 ± 2.01˚. However, this decrease in the water contact angle was not found to be statistically significant (**figure 1E**), indicating that CHX can be incorporated into epoxy resin without significantly altering the wettability of the material.

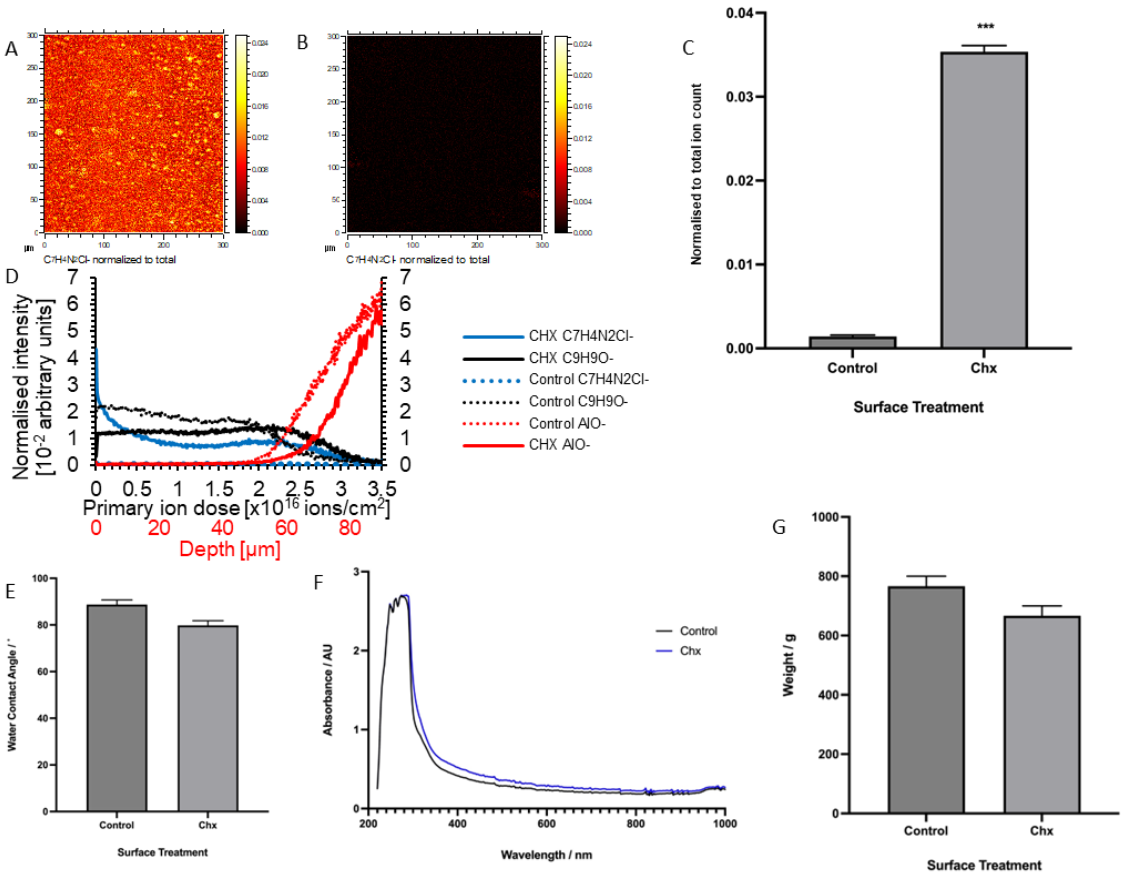


Figure 1: Surface characterisation of painted surfaces. **A:** Scan across a steel surface painted with chlorhexidine epoxy resin, showing the intensity of the $C_7H_4N_2Cl^-$ ion normalized to total ion count. **B:** Scan across a steel surface painted with control epoxy resin, showing the intensity of the $C_7H_4N_2Cl^-$ ion normalized to total ion count. **C:** Quantification of $C_7H_4N_2Cl^-$ ion intensity across steel surfaces painted with control and chlorhexidine epoxy resin, respectively (n=8). **D:** The normalized ion intensity of the $C_7H_4N_2Cl^-$ ion (blue), $C_9H_9O^-$ paint marker (black) and AlO^- substrate marker (red) through control (dotted line) and chlorhexidine epoxy resin (solid line). **E:** Quantification of water contact angle measurements for steel surfaces painted with control and chlorhexidine epoxy resin and cured horizontally (n=5). **F:** The optical transparency of control and chlorhexidine epoxy resin, as evaluated by measurements of the absorbance from 220-1000nm (n = 144). **G:** The scratch resistance of control and CHX epoxy resin (n = 3). *** indicates $p < 0.001$, error bars show standard error of the mean.

3.2 Material Characterisation

The optical transparency of control and chlorhexidine epoxy resin was investigated alongside the curing time, finding that both the control and the CHX epoxy resin took 80 minutes to cure. After curing, the absorbance peaked at 274 nm for both control and chlorhexidine epoxy resin (**figure 1F**). This shows that the absorbance peak of epoxy resin is not altered by the presence of CHX. Despite the absorbance spectra following a similar pattern for all samples - absorbance peaking at 274nm, and gradually decreasing as the wavelength increases - the absorbance of chlorhexidine epoxy resin was found to be increased at higher wavelengths in comparison to control epoxy resin. For example, at 1000nm, the absorbance for control epoxy resin was 0.241 ± 0.0111 a.u., and was 0.266 ± 0.016 a.u. for chlorhexidine epoxy resin. This increase in

absorbance at 1000 nm was not found to be statistically significant (n = 3, $p = 0.14$), indicating that CHX does not significantly increase the optical transparency of epoxy resin at higher wavelengths.

The scratch resistance of the two types of paint was determined. It was found that control epoxy resin was scratch resistant up to a weight of 766.67 ± 33.33g, whereas chlorhexidine epoxy resin was scratch resistant up to a weight of 666.67 ± 33.33g (**figure 1G**). Despite this observed decrease, this was not found to be statistically significant, and as such, it can be concluded that the addition of chlorhexidine to the epoxy resin does not significantly reduce the scratch resistance of the epoxy resin. As well as this, it was also determined that the addition of CHX did not impact the adhesion of the epoxy resin.

3.3 Antimicrobial Efficacy

With the ability to incorporate CHX into clear gloss epoxy resin established, and the presence of CHX on painted surfaces confirmed, the antimicrobial efficacy of the epoxy resin was next assessed. To replicate the contamination of abiotic surfaces observed in real-world scenarios, low-volume, high-concentration cultures ($OD_{600} = 1.0$) of *E. coli*, *S. aureus*, *P. aeruginosa* and *C. albicans* were used to inoculate the surfaces in a simulated splash pattern, as model Gram-negative, Gram-positive, and fungal organisms. For *E. coli*, following an overnight incubation, a CFU of $7.20\times10^6 \pm 1.75\times10^6$ CFU/mL was recovered from surfaces painted with control epoxy resin. By contrast, no viable bacteria could be recovered from surfaces painted with chlorhexidine epoxy resin. This was found to be highly statistically significant ($p < 0.001$) and is indicative of excellent antimicrobial efficacy (**figure 2A**).

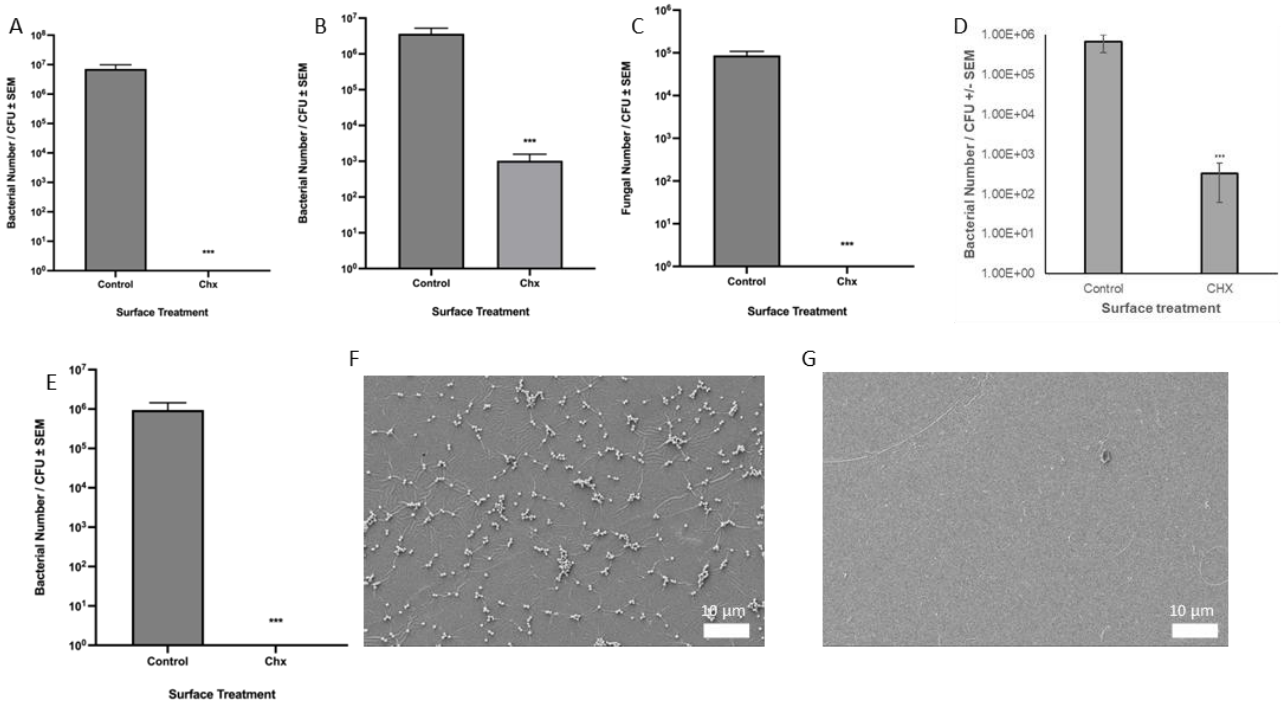


Figure 2: Antimicrobial efficacy of surfaces painted with chlorhexidine epoxy resin. **A**: The survival of *E. coli* ATCC25922 on steel surfaces painted with control and chlorhexidine epoxy resin. **B**: The survival of *S. aureus* ATCC6538 on steel surfaces painted with control and chlorhexidine epoxy resin. **C**: The survival of *C. albicans* SC5314 on steel surfaces painted with control and chlorhexidine epoxy resin **D**: The survival of *P. aeruginosa* PA14 on steel surfaces painted with CHX epoxy resin. **E**: The survival of chlorhexidine-resistant *E. coli* BW25113 on steel surfaces painted with control and chlorhexidine epoxy resin (n = 9). *** indicates $p < 0.001$, error bars represent standard error of the mean. **F**: SEM image of steel surface painted with control epoxy resin and inoculated with *S. aureus* ATCC6538. Image taken at 10 µm resolution and is representative of three repeats. **G**: SEM image of steel surface painted with chlorhexidine epoxy resin and inoculated with *S. aureus* ATCC6538. Image taken at 10 µm resolution and is representative of three repeats.

Similar trends were observed for *S. aureus*; surfaces painted with control epoxy resin saw a CFU of $3.66\times10^6 \pm 1.29\times10^6$ CFU/mL recovered following an overnight incubation, whilst a CFU of $1.04\times10^3 \pm 4.21\times10^2$ CFU/mL was recovered from surfaces painted with chlorhexidine epoxy resin (**figure 2B**). This three-log reduction in CFU was found to be statistically significant ($p < 0.001$), and shows that the material exerts antibacterial efficacy against both Gram-positive and Gram-negative bacteria. The final bacterial species assayed was *P. aeruginosa*, and similarly, surfaces painted with control epoxy resin saw a CFU of $6.75\times10^5 \pm 3.20\times10^5$ CFU/mL recovered following an overnight incubation, whilst a CFU of $3.33\times10^2 \pm 2.72\times10^2$ CFU/mL was recovered from surfaces painted with CHX epoxy resin (**figure 2D**). This three-log reduction in CFU was found to be statistically significant ($p < 0.001$). The antifungal efficacy of the chlorhexidine epoxy resin was assessed utilising *C. albicans*. Following inoculation and incubation as described above, a CFU of $9.21\times10^4 \pm 1.44\times10^4$ CFU/mL was recovered from surfaces painted with control epoxy resin. By contrast, no viable fungi could be recovered from surfaces painted with chlorhexidine epoxy resin. This was found to be statistically significant ($p < 0.001$), indicating that the addition of chlorhexidine to epoxy resin confers antifungal efficacy (**Figure 2C**).

Finally, to determine if the chlorhexidine epoxy resin could continue to exert its well-established antimicrobial efficacy in the event of the development of resistance to CHX, the surfaces were challenged with *E. coli* that had been evolved to possess a significantly elevated MIC against chlorhexidine, of 32 μM [30]. Following inoculation and incubation as described above, a CFU of $9.46\times10^5 \pm 5.95\times10^4$ CFU/mL was recovered from surfaces painted with control epoxy resin. By contrast, no viable bacteria could be recovered from surfaces painted with chlorhexidine epoxy resin. This was found to be highly statistically significant ($p < 0.001$), demonstrating that chlorhexidine epoxy resin retains its antimicrobial efficacy, even against strains that have evolved significant resistance to this biocidal agent (**figure 2E**).

This was also reflected in SEM images obtained from painted surfaces inoculated with *S. aureus* – a large concentration of bacteria was observed on surfaces painted with control epoxy resin (**figure 2F**), whilst little to no bacteria could be observed on surfaces painted with chlorhexidine epoxy resin (**figure 2G**).

3.4 Surface Leaching and Durability of Efficacy

Once the antimicrobial efficacy of the chlorhexidine epoxy resin was determined, the durability of this efficacy was investigated. The painted control and CHX surfaces were immersed in PBS for 14 days. On day 0, background readings were taken before adding painted samples: for control epoxy resin leachate, the average day 0 reading was 36772 ± 3579 au, and was 38676 ± 4428 au for chlorhexidine epoxy resin leachate. Throughout the study, the absorbance readings fluctuated, with increases and decreases being observed for leachate obtained from surfaces painted with both control and chlorhexidine epoxy resin, respectively. No significant differences were found between any of the control and chlorhexidine leachate absorbance readings for any of the measurements, indicating that there was no leaching of chlorhexidine from the epoxy resin upon immersion in PBS (**figure 3A**).

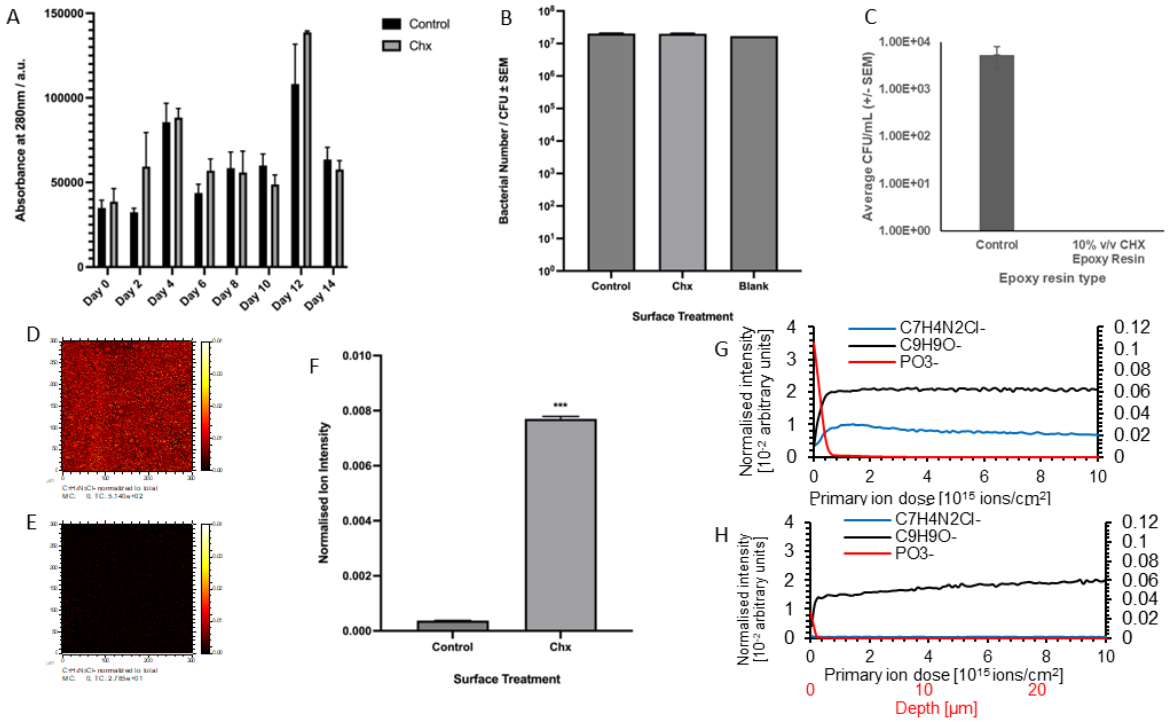


Figure 3: The effects of leaching in PBS on chlorhexidine epoxy resin. **A:** The absorbance of leachate from steel surfaces painted with control and chlorhexidine epoxy resin (n = 9). **B:** The antimicrobial efficacy of leachate obtained from steel samples painted with control and chlorhexidine epoxy resin (n = 3). **C:** The survival of *E. coli* ATCC25922 on steel surfaces painted with control and chlorhexidine epoxy resin, following leaching (n = 9). **D:** Scan across a steel surface painted with chlorhexidine epoxy resin following leaching, showing the intensity of the $C_7H_4N_2Cl^-$ ion. **E:** Scan across a steel surface painted with control epoxy resin following leaching, showing the intensity of the $C_7H_4N_2Cl^-$ ion. **F:** Quantification of $C_7H_4N_2Cl^-$ ion intensity across steel surfaces following leaching, painted with control and chlorhexidine epoxy resin, respectively (n=8). **G:** The normalized ion intensity of $C_7H_4N_2Cl^-$, $C_9H_9O^-$, and PO_3^- ions through successive layers of chlorhexidine epoxy resin following leaching in PBS. **H:** The normalized ion intensity of $C_7H_4N_2Cl^-$, $C_9H_9O^-$, and PO_3^- ions through successive layers of control epoxy resin following leaching in PBS. In both chlorhexidine and control resins the PO_3^- ion intensity is presented on secondary scale for clarity due to high intensity of the PO_3^- peak. *** indicates $p < 0.001$, error bars show standard error of the mean.

To confirm that there was no CHX leaching from the epoxy resin, the antimicrobial efficacy of the leachate was assessed. For the leachate from the control surfaces, a bacterial concentration of $2.04\times10^7 \pm 4.02\times10^6$ CFU/ml was recovered, whilst for the leachate from the chlorhexidine-painted surfaces, the CFU was $1.85\times10^7 \pm 1.06\times10^6$ CFU/ml. It was found that there was no significant difference between the two bacterial concentrations ($p = 0.666$) (**figure 3B**). The leachate from the chlorhexidine-painted surfaces does not exhibit any antimicrobial efficacy, which indicates that there is no leaching of the CHX from the surface. This was confirmed with HPLC analysis of the leachate, and compared to a CHX standard, and no CHX was detected in the leachate from either the CHX epoxy resin or control epoxy resin. It can therefore be concluded that the chlorhexidine remains suspended inside the epoxy resin, and indicates that the antimicrobial efficacy is durable.

Lastly, following the leaching assay, the painted surfaces were removed from the leachate, and the post-leaching surfaces were inoculated with *E. coli*. The results showed that a bacterial

concentration of $5.33\times10^3 \pm 2.62\times10^3$ CFU/mL was recovered from control surfaces, whilst no viable *E. coli* were recovered from surfaces painted with chlorhexidine epoxy resin (**figure 3C**). This was found to be highly significant (p=0.022), indicating that the painted surfaces remain antimicrobial following leaching, which is supported by the other data obtained in this study, demonstrating that CHX remains within the epoxy resin.

After the samples were removed from the leachate and dried, ToF-SIMS was performed, to see if chlorhexidine could continue to be detected in the epoxy resin following leaching. It was found that the $C_7H_4N_2Cl^-$ ion could be detected uniformly across a layer painted with chlorhexidine epoxy resin (**figure 3D**), whilst it could not be detected in samples painted with control epoxy resin (**figure 3E**). The average ion intensity for samples painted with chlorhexidine epoxy resin was found to be 0.0077 ± 0.0000044, whereas this ion intensity was 0.00038 ± 0.0000041 for samples with control epoxy resin; this difference was found to be highly statistically significant ($p < 0.001$) (**figure 3F**). This shows that CHX remains incorporated in epoxy resin after leaching. ToF-SIMS analysis also revealed that, following leaching, a high concentration of phosphate salt ions could be detected on surfaces painted with control and chlorhexidine epoxy resin, respectively (**figures 3G** and **H**). This confirms that the immersion of painted surfaces in PBS does not prevent the chlorhexidine epoxy resin from acting as an antimicrobial material.

3.5 Stability of Chlorhexidine in Epoxy Resin

To determine the ability to store chlorhexidine epoxy resin under shelf-storage conditions, we mixed CHX into the epoxy base, and kept the mixture in dark conditions for one month. After this, the chlorhexidine base was mixed with the catalyst, and applied to steel surfaces for the determination of antimicrobial efficacy. Following inoculation and incubation, a bacterial concentration of $5.64\times10^5 \pm 9.50\times10^4$ CFU/mL was recovered from surfaces painted with control epoxy resin. Conversely, no viable bacteria could be recovered from surfaces painted with the aged chlorhexidine epoxy resin; this was found to be highly statistically significant ($p < 0.001$) (**figure 4A**). This shows that the excellent antimicrobial efficacy of the paint is not affected by storing for extended periods of time, and that the material could be stored on the shelf without sacrificing antimicrobial efficacy. The experiment was repeated with chlorhexidine base that had been stored for three months, and it was found that a bacterial concentration of $4.72\times10^5 \pm 3.77\times10^4$ CFU/mL was recovered from surfaces painted with control epoxy resin. By contrast, no bacteria could be recovered from surfaces painted with chlorhexidine epoxy resin prepared with the three-month aged base (**figure 4B**). This was found to be highly statistically significant ($p < 0.001$), demonstrating that the material can be stored for three months without adversely affecting the well-demonstrated antimicrobial efficacy of the material. Furthermore, scratch testing the painted surface post-leaching also showed that aging the surface not only has no effect on the antimicrobial efficacy, but also no significant impact on the surface integrity itself ($p = 0.197$) (**figure 4D**).

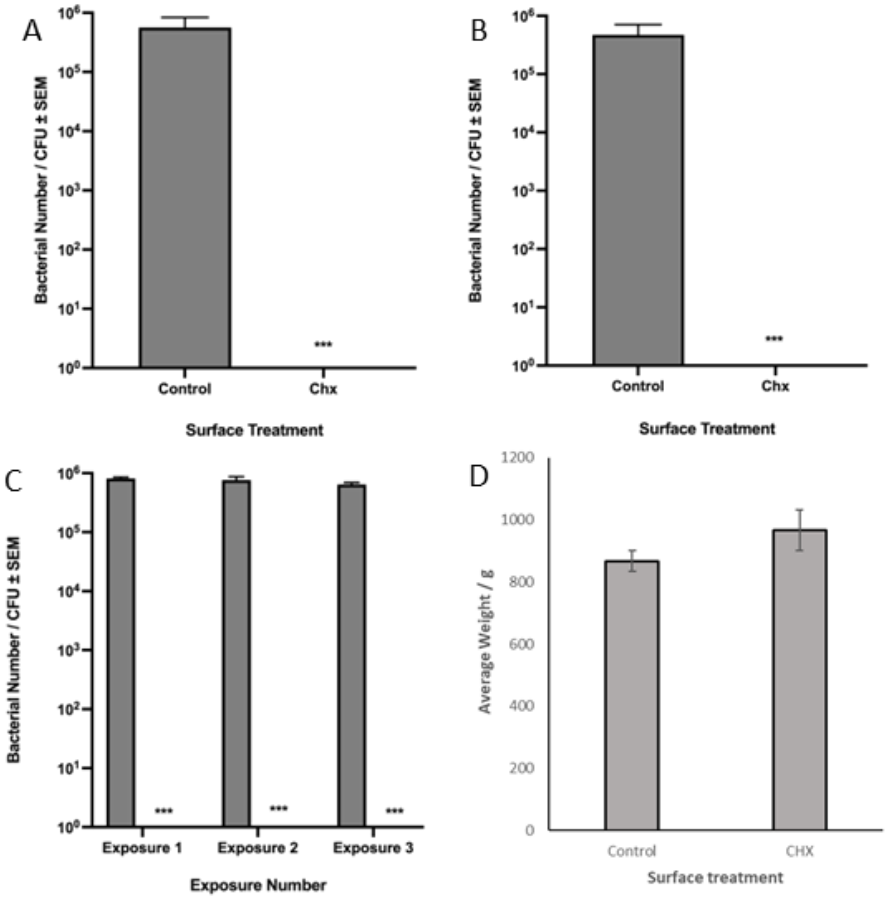


Figure 4: Continued explorations of the antimicrobial efficacy of chlorhexidine epoxy resin. **A**: The survival of *E. coli* ATCC25922 on steel surfaces painted with control epoxy resin, or surfaces painted with one-month aged chlorhexidine epoxy resin (n = 9). **B**: The survival of *E. coli* ATCC25922 on steel surfaces painted with control epoxy resin, or surfaces painted with three-month aged CHX epoxy resin (n = 9). **C**: The survival of *E. coli* on steel surfaces painted with control and CHX epoxy resin without sterilization between repeat exposures (n = 9). **D**: The scratch resistance of both control and CHX epoxy resin, after 14 days leaching in PBS (n=3). *** indicates $p < 0.001$, error bars indicate the standard error of the mean.

3.6 Repeated Exposures of Chlorhexidine Epoxy Resin to E. coli

To observe if the chlorhexidine epoxy resin was able to exert its antimicrobial efficacy in a realistic setting, the painted surfaces were challenged with multiple exposures to *E. coli* without sterilisation in between exposures. On the first exposure, a bacterial concentration of $8.13\times10^5 \pm 4.31\times10^4$ CFU/mL was recovered from surfaces painted with control epoxy resin, with no viable bacteria being recovered from surfaces painted with chlorhexidine epoxy resin. After the second exposure, a bacterial concentration of $7.62\times10^5 \pm 1.10\times10^5$ CFU/mL was recovered from surfaces painted with control epoxy resin, whilst, once again, no viable bacteria could be recovered from surfaces painted with chlorhexidine epoxy resin. After the third and final exposure, a bacterial concentration of $6.44\times10^5 \pm 5.12\times10^4$ CFU/mL was recovered from surfaces painted with control epoxy resin, whilst no bacteria could be recovered from surfaces painted with chlorhexidine epoxy resin. The bacterial concentration was significantly reduced for chlorhexidine epoxy resin in comparison to control epoxy resin after each exposure ($p <$

0.001 for each exposure), indicating that the antimicrobial efficacy of the chlorhexidine epoxy resin is not diminished by repeatedly exposing the material to *E. coli* (**figure 4C**).

4. Discussion

In this study, we have shown the ability to impregnate commercially available epoxy resin with the broad-spectrum biocidal agent CHX. Detection of the $C_7H_4N_2Cl^-$ ion using ToF-SIMS is used to confirm the presence of chlorhexidine in a material.[31] The detection of this ion confirms the presence of chlorhexidine within the epoxy resin, and shows that the distribution of this ion is uniform across the painted layer, whilst the ion could not be detected in control samples. Further analysis revealed that, despite the ion being detected throughout the applied layer of epoxy resin, it predominantly accumulates at the surface. The reason for this is unclear, although it could potentially be due to phase separation. The preferential aggregation of chlorhexidine at the uppermost layer of the applied epoxy resin upon curing may enhance the antimicrobial efficacy of the material, as this would ensure constant contact between the pathogen and the biocide; this is important, as CHX exerts its antimicrobial effects through contact killing mechanisms and interactions with the microbial membrane.[34,35] This would lead to effective clearance of the microorganism from the surface, preventing colonisation and future transmission. Further investigations found that the addition of CHX to epoxy resin led to minimal alterations to the water contact angle, optical transparency, and bonding and adhesion strength of the epoxy resin. Demonstrating that the incorporation of CHX does not adversely affect the well-established properties of epoxy resin,[36] and that the material can be used by the consumer in the same manner as control epoxy resin.

The antimicrobial efficacy results show that CHX epoxy resin exhibits significant antimicrobial activity against both Gram-positive and Gram-negative bacteria, although the antimicrobial efficacy was stronger against *E. coli* (Gram-negative) than against *S. aureus* (Gram-positive), as determined through surface testing and SEM imaging of inoculated surfaces. Previous research has suggested that CHX is most effective against Gram-positive bacteria; as such, more research will need to be undertaken to understand why the converse is true for the CHX epoxy resin we have developed.[37] CHX epoxy resin was also highly efficacious against pathogenic *C. albicans*, indicating that the broad-spectrum biocidal activity of CHX is not diminished by suspension in epoxy resin. Lastly, the CHX epoxy resin was also highly effective against prolific biofilm former, *P. aeruginosa*. The exhibited antimicrobial efficacy was repeatable and significant, indicating that this technology could be used in real-world settings as a potent biocide. This indicates that the epoxy resin can be applied to a variety of pre-existing surfaces without affecting the biocidal action of the suspended CHX, due to the flexibility afforded by the ease of application and curing.

With the importance of antimicrobial resistance well established, and the knowledge that resistance to chlorhexidine has been observed in clinical settings, it is important to determine if the chlorhexidine epoxy resin we have developed will continue to exert its antimicrobial efficacy even if resistance arises. As such, we tested the material against a strain of *E. coli* that was engineered to have a significantly elevated MIC against chlorhexidine. The MIC of this evolved strain was 28.7 μg/mL; this is significantly greater than the MIC value of 0.9 μg/mL that wild-type *E. coli* possesses.[38] Furthermore, this is a greater MIC value than is considered the threshold for chlorhexidine resistance, which is typically cited as an MIC greater than 4 μg/mL.[39] Despite this, the chlorhexidine paint was still highly effective, with no viable bacteria being recovered from the paint surface after inoculation and incubation. This is a highly

positive development, and suggests that the material could be used to provide low-cost antimicrobial efficacy to pre-existing surfaces, and will continue to do so when colonised by chlorhexidine-resistant strains. This ensures that multidrug-resistant strains of pathogenic microorganisms will be eliminated from surfaces painted with the chlorhexidine epoxy resin, preventing the transmission of these dangerous pathogenic species from abiotic surfaces to the most vulnerable.

In addition to this, it is of the utmost importance that the antimicrobial efficacy of the material is durable; this was assessed by determining the efficacy of the chlorhexidine epoxy resin after 14 days immersion in sodium chloride solution. This environment places the chlorhexidine epoxy resin under stress conditions, as the diffusion of water into the polymer leads to the irreversible chemical degradation of the epoxy resin in a process known as plasticisation. As such, it is not recommended to expose epoxy resin materials to water for extended periods of time.[40,41] It was found that the material continued to exert excellent antimicrobial efficacy against *E. coli*, demonstrating that the antimicrobial efficacy is durable, indicating that the chlorhexidine epoxy resin would remain biocidal for extended application times. Previous studies that have incorporated chlorhexidine into epoxy resin materials for antimicrobial coatings have relied on the principle of diffusion of chlorhexidine out of the epoxy resin in order to exert antimicrobial efficacy.[42,43,44] By contrast, we have developed a paintable material in which the CHX remains stably incorporated into the epoxy resin, without leaching of the biocide from the painted layer, as demonstrated by the retained antimicrobial efficacy and HPLC. This indicates that the material is suitable for long-term applications, without the need to reapply the painted layer.

We have shown that the chlorhexidine retains its antimicrobial efficacy when mixed into the epoxy resin base, and stored at room temperature for three months. This is of the utmost importance, as a product would be kept in shelf storage conditions when it is commercially available, until purchased by the consumer. As many antimicrobial and biocidal paints and coatings have been found to be unstable under extended storage conditions[45,46,47,48] the evidence of the storage stability of chlorhexidine epoxy resin, and the retention of its well-established antimicrobial efficacy under these extended storage conditions, has excellent implications for the implementation of this material in real-world settings. As well, further suggests that the material could successfully be made available commercially for purchase by the consumer. We have also shown that the chlorhexidine epoxy resin is highly effective against repeat exposures to pathogenic microorganisms without sterilisation in between inoculations. This is important, as previous studies have shown that surfaces can continue to be contaminated by a variety of pathogenic microorganisms even after cleaning has taken place[49]. Furthermore, many abiotic surfaces do not undergo regular deep cleaning, leading to continual contamination of the surface environment[50] As such, this shows that the paint will be effective in a real-world setting, being capable of eliminating pathogenic microorganisms from the surface environment when enhanced hygiene measures are not being implemented.

To conclude, we show the ability to suspend CHX in epoxy resin, and that the distribution of CHX across the exposed, painted layer of this material is uniform. The addition of CHX was found to have little effect on the water contact angle of painted surfaces, and to have a minimal effect on the optical transparency of the paint upon curing. The material also had bonding strength and scratch resistance comparable with control samples. The resulting epoxy resin was found to possess a significant, reproducible antimicrobial effect against Gram-positive and Gram-negative bacteria, and against pathogenic fungi. It was also found that the paint continues to exert its antimicrobial efficacy when challenged with bacteria evolved to exhibit resistance

to chlorhexidine. Chlorhexidine epoxy resin was found to be highly effective against pathogenic microorganisms when challenged with repeat inoculations without sterilisation, and that the paint can be stored for extended periods without a loss of biocidal activity. It was also found that the antimicrobial efficacy of the paint was durable, and is suitable for long-term applications without sacrificing its biocidal activity. We believe that these developments could be used by companies and individuals to provide highly effective, but affordable, antimicrobial surfaces, to eliminate the role of the contamination of abiotic surfaces in the transmission of infection, with a broad range of applications. Following on from this work, we shall be investigating the possibility of aerosolising chlorhexidine epoxy resin, and shall also determine what concentration of CHX is required to confer antimicrobial efficacy to epoxy resin as a minimum. These steps will reduce the costs of synthesis, reducing costs to the consumer. We shall also be investigating the possibility of impregnating a water-based epoxy resin with CHX. Epoxy resin materials that do not contain an organic solvent base are more environmentally friendly, and altering the base material will be of significant commercial benefit.

Acknowledgments

This work was funded by the Royal Academy of Engineering Industrial Fellowship. D.S. is funded by the Engineering and Physical Sciences Research Council. We thank Indestructible Paint Ltd. for providing all epoxy resin used in this study. The Host and Pathogen Interactions Group of the University of Birmingham kindly provided *Candida albicans* SC5314 for use in this study.

References

1. Hayden, M. K., Blom, D. W., Lyle, E. A., Moore, C. G. & Weinstein, R. A. Risk of Hand or Glove Contamination After Contact With Patients Colonized With Vancomycin-Resistant *Enterococcus* or the Colonized Patients' Environment. *Infect Control Hosp Epidemiol* **29**, 149–154 (2008).

2. Otter, J. A., Yezli, S., Salkeld, J. A. G. & French, G. L. Evidence that contaminated surfaces contribute to the transmission of hospital pathogens and an overview of strategies to address contaminated surfaces in hospital settings. Am J Infect Control 41, S6 (2013).

3. Stiefel, U. *et al.* Contamination of Hands with Methicillin-Resistant Staphylococcus aureus after Contact with Environmental Surfaces and after Contact with the Skin of Colonized Patients. *Infect Control Hosp Epidemiol* **32**, 185–187 (2011).

4. Aydogdu, M. O. *et al.* Surface interactions and viability of coronaviruses: Surface interactions and viability of coronaviruses. *Journal of the Royal Society Interface* vol. 18 Preprint at https://doi.org/10.1098/rsif.2020.0798 (2021).

5. Zou, L. *et al.* SARS-CoV-2 Viral Load in Upper Respiratory Specimens of Infected Patients. *New England Journal of Medicine* **382**, 1177–1179 (2020).

6. Wilks, S. A., Michels, H. & Keevil, C. W. The survival of Escherichia coli O157 on a range of metal surfaces. *Int J Food Microbiol* **105**, 445–454 (2005).

7. Otter, J. A. & French, G. L. Survival of nosocomial bacteria and spores on surfaces and inactivation by hydrogen peroxide vapor. *J Clin Microbiol* **47**, 205–207 (2009).

8. Neely, A. N. A Survey of Gram-Negative Bacterial Survival on Hospital Fabrics and Plastics. Journal of Burn Care & Rehabilitation 21, 523–527 (2000).

9. Wendt, C., Dietze, B., Dietz, E., Ru¨den, H. & Ru¨den, R. Survival of Acinetobacter Baumannii on Dry Surfaces. JOURNAL OF CLINICAL MICROBIOLOGY vol. 35 (1997).

10. Jawad, A., Seifert, H., Snelling, A. M., Heritage, J. & Hawkey, P. M. *Survival of Acinetobacter Baumannii on Dry Surfaces: Comparison of Outbreak and Sporadic Isolates*. *JOURNAL OF CLINICAL MICROBIOLOGY* vol. 36 (1998).

11. Chen, J. C. et al. Survival of bacterial strains on wood (Quercus petraea) compared to polycarbonate, aluminum and stainless steel. Antibiotics 9, 1–9 (2020).

12. Traore, O., Springthorpe, V. S. & Sattar, S. A. A quantitative study of the survival of two species of Candida on porous and non-porous environmental surfaces and hands. J Appl Microbiol 92, 549–555 (2002).

13. Neely, A. N. & Orloff, M. M. Survival of some medically important fungi on hospital fabrics and plastics. J Clin Microbiol 39, 3360–3361 (2001).

14. Rozman, U., Pušnik, M., Kmetec, S., Duh, D. & Turk, S. Š. Reduced susceptibility and increased resistance of bacteria against disinfectants: A systematic review. Microorganisms vol. 9 Preprint at https://doi.org/10.3390/microorganisms9122550 (2021).

15. Turner, N. A. et al. Methicillin-resistant Staphylococcus aureus: an overview of basic and clinical research. Nature Reviews Microbiology vol. 17 203–218 Preprint at https://doi.org/10.1038/s41579-018-0147-4 (2019).

16. Abbood, H. M., Hijazi, K. & Gould, I. M. Chlorhexidine Resistance or Cross-Resistance, That Is the Question. Antibiotics vol. 12.

17. Kampf, G. Acquired resistance to chlorhexidine – is it time to establish an 'antiseptic stewardship' initiative? Journal of Hospital Infection vol. 94 213–227.

18. Dang, X., Yu, Z., Wang, X., Du, Y. & Wang, C. Sustainable one-pot synthesis of novel soluble cellulose-based nonionic biopolymers for natural antimicrobial materials. Chemical Engineering Journal 468, (2023).

19. Cassidy, S. S. et al. Antimicrobial surfaces: A need for stewardship? PLoS Pathog 16, (2020).

20. Kumar, A., Vemula, P. K., Ajayan, P. M. & John, G. Silver-nanoparticle-embedded antimicrobial paints based on vegetable oil. Nat Mater 7, 236–241 (2008).

21. Montero, D. A. et al. Antimicrobial properties of a novel copper-based composite coating with potential for use in healthcare facilities. Antimicrob Resist Infect Control 8, (2019).

22. Querido, M. M. et al. Self-disinfecting paints with the natural antimicrobial substances: Colophony and curcumin. Antibiotics 10, (2021).

23. Hoque, J. et al. Broad spectrum antibacterial and antifungal polymeric paint materials: Synthesis, structure-activity relationship, and membrane-active mode of action. ACS Appl Mater Interfaces 7, 1804–1815 (2015).

24. Querido, M. M. et al. Development and In Vitro Validation of Antibacterial Paints Containing Chloroxylenol and Terpineol. Toxics 10, (2022).

25. Biswas, D., Tiwari, M. & Tiwari, V. Molecular mechanism of antimicrobial activity of chlorhexidine against carbapenemresistant Acinetobacter baumannii. PLoS One 14, (2019).

26. Cheung, H. Y. et al. Differential actions of chlorhexidine on the cell wall of bacillus subtilis and escherichia coli. PLoS One 7, (2012).

27. Cieplik, F. et al. Resistance toward chlorhexidine in oral bacteria-is there cause for concern? Frontiers in Microbiology vol. 10.

28. Bryant, J. A. et al. Developing Novel Biointerfaces: Using Chlorhexidine Surface Attachment as a Method for Creating Anti-Fungal Surfaces. Global Challenges 6, 2100138 (2022).

29. Watson, R. et al. Efficacy of antimicrobial and anti-viral coated air filters to prevent the spread of airborne pathogens. Sci Rep 12, (2022).

30. Watson, R. et al. Development of biocide coated polymers and their antimicrobial efficacy. Nano Select (2023).

31. Judd, A. M., Scurr, D. J., Heylings, J. R., Wan, K. W. & Moss, G. P. Distribution and visualisation of chlorhexidine within the skin using ToF-SIMS: A potential platform for the design of more efficacious skin antiseptic formulations. Pharm Res 30, 1896–1905 (2013).

32. Lee, JLS et al Organic Depth Profiling of a Nanostructured Delta Layer Reference Material Using Large Argon Cluster Ions, Analytical Chemistry, 2010, 82, 98-105.

33. International Organisation of Standardization (2007)

34. Rzycki, M., Drabik, D., Szostak-Paluch, K., Hanus-Lorenz, B. & Kraszewski, S. Unraveling the mechanism of octenidine and chlorhexidine on membranes: Does electrostatics matter? Biophys J 120, 3392–3408 (2021).

35. Barrett-Bee, K., Newboult, L. & Edwards, S. The membrane destabilising action of the antibacterial agent chlorhexidine. FEMS Microbiol Lett 119, 249–253 (1994).

36. Gao, W. et al. Preparation of antistatic epoxy resin coatings based on double comb-like quaternary ammonium salt polymers. RSC Adv 10, 43523–43532 (2020).

37. Kampf, G. & Kramer, A. Epidemiologic background of hand hygiene and evaluation of the most important agents for scrubs and rubs. Clinical Microbiology Reviews vol. 17 863–893

38. Leshem, T., Gilron, S., Azrad, M. & Peretz, A. Characterization of reduced susceptibility to chlorhexidine among Gram-negative bacteria. Microbes Infect 24, (2022).

39. Horner, C., Mawer, D. & Wilcox, M. Reduced susceptibility to chlorhexidine in staphylococci: Is it increasing and does it matter? Journal of Antimicrobial Chemotherapy vol. 67 2547–2559

40. Kojnoková, T., Nový, F. & Markovičová, L. The Study of Chemical and Thermal Influences of the Environment on the Degradation of Mechanical Properties of Carbon Composite with Epoxy Resin. Polymers (Basel) 14, (2022).

41. Le Guen-Geffroy, A., Le Gac, P. Y., Habert, B. & Davies, P. Physical ageing of epoxy in a wet environment: Coupling between plasticization and physical ageing. Polym Degrad Stab 168, (2019).

42. Riool, M. et al. A chlorhexidine-releasing epoxy-based coating on titanium implants prevents Staphylococcus aureus experimental biomaterial-associated infection. Eur Cell Mater 33, 143–157 (2017).

43. Alves, D., Borges, P., Grainha, T., Rodrigues, C. F. & Pereira, M. O. Tailoring the immobilization and release of chlorhexidine using dopamine chemistry to fight infections associated to orthopedic devices. Materials Science and Engineering C 120, (2021).

44. Thajai, N. et al. Antimicrobial thermoplastic starch reactive blend with chlorhexidine gluconate and epoxy resin. Carbohydr Polym 301, (2023).

45. Fan, D. et al. Functional insights to the development of bioactive material for combating bacterial infections. Frontiers in Bioengineering and Biotechnology vol. 11

46. La, D. D. et al. Effects of antibacterial ZnO nanoparticles on the performance of a chitosan/gum arabic edible coating for post-harvest banana preservation. Prog Org Coat 151, (2021).

47. Bajpai, P. The Control of Microbiological Problems∗∗Some excerpts taken from Bajpai P (2012). Biotechnology for Pulp and Paper Processing with kind permission from Springer Science1Business Media. in Pulp and Paper Industry 103–195 (Elsevier, 2015).

48. Wang, H. et al. Research Progress on Antibacterial Coatings for Preventing Implant-Related Infection in Fractures: A Literature Review. Coatings vol. 12

49. Tuladhar, E. *et al.* Residual viral and bacterial contamination of surfaces after cleaning and disinfection. *Appl Environ Microbiol* **78**, 7769–7775 (2012).

50. Wißmann, J. E. *et al.* Persistence of pathogens on inanimate surfaces: A narrative review. *Microorganisms* vol. 9 1–37

Conclusions of chapter 3

This work highlights that the CHX epoxy resin coatings are a highly effective at eliminating/reducing many clinically relevant pathogens from their surface. This paper also concludes that the CHX is well distributed throughout the coating as well as displaying no significant change in properties such as hydrophobicity, scratch resistance, optical transparency or adherence. These CHX epoxy resin coatings also demonstrate good durability in PBS with no leaching of the antimicrobial from the surface and good stability of CHX epoxy reagents for up to 3 months. Further, this paper highlights that these surfaces may exploit a completely different antimicrobial mode of action as CHX is immobilised and does not leach out of the epoxy resin. Further, no CHX-resistant *E. coli* was recovered from these surfaces after ~18 hours of contact time. Unlike free-in-solution CHX, which requires the CHX to diffuse into the bacterial cell to cause toxicity, these CHX surfaces may interact with bacteria at their surface, causing disruptions to their cell wall and membrane integrity, although this requires further investigation.

The findings from this work highlight the effectiveness of these surfaces as a potential strategy to reduce environmental pathogens and therefore disease transmission as a result of contact with contaminated, high-touch surfaces, such as hospitals, airports, public toilets, retail complexes and on public transport.

Chapter 4: Stability, durability and application of antimicrobial epoxy resin

Chapter 4 is a continuation from chapter 3 and discusses the further development of the CHX epoxy resin coatings. This chapter shows a research paper that was submitted to Materials Advances.The work investigates the long-term efficacy of CHX epoxy resin by evaluating their antimicrobial efficacy against *E. coli* following both natural and artificially accelerated aging processes. This chapter also explores the CHX epoxy resin's antibiofilm efficacy and durability in marine environments. Finally, the paper discusses the cytotoxicity profile of the antimicrobial coatings against mammalian cells and their effectivity when applied to real-life surfaces within the community.

My contributions to this paper include method development and data collection, analysis and presentation for all experimental work, including long-term antimicrobial efficacy, antibiofilm activity (including SEM imaging), investigations of stability in seawater (including ToF-SIMS depth profile of salt residues), real life efficacy of the epoxy resin coatings and mammalian cytotoxicity. Further, I was responsible for writing the manuscript and figure curation.

Stability, Durability and Application of Antimicrobial Epoxy Resin

Madeline Berrow [a], Li Lu [a], Christopher Parmenter [b], Eva Simpson [b], Jean Dubern [c], David J. Scurr [a], Simon Greenway [d], Violaine Mendez [d], Brian Norton [d], Felicity de Cogan [a]

[a] School of Pharmacy, University of Nottingham, University Park, Nottingham, NG7 2RD, United Kingdom
[b] Nanoscale and Microscale Research Centre, University of Nottingham, University Park, Nottingham, NG7 2RD, United Kingdom
[c] School of Life Sciences, University of Nottingham, University Park, Nottingham, NG7 2RD, United Kingdom
[d] Indestructible Paint Ltd, 16-25 Pentos Drive, Birmingham, United Kingdom

Abstract

Microbially-contaminated surfaces play a significant role in the transmission of disease which can lead to epidemic or even pandemic outbreaks. Developing antimicrobial materials that eliminate microbes on surfaces will reduce the spread of pathogenic species. This is particularly important in hospitals, where many patients are immunocompromised and the spread of virulent or antimicrobial-resistant superbugs is problematic. This study determined that CHX epoxy resin coatings exhibit antimicrobial efficacy for at least 12 months following curing. These coatings also demonstrate antibiofilm properties by reducing the growth of *Pseudomonas aeruginosa* biofilms. Cryogenic scanning electron microscopy allowed visualisation of the reduction of film communities on the antimicrobial coatings. CHX epoxy resin, whilst remaining antimicrobial, exhibits reduced potency following immersion in seawater for up to 6 months. HPLC analysis detects no CHX leaching from the epoxy resin in seawater and ToF-SIMS confirms that the reduction in antimicrobial efficacy is attributable to salt build-up on the CHX paint surface, preventing contact with microbes. Real-life applications of these coatings displayed reductions in environmental microbial populations, and no cytotoxicity was exhibited by these surfaces ensuring that they are safe to touch.

Keywords: Antimicrobial; Biocidal, Chlorhexidine, Epoxy resin; Paint; Polymer.

1.0. Introduction

Many disease-causing microorganisms reside upon inanimate objects and environmental surfaces, with high-touch surfaces such as handrails, door handles, light switches and countertops contributing significantly to the spread of disease (1). Methicillin-resistant *Staphylococcus aureus* (MRSA), vancomycin-resistant *Enterococci* (VRE), *Enterobacteriaceae, Pseudomonas aeruginosa, Clostridium difficile, Acinetobacter baumannii, Stenotrophomonas maltophilia, Burkholderia cepacia, Candida spp.,* Norovirus and Coronavirus are frequently found on healthcare-associated equipment and environmental surfaces which significantly contribute to infection risk (**2**). Microorganisms that colonise environmental surfaces also contribute to the transmission of community-associated infections. A study by Meadow *et al.,* 2014 conducted 16S rRNA sequencing on environmental swabs from classroom desktops, chairs, floors and walls. They detected *Lactobacillus, Corynebacterium, Salmonella, Staphylococcus, Streptococcus, Cyanobacteria, Sphingomonas, Alicyclobacillus* and *Brevundimonas spp.*, amongst others, which were traced to human sources including the skin, mouth, gut, vagina and urinary tract, as well as environmental sources such as the soil, pond water and saline aquatic locations (3). Pathogenic microorganisms that reside on environmental surfaces are a key factor in the transmission of disease within the community, particularly in regions with high footfall, such as schools, public toilets, retail complexes, airports and on public transport.

Chemical disinfection of surfaces is a global strategy to eliminate environmental pathogens for infection prevention. Many compounds are currently licensed for chemical disinfection purposes, including alcohol-based products (ethyl or isopropyl alcohol), hydrogen peroxide, hypochlorite solutions, peracetic acid, iodophors and quaternary ammonium, as well as no-touch technologies, such as vaporised hydrogen peroxide or ultraviolet radiation treatment (4, 5). Further, effective microbial elimination with chemical sanitisers is highly limited by cursory manual cleaning of surfaces, with to 50-60% of surfaces that require regular disinfection not receiving treatment (4). Studies have also concluded that manual disinfectant preparation can result in over-dilution of chemicals, lowering their concentration and antimicrobial efficacy, whilst promoting biocide resistance (4). It has also been suggested that detergent wipes demonstrate inconsistencies with microbial elimination and actually increase the transfer of pathogens between surfaces (4). In addition, the material of the surface can significantly affect the efficacy of traditional chemical disinfectants (4). Health complications, including eye and skin irritation, respiratory problems and asthma, headaches, alcohol poisoning, neurologic problems, dermal burns and skin may arise from prolonged exposure to UV and chemical disinfectants, contributing the many issues with traditional surface sterilisation methods (6, 7, 8, 9).

Environmental microorganisms also contribute significant to marine biofouling and biocorrosion. Marine biofilms are ubiquitous within marine environments. These complex microbial communities attach and form films on artificial objects within the sea, such as ship hulls, submarines and offshore oil platforms. Over time, these marine biofilm communities can damage surfaces causing the erosion/corrosion of materials. Every year, marine biofilms cost maritime industries including oil and gas, aquaculture, desalination and transport, trillions of US dollars in economic loss (10). Current methods to eradicate marine biofilms from seawater-immersed surfaces include physical disruption (mechanical cleaning, ultrasound), thermal treatments (heal, UV, irradiation) or chemical/biochemical treatments (biocides, enzymes, alkaline cleaners), however are significantly hindered by high cost, poor efficacy, compatibility and impact on the environment (11).

Antimicrobial surfaces are interfaces which prevent the survival of microorganisms to prevent the transmission of disease (12). Antimicrobial surfaces are either microbial repellents, which work by preventing cell attachment or growth through superhydrophobic or superhydrophilic surface modifications, or microbiocidal, which functions by killing the microbes that make contact with the surface, usually by incorporation of metal nanoparticles, cationic polymers or biocidal drugs (9, 12). Efficacy of early antimicrobial surfaces relied upon the leaching of encapsulated biocides (e.g. Triclosan); however, this led to bacterial biocide resistance and environmental pollution (12). Despite this, modern antimicrobial surfaces are less harmful to the environment and provide long-term efficacy unlike chemical biocide disinfection strategies (12). In most recent years, surfaces coated or embedded with silver nanoparticles have been developed which have showed potent antibacterial and antiviral properties (13, 14). Silver cations cause an osmotic imbalance and metabolite loss by creating punctures in microbial cell walls (15) making them an excellent candidate for antimicrobial medical materials such a wound dressings (16). Copper nanoparticles are also used for producing antimicrobial surfaces which interfere with the microbial cell wall and cell membrane integrity, in addition to generating reactive oxygen species, contributing to their potent antimicrobial activity (17, 18). However, modern antimicrobial surface coatings are limited by their need for production in expert factories or laboratories using specialised equipment, reagents and personnel, raising production costs and consequently retail costs, lowering their widescale availability (19, 20). There is a demand for alternative materials such as easy-application antimicrobial coatings that can be applied to pre-existing surfaces, lowering their production and retail costs and increasing widespread accessibility for public use.

This study explores the development of our chlorhexidine digluconate (CHX)-containing industrial epoxy resin coating when applied and cured onto a pre-existing surface. CHX is a potent antimicrobial agent that exhibits broad-spectrum microbiocidal activity by increasing cell membrane permeability and metabolite leakage. This occurs due to permeation through the cell membrane facilitated by electrostatic attractions between the cationic CHX and phosphate- and sulphate-containing cell surface structures. CHX binds to deoxyribonucleic acid (DNA), ribonucleic acid (RNA), adenosine-trisphosphate (ATP) and other phosphorylated compounds resulting in cytoplasmic coagulation and cell death (21, 22). Further, CHX elevates the production of reactive oxygen species which contribute to cell membrane leakiness, lipid peroxidation and microbial cell death (23, 24, 25).

Previous work demonstrated that these CHX epoxy resin coatings exhibit potent antimicrobial activity against pathogenic fungi, gram-positive and gram negative bacteria, and bacteria evolved to exhibit CHX resistance. CHX distribution throughout the epoxy resin was uniform, along with no significantly altered water contact angle, scratch resistance, adhesion strength or optical transparency compared to control epoxy resin. Further, the antimicrobial coating demonstrated highly effective microbial elimination following repeat inoculations without sterilisation, high durability and suitability for long-term storage (26). This study progresses on the development of our CHX epoxy resin coatings by exploring the long-term stability of the antimicrobial surface over 12 months, as well as artificially accelerated aging using UV to degrade these surfaces. Further, we demonstrate the antimicrobial efficacy of these CHX epoxy resin coatings on real-life, inanimate objects/surfaces to explore how they could be used within the community to reduce transmission of disease. Finally, this work explores the antibiofilm efficacy of the CHX paint against *Pseudomonas aeruginosa* biofilms and its stability and durability following short- and long-term immersion in seawater, to determine whether these antimicrobial coatings could be used to tackle the ongoing challenge with marine biofouling.

2.0. Materials and methods

2.1. Materials

Epoxy resin raw materials were provided by Indestructible Paint Ltd. *Escherichia coli* ATCC25922 was purchased from the American Type Culture Collection. Seawater was acquired from Praia da Mina beach in Pataias, Portugal, Largs Bay Beach in Largs, United Kingdom and Southsea Beach, Portsmouth, UK. Chlorhexidine digluconate (20% *w/v*, aqueous solution), Luria-Bertoni (LB) broth and agar, sodium phosphate monobasic monohydrate (molecular weight 119.98 g/mol) and phosphoric acid (85%) were purchased from Sigma Aldrich, Dorset, UK. HPLC grade acetonitrile, triethylamine (99%), Oxoid blood agar base No.2 and syringe filters (0.22 μM, 33 mm diameter) were purchased from Fisher Scientific, Loughborough, UK. Defibrinated horse blood was acquired from Scientific Laboratory Supplies, Nottingham, UK. Flat-bottomed, transparent 96-well and black bottomed, black-sided 96-well cell culture plates were purchased from Corning, New York, US. HPLC 1260 Infinity II Liquid Chromatography System was acquired from Agilent, Santa Clara, US. 2 mL amber robotic 9 mm thread vials and 9 mm screw caps with white silicon/red polytetrafluoroethylene septa were acquired from Chromatography Direct, Wellingborough, UK. An ACE HPLC column (C_{18} dimension, 150 x 2.1 mm, 3 μM) was purchased from Hichrom Limited, Reading, UK. SEM CrossBeam 550 was acquired from Oberkochen, Germany.

2.2. Epoxy resin preparation

All epoxy clear gloss resin (control) and antimicrobial CHX epoxy resin samples were prepared on 1 cm x 1 cm glass tiles and prepared to a 2% *w/v* concentration as described by Berrow *et al*., 2025 (26) unless otherwise stated.

2.3. Artificially accelerated aging of epoxy resin coatings

Prepared epoxy resin samples (control and CHX-treated) were ultraviolet (UV) treated for 1, 2, 3 or 4 hours using a CUREbox™ UV lamp that emits a wavelength of 365-405 nm and an LED power 36 W. Another set of samples were UV treated with multiple 4 hour sessions cumulating to 24 hours. All samples were analysed for antimicrobial efficacy following UV treatments against *E. coli* ATCC25922 using methodology described by Berrow *et al*., 2025 (26)**.** 3 biological and 3 technical repeats were conducted for each treatment.

2.4. 12-Month stability of antimicrobial efficacy

Control and CHX-treated epoxy resin samples were stored in a transparent, plastic box, exposed to sunlight for 12 months after curing and antimicrobial efficacy against *E. coli* ATCC25922 was tested following the protocol outlined by Berrow *et al*., 2025 (26). Separate samples were prepared and antimicrobial efficacy tested as previously described every month for 12 months to determine the long-term potency of the coatings.

2.5. Antibiofilm efficacy

Briefly, the plasmid pMRE140 harbouring mTagBFP2 fluorescent protein (Supplementary information, Figure 1) was introduced into *P. aeruginosa* PAO1-washington subline (Washington collection) by electroporation as described by Schlechter *et al*., 2018 (27). Resulting transformants were selected by plating on LB agar supplemented with gentamicin (20ug/ml) and fluorescence output was tested under a confocal laser scanning microscope (LSM700, Zeiss).

Under sterile conditions, 50 µL of uncured CHX and control epoxy resin was transferred into separate wells of a transparent, flat-bottomed 96-well cell culture plate. The plate was tilted to spread out the epoxy resin on all surfaces of the well before being heat curing at 60°C for 90 minutes. *P. aeruginosa* PA01 mTagBFP2 was cultured in LB broth supplemented with 20 mg/mL gentamicin to select for bacteria containing the pMRE140 plasmid that encodes both a blue fluorescent protein and a gentamicin acetyltransferase protein (conferring gentamicin resistance), at 37°C, 180 rpm for 18 hours. Bacterial cultures were adjusted to $1x10^9$ CFU/mL and 150 µL was pipetted into each well (CHX and control treatments). The plate was statically incubated at 37°C for 24 hours to allow biofilm to develop. Following incubation, the culture was discarded and biofilms gently washed with PBS, removing planktonic bacteria. Fluorescence (λ_{ex}: 399 nm, λ_{em}: 454 nm) was measured to quantify the biofilm biomass.

2.6. Visualisation of biofilms using cryo-scanning electron microscopy (Cryo-SEM)

Glass tiles treated with cured CHX or control epoxy resin were inoculated with 50 µL of *P. aeruginosa* PA01 mTagBFP2 adjusted to $1x10^9$ CFU/mL and subject to static incubation at 37°C for 24 hours to allow biofilm to form. Following incubation, painted tiles were gently washed in sterile deionised water to remove planktonic bacteria.

Biofilm samples were transferred into a PP3010T Cryo Sample Preparation System (Quorum, East Sussex, England) where they experienced nitrogen slush freezing. Cryogenically prepared samples were then transferred to the preparation chamber of the scanning electron microscope, which was maintained under high vacuum at a temperature of -150°C to prevent sample thawing. Biofilms received a Platinum coating treatment (10 mA, 60 seconds) to increase the conductivity of the samples and SEM observations were performed with an operating voltage of 2 kV, approximate working distance of 5.0 – 6.1 mm and a secondary electrons secondary ions (SESI) detector.

2.7. Durability of antimicrobial efficacy in seawater

Initially, the limit of detection (LOD) and the limit of quantification (LOQ) for the HPLC method used was confirmed by analysing the concentrations of a series of standard solutions that were known to be 1.0, 0.8, 0.6, 0.4, 0.2, 0.1, 0.01 and 0.001 mg/mL CHX diluted in deionised water. Regression analysis was conducted in Microsoft Excel and the LOD and LOQ were calculated using the standard deviation of the y-intercept and the slope of the curve. The calculations used were:

$$\text{LOD} = \frac{3.3 \times \text{Standard Deviation of y} - \text{intercept}}{\text{Slope of the curve}}$$

$$\text{LOQ} = \frac{10 \times \text{Standard Deviation of y} - \text{intercept}}{\text{Slope of the curve}}$$

The durability of the CHX epoxy resin antimicrobial efficacy following immersion in seawater was investigated by conducting leaching studies using seawater collected from various geographical locations. Prepared coatings (as previously described) were immersed in 10 mL seawater for 14 days under room temperature and dark conditions. Following 14 days immersion, 1 mL leachate was sampled, centrifuged (10,000 rpm, 5 mins) to remove large debris, filter sterilised (0.22 μM) to eliminate microscopic debris and microorganisms before conducting quantification of CHX using High Performance Liquid Chromatography (HPLC). 200 μL leachate was also aliquoted into a flat-bottomed, transparent 96-well cell culture plates for quantification of CHX in the leachate using absorbance (280 nm) following the method outlined by Berrow *et al*., 2025 (26).

To ensure that the CHX didn't leach out of the epoxy resin, the antimicrobial efficacy of the leachate was also determined by quantifying bacterial colonies that survived in the seawater using a method outlined by Berrow *et al*., 2025 (26). The antimicrobial efficacy of the CHX epoxy resin coatings were analysed to confirm whether the antimicrobial was retained in the coating or had leached out. Previously immersed epoxy resin samples (CHX and control) were washed in deionised water to remove salt build-up on coatings before following the methodology described by Berrow *et al*., 2025 (26) to test efficacy against *E. coli*.

Long-term leaching studies were also conducted on the CHX and control epoxy resin samples to determine whether the coating demonstrated prolonged durability in marine environments. Samples were immersed in 5 mL seawater for either 1, 2, 3, 4, 5 or 6 months before the leachate was sampled for CHX quantification by HPLC and absorbance. Antimicrobial efficacy of the leachate and immersed coating were also analysed to determine whether CHX was retained in the epoxy resin or leached out into the seawater (methods as previously described).

To determine the effect of seawater motion on the durability of these coatings in marine environments, CHX and control epoxy resin-painted tiles were immersed in 10 mL seawater for 2 weeks on an orbital shaker (60 rpm), to simulate tidal movements. Following the immersion period, absorbance, HPLC and antimicrobial efficacy experiments were conducted on the seawater leachate, whilst the post-leaching antimicrobial efficacy of the epoxy resin surfaces was analysed following the methodology outlined above in section 2.7.

To understand whether the salt residue on the CHX epoxy resin samples following 2 week immersion in seawater was impacting the antimicrobial efficacy of the coatings, rather than the leaching of the antimicrobial, post-leached CHX paint samples were immersed in 10 mL of deionised water and placed on an orbital shaker (60 rpm) for 24 hours to dissolve salts. CHX coatings were tested for their antimicrobial efficacy against *E. coli* following the methodology outline above. The control epoxy resin coatings were treated and tested the same as the CHX coatings.

2.8. Time of flight- secondary ion mass spectrometry of post-leaching salt residue

Time of flight- secondary ion mass spectrometry (ToF-SIMS) was deployed to depth profile through the residue on the surface of CHX and control epoxy resin samples following durability of antimicrobial efficacy testing (section 2.7), to determine whether the salts present in the seawater were building up on the coating interface. Analysis was acquired using a ToF V (IONTOF GmbH, Germany) instrument. Depth profile analysis was performed by dual-beam mode. A 300 x 300 μm^2 crater was formed by using a 10 keV Ar_{1600}^+ gas cluster ion beam (GCIB) with a 10 nA current and total ion dose of 7.9 x 10^{11} ions/cm^2. A 25 keV Bi_3^+ liquid metal ion gun (LMIG), with approximately 0.4 pA current in spectrometry mode was deployed to analyse a 200 x 200 μm^2 patch with a random raster mode and a 128 x 128pixel density. A noninterlaced depth profile measurement was conducted with 3 sputter frames followed by 1 analysis frame per cycle, with a 0.5 second pause time in between. A low-energy (21 eV electron flood gun was used for charge compensation, and the surface potential was set as 90.3 V for negative mode.) Data was acquired in only negative polarity, with a 200 µs cycle time of ToF analyser (mass range: *m/z* 0 – 1500). The ion used to characterise CHX was the CHX fragment ion $C_7H_4N_2Cl^-$ as previously used by Berrow et al., 2025 (26). The $C_9H_9O^-$ ion was also used to characterise the epoxy resin as described by Berrow et al., 2015 (26). Further, the ions used to analyse seawater salts were Cl^-, SO_3^-, $FeSO_4H^-$, $FeCl_3^-$, SO_4H^-, $NaCl_2^-$ and K_2ClO^-.

2.9. Mammalian cytotoxicity of CHX epoxy resin

Approximately 1.5 x 1.5 cm steal squares were coated in CHX epoxy resin (preparation as described in section 2.2.) and sterilised by submerging in isopropanol (70%) followed by sterile deionised water. Murine 3T3 fibroblast cells were cultured in cell culture media consisting of DMEM supplemented with 10% newborn calf serum, 4 mM GlutaMAX™, 100 IU/mL penicillin, 100 µg/mL streptomycin and 20 mM HEPES buffer solution. Coated squares were placed in a transparent 12-well plate and incubated (37°C, 5% CO_2) for 20 minutes to prevent temperature shock when adding cells. Following incubation, 4,000 cells were seeded onto each coating surface. Seeded coatings were incubated for 30 mins to allow cell attachment to the coating before adding 2 mL cell culture media to each well to prevent desiccation. Plates were incubated for 24 hours.

Following incubation, cell culture media was removed and coatings were washed with PBS (with Mg^{2+}/Ca^{2+}). 750 µL Alamar Blue solution was added to the cells and incubated for 2 hours before measuring absorbance at 570 nm. Absorbance was normalised to the number of cells per well.

2.10. Antimicrobial efficacy on real life coated surfaces

To determine whether the potent antimicrobial efficacy of CHX epoxy resin coatings demonstrated in the lab was comparable to real-life application, 8 locations were selected to receive coatings. Prior to treatment, all locations were swabbed and samples microbes were cultured onto horse blood agar. Plates were sealed with parafilm and incubated at 37°C for 48 hours to ensure culture of any slow-growing species. In the same locations, a 2 separate 2 cm^2 patches were marked, 1 painted with CHX epoxy resin and the other the control epoxy resin.

Epoxy resin coatings were time cured and swabs were taken 1 month after treatments were applied. Microbes swabbed from locations were cultured on horse blood agar and CFU's were counted after 48 hours incubation at 37°C to determine percentage reduction in microbial growth.

2.11. Statistical analysis

Statistical analysis was conducted using IBM SPSS Statistics version 29.0.1.0 (171). Datasets were analysed to determine whether they were normally distributed using the Shapiro-Wilk test. Log transformations were attempted if normal distribution was not achieved (Shapiro-Wilk, $p < 0.05$). Experiments with artificial and natural aging of the epoxy resin were analysed by independent samples T-Tests (parametric) or Mann Whitney U (non-parametric), along with data acquired from antibiofilm, durability in seawater and real-life efficacy (10 months) experiments. Data from real-life efficacy (1 month) and cytotoxicity experiments were analysed by ANOVA (parametric) or the Kruskal Wallis test (non-parametric).

3.0. Results and Discussion

3.1. Long-term stability of antimicrobial CHX epoxy resin coatings

The long-term stability of antimicrobial efficacy of the CHX epoxy resin coatings was explored using artificially simulated and natural aging techniques to ensure that these surfaces are a durable and practical strategy for microbial eradication.

Artificially accelerated aging of these coatings using UV light for surface degradation was conducted. 0.00 ± 0.00 CFU/mL *E. coli* was recovered from CHX epoxy resin surfaces following UV treatment for 1 - 4 hours, demonstrating 100% elimination of bacteria (figure 1A). This was significantly ($p<0.001$) fewer than recovered bacteria from the surface of the control epoxy resin after 1 hour ($2.56 \times 10^4 \pm 1.61 \times 10^4$ CFU/mL), 2 hours ($1.27 \times 10^4 \pm 1.09 \times 10^4$ CFU/mL), 3 hours ($6.56 \times 10^3 \pm 2.78 \times 10^3$CFU/mL) and 4 hours ($1.11 \times 10^4 \pm 5.64 \times 10^3$ CFU/mL). Many natural and synthetic polymers-based material have time-dependent properties such as strength and durability deplete over time (28). Artificially accelerated aging tests simulate the aging process by mimicking environmental factors and exposing materials to elevated UV light allowing long-term material degradation to be achieved within hours or days (29). According to one manufacturer, 1 hour UV treatment within a 40 W UV aging test chamber (320 – 400 nm) is equal to approximately 27 days exposure under natural environmental UV, however this is dependent on equipment and test conditions (30). In comparison, CHX epoxy resin samples were subject to UV degradation equivalent to up to 27, 54, 81 and 108 days natural aging (figure 1A), suggesting that antimicrobial efficacy against *E. coli* remains potent within 108 days of production.

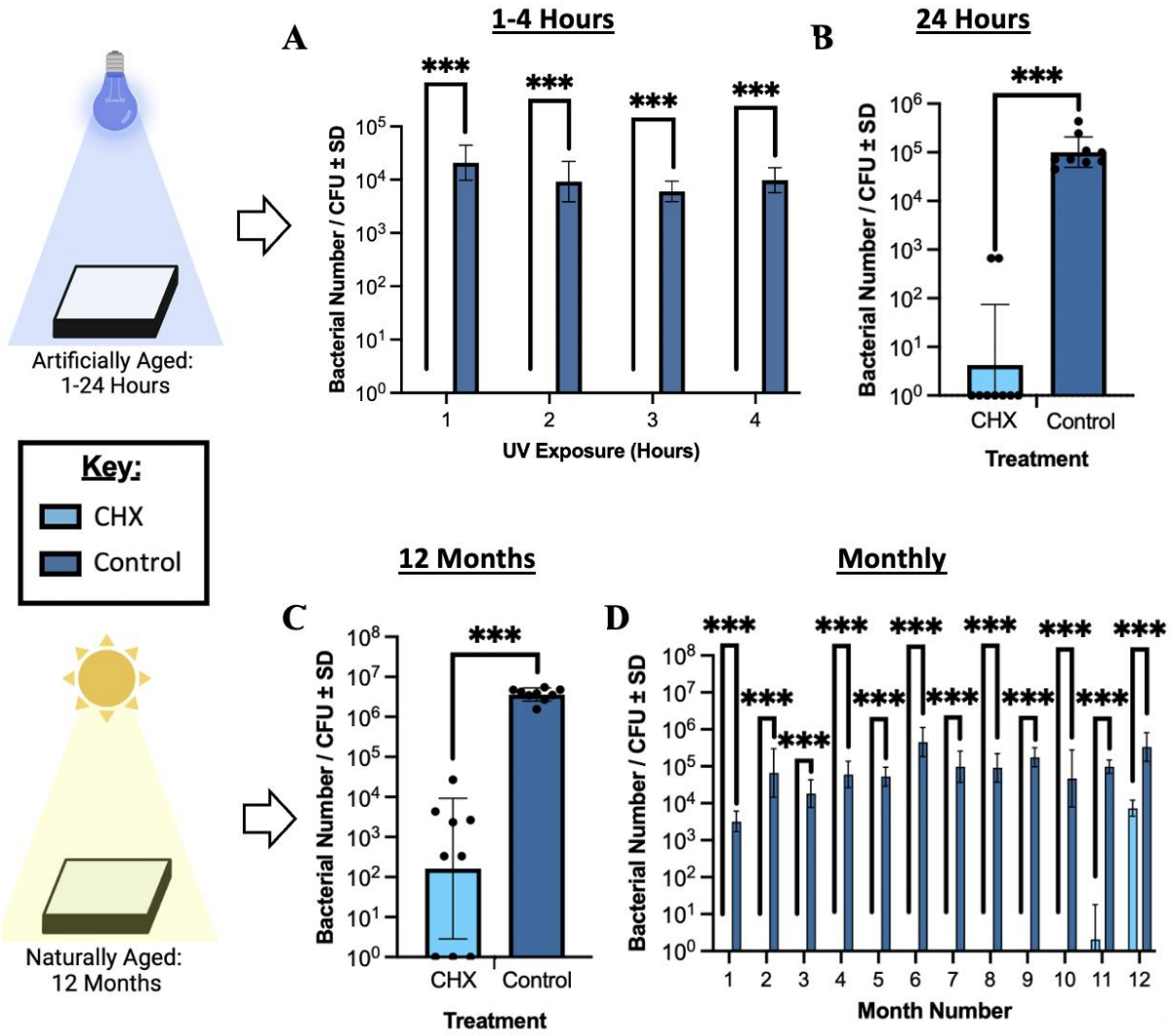


Figure 1. Long-term stability of antimicrobial efficacy of CHX epoxy resin coatings. Antimicrobial efficacy against *E. coli* was analysed following artificially accelerated aging treatments using UV for 1-4 hours (A) and 24 hours (B). In addition, antimicrobial efficacy against *E. coli* was tested after naturally aging the coatings for 12 monthly (C) as well as monthly efficacy tests for a period of 12 months (D). For all figures, n=9. *** denotes statistical significance $p<0.001$. Error bars represent standard deviation of the mean (Figure designed using BioRender).

CHX and control epoxy resin coating were also subject to 24 hours of UV light treatment roughly equivalating to 648 days (1 year and 9 months) exposure to natural degradation. $1.48 \times 10^2 \pm 2.93 \times 10^2$ CFU/mL *E. coli* was recovered from the surface of 24 hour UV treated CHX epoxy resin compared to $1.33 \times 10^5 \pm 1.26 \times 10^5$ CFU/mL from the control epoxy resin (Figure 1B). Although the difference in recovered bacteria counts between the CHX and control coatings was statistically significant ($p<0.001$), *E. coli* survival was recorded on the antimicrobial surface which was not observed following 1 – 4 hours UV treatment. This suggests that the antimicrobial potency of these coatings may be finite and may require reapplication over time.

Further, epoxy resin coatings naturally aged for 12 months demonstrated significant microbial elimination ($p<0.001$) compared to the control epoxy resin (figure 1C). $3.82 \times 10^6 \pm 1.2 \times 10^6$ CFU/mL *E. coli* was recovered from the 1 year old control coatings, compared to $4.11 \times 10^3 \pm 8.72 \times 10^3$ CFU/mL from the CHX coatings. Berrow *et al*., 2025 (26) demonstrated that freshly prepared CHX epoxy resin coatings exhibit 100% antimicrobial efficacy against a variety of clinically-relevant pathogens, including *E. coli*. It is therefore evident that natural surface degradation occurring within 12 months doesn't nullify the antimicrobial efficacy of the coatings but does begin to impede its potency.

Monthly evaluation of antimicrobial potency of these epoxy resin coatings was conducted to determine where within the first year after production these surfaces exhibit reduced efficacy. CHX epoxy resin coatings naturally aged for 1-10 months resulted in 0.00 ± 0.00 CFU/mL recovery of *E. coli* from the surfaces and therefore displayed 100% efficacy against the bacteria (figure 1D). This was significantly ($p<0.001$) lower than bacteria recovered from control epoxy resin after month 1 ($3.78 \times 10^3 \pm 1.99 \times 10^3$ CFU/mL), month 2 ($1.64 \times 10^5 \pm 2.34 \times 10^5$ CFU/mL), month 3 ($2.60 \times 10^4 \pm 2.44 \times 10^4$ CFU/mL), month 4 ($7.60 \times 10^4 \pm 4.53 \times 10^4$ CFU/mL), month 5 ($6.00 \times 10^4 \pm 2.88 \times 10^4$ CFU/mL), month 6 ($6.05 \times 10^5 \pm 3.81 \times 10^5$ CFU), month 7 ($1.43 \times 10^5 \pm 1.30 \times 10^5$ CFU/mL), month 8 ($1.35 \times 10^5 \pm 1.47 \times 10^5$ CFU/mL), month 9 ($2.00 \times 10^5 \pm 9.41 \times 10^4$ CFU/mL) and month 10 ($1.62 \times 10^5 \pm 2.57 \times 10^5$ CFU/mL).

Following 11 months of natural aging, the antimicrobial epoxy resin coating demonstrated 99.9% antimicrobial efficacy against *E. coli*, resulting in $7.40 \times 10^1 \pm 2.22 \times 10^2$ CFU/mL bacteria being recovered from the surface (figure 1D). This was significantly ($p<0.001$) different from the $1.06 \times 10^5 \pm 4.69 \times 10^4$ CFU/mL recovered from the control epoxy resin. Although high, following 12 months of natural aging the antimicrobial potency of the CHX epoxy resin coatings continued to reduce to 98.2% antimicrobial efficacy. $8.15 \times 10^3 \pm 3.93 \times 10^3$ CFU was recovered from the antimicrobial surface which was significantly ($p<0.001$) fewer than bacteria recovered from the control ($4.43 \times 10^5 \pm 2.89 \times 10^5$ CFU). Although still a highly potent antimicrobial surface, the loss of efficacy observed after 11 and 12 months of natural aging supports findings from the artificially accelerated aging tests (figure 1B), suggesting that the cured antimicrobial coatings may have a shelf-life and will require annual or biannual reapplication to maintain effective microbial elimination.

3.2. Antibiofilm efficacy of CHX epoxy resin coatings

The antibiofilm efficacy of the CHX epoxy resin coatings were analysed against fluorescently-tagged *P. aeruginosa* PA01 bacteria. 24 hours after inoculation, significantly ($p<0.001$) less fluorescence was detected from the antimicrobial epoxy resin compared to the control coatings (figure 2A). Fluorescence measured from CHX-treated surfaces was 6848.44 ± 3176.89, whilst 22359.67 ± 4771.36 was detected from the control. This suggests that the biofilm biomass to inhabit the epoxy resin surface was much fewer in the presence of CHX. Whilst biofilm formation has been significantly hindered on the CHX resin surfaces, they did not prevent the development of these complex bacterial communities. Berrow *et al*., 2025 (26) indicated that these antimicrobial coatings do not completely eliminate planktonic *P. aeruginosa* cultures, which may explain why the bacterial cultures were able to propagate into biofilm communities on these surfaces.

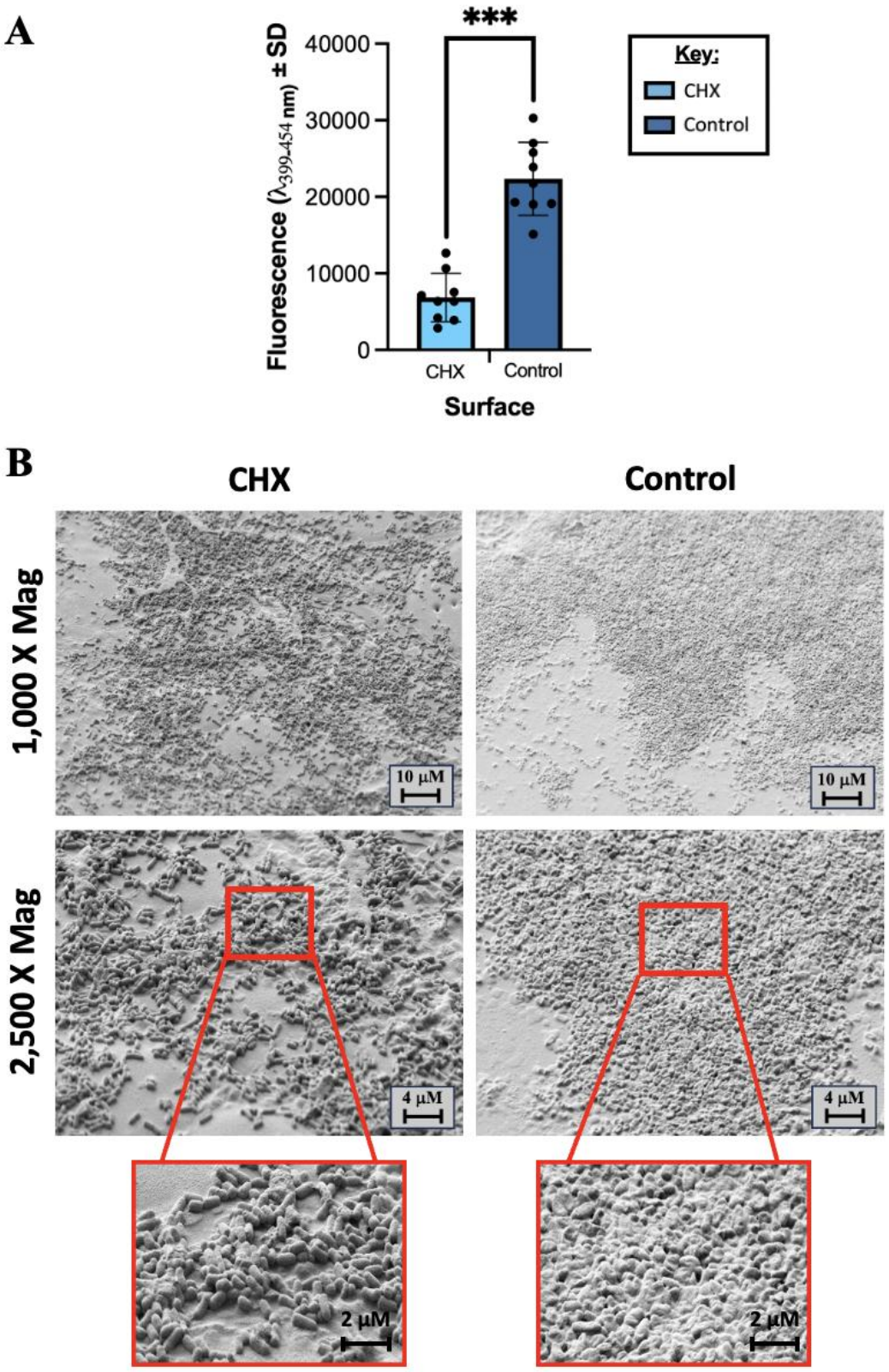


Figure 2. Antibiofilm efficacy of CHX and Control epoxy resin against *P. aeruginosa* PA01 bacteria containing pMRE140 plasmid. (A) Biofilm was quantified using fluorescence (λ_{ex}: 399 nm, λ_{em}: 454 nm) to measure blue fluorescent protein following 24 hours exposure to epoxy resin. (B) CryoSEM images of *P. aeruginosa* after 20 hours of growth on CHX-treated and control epoxy resin at 1,000 X and 2,500 X magnification with zoom-in to depict bacterial morphology.

CryoSEM images of the CHX and control epoxy resin surfaces following inoculation with *P. aeruginosa* and static incubation confirmed the presence of bacterial biofilms on the coatings. Figure 2B shows that biofilm formation had occurred on both the antimicrobial and control coatings, supporting the findings of the fluorescence assay and concluding that these surfaces do not prevent formation of these bacterial communities. Despite this, 1000 X magnification images highlight that biofilm cultivated on the CHX resin were significantly less dense than communities grown on the control resin, suggesting that biofilm formation was hindered by the presence of the antimicrobial in the coating. 2500 X magnification images detailed the shift in morphology of the bacteria within the biofilms. When exposed to the CHX coatings, *P. aeruginosa* appear to form smooth, rod-shaped bacilli, and approximately 1.40 μM long and 0.47 μM wide (figure 2B). When grown on the control epoxy resin, individual bacteria shift to a smaller, rough, mushroom-shaped morphology approximately 0.96 μM in length and 0.47 μM wide (figure 2B). Under optimal growth conditions, *P. aeruginosa* form rod-shaped bacteria, typically 1 – 5 μM in length and 0.5 – 1 μM in width (31). However, when populations become overcrowded and bacteria are competing for nutrients, their morphology can shift from bacilli to mushroom-shaped (32). The shrivelled appearance of individual bacteria on the control epoxy resin coatings suggest that the biofilm community is highly overpopulated, leading to nutrient deprivation in many areas of the structure. Further, in a state of hypoxia, *P. aeruginosa* produce phenazines, a redox-active compound, which function as alternative electron acceptors. This adaption causes a wrinkling morphology (33) which can be visualised in the biofilm inhabiting the control epoxy resin coating (figure 2B). Environmental temperature has also been associated with alterations to gene expression and protein synthesis profiles resulting in physiological and morphological adaptions in *P. aeruginosa* biofilms (34). Fluctuations in temperature surrounding the more densely populated regions of the biofilm may also contribute to the effect of the shrivelled appearance. The smooth, rod-shaped bacilli observed on the CHX epoxy resin coatings suggest that biofilm growth is significantly less rapid than the control, hence these antimicrobial surfaces may be an effective approach to reducing biofilm development.

3.3. Short-term durability of antimicrobial efficacy in seawater

Following 2 weeks of immersion in seawater, numerous tests were carried out on the CHX and control epoxy resin surfaces and leachate solutions to determine whether the coatings would be suitable for application in marine environments (Figure 3A). The CHX and control epoxy resin leachate solutions resulted in 2.99 ± 0.004 and 2.96 ± 0.05 absorbance at 280 nm, respectively (figure 3B). No significant difference in this absorbance was detected between the two sample types suggesting that zero or minimal CHX is leached from the epoxy after 2 weeks submersion in seawater, below the sensitivity limit of the instrument. HPLC analysis showed that the CHX in the same leachate was below the detection limit for the HPLC method (Supplementary information, Table 1) and no CHX was detected in the control leachate.

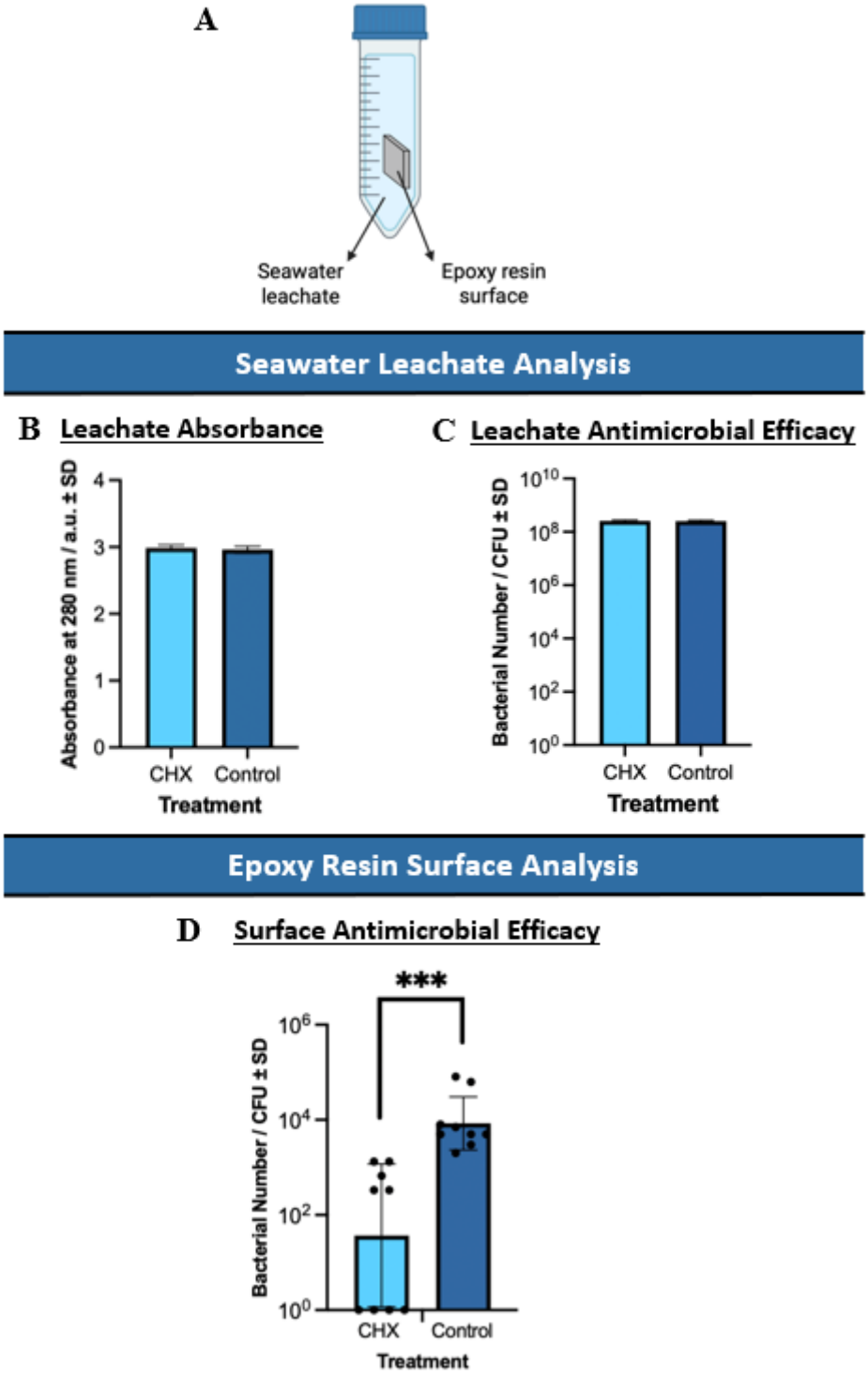


Figure 3. Durability of CHX epoxy resin coatings after 2 weeks immersion in seawater. (A) schematic of sample acquisition for analysis. (B) The absorbance at 280 nm of leachate from glass tiles painted with CHX and control epoxy resin (n = 9). (C) The antimicrobial efficacy of the seawater leachate from the same CHX and control painted samples against *E. coli* ATCC25922. (D) The survival of *E. coli* ATCC25922 on glass tiles painted with CHX and control epoxy resin following 2 weeks immersion in seawater (n = 27). *** resembles statistical significance of $p<0.001$. Figure designed using BioRender.

Previous findings from Berrow *et al*., 2025 (26) demonstrated that no leaching of CHX occurred when immersed in PBS for 14 days. However, the salinity and alkalinity of seawater is known to contribute to the breakdown of materials exposed to these environments (35). Further, ionic compounds present within seawater are known to cause friction and abrasion on submerged materials. As CHX is toxic to aquatic life according to the U.S Environmental Protection Agency, further investigation into the durability of large-scale instillations of CHX epoxy resin in marine environments is required (36, 37).

The antimicrobial efficacy of the seawater leachate was conducted to confirm the findings by absorbance and HPLC analysis. $2.60 \times 10^8 \pm 1.89 \times 10^7$ CFU/mL was cultured from the CHX epoxy resin leachate, whilst $2.55 \times 10^8 \pm 1.86 \times 10^7$ CFU/mL was cultured from the control epoxy resin leachate (figure 3C). No significant difference was observed in bacterial growth from the seawater leachate from the two coatings suggesting that the concentration of CHX leached into the seawater was below the minimum inhibitory concentration (MIC) for *E. coli* (MIC_{90} = 4 mg/L [38]).

The antimicrobial efficacy of the epoxy resin coatings following 2 weeks immersion in seawater was tested to determine the durability of the antimicrobial surfaces in marine environments. $4.44 \times 10^2 \pm 5.53 \times 10^2$ CFU/mL was recovered from the CHX epoxy resin surface post-leaching, compared to $1.99 \times 10^4 \pm 2.99 \times 10^4$ CFU/mL, which was recovered from the control coating (figure 3D). This was found to be highly significant *($p<0.001$)* suggesting that the CHX surface remains antimicrobial following 2 weeks exposure to seawater. Berrow *et al.,* 2025 (26) demonstrated that CHX epoxy resin immersed in PBS for 2 weeks resulted in no viable *E. coli* being recovered from the surface, highlighting that a reduction in antimicrobial efficacy of these coatings occurs when exposed to marine environments.

It is important to note that a colourless residue was present on the CHX epoxy resin coatings after 2 weeks immersion in seawater which may contribute to the reduction in antimicrobial efficacy exhibited by these surfaces. These residues are explored and discussed further in section 3.6.

3.4. Long-term durability of antimicrobial efficacy in seawater

CHX and control epoxy resin coatings were immersed in seawater for 1, 2, 3, 4, 5 and 6 months. Following this, analysis was conducted on the leachate solution and surface as previously carried out after 2 weeks exposure to seawater to determine whether these coatings would be suitable for long-term application in marine environments. Absorbance analysis on the CHX leachate after 1 month submersion in seawater resulted in an average reading of 3.05 ± 0.004 au whilst the average control read 3.00 ± 0.04 au (figure 4A). This difference was not statistically significant. The optical density of the seawater leachate at 280 nm after 2 – 6 months submersion remained stable for both CHX and control epoxy resin. No statistically significant differences were found.

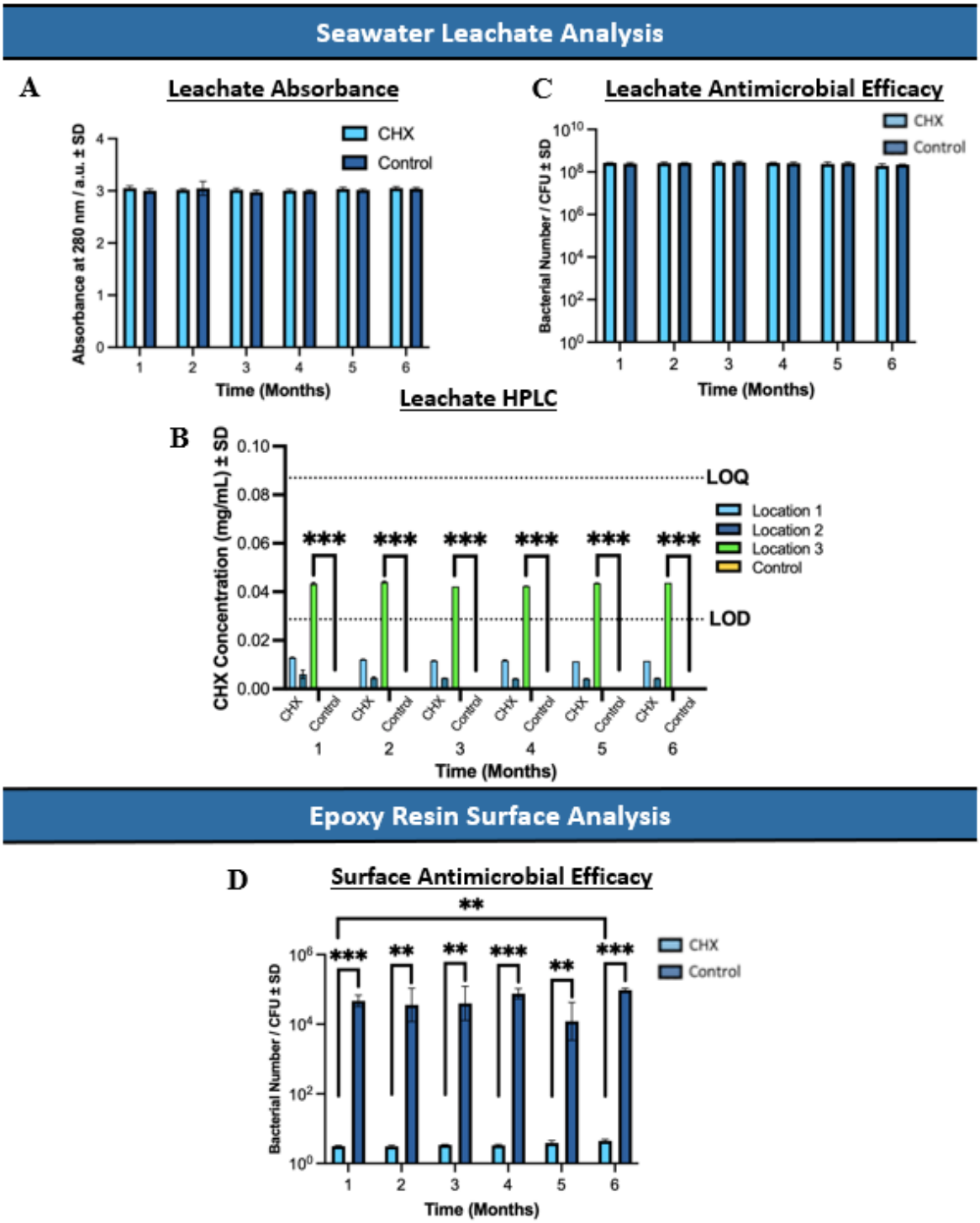


Figure 4. Durability of CHX epoxy resin coatings after 1 - 6 months immersion in seawater. (A) The absorbance at 280 nm of leachate from glass tiles painted with CHX and control epoxy resin (n = 9). (B) HPLC analysis of seawater leachate from the same glass tiles painted with CHX and control epoxy resin (n = 9). Dotted lines show the limit of detection (LOD) and limit of quantification (LOQ). (C) The antimicrobial efficacy of the seawater leachate from the same CHX and control painted samples against *E. coli* ATCC25922. (D) The survival of *E. coli* ATCC25922 on glass tiles painted with CHX and control epoxy resin following 1 – 6 months immersion in seawater (n = 27). *** resembles statistical significance of $p<0.001$ and ** $p<0.01$.

In contrast with the absorbance data, HPLC analysis of the leachate showed that CHX was detectable in the leachate following 1 - 6 months immersion in seawater sampled from location 3 (Figure 4B). After 1 month, 0.043 ± 0.001 mg/mL CHX was detected in the seawater leachate from location 3. There was very little variation in the concentration of leached CHX at the different sampling intervals (1 – 6 months), with 0.044 ± 0.00 mg/mL CHX detected after 6 months from seawater sampled from the same location. The CHX concentration of all CHX epoxy resin leachate when immersed in seawater from location 3 was significantly greater ($p < 0.001$) than the control epoxy resin leachate. Any CHX that leached from CHX epoxy resin immersed in seawater sampled from location 1 or 2 was below the detection limit for the HPLC method (Supplementary information, Table 1) and no CHX was detected in the control epoxy resin leachate.

It is clear from figure 4B that the amount of leached CHX varies depending on the location the seawater was sampled from. Seawater obtained from location 3 was sampled from Southsea beach, Portsmouth, United Kingdom. It is reported that water from the English Channel is heavily polluted with polycyclic aromatic hydrocarbons that are released from combustion of organic matter such as coal, oil and gas, as well as microplastics, radionuclides, metals (including cadmium, lead and mercury), xenobiotics, toxic substances including polychlorinated biphenyls and suspended particulate matter (39). Pollution increases the corrosivity of seawater and therefore material degradation (40). For example, Valdez *et al*., 2016 concluded that exposure to polluted seawater accelerated the corrosion rate of steel by up to 40-fold compared to fresh seawater (40). It is possible that the seawater sampled from location 3 was more polluted than the other seawater samples, therefore increasing the corrosion that occurred on the epoxy resin coatings, hence the release of antimicrobial into the leachate.

The antimicrobial efficacy of seawater leachate following 1 – 6 months immersion was conducted to determine whether the antimicrobial leached out of the coatings following long-term exposure to marine environments. The amount of recovered *E. coli* cultured from the CHX resin leachate after 1 month was $2.7 \times 10^8 \pm 6.20 \times 10^6$ CFU/mL, whilst $2.47 \times 10^8 \pm 2.68 \times 10^7$ CFU/mL was recovered from the control resin leachate (figure 4C). The quantified bacteria cultured from CHX and control resin leachate remained stable across all samples and no significant difference was identified in bacterial growth between the two groups.

To determine whether the CHX epoxy resin coatings would be suitable for long-term use in marine environments, the antimicrobial efficacy of the surfaces were tested following the 1 – 6 months immersion in seawater. After 1 month exposure to seawater, $1.11 \times 10^3 \pm 3.85 \times 10^2$ CFU/mL was recovered from the surface of the CHX epoxy resin compared to $4.90 \times 10^4 \pm 2.00 \times 10^4$ CFU/mL from the control, which was significantly different *($p < 0.001$)* (Figure 4D). After 2 months, $1.33 \times 10^3 \pm 5.77 \times 10^2$ and $4.83 \times 10^4 \pm 3.32 \times 10^4$ CFU/mL was recovered from the CHX and control coatings, respectively. This was statistically significant *($p = 0.004$)*. The bacteria recovered from the surface of 4 month leached CHX and control epoxy resin was also significantly different *($p = 0.005$)*, resulting in $1.33 \times 10^3 \pm 6.67 \times 10^2$ and $5.47 \times 10^4 \pm 4.13 \times 10^4$ CFU/mL, respectively. Further, $2.33 \times 10^3 \pm 8.82 \times 10^2$ CFU/mL was recovered from CHX coatings following 4 months immersion in seawater compared to $7.80 \times 10^4 \pm 2.38 \times 10^4$ CFU/mL from the control, which was highly significantly different *($p < 0.001$)*. Significantly *($p = 0.007$)* less bacteria were recovered from the surface of CHX epoxy resin following 5 months in seawater compared to the control, resulting in $1.89 \times 10^3 \pm 5.09 \times 10^2$ and $2.10 \times 10^4 \pm 2.60 \times 10^4$ CFU/mL, respectively. Finally, after 6 months immersion in seawater,

$3.89 \times 10^3 \pm 2.22 \times 10^3$ CFU/mL was recovered from the CHX coatings compared to the control, $9.50 \times 10^4 \pm 1.21 \times 10^4$ CFU/mL, which was highly significant *($p < 0.001$)*. The recovered bacteria from the CHX epoxy resin coatings after 6 months immersion in seawater compared to 1 month were also significantly higher *($p = 0.005$)*. This suggests that over time, the antimicrobial coatings are becoming less bactericidal and therefore may lose efficacy if exposed to marine environments long-term. It is evident that CHX can leach out of the antimicrobial epoxy resin when immersed in seawater. However, the reduction in antimicrobial efficacy could be due to a combination of this and the colorless residue that was observed on the CHX epoxy resin surface following 6 months seawater immersion that may limit microbial contact with the CHX surface.

3.5. Durability of antimicrobial efficacy with simulated oceanic motion

The durability of CHX epoxy resin coatings were analysed when exposed to simulated ocean movement by immersing samples in seawater with orbital motion for 2 weeks. Analysis on the seawater leachate and post-immersed coatings were conducted as previously described for section 3.3 and 3.4. Absorbance (280 nm) of the leachates resulted in 2.99 ± 0.03 au and 3.02 ± 0.03 au being measured from the CHX and control coatings, respectively (figure 5A). These measurements were not statistically significant, meaning if any CHX had leached out of the coatings, it was below the sensitivity limit of the technique. HPLC of the leachate detected leaching of the antimicrobial when immersed in moving seawater (Figure 5B). 0.13 ± 0.00 mg/mL CHX was detected in the leachate whilst no CHX was detected in the control leachate (figure 5B), which was a statistically significant difference *($p<0.001$)*. Antimicrobial efficacy against *E. coli* of the leachate from CHX and control epoxy resin resulted in $2.13 \times 10^8 \pm 1.68 \times 10^7$ CFU/mL and $2.22 \times 10^8 \pm 2.56 \times 10^6$ CFU/mL, respectively (figure 5C). This difference in bacterial growth was not statistically significant, therefore the presence of CHX in the leachate was below the MIC for the bacteria.

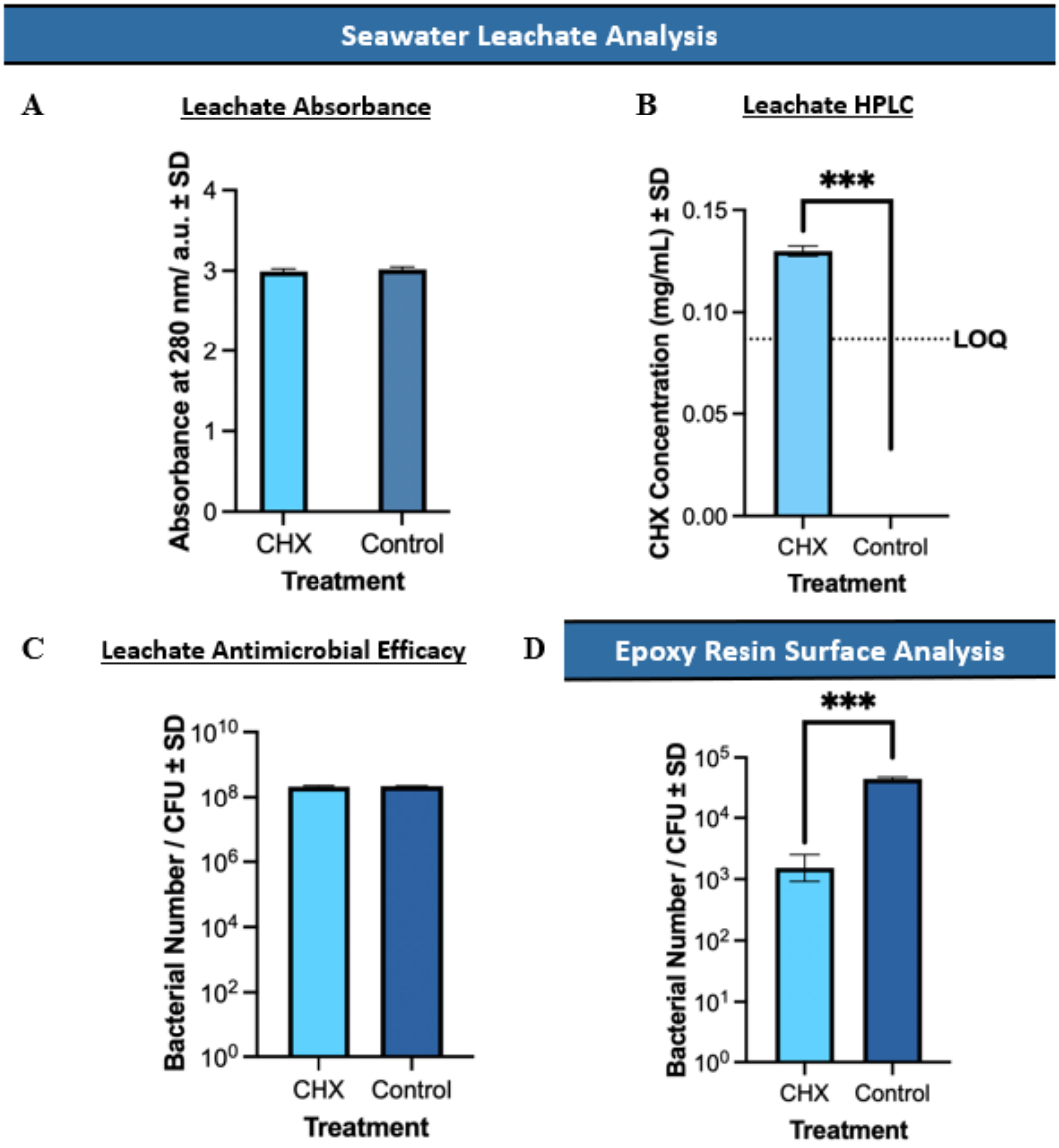


Figure 5. Antimicrobial efficacy of CHX epoxy resin following immersion in seawater with simulated oceanic motion for 2 weeks. (A) Absorbance at 280 nm of leachate from glass tiles painted with CHX and control epoxy resin (n = 9). (B) HPLC analysis of seawater leachate from the same glass tiles painted with CHX and control epoxy resin (n = 9). The dotted line shows the limit of quantification (LOQ) of the HPLC method. (C) Antimicrobial efficacy of the seawater leachate from the same CHX and control painted samples against *E. coli* ATCC25922 (n = 9). (D) The survival of *E. coli* ATCC25922 on glass tiles painted with CHX and control epoxy resin following 2 weeks immersion in seawater (n = 9). *** resembles statistical significance of $p<0.001$.

Antimicrobial efficacy against *E. coli* of the post-immersed coatings showed that $1.67 \times 10^3 \pm 8.82 \times 10^2$ CFU/mL and $4.50 \times 10^4 \pm 3.00 \times 10^3$ CFU/mL were recovered from the CHX and control epoxy resin surfaces, respectively (figure 5D). The CHX coatings significantly ($p < 0.001$) reduced the recovery of viable bacteria compared to epoxy resin without the antimicrobial, which are consistent with short- and long-term seawater exposure experiments in section 3.3 and 3.4. However, Berrow *et al,* 2025 (26) concluded that no *E.coli* could be recovered from CHX epoxy resin (not immersed in seawater), highlighting that these surfaces

display reduced antimicrobial efficacy when exposed to seawater, even short-term. When CHX epoxy resin coating were exposed to seawater with simulated ocean movement, it was evident that greater CHX leaching occurs. Although, this quantity is small as is not detectible by absorbance or microbial assays, large-scale use of CHX epoxy resin in marine environments may cause localised CHX leaching in concentrations great enough to cause harm to marine ecosystems as CHX is toxic to aquatic life (36, 37).

3.6. Salt build-up impacts the antimicrobial efficacy following seawater exposure

A ToF-SIMS depth profile was conducted to determine the composition of the residue build-up on the surface of the CHX epoxy resin coatings following seawater immersion. A thicker layer of salts can be identified on the surface of the CHX surfaces (figure 6A) compared to the control surfaces (figure 6B). The Cl^- depth profile is shown to be the greatest component of the surface salt reside on CHX surfaces and is relatively consistent throughout the salt layer (figure 6A). The intensity of the Cl^- drops of quickly when the epoxy resin interface begins, where the $C_7H_4N_2Cl^-$ CHX fragment ion and $C_9H_9O^-$ diagnostic epoxy resin ion elevate after approximately 85 seconds of Ar_{1600}^+ GCIB sputtering. This pattern is similar for the $NaCl_2^-$ intensity throughout the salt layer. Other ions present within the residue layer include K_2ClO^-, $FeSO_4H^-$ and SO_3^-, as well as SO_4H^- and $FeCl_3^-$ in small intensities. On average, seawater salinity is approximately 3.5% 99% of this salinity is attributable to Cl^- (55%), Na^+ (30.6%), SO_4^{2-} (7.7%), K^+, Mg^{2+} and Ca^{2+} ions (41), which appear to aggregate at the surface of the CHX epoxy resin.

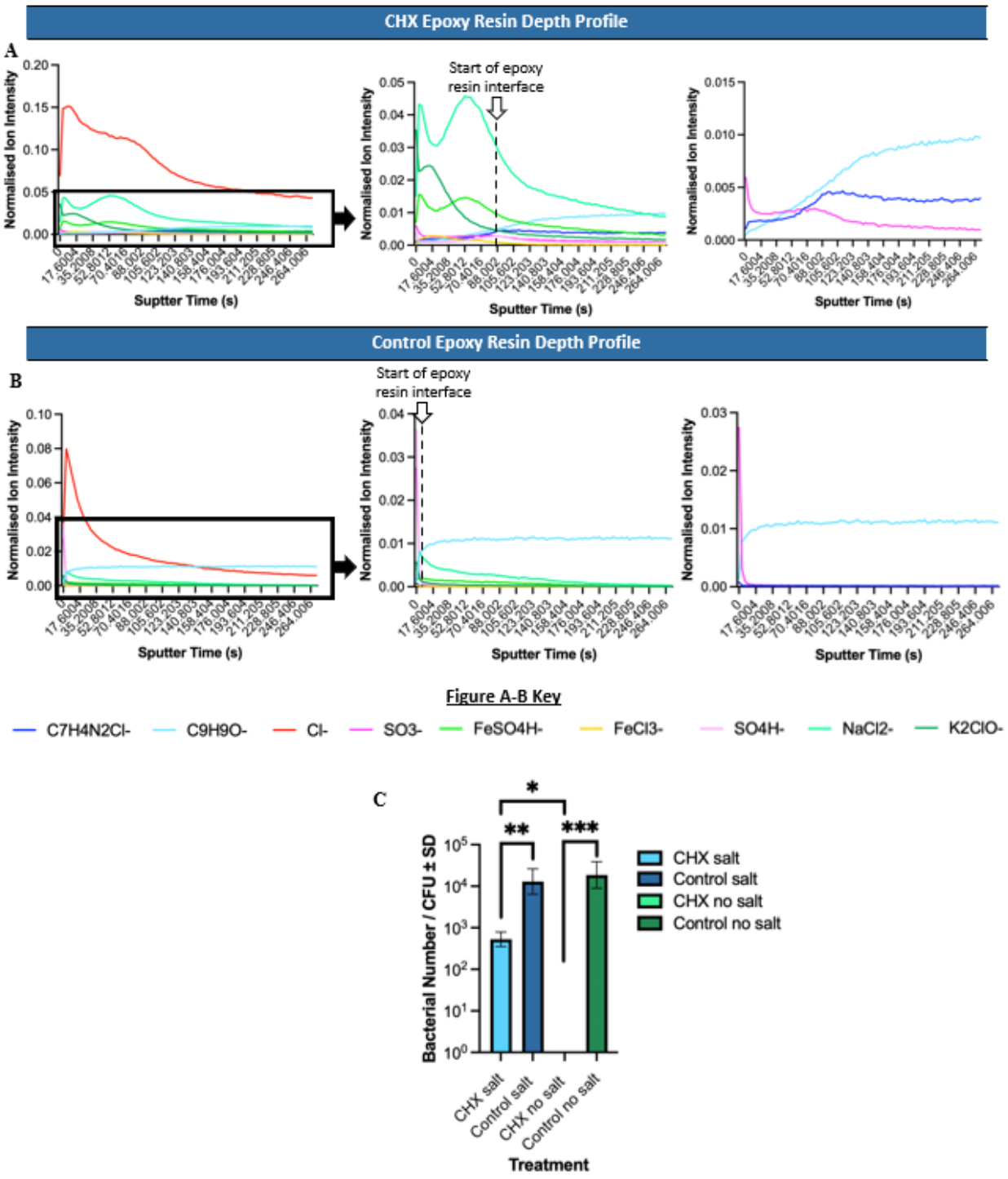


Figure 6. Salt residue build-up on epoxy resin coatings and impact on antimicrobial efficacy. (A) ToF-SIMS depth profile of CHX epoxy resin coatings showing distribution of the CHX fragment ion $C_7H_4N_2Cl^-$, the epoxy resin marker $C_9H_9O^-$, and a range of ions that represent salt build-up from the seawater, including Cl^-, SO_3^-, $FeSO_4^-$, $FeCl_3^-$, SO_4^-, $NaCl_2^-$ and K_2ClO^-. (B) ToF-SIMS depth profile of the control epoxy resin depicting the spatial distribution of the same ions throughout the depth of the coating. (C) Antimicrobial efficacy of the CHX and control epoxy resin coatings before (salt) and after salt removal (no salt) against *E. coli* (n = 9). Error bars display the standard deviation. *** represents statistical significance of P<0.001, *** represents P<0.01 and * represents P<0.05.

A ToF-SIMS depth profile of the control epoxy resin showed a very sharp intensity of Cl^- ions, which rapids declined at the start of the coating interface after approximately 5 seconds of Ar_{1600}^+ GCIB sputtering (figure 6B). Further, SO_3^- and SO_4H^- ion intensities appear to be moderate prior to the start of the epoxy resin surface. However, this salt layer is significantly thinner than the build-up on the CHX. The thicker salt residue on the antimicrobial coatings following immersion may reduce exposure and contact of bacteria to the CHX within the resin, therefore justifying the reduction in surface efficacy in marine environments.

The antimicrobial efficacy of the CHX epoxy resin surfaces was analysed before and following the removal of this salt layer to determine whether the drop in antimicrobial efficacy following exposure to seawater was attributable antimicrobial leaching or the build-up of salts preventing contact with the surface. Prior to salt removal, 666.67 ± 707.12 CFU/mL were recovered from the CHX surface, whilst 15000.00 ± 9000.00 CFU/mL were recovered from the control, which were significantly different *($p = 0.002$)*. following salt removal, 0.00 ± 0.00 CFU/mL and 21666.00 ± 15354.15 CFU/mL were recovered from the CHX and control coatings, respectively. This difference was statistically significant *($p<0.001$).* The number of bacteria recovered from the antimicrobial coatings before and after salt removal was also statistically significant *($p = 0.005$)* suggesting that these surfaces are still highly antimicrobial following 2 weeks immersion in seawater, however, the salt residue prevents the microbes from making contact with the surface, hence cannot be eliminated.

The reduction in antimicrobial efficacy of these CHX epoxy resin coatings when immersed in seawater for 2 weeks (sections 3.3 and 3.5) and 1-6 months (section 3.4) is highly likely to be attributable to this salt build-up as antimicrobial efficacy was restored when the salt layers were removed.

3.7. Antimicrobial efficacy of real-life coated surfaces

A range of surfaces were painted with CHX and control epoxy resin and swabbed 1 month following curing to determine microbial reduction. This was compared to the growth cultured from swabs take prior to coating with CHX and control epoxy resin to assess the effectiveness of the antimicrobial coatings for real-life applications. Environmental sampling of 1 month old CHX epoxy resin on indoor locations showed a 77.78 ± 22.22% (mean ± SE) reduction in in microbial growth (Figure 7A). This was not statistically different from the bacterial reduction observed with 1 month old control epoxy resin in the same indoor locations, -845.83 ± 649.95%. Large variation in the data that contributed to a lack of statistical significance is characteristic of environmental sampling due to the lack of experimental control over and therefore inconsistency with measurements (42). Further, whilst blood agar is nutrient-rich and non-selective media, not all microbial species will grow in the presence of this growth medium, for example, the growth of some *Streptococcus* variants (43), *Haemophillus spp.* (44), obligate anaerobes (45) and fungal species (46) are all limited by blood agar and therefore environmental cultures using this media do not account for all microbial growth. Despite this, the trend observed in Figure 7A shows that fewer microbes reside on CHX epoxy resin compared to epoxy resin without the antimicrobial, highlighting that these coatings may be an effective strategy to reduce microbial reservoirs on public surfaces and therefore transmission of pathogens.

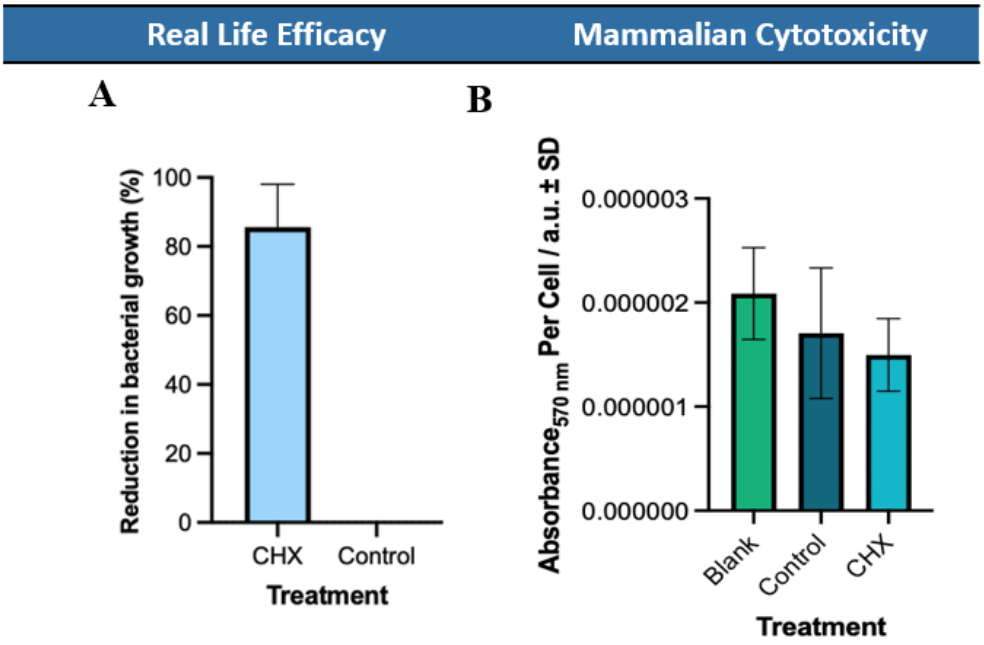


Figure 7. Continued explorations of CHX epoxy resin. (A) Percentage reduction in bacterial growth cultured 1 month following curing of CHX and control epoxy resin on real-life surfaces (n = 8). (B) Cytotoxicity of CHX and control epoxy resin against murine 3T3 fibroblasts compared to a cell media only control (n = 9). Error bars display the standard deviation of the mean.

3.8. Cytotoxicity and CHX Concentration Effect on Antimicrobial Efficacy

The cytotoxicity of the cured CHX epoxy resin surfaces was tested to determine whether these coatings would cause damage to mammalian cells following long-term contact. The average absorbance read from cells cultured on the CHX coating was $1.50 \times 10^{-6} \pm 3.49 \times 10^{-7}$ au (figure 7C). There was no significant difference in absorbance readings between the antimicrobial coating and the control epoxy resin coating or the cell culture (blank) control, which resulted in absorbance readings of $1.17 \times 10^{-6} \pm 6.27 \times 10^{-7}$ and $2.08 \times 10^{-6} \pm 4.41 \times 10^{-7}$ au, respectively. These findings show that cellular viability after 24 hours contact with the CHX epoxy resin was not significantly altered by the surface, suggesting that these coatings will not cause harm when touched by humans.

Conclusions

To conclude, we demonstrate that our CHX epoxy resin coatings demonstrate long-term antimicrobial efficacy with significantly reduced bacterial recover after 12 months from curing. These coatings also exhibit antibiofilm properties by reducing the biofilm biomass growing on the surfaces. Whilst biofilm growth wasn't completely prevented, these surfaces have demonstrated an ability to significantly slow down the growth of these complex film communities and may reduce the burden of marine biofilms when applied in these environments. After examination of CHX epoxy resin following immersion in seawater, evidence suggests that any CHX that leached from these coatings was below the detection limit of our HPLC method, however depending on the composition of the seawater, small traces of

the antimicrobial could be detected in the leachate. This needs further exploration as large scale use of CHX epoxy resin in marine environments may cause disruption to aquatic ecosystems and toxicity to marine life due to trace leaching. Further, it is unknown whether more CHX leaches from the epoxy resin after 6 months immersion in seawater, hence the effectiveness and suitability of these coatings within marine environments is not fully understood.

Salt residues that builds up on the CHX coatings following immersion in seawater appears to prevent contact between the surface and the microbes, which is essential for antimicrobial activity of these surfaces. The antimicrobial efficacy of these coatings can be restored following salt removal. Real-life indoor and outdoor surfaces coated with CHX epoxy resin demonstrate reductions in microbial populations, however, it is difficult to understand the extent of the efficacy due to lack of control and variability with environmental sampling. Finally, these antimicrobial surfaces demonstrate no cytotoxicity against mammalian cells meaning that these coatings are safe to touch by the public.

Author Contributions

Madeline Berrow: Conceptualization, Methodology, Validation, Formal analysis, Investigation, Writing- original draft, Writing- review and editing. **Li Lu:** Methodology, Investigation, Writing- review and editing. **Christopher Parmenter:** Methodology, Investigation. **Eva Simpson:** Investigation. **Jean Dubern:** Resources. **David Scurr:** Conceptualization, Funding acquisition, Supervision, Writing- review and editing. **Simon Greenway:** Conceptualization. **Violaine Mendez:** Conceptualization **Brian Norton:** Resources, Funding acquisition, Conceptualisation. **Felicity de Cogan:** Conceptualization, Funding acquisition, Supervision, Project administration, Writing- review and editing.

Declaration of Competing Interests

The authors of this manuscript declare no conflicts of interest.

Data Availability

Data is available in the University of Nottingham's Data Repository.

Acknowledgements

This research was financially supported by the EP/P029868/1 Engineering and Physical Sciences Research Council (EPSRC) grant.

References

1. Konno A, Okubo T, Enoeda Y, Uno T, Sato T, Yokota SI, Yano R, Yamaguchi H. Human pathogenic bacteria on high-touch dry surfaces can be controlled by warming to human-skin temperature under moderate humidity. *Plos one*. 2023;*18*(9).

2. Cobrado L, Silva-Dias A, Azevedo MM, Rodrigues AG. High-touch surfaces: microbial neighbours at hand. *Eur J Clin Microbiol Infect Dis*. 2017.*36*(11):2053-2062.

3. Meadow JF, Altrichter AE, Kembel SW, Moriyama M, O'Connor TK, Womack AM, Brown GZ, Green JL, Bohannan BJ. Bacterial communities on classroom surfaces vary with human contact. *Microbiome*. 2014;*2*(1):7.

4. Boyce JM. Modern technologies for improving cleaning and disinfection of environmental surfaces in hospitals. *Antimicrob. Resist Infect. Control*. 2016;5:10.

5. Exner M, Bhattacharya S, Gebel J, Goroncy-Bermes P, Hartemann P, Heeg P, et al. Chemical disinfection in healthcare settings: critical aspects for the development of global strategies. *GMS Hyg. Infect*. Control. 2020;15:36.

6. Casey ML, Hawley B, Edwards N, Cox-Ganser JM, Cummings KJ. Health problems and disinfectant product exposure among staff at a large multispecialty hospital. *Am. J. Infect. Control.* 2017;45(10):1133-8.

7. Clausen PA, Frederiksen M, Sejbaek CS, Sorli JB, Hougaard KS, Frydendall KB, et al. Chemicals inhaled from spray cleaning and disinfection products and their respiratory effects. A comprehensive review. *Int. J. Hyg. Environ. Health*. 2020;229:113592.

8. D'Orazio J, Jarrett S, Amaro-Ortiz A, Scott T. UV radiation and the skin. *Int. J. Mol. Sci.* 2013;14(6):12222-48.

9. Mahanta U, Khandelwal M, Deshpande AS. Antimicrobial surfaces: a review of synthetic approaches, applicability and outlook. *J. Mater. Sci.* 2021;56(32):17915-41.

10. Qian PY, Cheng A, Wang R, Zhang R. Marine biofilms: diversity, interactions and biofouling. *Mat. Rev. Microbiol*. 2022; *20*(11):671-684.

11. Alkawareek MY, Gorman SP, Graham WG. Gilmore BF. Eradication of marine biofilms by atmospheric pressure non-thermal plasma: A potential approach to control biofouling?. *Int Biodeter Biodegradation*. 2014;*86*:14-18.

12. Yang X, Hou J, Tian Y, Zhao J, Sun Q, Zhou S. Antibacterial surfaces: Strategies and applications. *Sci. China. Technol. Sci.* 2022;65(5):1000-10.

13. Franci G, Falanga A, Galdiero S, Palomba L, Rai M, Morelli G, et al. Silver nanoparticles as potential antibacterial agents. *Mol.* 2015;20(5):8856-74.

14. Sharma P, Fialho L, Figueiredo NM, Serra R, Cavaleiro A, Carvalho S. Antimicrobial Polymeric Surfaces Using Embedded Silver Nanoparticles. *J. Antibiot.* 2023;12(2).

15. Sim W, Barnard RT, Blaskovich MAT, Ziora ZM. Antimicrobial Silver in Medicinal and Consumer Applications: A Patent Review of the Past Decade (2007(-)2017). *J. Antibiot.* 2018;7(4).

16. Edwards-Jones V. The benefits of silver in hygiene, personal care and healthcare. Lett *Appl. Microbiol*. 2009;49(2):147-52.

17. Gabbay JB, G.; Mishal, J.; Magen, E.; Zatcoff, R.; Shermer-Avni, Y. Copper oxide impregnated textiles with potent biocidal activities. *J. Ind. Text*. 2006;35:323–35.

18. Arendsen LP, Thakar R, Sultan AH. The Use of Copper as an Antimicrobial Agent in Health Care, Including Obstetrics and Gynecology. *Clin. Microbiol. Rev*. 2019;32(4).

19. Dang XY, Z.; Wang, X.; Du, Y.; Wang, C. Sustainable one-pot synthesis of novel soluble cellulose-based nonionic biopolymers for natural antimicrobial materials. *Chem. Eng. J*. 2023;468.

20. Cassidy SS, Sanders DJ, Wade J, Parkin IP, Carmalt CJ, Smith AM, et al. Antimicrobial surfaces: A need for stewardship? *PLoS Pathog*. 2020;16(10):e1008880.

21. Lim KS, Kam PCA. Chlorhexidine - pharmacology and clinical applications. *AIC*. 2008;36(4):502-12.

22. Poppolo Deus F, Ouanounou A. Chlorhexidine in Dentistry: Pharmacology, Uses, and Adverse Effects. *Int. Dent. J.* 2022;72(3):269-77.

23. Cieplik F, Jakubovics NS, Buchalla W, Maisch T, Hellwig E, Al-Ahmad A. Resistance Toward Chlorhexidine in Oral Bacteria - Is There Cause for Concern? Front *Microbiol.* 2019;10:587.

24. Biswas D, Tiwari M, Tiwari V. Molecular mechanism of antimicrobial activity of chlorhexidine against carbapenem-resistant Acinetobacter baumannii. *PLoS One*. 2019;14(10):e0224107.

25. Cheung HY, Wong MM, Cheung SH, Liang LY, Lam YW, Chiu SK. Differential actions of chlorhexidine on the cell wall of Bacillus subtilis and Escherichia coli. *PLoS One*. 2012;7(5):e36659.

26. Berrow M, Brooks A, Kotowska AM, Watts J, Riordan L, Kidger L, Scurr DJ, Nikoi ND, Banzhaf M, Bryant J, Greenway S, Mendez V, Norton B, de Cogan F. Development and characterisation of antimicrobial epoxy resin. *Sci. Rep.* 2025;15:12463.

27. Schlechter RO, Jun H, Bernach M, Oso S, Boyd E, Munoz-Lintz DA, Dobson RCJ, Remus DM, and Remus-Emsermann MNP. Chromatic Bacteria - A Broad Host-Range Plasmid and Chromosomal Insertion Toolbox for Fluorescent Protein Expression in Bacteria. *Front. Microbiol*. 2018 Dec 12;9:3052.

28. Emri I, Gonzalez-Gutierrez J, Gergesova M, Zupancic B, Saprunov I. Experimental determination of material time-dependent properties. *ETS*. 2014 p.1494-1510.

29. Fidan M. Accelerated aging effects on color change, translucency parameter, and surface hardness of resin composites. *BioMed. Res. Int. 2022*(1):6468281.

30. ChiuVention. UV aging test chamber. [Available at: https://chiuventionclimatechamber.com/product/temperature-humidity-chamber/uv-aging-test-chamber] 2025.

31. Diggle SP, Whiteley M. Pseudomonas aeruginosa: opportunistic pathogen and lab rat. *Microbiol.* 2020; 166(1):30-33.

32. Ghanbari A, Dehghany J, Schwebs T, Müsken M, Häussler S, Meyer-Hermann M. Inoculation density and nutrient level determine the formation of mushroom-shaped structures in Pseudomonas aeruginosa biofilms. *Sci. Rep.* 2016; 6(1):1-12.

33. Kåhrström CT. Survival of the wrinkliest. *Nat. Rev. Microbiol.* 2013;11(3):149-149.

34. Bisht K, Luecke AR, Wakeman CA. Temperature-specific adaptions and genetic requirements in a biofilm formed by Pseudomonas aeruginosa. *Front. Microbiol.* 2023;13:1032520.

35. Chohan, I.M., Ahmad, A., Sallih, N., Bheel, N., Salilew, W.M. and Almaliki, A.H., 2024. Effect of seawater salinity, pH, and temperature on external corrosion behavior and microhardness of offshore oil and gas pipeline: RSM modelling and optimization. *Scientific Reports*, *14*(1), p.16543.

36. Lawrence, J.R., Zhu, B., Swerhone, G.D.W., Topp, E., Roy, J., Wassenaar, L.I., Rema, T. and Korber, D.R., 2008. Community-level assessment of the effects of the broad-spectrum antimicrobial chlorhexidine on the outcome of river microbial biofilm development. *Applied and Environmental Microbiology*, *74*(11), pp.3541-3550.

37. Jesus, F.T., Oliveira, R., Silva, A., Catarino, A.L., Soares, A.M., Nogueira, A.J. and Domingues, I., 2013. Lethal and sub lethal effects of the biocide chlorhexidine on aquatic organisms. *Ecotoxicology*, *22*(9), pp.1348-1358.

38. Lutgring, J.D., Grass, J.E., Lonsway, D., Yoo, B.B., Epson, E., Crumpler, M., Galliher, K., O'Donnell, K., Zahn, M., Evans, E. and Jacob, J.T., 2023. Development of a broth microdilution method to characterize chlorhexidine MICs among bacteria collected from 2005 to 2019 at three US sites. *Microbiology Spectrum*, *11*(3), pp.e04134-22.

39. Tappin, A.D. and Millward, G.E., 2015. The English Channel: contamination status of its transitional and coastal waters. *Marine Pollution Bulletin*, *95*(2), pp.529-550.

40. Valdez, B., Ramirez, J., Eliezer, A., Schorr, M., Ramos, R. and Salinas, R., 2016. Corrosion assessment of infrastructure assets in coastal seas. *Journal of Marine Engineering & Technology*, *15*(3), pp.124-134.

41. Štanfel, D., Kalogjera, L., Ryazantsev, S.V., Hlača, K., Radtsig, E.Y., Teimuraz, R. and Hrabač, P., 2022. The role of seawater and saline solutions in treatment of upper respiratory conditions. *Marine drugs*, *20*(5), p.330.

42. van der Schoor, A.S., Boyle, M., Voor, A.F., Vos, M.C. and Humphreys, H., 2022. Environmental sampling of innate hospital surfaces: a survey of current practices and the need for guidelines. *Journal of Hospital Infection*, *128*, pp.92-95.

43. Reimer, L.G. and Reller, L.B., 1981. Growth of nutritionally variant streptococci on common laboratory and 10 commercial blood culture media. *Journal of Clinical Microbiology*, *14*(3), pp.329-332.

44. Musher, D.M., 1996. Haemophilus Species. *Medical Microbiology*. 4th edition. Chapter 30. Available at: https://www.ncbi.nlm.nih.gov/books/NBK8458/

45. Hentges, David J., 2011. Anaerobes: general characteristics.

46. Reddy, A.K., Brahmaiah, U., Narayen, N., Reddy, R.K., Reddy, R.K., Chitta, M., Prasad, S., Swarup, R., Mohiuddin, S.M., Reddy, M. and Aasuri, M.K., 2013. Is blood agar an alternative to sabouraud dextrose agar for the isolation of fungi in patients with mycotic keratitis. *International ophthalmology*, *33*(3), pp.251-254.

Supplementary Information for

Stability, durability and application of antimicrobial epoxy resin

Madeline Berrow [a], Li Lu [a], Christopher Parmenter [b], Eva Simpson [b], Jean Dubern [c], David J. Scurr [a], Simon Greenway [d], Violaine Mendez [d], Brian Norton [d], Felicity de Cogan [a*]

[a] School of Pharmacy, University of Nottingham, University Park, Nottingham, NG7 2RD, United Kingdom
[b] Nanoscale and Microscale Research Centre, University of Nottingham, University Park, Nottingham, NG7 2RD, United Kingdom
[c] School of Life Sciences, University of Nottingham, University Park, Nottingham, NG7 2RD, United Kingdom
[d] Indestructible Paint Ltd, 16-25 Pentos Drive, Birmingham, United Kingdom
[*] Corresponding author

This PDF includes:

Conjugation Plasmid Gene Sequence: Figure 1
HPLC limit of detection and limit of quantification: Table 1

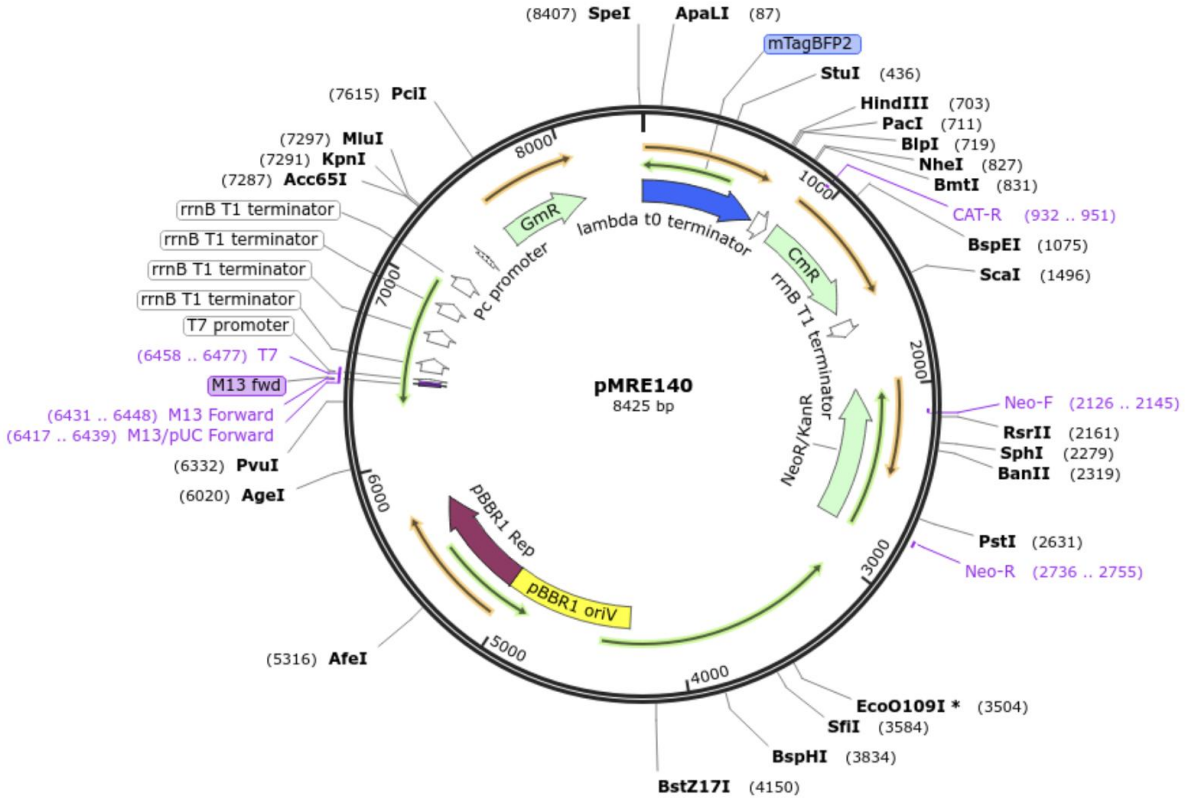


Figure S1. pMRE140 plasmid gene sequence containing mTagBFP2 (blue fluorescent protein) used for bacterial conjugation of *P. aeruginosa* PA01. (Figure available at: https://www.addgene.org/118492/)

Table 1. Limit of detection (LOD) and limit of quantification (LOQ) of CHX using the HPLC method described by Berrow et al., 2025.

Limit Type	Limit Concentration (mg/mL)
Detection (LOD)	0. 028696331
Quantification (LOQ)	0. 086958579

Conclusions of chapter 4

This work highlights that the CHX epoxy resin coatings sustain high antimicrobial efficacy over a 12 month period, and possibly for longer, without the requirement of coating reapplication. This paper also concludes that CHX epoxy resin can significantly reduce biofilm formation, which may be particularly useful for medical or maritime industries. However, this paper also concludes that use of this antimicrobial coating may be limited in marine environments due to the build-up of salt deposits on the coating surface, preventing pivotal contact between the antimicrobial layer and microorganisms. In addition, this paper concludes that CHX epoxy resin coatings cause no cytotoxicity to mammalian cells following 24 hour contact and despite complications with environmental sampling, these antimicrobial coatings demonstrate increased microbial elimination and hence may aid in the reduction in disease transmission within the community.

Chapter 5: Conclusions and future work

5.1. Conclusions

The main aim of this thesis was to develop, analyse and optimise novel formulations of CHX for various applications to reduce infection and disease transmission within hospitals and throughout the community. This work builds on previous research carried out within the Scurr group which assessed *in vivo* and *in vitro* permeation of CHX through skin using commercially available products. This previous work highlighted poor permeation of CHX to the lower *stratum corneum* as well as highlighting problems with uniformity of antimicrobial distribution past the second layer of corneocytes. This thesis concludes that CHX delivery through the entire *stratum corneum* can be significantly enhanced with the addition of R6 polyarginine, glycolic acid or Kolliphor® HS15 permeation enhancer compounds after only 2 minutes of exposure to the skin. The improved permeation of the antimicrobial results in significantly better clearance of the skins microbiome which will reduce the infection risk following surgical procedures.

The potent, broad-spectrum antimicrobial properties of CHX can also be exploited for reducing environmental microorganisms that reside on surfaces and transmit disease upon contact. CHX has been integrated into clear epoxy resin, which when cure, forms a hard, durable antimicrobial surface that can be applied to a variety of pre-existing materials and surfaces. This CHX epoxy resin coating demonstrated high antimicrobial efficacy against a variety of clinically relevant pathogens, including *E. coli, S. aureus, P. aeruginosa* and *C. albicans*, as well as CHX-resistant *E. coli*, suggesting that these surfaces may be an effective strategy to reduce microbial contamination of high-touch surfaces, particularly those within hospitals. These surfaces are also highly durable and maintain satisfactory scratch resistance and adhesion properties, as well as retaining high antimicrobial efficacy long-term, demonstrating their suitability for long-term instillation.

CHX epoxy resin coatings also display antibiofilm efficacy by reducing the growth of *P. aeruginosa* biofilm formation. This property of these antimicrobial coatings may be highly beneficial to environments where biofilms frequently grow and cause problems, such as within medical or maritime industries. However, the application of these coatings within marine environments is significantly hindered by the build-up of salt residues that prohibit complete contact of these surfaces with contaminating microbes. This causes a reduction in antimicrobial efficacy even after short-term immersion in seawater, which questions the suitability of this material for application within marine environments. Despite this, CHX epoxy resin has demonstrated an ability to effectively reduce environmental microorganism on real-life surfaces, highlighting that applications of these coatings may be an effective strategy to reduce disease transmission within the community, as well as in hospitals.

5.2. Future work

5.2.1. CHX for skin sanitation

Further work is necessary to allow these novel CHX formulations to progress into use in the clinic. Immediate work on this project would include setting up a Transwell *in vitro* cell

migration assay using epithelial cells to investigate the effects of the R6 polyarginine, glycolic acid and Kolliphor® HS15 formulations on the skin's barrier function. Measuring the transepithelial electrical resistance (TEER) to determine the integrity of the cell monolayer will give insight into the effects on the epithelial tight junctions and therefore understanding on the mechanism of action of the permeation enhancer compounds (1). Further, the work detailed in this thesis uses one concentration of R6 polyarginine, glycolic acid and Kolliphor® HS15 based on previous work or the highest concentration that does not cause cytotoxicity. This project would require formulation optimisation to determine the lowest concentration of permeation enhancer compounds necessary to significantly enhance biocide delivery through the entire *stratum corneum* to optimise microbial clearance without delivering excess CHX into bloodstream. Investigating how the incorporation of R6 polyarginine, glycolic acid and Kolliphor® HS15 effect the antibacterial efficacy of CHX in different culture environments (i.e. different temperatures and medias) to account for bias in culturing conditions in the protocols used. The antifungal and antiviral efficacy of the formulation would help understand the true advantage of formulating CHX with these permeation enhancer compounds.

In addition, the use of a biomimetic skin model such as a skin-on-a-chip (SoC) microfluidic device may aid in the assessment of the safety and effectivity of these permeation enhancer formulations. These dynamic, three-dimensional microenvironments replicate properties of human skin such as the skin's barrier function, cellular interactions and stimuli responses (2, 3). Due to limitations of the *in vitro* Franz-type diffusion model and subsequent tape stripping methods, the use of a SoC device would allow the study of the safety and effectiveness of these permeation enhancer formulations with greater accuracy.

Once the CHX formulations have been optimised and finalized, future plans for this project would include *in vivo* animal studies using rodents (rats or mice) due to low cost and easy handling. Based on the results of animal studies, clinical trials using human volunteers will be essential before these formulations are used in clinical practice.

5.2.2. CHX epoxy resin coatings

This project requires further work before the CHX epoxy resin can be used within the community or clinic. This antimicrobial coating would be highly beneficial in areas where pathogenic microbes are highly prevalent, such as hospitals. However, it is important to better understand the extent of the coatings antimicrobial properties by exploring efficacy against other common nosocomial bacterial pathogens such as *Klebsiella spp., Enterococci spp., Enterobacter spp.* and *Clostridium difficile,* as well as fungal pathogens such as *Candida auris, Aspergillus spp., Pneumocystis jirovecii,* Mucorales*, Fusarium spp. and Scedosporium spp.* Further, antimicrobial-resistant infections are becoming more prevalent and complicated to treat, hence understanding whether CHX epoxy resin can eradicate pathogens such as MRSA, VRE, carbapenem-resistant Enterobacteriaceae (CRE), multidrug-resistant *P. aeruginosa* and ESBL-producing *E. coli and K. pneumoniae* will be important for understanding the full potential of these antimicrobial surfaces. In addition to antimicrobial efficacy, investigations into whether these surfaces can eradicate spores or bacterial endospores will also be crucial for understanding how effective these surfaces are at reducing disease. Spores and endospores are more complicated to eliminate as they are resistant to heat, radiation and various chemicals and are therefore problematic in infection and disease transmission (4). Further, it is essential to investigate how these antimicrobial surfaces effect human corneocyte cell lines *in vivo* to ensure minimal or no damage is caused by human contact with these surfaces.

Long-term future work for this project includes understanding the mechanism of action of these antimicrobial surfaces. It is widely recognised that CHX requires mobility to diffuse through bacterial membranes and cause disruption to cellular processes to cause bactericidal effects. However, CHX is immobilised in the epoxy resin and antimicrobial efficacy is still potent against various pathogens. In addition, these antimicrobial coatings demonstrate high efficacy against CHX-resistant *E. coli* strains hence it is clear that these surfaces exploit an undefined mechanism of action. Understanding this will give further insight into how these surfaces can be used.

Further, due to the rapid build-up of salt residue on the CHX epoxy resin coatings following immersion in seawater, future work may focus on incorporating additives into the surface to prevent this occurring and therefore permit the use of the paint in marine environments. However, it is crucial that any additives do not affect the function, durability or stability of the antimicrobial surface.

References for chapter 5

1. Pell TJ, Gray MB, Hopkins SJ, Kasprowicz R, Porter JD, Reeves T, Rowan WC, Singh K, Tvermosegaard KB, Yaqub N, Wayne GJ. Epithelial barrier integrity profiling: combined approach using cellular junctional complex imaging and transepithelial electrical resistance. SLAS Discovery. 2021 Aug 1;26(7):909-21.
2. Zoio P, Oliva A. Skin-on-a-chip technology: microengineering physiologically relevant in vitro skin models. Pharmaceutics. 2022 Mar 21;14(3):682.
3. Risueño I, Valencia L, Jorcano JL, Velasco D. Skin-on-a-chip models: General overview and future perspectives. APL bioengineering. 2021 Sep 1;5(3).
4. Setlow P. Spores of Bacillus subtilis: their resistance to and killing by radiation, heat and chemicals. Journal of applied microbiology. 2006 Sep 1;101(3):514-25.

Appendix 1: Oligoarginine peptide structure and effect on cell penetration in ocular drug delivery

Appendix 1 presents a paper that was published in Heliyon in 2024. It discusses the cell permeation enhancement of a series of cell penetrating peptides called oligoarginines for the delivery of ocular therapeutics. I collaborated with the authors and contributed knowledge and expertise to analyse the cytotoxicity profiles of R_3, R_6, R_9 and R_{12} oligoarginine compounds on mammalian keratocytes. I conducted an Alamar Blue® assay to determine the cell viability through the measurement of metabolic activity. I was able to conclude that the cell penetrating peptides were not cytotoxic to mammalian cells at the concentration tested.

Oligoarginine peptide structure and effect on cell penetration in ocular drug delivery

Stefana Duca[1#], Naa Dei Nikoi[1#], Madeline Berrow[1], Lois Barber[2], Louise N Slope[3], Anna F A Peacock[3], Felicity de Cogan[1].

1. School of Pharmacy, University of Nottingham, Nottingham, UK
2. Institute of Microbiology and Infection, University of Birmingham, Birmingham, UK
3. School of Chemistry, University of Birmingham, Birmingham, UK

# These authors contributed equally and will be joint first authors.

Keywords: cell-penetrating peptides; oligoarginine; ocular drug delivery; antibacterial
Words: 5574
Figures: 6
Author for correspondence: Felicity de Cogan (felicity.decogan@nottingham.ac.uk)

Abstract

Oligoarginine cell-penetrating peptides (CPPs) are short peptides that can enhance drug delivery into cells and are of particular interest in ocular topical formulations for age-related macular degeneration (AMD) treatments. The length and structural characteristics of these peptides are considered crucial for drug delivery. This study investigates how oligoarginine length (R_n) affects their penetration mechanism, drug delivery capabilities, and antimicrobial properties, providing insights into their potential roles in AMD treatment delivery. In this study, oligoarginine peptides showed limited pore-forming abilities in a carboxyfluorescein-containing liposomal model, with R_9 being the only oligoarginine length recording a significant pore-formation level. Their antibacterial efficacy depended on both the CPP length and bacterial class, with longer peptides exhibiting stronger antibacterial effects. Importantly, oligoarginine was found nontoxic to relevant mammalian cells for ocular delivery. The membrane translocation abilities of oligoarginine were consistent regardless of cargo presence. Additionally, cargo delivery by oligoarginine across *in vitro* cellular models for ocular delivery was dependent on peptide length and cell type, with longer chains being more effective at cargo uptake in a corneal epithelium cell line, and with shorter chains proving more effective for cargo delivery in a retinal epithelium cell line. This proposes that the chain length of oligoarginine could be used as a strategic tool in the formulation process to selectively target distinct regions of the eye. Overall, this study expands our understanding of how oligoarginine CPPs can be applied as penetration enhancers to improve the delivery of therapeutics in an ocular topical formulation within the clinical context of AMD.

Introduction

Cell-penetrating peptides (CPPs) are short peptides that can deliver membrane-impermeable molecules inside the cytosol due to their ability to translocate through cell membranes to access intracellular structures [1]. The use of CPPs as a tool to access the cell by acting as penetration enhancers for therapeutics and biological molecules of interest is well established [1]. CPPs have the advantage of having a low-cost, simple manufacturing process and being biocompatible and readily processed by the body. In a clinical setting, CPPs can be formulated for topical administration to enhance the ocular absorption of age-related macular degeneration (AMD) therapies, such as protein-based therapies (e.g., anti-vascular endothelial growth factor agents) and small peptide therapies (e.g., the novel therapeutic candidate Apolipoprotein A-I

mimetic peptide 4F, ApoAI) [2, 3]. This approach can help prevent serious side effects associated with the current AMD drug delivery platforms (i.e., intravitreal injections) and improve patient compliance [4–7]. There are promising studies that have demonstrated the ability of CPPs to successfully deliver AMD agents to the posterior region of the eye both *in vitro* and *in vivo* whilst preserving drug action [8, 9]. The most common type of CPP is a cationic peptide. As a class, they show excellent cellular intake across a wide range of cell types, with oligoarginines being the most utilised type for topical drug delivery [10].

Oligoarginines are polypeptides composed solely of arginine residues (R_n) and possess a large positive charge that enables them to pass the cell membrane efficiently. Oligoarginine CPPs have previously been employed to deliver a range of molecules [9, 11, 12]. For instance, they have been utilised to form protein–protein complexes with insulin, thereby facilitating its delivery across the gut epithelium both *in vitro* and *in vivo* [11]. Similarly, the topical anti-inflammatory drug cyclosporine A, covalently linked to oligoarginines, demonstrated enhanced penetration through the outermost layer of the skin to access the underlying epidermis [12]. de Cogan *et al.* (2017) demonstrated the potential of oligoarginines as penetration enhancers for ocular delivery, as they successfully internalised anti-VEGF agents in an *in vivo* rat retinal model [9]. Furthermore, additional studies showed that oligoarginine peptides can form stable conjugates with anti-VEGF therapeutics like bevacizumab, further supporting their suitability as a novel form of AMD drug delivery technology [13]. While the ability of oligoarginine peptides to internalise therapeutic cargo into cells due to their high positive charge has been established, the exact mechanism by which they enter the cells remains controversial due to conflicting evidence in the literature [14, 15].

Several studies have suggested that oligoarginine can be internalised via various mechanisms, such as absorption-mediated endocytosis and passive translocation via pore formation [14, 15]. However, no definitive evidence establishes the precise mechanism behind their cell delivery abilities. The guanidine head group, a potentially crucial structure required for peptide uptake into cells, has been found to directly influence the translocation of oligoarginine within cells, with peptide length playing a key role in this process [10, 16]. As such, it is believed that the length and charge of oligoarginine CPPs are critical factors in their drug delivery abilities. Studies have been conducted to evaluate the optimal oligoarginine length for efficient cellular uptake [10, 16]. Some reports indicate that a minimum of six arginine residues (R_6) is required for effective internalisation. In contrast, others propose that oligoarginine lengths of R_6–R_8 present optimal cargo uptake compared to longer variants, and still, other sources suggest that longer oligoarginines (e.g., R_{10} and R_{12}) can achieve significant internalisation at lower concentrations than shorter oligoarginines (e.g., R_7 and R_9) [10, 16, 17]. However, no study to date has been conducted to investigate the optimal length of oligoarginines required for efficient ocular drug delivery.

Furthermore, in addition to their role as penetration enhancers in AMD therapeutics, oligoarginine peptides could potentially serve as preservatives in topical formulations, as several studies indicate that these peptides possess antimicrobial activity [18, 19]. It has been suggested that arginine-rich polypeptides can act as antimicrobial peptides (AMPs) by inducing pore formation in bacterial cells [20]. As oligoarginine length appears to be critical in their delivery mechanism and CPP characteristics, chain length may also play a key role in their antimicrobial abilities.
Therefore, this investigation aimed to evaluate the structure–activity relationship of oligoarginine peptides as a novel drug delivery system for AMD therapeutics in the form of an ocular topical formulation. To accomplish this, the impact of oligoarginine structure and length

(R_n) on its drug delivery and antimicrobial capabilities was studied. In this study, we have examined oligoarginine-mediated delivery of both large and small target molecules. Bovine serum albumin-Texas Red (BSA-TR) was used as a representative model for protein molecules, and ApoAI (molecular weight 2.31 kDa) as a model for small peptide molecules [21][3].

1. Materials and Methodology

2.1 Materials

1X Gibco Dulbeco's modified Eagle's medium (DMEM), F-12 containing L-glutamine and 15 mM HEPES buffer, foetal bovine serum (FBS), penicillin-streptomycin, 0.25% 1X trypsin-EDTA were obtained from Gibco, UK. Trypan Blue and Texas Red-tagged BSA (BSA-TR) (LOT# 2136779) were from Invitrogen, UK. Dipalmitoylphosphatidylcholine (DPPC) phospholipid was purchased from Avanti® Polar Lipids, USA. All other reagents, including phosphate buffered saline (PBS), amphotericin B solution (250 µg/mL), chloroform, diethyl ether, Triton X-100, carboxyfluorescein, AlamarBlue® solution, and Luria-Bertani (LB) broth were procured from Merck, UK. Oligoarginine peptides (R_3, RRR; R_6, RRRRRR; R_9, RRRRRRRRR; R_{12}, RRRRRRRRRRRR) were purchased from GenScript, UK, as untagged peptides (R_n) and carboxyfluorescein tagged peptides (FAM-R_n). Carboxyfluorescein-tagged Apolipoprotein A-I mimetic peptide 4F (FAM-ApoAI) was obtained from Alta Bioscience, UK.

1.2 Liposome Preparation

Carboxyfluorescein-containing liposomes were synthesised by adapting a protocol from Jimah *et al.* (2017) [22]. The phospholipid used for liposome preparation was DPPC, and the buffer of choice was HEPES-NaCl (10 mM HEPES pH 7.4 combined with 150 mM NaCl and deionised water). Initially, 10 mg of DPPC was dissolved in 1 mL chloroform. A phospholipid film was created by solvent evaporation under a gentle stream of nitrogen gas. The lipid film was re-hydrated by adding 500 µL of 20 mM carboxyfluorescein solution substituted in HEPES-NaCl buffer and 500 µL diethyl ether using a Pasteur pipette. This was sonicated three times for 60-second intervals at 50 °C and vortexed for 15 seconds between each sonication. Using a rotary evaporator, the solvent was removed at 25 °C, 500 mbar, and 100 RPM. An Avanti Mini Extruder set was used to obtain uniform-sized liposomes. The extruder was primed in HEPES-NaCl buffer and pre-warmed to 50 °C. Finally, the liposome suspension was purified using a desalting column (Cytiva, US) according to the manufacturer's instructions, and a liposome stock solution was prepared in HEPES-NaCl buffer in a 1:100 ratio.

1.3 Liposome Disruption Assay

Untagged oligoarginine peptides (R_n) were prepared in HEPES-NaCl buffer at a concentration of 200 mM. A volume of 2 µL of liposome stock was added per well with sufficient HEPES-NaCl buffer to give a total volume of 100 µL, and the fluorescence was read at an excitation/emission wavelength of 485/535nm using a TECAN plate reader. Subsequently, 1 µL of the 200 mM untagged oligoarginine stock solution or HEPES-NaCl buffer (acting as a negative control) was added per well and incubated for 10 minutes at room temperature, and fluorescence was read at the described settings. To ensure complete liposome disruption, 0.1%

Triton X-100 was added to each well. Triton X-100 is known for its ability to disrupt phospholipid membranes and served as a positive control to validate the assay [22].

1.4 Minimum inhibitory concentration (MIC)

A broth microdilution assay was performed to determine the minimum inhibitory concentration (MIC) for the oligoarginine peptides. *Escherichia coli* (*E. coli*) ATCC25922 and *Staphylococcus aureus* (*S. aureus*) ATCC6538 were used as model organisms for Gram-negative and Gram-positive bacteria, respectively. Both strains were cultured in LB broth for ~18 hours overnight at 37°C and shaking set to 180 RPM. The culture was diluted to obtain a 0.01 optical density (OD) bacterial suspension in LB. Using a 96-well plate, oligoarginine concentrations ranging from 1 mM to 0.001 mM were obtained, and each peptide concentration was tested against both bacterial strains. The bacteria were incubated overnight at 37°C for 18 hours, and the lowest concentration of the treatment with no visible bacterial growth was recorded as the MIC of the respective oligoarginine treatment.

1.5 Cell culture

The *in vitro* cellular models chosen are to represent barriers relevant to ocular drug delivery, human keratocyte cells as a component of the corneal epithelium, and the retinal pigment epithelium and blood-retina barrier as ARPE-19 cells [23, 24]. Primary human keratocyte cells (Innoprot, Spain) were cultured in DMEM/F12 media supplemented with 10% foetal bovine serum (FBS), 1% penicillin-streptomycin, 0.1% amphotericin B, and 10 ng/mL basic fibroblast growth factor (b-FGF). ARPE-19 cells, a gift from the University of Birmingham, were cultured in DMEM/F12 media supplemented with 10% FBS, 1% penicillin-streptomycin, and 0.1% amphotericin B. Cells were harvested for passaging or seeding once a cell confluency of > 80% was reached.

1.6 Cell toxicity

Keratocyte and ARPE-19 cells were seeded into 96-well plates at a density of 5 x 10^3 cells/well in 50 µL of their respective cell media at 37 °C and 5 % CO_2. After 24 hours, cell media was removed, and fresh media supplemented with oligoarginine peptides at 56 µM was added to each well. Following a 72-hour incubation at 37 °C and 5 % CO_2, cell viability was measured using AlamarBlue® solution (0.1 mg/mL). AlamarBlue® uses the fluorometric redox indicator resazurin (7-hydroxy-3H-phenoxazin-3-one 10-oxide), initially a blue-coloured non-fluorescent compound. Once internalised by viable cells, resazurin is reduced to the fluorescent resorufin (7-hydroxy-3H-phenoxazin-3-one) allowing measurement of cell viability [25]. A volume of 5 µL/well AlamarBlue® stock solution was added in 45 µL/well cell media for two hours. Each well was measured at a fluorescence wavelength of 545/590 nm using a TECAN plate reader. Subsequently, a cell count was performed by washing the cell monolayer three times in PBS and by harvesting the cells from the 96-well plate using 20 µL/well 0.25% Trypsin-EDTA. The cells were counted in a 1:1 ratio with Trypan Blue, using a Countess automated cell counter (Invitrogen, UK). Performing a full cell count alongside a metabolic rate assay provides an understanding of the compound's toxicity beyond metabolic activity, as it directly quantifies cell numbers. Each polypeptide length was tested in triplicate across three experimental repeats, and a no-peptide positive control was included in each experiment.

1.7 Cell monolayer assay

Keratocyte and ARPE-19 cells were seeded into 96-well plates at a density of 4 x 10^4 cells/well in 100 µL of their respective cell media at 37 °C and 5% CO_2 for 24 hours. Prior to performing the assay, cell media was discarded, and cells were washed three times in PBS. A pre-treatment reading with 100 µL PBS at excitation/emission wavelengths of 485/535 nm (FAM-tagged molecules), 570/630 nm (Texas Red-tagged BSA, BSA-TR) or both was measured to identify background fluorescence reading. Subsequently, 50 µL/well of the constituted formulation (FAM-R_n only formulation: 25 µM FAM-R_n in PBS; FAM-R_n/BSA-TR formulation: 200 µM FAM-Rn with 250 µg/mL BSA-TR in PBS; R_n/FAM-ApoAI formulation: 2.5 mM R_n with 200 µg/mL FAM-ApoAI in PBS) was applied to the cell monolayer and incubated for 60 seconds. The solution was removed, and the wells were washed five times with PBS. A volume of 100 µL/well of PBS was added, and the fluorescence was read at excitation/emission wavelengths of 485/535 nm and/or 570/630 nm. Matching control samples treated with PBS only or cargo only (at the same concentrations used in their corresponding experiments) were included where appropriate.

1.8 Calibration curves of oligoarginine peptides and BSA

To estimate uptake of oligoarginine and BSA in cell monolayer experiments, calibration curves have been developed (*Figure 1*). For FAM-tagged oligoarginines (FAM-R_n), standards ranging from 7.8 to 600 nM were prepared for each peptide length. Due to consistent fluorescence readings across different peptide lengths, a single calibration curve was generated using the average fluorescence readings across all tested oligoarginines (*Figure 1A*). Fluorescence was measured at excitation/emission wavelengths of 485/535 nm. Similarly, for TexasRed-tagged BSA (BSA-TR), standards with concentrations ranging from 50 to 1000 ng/mL were prepared, with fluorescence readings taken at excitation/emission wavelengths of 570/630 nm. Separate calibration curves were created for BSA-TR fluorescence in keratocyte (*Figure 1B.i*) and ARPE-19 (*Figure 1B.ii*) cell monolayers to accommodate differences in measurement settings. All calibration curves were constructed in Microsoft Excel utilising the linear regression trendline function, ensuring an R^2 value of ≥ 0.99 to validate the data fitting appropriately. The fitted equation (as seen in *Figure 1*) was then used to estimate unknown concentrations of each treatment.

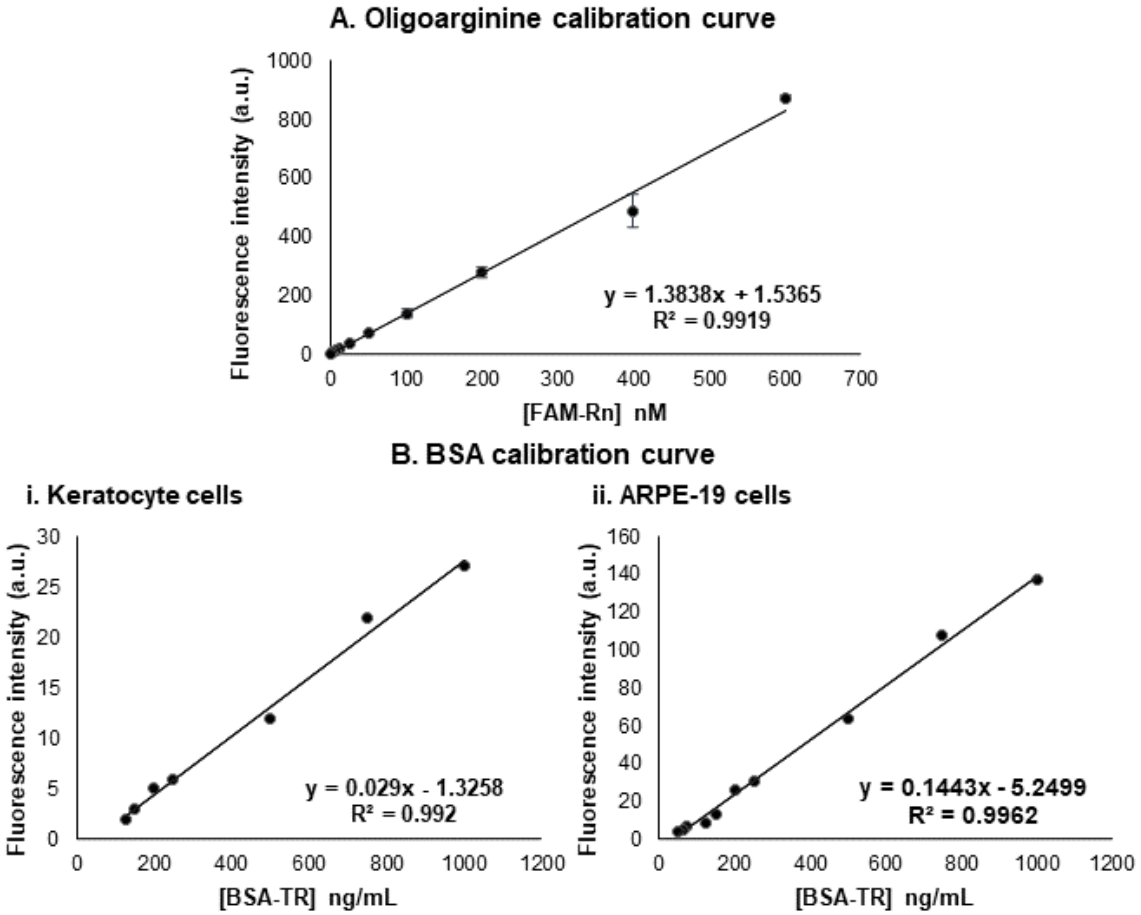


Figure 1. Calibration curves for A. FAM-tagged oligoarginine peptides (FAM-Rn) and B. TexasRed-tagged BSA (BSA-TR) for B.i. keratocyte and B.ii. ARPE-19 cell monolayers. *Fluorescence intensity is measured in arbitrary units (a.u.). Data is presented as the mean±SEM (n=4) where applicable. The data was fitted using linear regression.*

1.9 Statistical analysis:

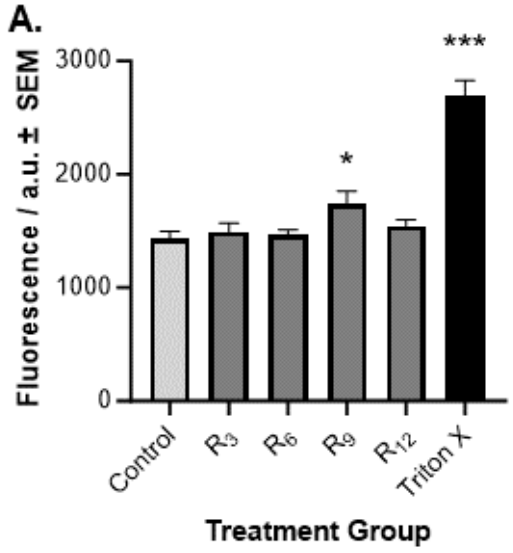
Statistical evaluation was performed using GraphPad Prism 10.0.2. All experiments included at least three experimental repeats with two, three, or more technical repeats, with matched control conditions. All datasets were tested for normality using the Shapiro-Wilks test. Where data failed the normality test (Shapiro-Wilk, $p < 0.05$), it was subject to log transformation to achieve a normal distribution. Differences in cell monolayer experiments were assessed with one-way ANOVA followed by Tukey's post-hoc test. In contrast, differences in liposome disruption assays and mammalian toxicity studies were assessed with one-way ANOVA followed by Dunnet's post-hoc test. Significance was taken at $p \leq 0.05$. All data is presented as the mean ± standard error of the mean (SEM).

Results

3.1 CPP membrane-disruption abilities

To examine the pore-forming abilities of different structures of oligoarginines, carboxyfluorescein-containing liposomes were synthesised to simulate a phospholipid bilayer, where an increase in fluorescence intensity is expected to denote liposomal membrane disruption. The pore-forming abilities of the oligoarginine CPPs were initially tested on carboxyfluorescein-containing liposomes (*Figure 2A*), where minimal penetration was observed from all tested oligoarginines. However, CPP R_9 was the only oligoarginine length that recorded a significant increase in fluorescence intensity ($p = 0.018$) following the 10-minute exposure of liposomes to the oligoarginines. Adding 0.1% Triton X, acting as a positive control, caused lysis of liposomes. Consequently, significant leakage of fluorescein was detected as an increase in fluorescence intensity ($p < 0.001$), establishing the validity of the assay.

To further evaluate the membrane-disrupting capabilities of oligoarginine peptides, their antibacterial effects were examined against both gram-positive (*S. aureus*) and gram-negative (*E coli*) bacteria. The MIC values of oligoarginines against *E. coli* and *S. aureus* are shown in *Figure 2B*. Across the tested oligoarginine concentration range (0.001–1 mM), neither R_3 nor R_6 displayed any reduction in bacterial growth against *S. aureus* over 18 hours. However, R_9 exhibited some degree of anti-bacterial activity, with an MIC of 1 mM, while R_{12} showed higher efficacy with an MIC of 0.61 ± 0.22 mM. A similar trend was observed with *E. coli*, where the shorter oligoarginines R_3, R_6, and R_9 all showed no antibacterial efficacy over the 18-hour duration. In contrast, R_{12} displayed the highest level of efficacy, recording an MIC of 0.94 ± 0.16 mM after the 18-hour timeframe.



B.

Peptide Length	S. aureus MIC (mM)	E. Coli MIC (mM)
R_3	>1	>1
R_6	>1	>1
R_9	1	>1
R_{12}	0.61 ± 0.22	0.94 ± 0.16

Figure 2. Membrane penetration of oligoarginine CPPs. *A) Stimulated leakage of fluorescence from liposomes. Data shows the mean ± SEM (n = 9) of carboxyfluorescein fluorescence from liposomes following a 10-minute incubation of the carboxyfluorescein-containing liposomes with oligoarginine peptides. Liposomes with no penetration agent added and 0.1% Triton-X act as a negative and positive control, respectively. Fluorescence intensity is measured in arbitrary units (a.u.). Significance was taken at p≤0.05 using One-way ANOVA and Dunnett's post-hoc test. ***p < 0.001 when compared to Control. B) Antimicrobial Efficacy of polyarginines. Data shows the average minimum inhibitory concentration (MIC) observed for each peptide ± SEM (n = 9) following an 18-hour exposure of Staphylococcus aureus (S. aureus) and Escherichia coli (E. coli) to the oligoarginines*

CPPs cytotoxicity against mammalian cells

As the peptides demonstrated a toxic effect against bacteria, their potential toxicity against mammalian cells was examined. Both keratocyte and ARPE-19 cell monolayers were exposed to the oligoarginine peptides for 72 hours. Cytotoxicity was evaluated by measuring the metabolic rate of cells using both the AlamarBlue® reagent and by performing a full cell count to provide a more comprehensive assessment of their toxicity profile *in vitro*. In both keratocyte and ARPE-19 cell monolayers, the oligoarginine CPPs recorded no significant difference in fluorescence intensity of AlamarBlue® when compared to PBS control cells (*Figure 3A, C*). Similarly, exposure to CPPs did not result in significant differences in cell numbers compared to PBS control cells in either cell line (*Figure 3B, D*). These results indicate that the CPPs were not cytotoxic to mammalian cells at the concentration tested.

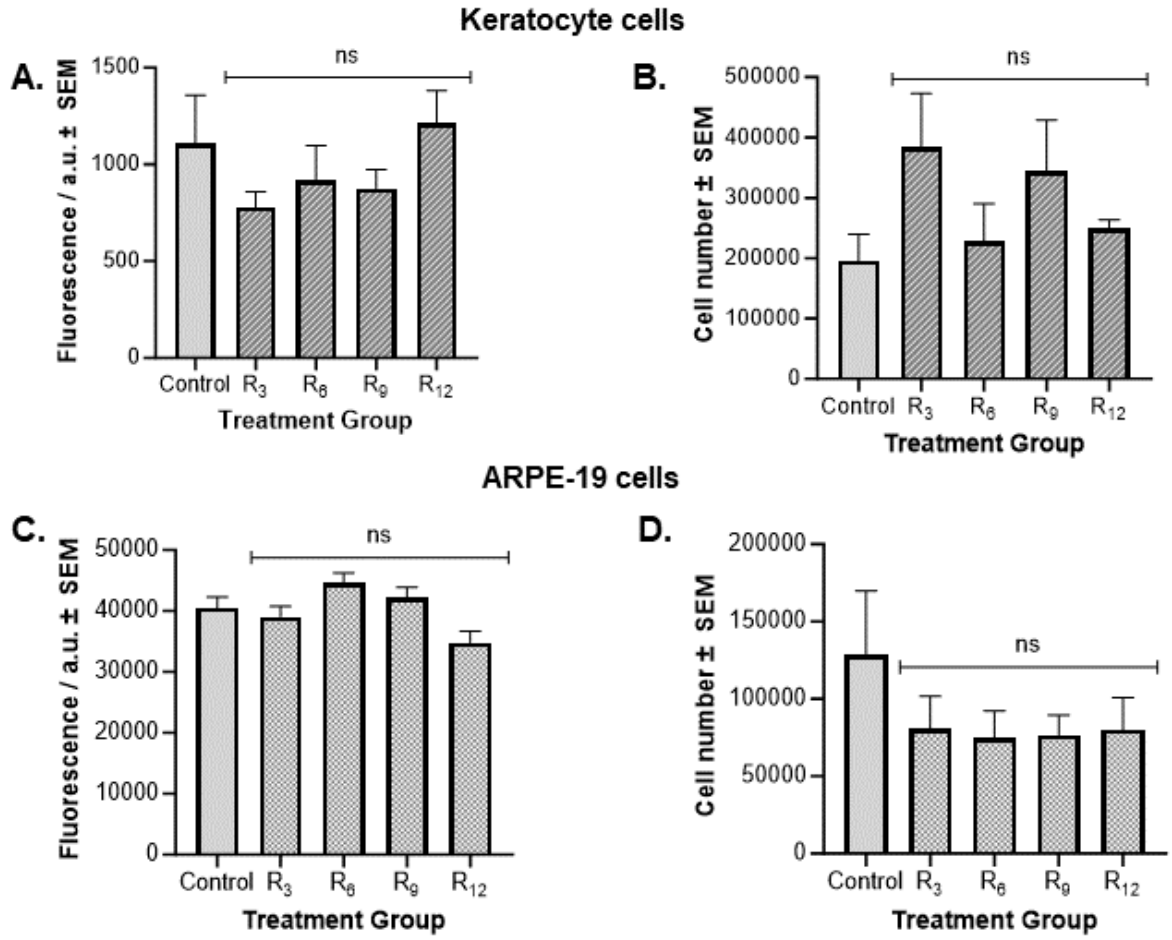


Figure 3. Cell toxicity of oligoarginine CPPs. *Metabolic rate of A) keratocyte and C) ARPE-19 cells following a 72-hour exposure to 56 µM oligoarginine treatments using AlamarBlue® assay. Data shows the mean fluorescence intensity ± SEM (n = 9) of AlamarBlue® reagent. Fluorescence intensity is measured in arbitrary units (a.u.). Cell number of B) Keratocyte and D) ARPE-19 cells after oligoarginine treatment. Data shows the mean cell number ± SEM (n = 9). Significance was taken at p≤0.05 using One-way ANOVA and Dunnett's post-hoc test. ns denotes no significance when compared to Control.*

Cell penetration by CPPs

To evaluate the penetration abilities of the peptides, keratocyte and ARPE-19 cells were treated with fluorescently-tagged oligoarginine CPPs (FAM-R_n) and the cell monolayer absorbance was monitored for bound/internalised CPPs fluorescence (*Figure 4*). A thorough washing procedure was employed to eliminate any remaining non-internalised or associated FAM-Rn. The level of oligoarginine present within cells in the monolayer was compared to that in untreated cells with no CPPs present (PBS control). In the keratocyte cell monolayers (*Figure 4A*), the data showed that the level of CPPs fluorescence found within or associated with the cell monolayer was significantly higher for all peptides compared to PBS control ($p < 0.001$). The calculated uptake concentrations for FAM-R_3, FAM-R_6, FAM-R_9, and FAM-R_{12} by keratocytes, as described in Section 2.8, were 8.0, 58.2, 62.7, and 48.9 nM, respectively. Additionally, cell monolayers treated with FAM-R_6, FAM-R_9, or FAM-R_{12} recorded a significantly higher level of fluorescence than the shorter peptide FAM-R_3 ($p < 0.001$). However, no significant differences in fluorescence intensity between FAM-R_6, FAM-R_9, and FAM-R_{12} treated keratocyte cells were recorded.

Similarly, within ARPE-19 cell monolayers (*Figure 4B*), cells treated with either length of oligoarginine presented statistically higher levels of fluorescence in comparison to the control cells ($p < 0.001$). An estimated 58.9 nM of FAM-R_3, 197.6 nM of FAM-R_6, 117.8 nM of FAM-R_9, and 34.6 nM of FAM-R_{12} penetrated ARPE-19 cells. However, in contrast to keratocyte cells, FAM-R_6-treated ARPE-19 cells displayed the highest level of fluorescence intensity, which was significantly different from the fluorescence levels observed in cells treated with FAM-R_3, FAM-R_9 and FAM-R_{12} ($p \leq 0.001$). Furthermore, the addition of FAM-R_9 resulted in a significantly higher level of fluorescence than both FAM-R_3 and FAM-R_{12} ($p \leq 0.001$), but no significant difference was observed between FAM-R_3 and FAM-R_{12} ($p > 0.066$).

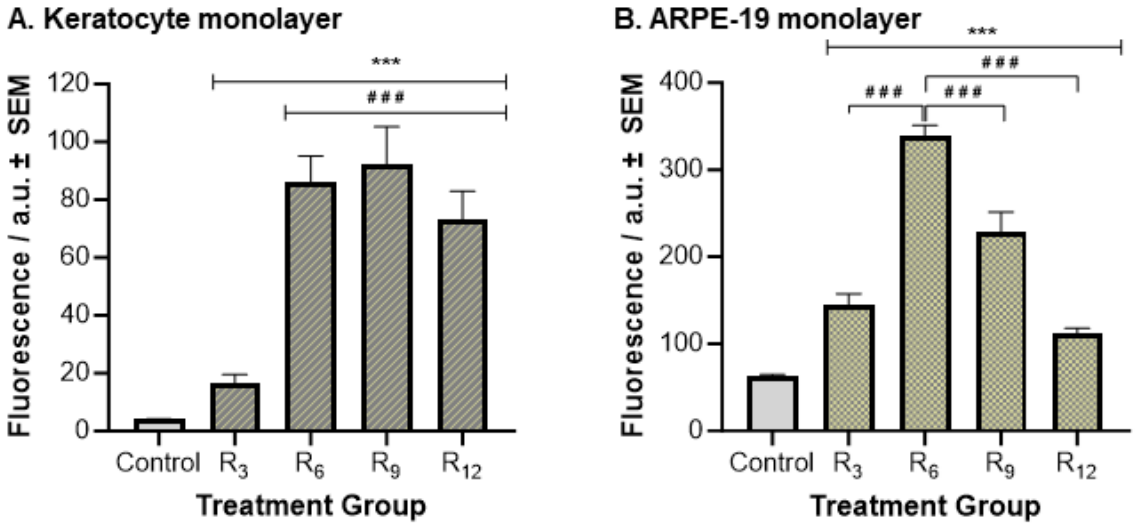


Figure 4. Oligoarginine CPPs accessing the cell monolayer of A) Keratocyte and B) ARPE-19 cells. Control samples denote PBS only treatment. *Fluorescence intensity is measured in arbitrary units (a.u.). All data is presented as the mean ± SEM (n = 24). Significance was taken at $p \leq 0.05$ using One-way ANOVA and Tukey's post-hoc test. ***$p < 0.001$ when compared to Control, ### $p < 0.001$ when A) compared to R_3 and B) between each pairwise comparison.*

CPPs effect on cell uptake of proteins

This study also examined the ability of different oligoarginine structures to carry proteins into the cell monolayers of keratocyte and ARPE-19 cells (*Figure 5*). BSA-TR was used as a model cargo for proteins, and the cell absorbance was monitored for BSA-TR fluorescence to measure BSA cellular uptake. For both keratocyte and ARPE-19 monolayer experiments, a significantly higher fluorescence intensity value was observed for cells treated with BSA-TR-only compared to the PBS-only control cells ($p \leq 0.001$). Thus, the BSA measurement served as a comparative control for the subsequent data analysis of BSA-TR delivery studies. In the keratocyte monolayers (*Figure 5A*), a significantly higher fluorescence intensity for BSA-TR was recorded in cells treated with all FAM-R_n/BSA-TR formulations compared to BSA control cells ($p \leq 0.001$). Concentrations of 254.1, 311.5, 347.4, and 579.3 ng/mL of BSA-TR cellular uptake were estimated for FAM-R_3, FAM-R_6, and FAM-R_9, and FAM-R_{12} containing formulations. Furthermore, an increasing trend between oligoarginine length and BSA-TR fluorescence intensity was observed, with chain length R_{12} recording the highest level of BSA-TR fluorescence. This intensity was significantly higher than FAM-R_3, FAM-R_6, and FAM-R_9 containing formulations ($p \leq 0.001$). Additionally, a statistically higher BSA-TR fluorescence level was recorded for FAM-R_9/BSA-TR treated cells than FAM-R_3/BSA-TR treated cells ($p = 0.005$).

In ARPE-19 monolayers (*Figure 5B*), all FAM-R_n/BSA-TR formulations led to a significant increase in BSA-TR fluorescence intensity compared to BSA control ($p \leq 0.001$), except for FAM-R_6/BSA-TR ($p = 0.488$). For FAM-R_3/BSA-TR, FAM-R_6/BSA-TR, and FAM-R_9/BSA-TR, and FAM-R_{12}/BSA-TR, approximately 91.8, 69.0, 115.1, and 111.5 ng/mL BSA-TR were taken up by ARPE-19 cells. Moreover, R_3, R_9, and R_{12} containing formulations led to significantly higher fluorescence levels for BSA-TR than the FAM-R_6/BSA-TR formulation ($p = 0.008$, $p \leq 0.001$, $p \leq 0.001$, respectively). No statistically significant fluorescence differences were recorded for the remaining pairwise comparisons in either cell line.

We also examined whether the presence of a protein cargo in the formulation influences the cell-penetrating abilities of CPPs by measuring the FAM-R_n signal in both cell lines. For both keratocyte and ARPE-19 cell monolayers, a minimal fluorescence signal was detected for BSA-TR when using FAM-R_n absorbance settings, which was not significantly different from PBS-only control ($p > 0.999$), indicating that there was no crossover in fluorescence readings between oligoarginine (i.e. FAM-R_n) and cargo (i.e. BSA-TR). In both keratocyte and ARPE-19 cells, the trend previously observed in the oligoarginine-only (FAM-R_n) monolayers (*Figure 4*) were similarly evident in the case of oligoarginine/cargo (FAM-R_n/BSA-TR) formulations. In the keratocytes, all FAM-R_n/BSA-TR formulations recorded a significantly higher FAM-R_n fluorescence intensity when compared to PBS control cells ($p \leq 0.001$), with longer chain CPPs containing formulations displaying significantly higher fluorescence levels for FAM-R_n than the shorter peptide FAM-R_3/BSA-TR formulation ($p \leq 0.001$). Concentrations of 15.9, 90.9, 95.2, and 88.6 nM of FAM-R_3, FAM-R_6, and FAM-R_9, and FAM-R_{12}, respectively, were estimated to have penetrated keratocyte cell monolayers. In ARPE-19 cells, all FAM-R_n/BSA-TR formulations recorded a significantly higher FAM-R_n fluorescence intensity when compared to PBS control cells ($p \leq 0.001$), with R_6 containing formulation displaying a significantly higher level of FAM-R_n fluorescence level than the other FAM-R_n/BSA-TR formulations ($p \leq 0.001$). The calculated uptake concentrations for FAM-R_3, FAM-R_6, and FAM-R_9, and FAM-R_{12} by ARPE-19 cells were 5.9, 117.9, 64.6, and 17.7 nM, respectively.

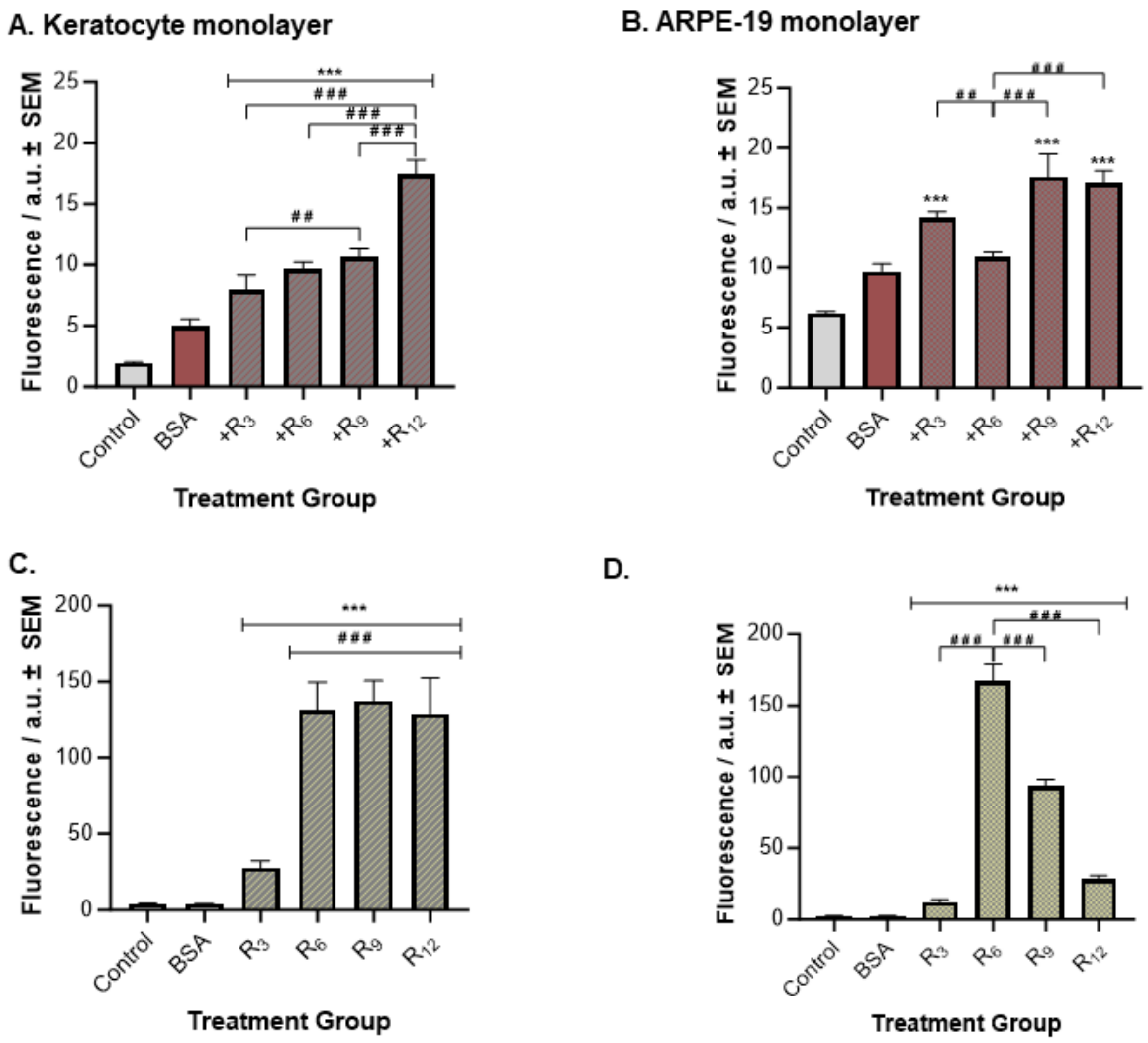


Figure 5. BSA-Oligoarginine complex uptake. *(A–B) BSA-TR fluorescence signal readings and (C–D) oligoarginine (FAM-R_n) fluorescence reading in Keratocyte and ARPE-19 cells. Control samples denote PBS-only treatment, and BSA samples denote BSA-TR-only control. Fluorescence intensity is measured in arbitrary units (a.u.). All data is presented as the mean ± SEM (n = 24). Significance was taken at $p \leq 0.05$ using One-way ANOVA and Tukey's post-hoc test. ***$p < 0.001$ when compared to (A–B) BSA control and (C–D) Control; ## $p < 0.01$ and ### $p < 0.001$ between each pairwise comparison.*

CPPs effect on cell uptake of small peptides

Just as proteins face challenges crossing cell membranes, small peptide-based therapies encounter the same limitations in drug delivery. Hence, we next investigated the ability of different oligoarginine CPPs to deliver small peptides into mammalian cells (*Figure 6*). ApoAI acts as a model small peptide, and it was fluorescently tagged with FAM to allow its measurement. For all experiments, a significantly higher fluorescence intensity value was observed for cells treated with FAM-ApoAI only compared to the PBS-only control cells ($p \leq 0.001$), and the FAM-ApoAI measurement was used as a comparative control for the following data analysis. In the keratocyte monolayers, only cells treated with the longer oligoarginines (i.e., R_6, R_9, R_{12}) in ApoAI formulations recorded significantly higher levels of FAM-ApoAI

fluorescence than ApoAI-only control cells ($p \leq 0.001$). Additionally, the longest chains of R_9 and R_{12} recorded significantly higher fluorescence levels than R_6-containing formulations ($p \leq 0.001$). No statistical difference in fluorescence intensity between R_9/FAM-ApoAI and R_{12}/FAM-ApoAI-treated cells was recorded ($p = 0.109$). In the ARPE-19 cells, only cells treated with R_3-, R_6-, and R_{12}-containing formulations significantly increased FAM-ApoAI fluorescence levels more than FAM-ApoAI control cells ($p \leq 0.001$). Unlike keratocyte cells, the shorter CPPs (i.e., R_3 and R_6) recorded the highest level of FAM-ApoAI fluorescence intensity compared to the longer CPP R_{12}-containing formulation ($p = 0.007$ and $p = 0.008$, respectively).

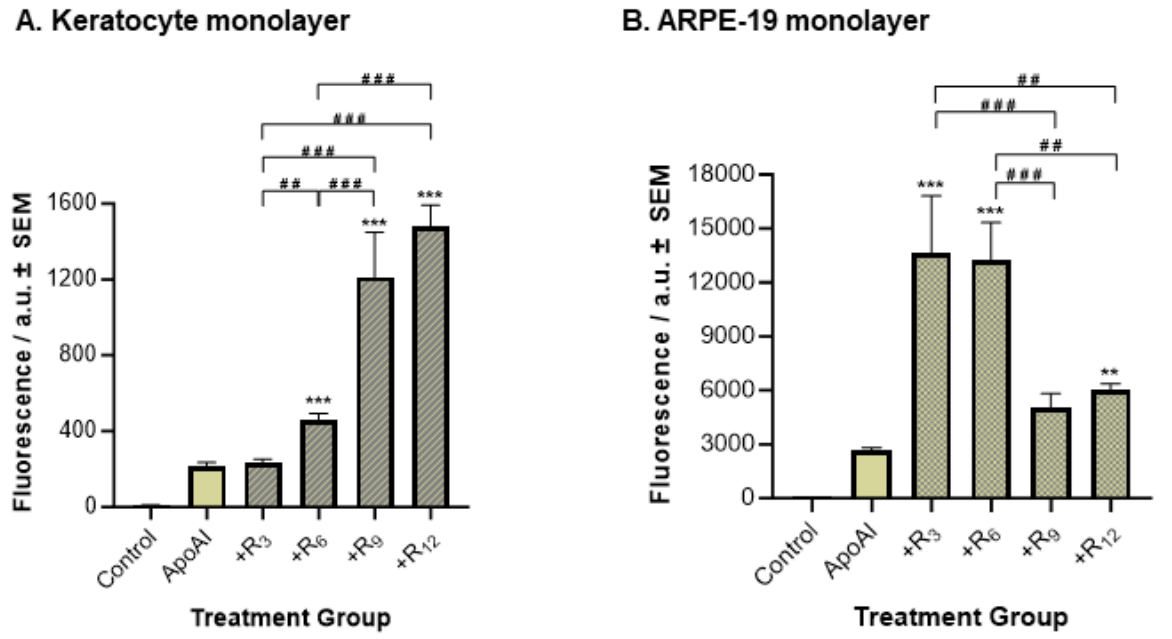


Figure 6. ApoAI uptake by A) Keratocyte and B) ARPE-19 cells. *Control samples denote PBS-only treatment and ApoAI denotes FAM-ApoAI only treatment. Fluorescence intensity is measured in arbitrary units (a.u.). All data is presented as the mean ± SEM (n = 6). Significance was taken at $p \leq 0.05$ using One-way ANOVA and Tukey's post-hoc test. ** $p < 0.01$ and *** $p < 0.001$ when compared to ApoAI control, ## $p < 0.01$ and ### $p < 0.001$ between each pairwise comparison.*

Discussion

In this study, we investigated the pore-forming abilities of oligoarginine peptides by utilising a carboxyfluorescein-containing liposomes, with R_9 being the only oligoarginine length causing a significant increase in fluorescence intensity. Additionally, the antibacterial efficacy of oligoarginine recorded differences depending on CPP length and bacterial class, with longer peptides exhibiting stronger antibacterial effects. Evaluation of mammalian cell toxicity showed no significant differences compared to control groups. Subsequent investigations on the membrane translocation abilities of oligoarginine in relevant *in vitro* cellular models relevant to ocular delivery revealed that both CPP translocation and cargo delivery across keratocyte and ARPE-19 cells were dependent on peptide length and cell type. Longer chains recorded a greater effect on cargo uptake in a corneal epithelium cell line (i.e. keratocyte cells), whereas shorter chains were more effective for cargo delivery in a retinal epithelium cell line (i.e. ARPE-19 cells).

Previous research investigating the role of oligoarginine peptides has identified multiple sequences that have proven effective in enhancing the penetration of therapeutic agents [16, 17]. To comprehensively understand the behaviour of oligoarginine peptides, we initially examined their ability to create pores and penetrate a phospholipid bilayer liposome. This experimental approach allowed us to simulate the interactions between CPPs and the cell membrane. However, the oligoarginine peptides exhibited negligible penetration into the liposomal structures. Notably, only R_9 showed an increase in fluorescence intensity of statistical significance compared to the control liposomes, suggesting some level of penetration through pore formation. This finding could suggest that pore formation might not be the primary mechanism responsible for cellular internalisation of the CPPs, with alternative processes such as endocytosis being their preferred mechanism [26].

The oligoarginines showed a stronger bacteriostatic effect on *S. aureus* than *E coli,* which agrees with *Sepahi et al.* (2017) [19]. This suggests that oligoarginine peptides may possess a stronger antibacterial effect against Gram-positive bacteria than Gram-negative bacteria. The species-related antimicrobial effect may be related to their different cell wall structures [27]. Additionally, in this study, we recorded a length-dependent antibacterial activity, as peptides with a larger number of arginine units, specifically R_9 and R_{12}, demonstrated greater antibacterial efficacy within an 18-hour exposure period. This is in line with previous work carried out by Duncan *et al.* (2021) that demonstrated that the antifungal effect of oligoarginine peptides varies based on the length of the arginine chains, with an oligoarginine consisting of 11 or more arginine residues required for an antifungal effect to be observed [28]. Similarly, Guzman *et al.* (2013) indicated that oligoarginines with more arginine residues generally exhibited a more potent antimicrobial effect [29]. Nevertheless, it is possible that the shorter oligoarginines, R_3 and R_6, may require a longer exposure period to observe their antibacterial effects, as a study by Nikoi *et al.* (2018) demonstrated that the oligoarginine R_6 displayed excellent antibacterial efficacy only after an extended incubation period of 15 days [13].

Importantly, although peptide length influenced their toxicity towards bacterial cells, none of the peptides exhibited cytotoxic effects on mammalian cells relevant to ocular drug delivery at a concentration of 56 μM. Our experiments involving keratocytes and ARPE-19 cells indicated that oligoarginines had no significant impact on either the metabolic rate or the cell number. These findings align with existing literature studies that have demonstrated the non-cytotoxic nature of oligoarginines such as R_6 and R_7 in other cell lines [9, 30].

The ability of oligoarginine peptides to penetrate cells has been extensively documented in scientific literature [26, 31, 32]. Furthermore, studies involving oligoarginines coupled directly onto target compounds have revealed that the length of the arginine chain can influence cellular uptake [33]. However, to the best of our knowledge, the suitability of oligoarginines and the influence of chain length have not been specifically examined in cells relevant to ocular delivery despite the evident potential for this technology to enhance AMD clinical treatments significantly. Therefore, we evaluated the cell-penetrating abilities of oligoarginines in the presence and absence of a protein cargo in both human keratocyte (i.e. corneal epithelium component) and ARPE-19 (i.e. retinal blood barrier cellular model) cells [23, 24]. Our study revealed that the cell-penetrating capabilities of oligoarginines depend on both the length of the peptide and the specific cell line. In both cell lines, all tested oligoarginine lengths (R_3, R_6, R_9, and R_{12}) demonstrated successful translocation into the cells at concentrations significantly higher than the control cells, regardless of the presence or absence of a protein cargo. However, in keratocyte cells, R_6, R_9, and R_{12} exhibited significantly greater translocation capabilities than R_3, with no significant differences observed among the three longer chain lengths. This

suggests that once a threshold level of six arginine residues is reached, penetration into the keratocyte cell is achieved, irrespective of further increases in peptide chain length. Therefore, no optimal oligoarginine length was identified for corneal epithelium penetration. This trend remained consistent even when the peptides were incubated with the protein cargo. On the other hand, in ARPE-19 cells, R_6 displayed the highest level of cell penetration, significantly surpassing all other chain lengths, while R_3 and R_{12} showed the lowest level of penetration. This pattern persisted regardless of the presence or absence of the protein cargo, indicating R_6 may be the optimal length for effective penetration across the retinal–blood barrier.

Following the identification of trends in cell translocation of oligoarginines, their ability to deliver cargo was evaluated. To mimic drug delivery relevant to current AMD therapeutics (i.e., anti-VEGF agents), BSA was employed as a model protein cargo for anti-VEGF agents. In contrast, ApoAI, a novel candidate in AMD therapeutics, was used as a model for small peptide drugs [2, 3]. Contrary to the observed trend in cell translocation of oligoarginines in the keratocyte cell line, a positive relationship between drug delivery and peptide length was indicated. Specifically, an increase in cellular uptake of both large and small molecule cargo was noted as the chain length of oligoarginine peptides increased, with R_{12} or both R_{12} and R_9 demonstrating the highest level of BSA or ApoAI delivered to keratocyte cells, respectively.

Additionally, a contradicting trend to the peptide cell translocation was discerned in the capability of oligoarginines to deliver a protein cargo in the ARPE-19 cells. We identified R_6 as the optimal oligoarginine chain length for achieving effective cell penetration across a cellular model of the retinal blood barrier. However, R_6 exhibited the lowest level of BSA delivery into ARPE-19 cells, which was not significantly different from control cells. Therefore, the penetration abilities of oligoarginine might not translate to its drug delivery abilities. Nevertheless, in the context of small peptide cargo (i.e., ApoAI), the shorter oligoarginine lengths, R_3 and R_6, recorded the highest level of ApoAI delivery in ARPE19 cells. This contrasts with the findings in keratocyte cells, where peptides with more arginine residues (i.e., R_9 and R_{12}) showed superior cell delivery of ApoAI. The cell-dependent differences could indicate the interaction of oligoarginine with various transporters or other components representative of each cell line, as both the retinal epithelium and the corneal epithelium constitute a different protein expression profile [34–36].

Additionally, it could indicate the possibility of utilising chain length as a tool in the formulation process to selectively target specific regions of the eye. For instance, longer chain lengths may exhibit greater efficacy in delivering drugs to the anterior part of the eye, while shorter oligoarginines may be more suitable for the posterior region. Alternatively, a combination of shorter and longer oligoarginine variants may be the preferred approach to achieve a more uniform drug distribution throughout the eye.

Therefore, the penetration and drug delivery abilities of oligoarginines are dependent on the number of arginine units, cell type, and cargo type. However, it is important to note that the observed differences could also be influenced by the different concentrations used in these experiments, as the study by Tünnemann *et al.* (2008) suggests that the concentration of the peptide has an effect as well as the chain length [17]. As our study only evaluated the drug delivery potential of different lengths of oligoarginine CPPs in *in vitro* cellular models, future work should focus to corroborate these findings using *ex vivo* and *in vivo* models for ocular delivery, and additional mechanistic studies are required to further elucidate the interaction of oligoarginines with cell membranes and their components to provide better insights into their cellular translocation mechanisms.

Conclusion

This study provides insights into the intricate relationship between the structural characteristics of oligoarginine CPPs, their ability to penetrate mammalian cell types, and their potential to facilitate large and small-sized cargo delivery into cells, particularly in the context of topical ocular drug delivery. Our research proposes that the length and structure of oligoarginine could be used as a strategic tool in the formulation process to selectively target distinct eye regions. This includes using shorter chains for the posterior region of the eye, longer chains for the anterior segment, or a combination of both. Notably, pore formation did not appear to be the primary mechanism of oligoarginine-based delivery, with R_9 being the sole peptide showing some degree of pore formation. In addition to oligoarginine drug delivery abilities, their antibacterial efficacy was contingent on the number of arginine residues and the specific bacterial species. It is worth emphasising that none of the evaluated oligoarginine structures exhibited toxicity towards mammalian cells relevant to the ocular barrier. This study extends our understanding of the applicability of oligoarginine CPPs as penetration enhancers for improving the delivery of therapeutics in an ocular topical formulation within the clinical context of AMD.

Declaration of Competing Interest: The authors declare no competing interests.

Acknowledgements: This study was supported by the Engineering and Physical Sciences Research Council (EPSRC) (EP/S023054/1, Stefana Duca) and a Royal Academy of Engineering Enterprise Fellowship (EF1920\9\162, Naa Dei Nikoi). The graphical abstract was created with BioRender.com.

Data Availability: Data will be made available on request.

References:

1. Xie, J., et al., *Cell-Penetrating Peptides in Diagnosis and Treatment of Human Diseases: From Preclinical Research to Clinical Application.* Front Pharmacol, 2020. **11**: p. 697. https://doi.org/10.3389/fphar.2020.00697
2. Kovach, J.L., et al., *Anti-VEGF Treatment Strategies for Wet AMD.* J Ophthalmol, 2012. **2012**: p. 786870. https://doi.org/10.1155/2012/786870
3. Rudolf, M., et al., *ApoA-I Mimetic Peptide 4F Reduces Age-Related Lipid Deposition in Murine Bruch's Membrane and Causes Its Structural Remodeling.* Curr Eye Res, 2018. **43**(1): p. 135–146. https://doi.org/10.1080/02713683.2017.1370118
4. Eghøj, M.S. and T.L. Sørensen, *Tachyphylaxis during treatment of exudative age-related macular degeneration with ranibizumab.* Br J Ophthalmol, 2012. **96**(1): p. 21–23. https://doi.org/10.1136/bjo.2011.203893
5. Hara, C., et al., *Tachyphylaxis during treatment of exudative age-related macular degeneration with aflibercept.* Graefes Arch Clin Exp Ophthalmol, 2019. **257**(11): p. 2559–2569. https://doi.org/10.1007/s00417-019-04456-2
6. Inan, S., Z. Baysal, and U.U. Inan, *Long-Term Changes in Submacular Choroidal Thickness after Intravitreal Ranibizumab Therapy for Neovascular Age-Related Macular Degeneration: 14-Mo Follow-Up.* Curr Eye Res, 2019. **44**(8): p. 908–915. https://doi.org/10.1080/02713683.2019.1600195
7. Urban, B., M. Szwabowicz, and A. Bakunowicz-Łazarczyk, *Effect of Repeated Intravitreal Ranibizumab and Aflibercept Injections on the Cornea in Patients with*

Age-Related Macular Degeneration. J Ophthalmol, 2020. **2020**: p. 4928905. https://doi.org/10.1155/2020/4928905

8. Chen, C., et al., *Anti-angiogenesis through noninvasive to minimally invasive intraocular delivery of the peptide CC12 identified by in vivo-directed evolution.* Biomaterials, 2017. **112**: p. 218–233. https://doi.org/10.1016/j.biomaterials.2016.09.022
9. de Cogan, F., et al., *Topical Delivery of Anti-VEGF Drugs to the Ocular Posterior Segment Using Cell-Penetrating Peptides.* Invest Ophthalmol Vis Sci, 2017. **58**(5): p. 2578–2590. https://doi.org/10.1167/iovs.16-20072
10. Mitchell, D.J., et al., *Polyarginine enters cells more efficiently than other polycationic homopolymers.* J Pept Res, 2000. **56**(5): p. 318–325. https://doi.org/10.1034/j.1399-3011.2000.00723.x
11. Morishita, M., et al., *A novel approach using functional peptides for efficient intestinal absorption of insulin.* J Control Release, 2007. **118**(2): p. 177–184. https://doi.org/10.1016/j.jconrel.2006.12.022
12. Rothbard, J.B., et al., *Conjugation of arginine oligomers to cyclosporin A facilitates topical delivery and inhibition of inflammation.* Nat Med, 2000. **6**(11): p. 1253–1237. https://doi.org/10.1038/81359
13. Nikoi, N.D., et al., *Stability of Cell-Penetrating Peptide anti-VEGF Formulations for the Treatment of Age-Related Macular Degeneration.* Curr Eye Res, 2021. **46**(5): p. 751–757. https://doi.org/10.1080/02713683.2020.1830117
14. Allolio, C., et al., *Arginine-rich cell-penetrating peptides induce membrane multilamellarity and subsequently enter via formation of a fusion pore.* Proc Natl Acad Sci U S A, 2018. **115**(47): p. 11923–11928. https://doi.org/10.1073/pnas.1811520115
15. Mäger, I., et al., *Assessing the uptake kinetics and internalization mechanisms of cell-penetrating peptides using a quenched fluorescence assay.* Biochimica et Biophysica Acta (BBA) - Biomembranes, 2010. **1798**(3): p. 338–343. https://doi.org/10.1016/j.bbamem.2009.11.001
16. Futaki, S., et al., *Arginine-rich peptides. An abundant source of membrane-permeable peptides having potential as carriers for intracellular protein delivery.* J Biol Chem, 2001. **276**(8): p. 5836–5840. https://doi.org/10.1074/jbc.M007540200
17. Tünnemann, G., et al., *Live-cell analysis of cell penetration ability and toxicity of oligo-arginines.* J Pept Sci, 2008. **14**(4): p. 469–476. https://doi.org/10.1002/psc.968
18. Gribova, V., et al., *Polyarginine as a Simultaneous Antimicrobial, Immunomodulatory, and miRNA Delivery Agent within Polyanionic Hydrogel.* Macromol Biosci, 2022. **22**(6): p. e2200043. https://doi.org/10.1002/mabi.202200043
19. Sepahi, M., R. Jalal, and M. Mashreghi, *Antibacterial activity of poly-l-arginine under different conditions.* Iran J Microbiol, 2017. **9**(2): p. 103–111.
20. Lei, J., et al., *The antimicrobial peptides and their potential clinical applications.* Am J Transl Res, 2019. **11**(7): p. 3919–3931.
21. Li, S.K., M.R. Liddell, and H. Wen, *Effective electrophoretic mobilities and charges of anti-VEGF proteins determined by capillary zone electrophoresis.* J Pharm Biomed Anal, 2011. **55**(3): p. 603–607. https://doi.org/10.1016/j.jpba.2010.12.027
22. Jimah, J.R., P.H. Schlesinger, and N.H. Tolia, *Liposome Disruption Assay to Examine Lytic Properties of Biomolecules.* Bio Protoc, 2017. **7**(15). https://doi.org/10.21769/BioProtoc.2433
23. Funderburgh, J.L., *The Corneal Stroma*, in *Encyclopedia of the Eye*, D.A. Dartt, Editor. 2010, Academic Press: Oxford. p. 515–521. https://doi.org/10.1016/B978-0-12-374203-2.00070-1

24. Mannermaa, E., et al., *Filter-cultured ARPE-19 cells as outer blood-retinal barrier model.* Eur J Pharm Sci, 2010. **40**(4): p. 289–296. https://doi.org/10.1016/j.ejps.2010.04.001
25. O'Brien, J., et al., Investigation of the Alamar Blue (resazurin) fluorescent dye for the assessment of mammalian cell cytotoxicity. Eur J Biochem, 2000. 267(17): p. 5421-6. https://doi.org/10.1046/j.1432-1327.2000.01606.x
26. Lättig-Tünnemann, G., et al., *Backbone rigidity and static presentation of guanidinium groups increases cellular uptake of arginine-rich cell-penetrating peptides.* Nat Commun, 2011. **2**: p. 453. https://doi.org/10.1038/ncomms1459
27. Rezansoff, A.J., et al., *Interactions of the antimicrobial peptide Ac-FRWWHR-NH(2) with model membrane systems and bacterial cells.* J Pept Res, 2005. **65**(5): p. 491–501. https://doi.org/10.1111/j.1399-3011.2005.00263.x
28. Duncan, V., et al., *Preliminary Characterization of NP339, a Novel Polyarginine Peptide with Broad Antifungal Activity.* Antimicrob Agents Chemother, 2021. **65**(8): p. e0234520. https://doi.org/10.1128/AAC.02345-20
29. Guzmán, F., et al., *Inhibitory effect of short cationic homopeptides against gram-positive bacteria.* J Pept Sci, 2013. **19**(12): p. 792–800. https://doi.org/10.1002/psc.2578
30. Kumar, S., et al., *Peptides as skin penetration enhancers: mechanisms of action.* J Control Release, 2015. **199**: p. 168–178. https://doi.org/10.1016/j.jconrel.2014.12.006
31. Copolovici, D.M., et al., *Cell-penetrating peptides: design, synthesis, and applications.* ACS Nano, 2014. **8**(3): p. 1972–1994. https://doi.org/10.1021/nn4057269
32. Ye, J., et al., *CPP-Assisted Intracellular Drug Delivery, What Is Next?* Int J Mol Sci, 2016. **17**(11). https://doi.org/10.3390/ijms17111892
33. Oh, D., et al., *Enhanced cellular uptake of short polyarginine peptides through fatty acylation and cyclization.* Mol Pharm, 2014. **11**(8): p. 2845–2854. https://doi.org/10.1021/mp500203e
34. Juuti-Uusitalo, K., et al., *Efflux protein expression in human stem cell-derived retinal pigment epithelial cells.* PLoS One, 2012. **7**(1): p. e30089. https://doi.org/10.1371/journal.pone.0030089
35. Mannermaa, E., et al., *Efflux protein expression in human retinal pigment epithelium cell lines.* Pharm Res, 2009. **26**(7): p. 1785–791. https://doi.org/10.1007/s11095-009-9890-6
36. Vellonen, K.S., et al., *Effluxing ABC transporters in human corneal epithelium.* J Pharm Sci, 2010. **99**(2): p. 1087–1098. https://doi.org/10.1002/jps.21878

Appendix 2: Wettability and Bactericidal Properties of Bioinspired ZnO Nanopillar Surfaces

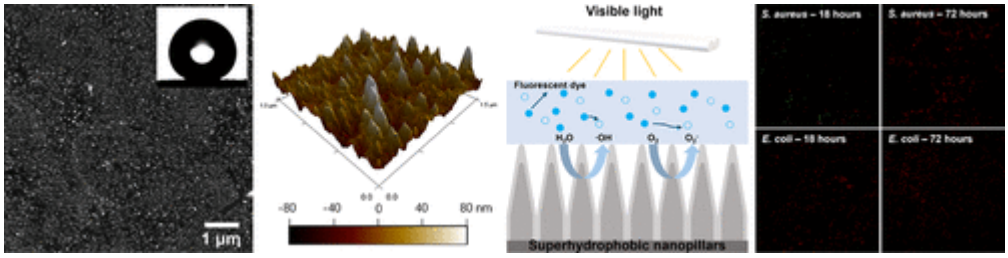
Appendix 2 presents a paper that I contributed to that was submitted to Langmuir in 2024. This paper investigates the use of zinc oxide nanopillars for the development of antibiofouling surfaces. I collaborated with the authors from the University of Birmingham to investigate the cytotoxicity profile of these ZnO surfaces on mammalian cells. I concluded that these antimicrobial surfaces did not display cytotoxic activity. This data is presented in the supplementary results in section S12 (Figure S22).

Wettability and Bactericidal Properties of Bioinspired ZnO Nanopillar Surfaces

Jitao Zhang[a] , Georgia Williams[b] , Thanaphun Jitniyom[a] , Navdeep Sangeet Singh[a] , Alexander Saal[a] , Lily Riordan[c] , Madeline Berrow[c] , James Churm[a] , Manuel Banzhaf[b#*] , Felicity de Cogan[c*] , Nan Gao[a*]

[a] School of Engineering, University of Birmingham, Edgbaston, Birmingham, B15 2TT, United Kingdom
[b] School of Biosciences, University of Birmingham, Edgbaston, Birmingham, B15 2TT, United Kingdom
[c] School of Pharmacy, University of Nottingham, University Park, Nottingham, NG7 2RD, United Kingdom
[*] Email: n.gao@bham.ac.uk
[*] Email: Felicity.DeCogan@nottingham.ac.uk
[*] Email: m.banzhaf@bham.ac.uk

Graphical Abstract



Abstract

Nanomaterials of zinc oxide (ZnO) exhibit antibacterial activities under ambient illumination that result in cell membrane permeability and disorganization, representing an important opportunity for health-related applications. However, the development of antibiofouling surfaces incorporating ZnO nanomaterials has remained limited. In this work, we fabricate superhydrophobic surfaces based on ZnO nanopillars. Water droplets on these superhydrophobic surfaces exhibit small contact angle hysteresis (within 2–3°) and a minimal tilting angle of 1°. Further, falling droplets bounce off when impacting the superhydrophobic ZnO surfaces with a range of Weber numbers (8–46), demonstrating that the surface facilitates a robust Cassie–Baxter wetting state. In addition, the antibiofouling efficacy of the surfaces has been established against model pathogenic Gram-positive bacteria *Staphylococcus aureus* (*S. aureus*) and Gram-negative bacteria *Escherichia coli* (*E. coli*). No viable colonies of *E. coli* were recoverable on the superhydrophobic surfaces of ZnO nanopillars incubated with cultured bacterial solutions for 18 h. Further, our tests demonstrate a substantial reduction in the quantity of *S. aureus* that attached to the superhydrophobic ZnO nanopillars. Thus, the superhydrophobic ZnO surfaces offer a viable design of antibiofouling materials that do not require additional UV illumination or antimicrobial agents.

Introduction

The formation of biofilms on the surface of medical devices and implants is a major cause of nosocomial or healthcare-associated infections. (1−5) The spreading and adhesion of bacteria are often more severe in the presence of liquid, for example, in the forms of slug flow and intermittent droplets. (6−9) It is therefore necessary to design surfaces that are not only liquid repellent but also resistant to biological contamination in order to prevent initial bacterial attachment. In recent years, there has been a lot of research toward the use of superhydrophobic surfaces to reduce bacterial adhesion and, thus, biofilm formation. (10−13) Superhydrophobic surfaces often rely on low-surface-energy coatings on nanostructures with a particular roughness. This allows a droplet to exhibit the so-called Cassie–Baxter wetting state on the surface with large contact angles greater than 150°. (14) More specifically, the key feature of the Cassie–Baxter state is that the droplet is partially supported by the surface nanostructure and partially suspended on air pockets entrapped underneath the droplet. (15−18)

The presence of air pockets minimizes the effective contact area between the liquid (e.g., bacteria-containing droplets) and the surface, thereby reducing interfacial adhesion. By contrast, recent studies have even demonstrated that the absence of air pockets greatly promotes bacterial adhesion. (19−22) Further, natural superhydrophobic surfaces such as cicada wings that facilitate the Cassie–Baxter wetting state have been shown to feature bactericidal properties, which are attributed to their rigid surface nanopillars resulting in direct bacterial membrane puncture. (23,24) It is thus desirable to make a surface intrinsically superhydrophobic and bactericidal, in order to achieve long-term antibiofouling effect. One of the approaches commonly used to make superhydrophobic surfaces is to coat a structured substrate with polydimethylsiloxane (PDMS), which is hydrophobic with static contact angles on the order of 100°. (25,26) PDMS, due to its flexibility, transparency, and biocompatibility, has been applied in a wide range of industrial and scientific applications, especially in biomedical devices, such as catheters and microfluidic devices. (27−29) However, PDMS is generally considered to be biologically inert, despite its inherent hydrophobicity. This means that PDMS does not interact with or directly affect microorganisms, and therefore, it does not have inherent antimicrobial properties of its own. As such, PDMS coatings can become contaminated and retain bacteria that are able to multiply and form biofilms in the absence of appropriate cleaning and sterilization protocols. (30)

By contrast, metal-oxide photocatalysts, such as TiO_2 and ZnO, have demonstrated antimicrobial properties, which are attributed to the reactive free radicals generated under illumination. (31−36) Specifically, their photocatalytic activities can either lead to cell membrane disorganization or induce oxidative stress in bacterial cells. Of particular interest is ZnO, which can exhibit photocatalytic activities under ambient illumination. (31−33) Yet, ZnO is intrinsically hydrophilic, which is undesired for applications that require low interfacial adhesion. In this work, we report the development of superhydrophobic surfaces based on PDMS-coated ZnO nanopillars that exhibit promising antibiofouling properties. Droplets of water on these superhydrophobic surfaces exhibit a large advancing contact angle of around 154° and a receding contact angle of around 152°, enabling a low tilt angle of 1°. Furthermore, the experimental results show that the superhydrophobic surfaces of PDMS-coated ZnO nanopillars can effectively kill Gram-negative bacterium *Escherichia coli* (*E. coli*) and inhibit the Gram-positive bacterium *Staphylococcus aureus* (*S. aureus*). The results reported here

generate insight into the combination of superhydrophobicity and bactericidal activity, which could facilitate a platform for the design of antibiofouling materials.

Experimental Section

Materials

Pure zinc foils (99.9%, 0.62 mm in thickness) were purchased from Fisher Scientific (UK) as the substrate for the fabrication of ZnO nanopillars. Sodium hydroxide (NaOH) pellets and zinc nitrate hexahydrate pellets ($Zn(NO_3)_2 \cdot 6H_2O$) were purchased from Sigma-Aldrich (UK). Polydimethylsiloxane (PDMS), SYLGARD 184 Silicone elastomer curing agent, and ethyl acetate (Sigma-Aldrich, UK) were used to coat the ZnO nanopillars. Ethanol, acetone, and deionized (DI) water were used to clean the bare substrates. *S. aureus* and *E. coli* were used in the bactericidal efficacy testing. The LIVE/DEAD BacLight bacterial viability kit was purchased from Fisher Scientific (UK).

Devices

Goniometer

Contact angle (CA) measurements were made with a DataPhysics OCA15EC goniometer. The static CAs were measured by dosing a water droplet of up to 12 μL on bare zinc, ZnO nanopillars, or PDMS-coated nanopillar surfaces. For the dynamic CAs (advancing and receding contact angles), the volume of the droplet was increased or decreased at a dosing rate of 1 μL/s each time. The image and video results were captured by the 6.5-fold zoom lens of the goniometer itself.

X-ray Diffractometer

X-ray diffraction (XRD) data was collected using a Proto AXRD Benchtop diffractometer (Proto, USA) operated at 30 kV and 20 mA with a Cu Kα source (λ = 1.54251 Å). The samples were analyzed over the 2θ range of 20–80° using 0.0149° increments.

Fourier Transform Infrared Spectrometer

Fourier transform infrared (FTIR) results were obtained using a Nicolet iS50 FTIR spectrometer. All spectra were recorded in the range of 4000 to 400 cm^{-1}, with a spectral resolution of 4 cm^{-1} in both absorbance and reflectance mode with the ATR module. Measurements were taken with 256 coadded scans.

Microplate Reader

Photocatalytic performance was measured using a BMG Labtech CLARIOstar Plus plate reader in fluorescence intensity mode to quantify the degradation rate of fluorescent dye CF633. An excitation wavelength of 625 ± 10 nm and an emission wavelength of 650 ± 20 nm were set for the fluorescence intensity mode. Thirty microliters of 0.01 mg/mL fluorescent dye was placed on different surfaces. Degradation was monitored indoors under ordinary lighting conditions with a light intensity of 400 lx, and the distance between the light source and the sample was 2.5 m. The experiment was repeated three times under the same lighting condition, with readings taken every 1 h.

Scanning Electron Microscopy (SEM)

SEM images were taken using Zeiss EVO 10 Materials SEM and Thermo Scientific Apreo 2S SEM at an acceleration voltage of 5.0–15.0 kV. PDMS-coated samples were coated with 8 nm of Au by sputter deposition before analysis. Bare zinc and ZnO nanopillar samples offered good conductivity but were also coated with gold layers to ensure consistency of the observation parameters.

Atomic Force Microscopy (AFM)

AFM studies were carried out using a Cypher S AFM instrument from Oxford Instruments. The AFM images were taken using the air contact mode (tapping mode), with a scan size of 3 × 3 or 1 × 1 μm^2 at a scan rate of 1.0 Hz.

High-Speed Videos

Water droplet impact behaviors were captured using a high-speed camera (FASTCAM Mini UX100, Photron) at a frame rate of 1000 fps.

Confocal Microscopy

Fluorescent images of LIVE/DEAD bacterial populations were captured using the Leica TCS SP8 confocal microscope (with a 40×/1.40 oil objective). Immersion oil (Immersol 518 F) was utilized to cover the sample surfaces. The excitation wavelength was at 488nm for the LIVE green signal SYTO 9 and 561 nm for the DEAD red signal propidium iodide.

Fabrication and Modification of ZnO Nanopillars

The zinc foils were cut into small substrates with the dimensions of 1 × 1 cm. Since zinc foils are very susceptible to oxidation, they were first polished with fine sandpaper to remove organic residues and natural oxide layers before washing with copious amounts of DI water. The zinc substrates were then ultrasonically degreased in ethanol, acetone, and DI water for 5 min each. The surfaces were afterward dried with nitrogen (N_2) flow and stored under desiccation in a sealed container or vacuum desiccator. Subsequently, a two-step fabrication process was used to fabricate superhydrophobic ZnO nanopillar structures on zinc foil surfaces. A hydrothermal synthesis method was used as the first step to grow ZnO nanopillars. Typically, 35 mL of 0.43 mol/L zinc nitrate hexahydrate ($Zn(NO_3)_2 \cdot 6H_2O$) was poured into 35 mL of 3.43 mol/L sodium hydroxide (NaOH) to form an alkaline zincate solution. The cleaned zinc substrate was then dipped into the solution and placed on a stirring hot plate with the beaker sealed at 100 °C for 45 min. During this process, a concentration gradient of zincate ions was created near the zinc substrate, eventually forming ZnO nanopillars. (37) After 45 min, the zinc substrate was removed from the solution and dried using nitrogen flow after rinsing with DI water. Then, the wettability of the nanopillars was modified by coating the surfaces with a thin PDMS layer. Typically, the PDMS solution was prepared by mixing 1 mL of PDMS, 0.1 mL of silicone elastomer curing agent, and 100 mL of ethyl acetate. It was stirred at 250–280 rpm in a beaker at room temperature. After the solution preparation, the surfaces of ZnO nanopillars were drop-casted with 5 μL of well-stirred PDMS solution for a thin layer of coating and then placed in an oven at 80 °C for 6 h to cure.

Bacterial Culture Preparation

Both *E. coli* ATCC25922 and *S. aureus* ATCC6528 were cultured in 5 mL of lysogeny broth (LB) overnight at 37 °C for ≈18 h with shaking at 180 rpm. The culture was then adjusted to ≈1×10^9 (colony-forming units) CFU mL^{-1}.

Agar Plate Preparation

LB Agar was prepared following the manufacturer's instructions and autoclaved for sterility. After removal from the autoclave, a brief cooling period of approximately 5 min was allowed, followed by gentle shaking to ensure homogeneity. The agar was then poured into plates near a Bunsen flame, ensuring coverage of the bottom of the plate with the agar. A minimum of 12 plates (with three plates for each type of sample, including control, bare zinc, ZnO nanopillars, and PDMS-coated nanopillars) were prepared for the experiment. Each agar plate was sectioned into eight segments labeled from A to H, as shown in Figure S1a.

Antibiofouling Efficacy Testing

All sample surfaces were incubated with cultured bacterial solutions for 18 and 72 h. The surfaces were inoculated with the bacterial suspensions in a 3 × 3 grid of 1 μL aliquots of bacterial culture across the sample surfaces, as shown in Figure S1b. The PDMS-coated ZnO nanopillar surfaces were an exception because of their superhydrophobicity, which allowed small droplets to roll off easily. Instead, a single 9 μL droplet was carefully pipetted onto the surface of PDMS-coated ZnO nanopillars. After the incubation, the samples were transferred into 15 mL centrifuge tubes containing 10 mL of Dey-Engley neutralizing broth, each accompanied by 7–10 sterile zirconium beads. Subsequently, the tubes were vortex-mixed for 1 min. Serial dilution of 1:3 (eight times) in sterile phosphate-buffered saline (PBS) within a 96-well plate was then carried out using the neutralizing broth suspension. Each row of broth corresponded to the previously sectioned agar plate.

Subsequently, three 10 μL droplets from each row of the PBS solutions that had been serially diluted in the 96-well plate were spotted in their designated sections on the LB agar plates, as shown in Figure S1c. Three sets of repeats for each surface were prepared. The plates were then allowed to dry thoroughly around a Bunsen burner. Once all plates had dried, they were placed in a static incubator at 37 °C for 16–18 h. The plates were removed from the incubator the following day, and the survival of the bacteria was assessed by counting colony-forming units (CFU), where colony numbers were multiplied by the relevant dilution factor. (38) The limit of detection for the assay was set to 1×10^3 CFU.

Samples Fixation for Scanning Electron Microscopy (SEM)

Bacterial suspensions were incubated on the surfaces as per the test procedure "antibiofouling efficacy testing" described previously. After 16–18 h of incubation, samples were fixed in 4% paraformaldehyde for 1 h, followed by dehydration in a series of ethanol solutions. These solutions consisted of 5 mL of mixtures of PBS/ethanol, with ethanol content increasing incrementally from 10 to 100% at the concentrations of 10, 30, 50, 70, 90, and 100%. Samples were incubated in each ethanol solution for 10 min and twice in the 100% ethanol solution. Following the treatment with these solutions, the samples were subjected to a 10 min incubation in hexamethyldisilazane (HMDS) solution. They were then placed in a fume hood to allow sufficient time for the evaporation and drying. Following this time, the samples were further prepared for observation by using SEM.

Confocal Microscopy

Preparation for confocal microscopy was performed following bacterial incubation on the surfaces described in the test procedure "antibiofouling efficacy testing". After the incubation period, each surface was gently washed with PBS (up to 40 μL) to ensure removal of any residual media. The surfaces were then covered with glass coverslips before using the confocal laser scanning microscope. One to two drops of immersion oil (Immersol 518 F) were added to the top of the glass coverslip for the imaging process to increase the resolution of the microscope.

Multicycle Surface Tests

A series of multicycle surface tests were performed across 3 × 18 or 5 × 18 h of incubation periods. The "antibiofouling efficacy testing" procedure was then followed for each multicycle test. Each test was subjected to a set of three repeats per surface type. After each test cycle, the surfaces were gently washed by using fresh sterile water. The surfaces were then left to dry thoroughly at room temperature with good ventilation for 1 h before being used for the next set of tests.

Cytotoxicity Tests

Murine 3T3 fibroblast cells were cultured in Dulbecco's Modified Eagle Medium (DMEM) supplemented with 10% newborn calf serum, 4 mM GlutaMAX, 100 IU/mL penicillin, 100 μg/mL streptomycin, and 20 mM HEPES (4-(2-hydroxyethyl)-1-piperazineethanesulfonic acid). The revived cell solutions were then seeded in Corning T75 cell culture flasks and incubated for 48 h at 37 °C with 5% CO_2. Subsequently, cell attachment and growth were monitored under a phase-contrast microscope, and fresh culture medium was replenished every 2–3 days. When a confluent monolayer was observed, cells were passaged using trypsin-EDTA (0.25%), distributed into new T75 flasks, and confirmed the detachment of cells under the microscope. In this process, the number of viable cells could be determined by measuring a 20-μL aliquot of cell suspension mixed with an equal volume of Gibco Trypan blue stain (0.4%) using the Invitrogen Countess automated cell counter.

3T3 cells were then seeded onto various surfaces. After 15 min of incubation at 37 °C with 5% CO_2 to facilitate cell adhesion, 2 mL of culture medium was added to each well. The cells were further incubated for 18 h. Alamar blue assay was performed by adding Alamar blue solution to each well, incubating for 2 h, and measuring absorbance at 570 nm using an Infinite 200 Tecan automated luminometer-spectrometer. Cell counting was done by staining cells with trypan blue and using the cell counter. Statistical analysis was carried out using one-way ANOVA in IBM SPSS Statistic, with a 95% confidence interval.

Results and Discussion

Surface Morphology and Characteristics

The morphology (roughness) and interfacial energy of a surface are the key factors in controlling its wettability. Therefore, an AFM characterization of surface roughness has been carried out on ZnO nanopillar surfaces with and without PDMS coating, as shown in Figure 1a,b. The height of the nanopillars produced was mainly distributed between 350 and 400 nm

with a typical diameter of 70–80 nm (Figure S2). It should also be noted that the height of the nanopillars can be controlled by adjusting the duration and the concentration of reactants during nanopillar growth. Table 1 presents a comparative analysis of surface roughness for different surface treatments; the related AFM images are shown in Figures S3 and S4. Specifically, the arithmetic average roughness (Ra) of the ZnO nanopillar surface without the PDMS coating was 58.9 ± 8.9 nm, and the root-mean-square deviation (Rq) was 73.9 ± 11.0 nm. For ZnO nanopillar surfaces coated with PDMS, their surface roughness was considerably retained, with the Ra being 39.9 ± 27.4 nm and the Rq being 49.8 ± 33.3 nm. The substantial disparity in standard deviation observed in the roughness of the PDMS-coated nanopillars can be ascribed to the thickness of the PDMS coating. Thinner PDMS layers manifest higher surface roughness, converging toward the roughness levels observed of the uncoated ZnO nanopillars. The high roughness of these nanopillar surfaces was in marked contrast to the flat zinc substrate, PDMS surface, and glass slide.

Table 1. Roughness of Surfaces

surface	Ra (nm)	Rq (nm)
ZnO nanopillars	58.9 ± 8.9	73.9 ± 11.0
PDMS-coated nanopillars	39.9 ± 27.4	49.8 ± 33.3
bare Zinc	9.0 ± 2.0	11.3 ± 2.6
pure PDMS	1.1 ± 0.3	1.3 ± 0.4
glass slide	3.2 ± 1.2	4.2 ± 1.8

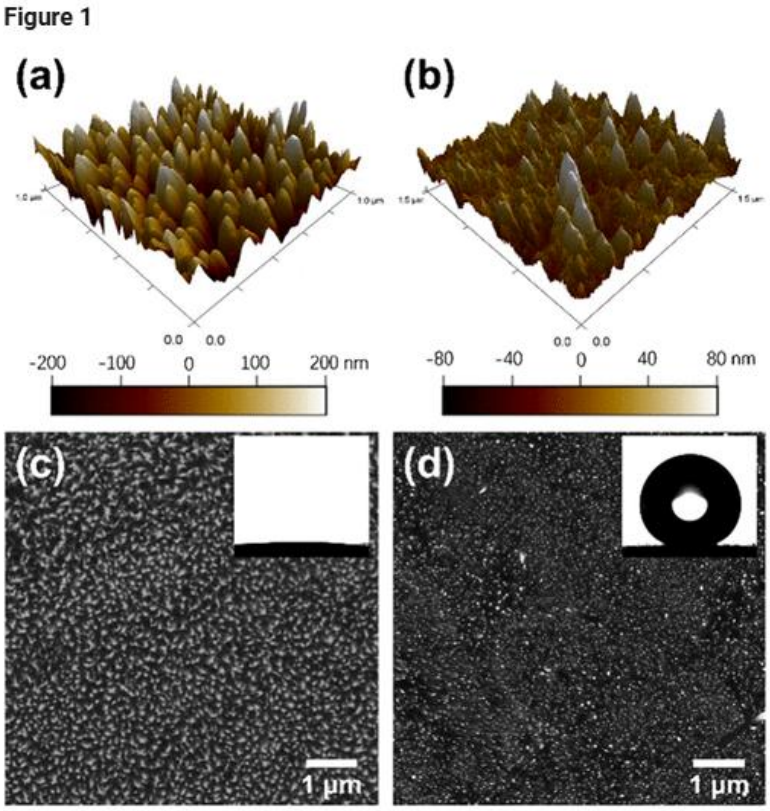


Figure 1. AFM images of ZnO nanopillars produced after 45 min of reaction time (a) without and (b) with PDMS coating. SEM images of the ZnO nanopillars (c) without and (d) with PDMS coating. The inset of panel (c) shows that the water contact angle is around 4.0 ± 0.5°, and the inset of panel (d) shows that the water contact angle is around 152.6 ± 2.8°.

In addition to AFM, SEM images were also captured to study the morphology of the nanopillar surfaces before and after PDMS coating. Figure 1c shows the surface of typical ZnO nanopillars prepared via a 45 min hydrothermal synthesis reaction. This provides further validation to Figure 1a that the surface was indeed composed of patterned pillar-like nanostructures. Similarly, Figure 1d reveals the pattern of the PDMS-coated nanopillar surfaces, which included a smaller quantity of pronounced nanopillars, in comparison to Figure 1c, because of the presence of the PDMS layer. Nonetheless, the outline of the nanopillars underneath is still noticeable from the SEM image, implying that the thickness of the PDMS coating was several nanometers. However, we note that the thickness of the PDMS coating could be subject to the volume and concentration of PDMS solution used in the coating process.

The crystallographic characteristics of the materials were investigated through XRD analysis, as shown in Figure S5. In the XRD spectrum of the ZnO nanopillars, a prominent diffraction peak is observed at $2\theta = 34.6°$ (002), indicating the highly preferential growth of ZnO nanopillars perpendicular to the substrate surface. The PDMS-coated nanopillars exhibited a similar trend. Further, according to the FTIR results (Figure S6), Zn–O bond signals within the range of 500–700 cm^{-1} were identified for ZnO nanopillars fabricated by the hydrothermal synthesis reaction. On the other hand, generally, the presence of impurities corresponding to carboxylate and hydroxyl groups on the surface manifests as a series of absorption peaks spanning 1000–4000 cm^{-1} in the FTIR results. For instance, the peak at 1300–1450 cm^{-1} corresponds to O–H bending, 1400–1600 cm^{-1} corresponds to O═C–O bending, and 1700–1800 cm^{-1} corresponds to C═O stretching. In addition, the peaks at 2800–3000 and 3200–3600

cm^{-1} correspond to C–H and O–H stretching, respectively. These impurity-related peaks are notably absent in the ZnO nanopillar spectrum. The ZnO nanopillars coated with PDMS coating resultant from being exposed to 5 μL of PDMS solution during the coating process exhibit a similar trend, with slight alterations in the Zn–O bond signal, ascribed to the coating. Noteworthy is the absence of Si–CH_3 rocking at 770–800 cm^{-1}, Si–O–Si stretching at 1100–1150 cm^{-1}, Si–CH_3 bending at 1260–1380 cm^{-1}, and Si–CH_3 stretching at 2960–2975 cm^{-1} in the results of PDMS-coated ZnO nanopillars, implying a low concentration of PDMS on the ZnO pillars. To examine the effect of PDMS coating thickness on surface characteristics, FTIR tests have been conducted on the ZnO nanopillar surface with a thick PDMS coating resultant from being exposed to an excessive 25 μL, instead of 5 μL, of PDMS solution during the coating procedure. In contrast, certain signals indicative of PDMS are more readily observed on surfaces with thick coatings.

The photocatalytic activities of each surface through fluorescence intensity decay are shown in Figure S7. The bare zinc surface exhibits slow degradation of the fluorescent dye. This suggests that the exposed zinc surface, which could form an oxide layer, lacks effective photocatalytic properties against fluorescent dyes. The pure PDMS surface exhibits negligible degradation of the fluorescent dye. In contrast, ZnO nanopillars exhibit rapid photocatalytic activities, degrading the dye within 3 h. The presence of PDMS coating on the ZnO nanopillars causes the degradation of the fluorescent dye to be slower (requiring 5 h) than the uncoated ZnO nanopillars, which is still more effective than the bare zinc surface.

Wetting Properties

Water is one of the mediums for bacteria to proliferate and spread in the initial stage of biofilm formation. (39−41) It is thus important to understand the wetting behavior of water on the surfaces. The nanostructured surfaces have been analyzed in terms of contact angle (CA) measurements. To better demonstrate the effect of the PDMS-coated nanopillars on wettability, we measured the bare zinc, ZnO nanopillars, and PDMS-coated nanopillars. Specifically, bare zinc exhibited a static contact angle of 77.8 ± 0.6° (Figure S8), with the advancing and receding contact angles being 84.3 ± 1.7 and 46.6 ± 0.7°, respectively. For pure PDMS, the static contact angle was 106.1 ± 1.7° (Figure S9), with the advancing and receding contact angles being 110.8 ± 1.6 and 85.6 ± 0.9°, respectively. The ZnO nanopillar structure directly obtained from the hydrothermal synthesis reaction appeared superhydrophilic with a contact angle of 4.0 ± 0.5° (Figure 1c inset; Video S1) and experimentally unmeasurable contact angle hysteresis. By contrast, the ZnO nanopillar structure coated with PDMS exhibited a contact angle of 152.6 ± 2.8° (Figure 1d inset). The stability of the superhydrophobicity on the PDMS-coated ZnO nanopillars was also assessed, as shown in Figure S10. The contact angle remained essentially unchanged during a 7 day exposure. Moreover, even after an extended exposure period of 21 days, a water contact angle of around 146° was still measured. Further, the contact angle hysteresis of the PDMS-coated ZnO nanopillar surface (now denoted as superhydrophobic) was negligible, with an advancing contact angle of 154.1 ± 0.2° and a receding contact angle of 152.3 ± 0.9°, as shown in Figure S11. In addition, it is interesting to note that water droplets can roll off of the PDMS-coated nanopillar surface at a tilting angle of 1°, as shown in Figure S12 and Video S2. This remarkable superhydrophobicity with minimal tilt angle is attributed to the combination of the low-surface-energy PDMS coating and the rough ZnO nanopillars. In particular, as shown in Figure 1d, the PDMS coating was sufficiently thin to allow the surface roughness and function resulting from the ZnO nanopillars to be preserved.

The superhydrophobic surfaces also repelled the impact of water droplets of 2.7 mm diameter at a range of velocities. Figure 2a,b shows the morphology variations of the droplets after impacting the surfaces with different values of the Weber number ($We = D_o\rho U^2/\sigma$), which represents the ratio of the inertial force to the capillary force. Here, D_o is the diameter of the droplet (m), ρ is the density of the liquid (kg/m^3), U is the velocity of the droplet (m/s), and σ is the interfacial tension (N/m). It is remarkable that the droplet directly rebounded from the superhydrophobic surface at a range of *We* values (*We* = 8.62 and *We* = 46.11) (Videos S3 and S4). At the beginning of the impact, the droplet recoiled to a pancake shape, which was dominated by inertial effects. This was followed by complete rebounding of the droplet from the superhydrophobic nanopillar structure. However, at a higher *We* (46.11), a satellite droplet was generated from the primary droplet. This was due to the high kinetic energy as compared to the surface tension, which caused the rim of the droplet to break up. In addition, the higher *We* also led to a higher maximum height and rebounding speed than the lower *We*. The initial rebound was followed by a series of subsequent rebounds with a gradual decrease in the impact velocity (Figure S13). By contrast, impacting droplets spread immediately against the uncoated surface of ZnO nanopillars (Figure S14a; Video S5). Similarly, the droplet did not rebound on the pure PDMS surface (Figure S14b; Video S6), although it retracted due to its hydrophobicity after spreading out upon impact. Therefore, it is deduced that the superhydrophobic nanopillar structure prevented the water droplets from spreading into the nanostructure even under substantial impalement pressure. This further implies that air pockets existed among the nanopillars coated with a thin layer of PDMS, which, as a result, repelled impacting droplets.

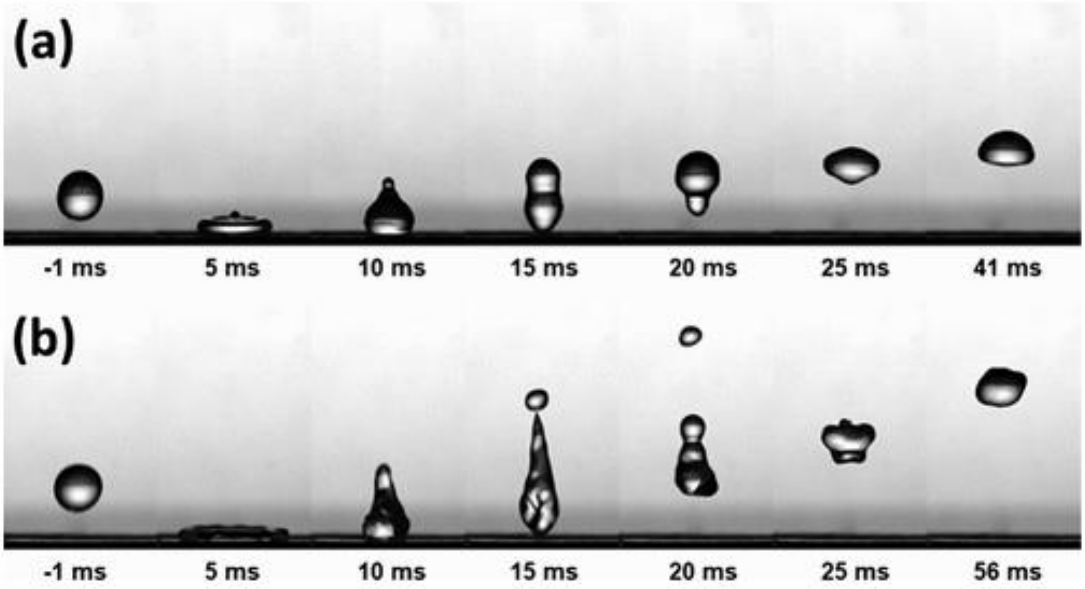


Figure 2. Water droplets impacting PDMS-coated nanopillar surfaces: (a) *We* = 8.62 and (b) *We* = 46.11. Droplet impact experiments were captured by a high-speed camera at a frame rate of 1000 fps.

Antibiofouling Properties

In order to examine the antibiofouling properties of the PDMS-coated ZnO nanopillars, bacterial viability tests were performed with dual staining kits. This allowed us to assess the

viability of bacterial populations on the superhydrophobic surfaces as a function of the cell's membrane integrity. Namely, cells that were dead or dying on the structured surfaces because of a compromised membrane stained red, whereas cells with an intact membrane appeared green, as schematically illustrated in Figure 3.

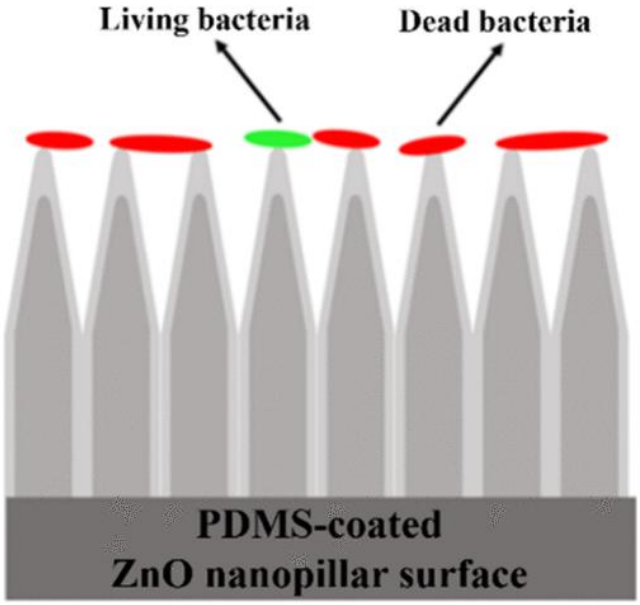


Figure 3. Schematic diagram of LIVE/DEAD staining experiments: dead bacteria (color of red) and living bacteria (color of green).

The confocal microscopy images of stained *S. aureus* bacterial suspensions incubated for 18 h on the bare zinc, ZnO nanopillars, and PDMS-coated nanopillars are shown in Figure 4a–c, respectively. The confocal microscopy examination revealed that a large portion of *S. aureus* remained alive when exposed to the bare zinc surface. In contrast, the bacteria were mostly dead on the superhydrophilic ZnO nanopillar surface. However, despite the bactericidal properties, the number of dead bacteria adhering to the superhydrophilic ZnO nanopillar surface accumulated over time, as shown in Figure 4e. The antibiofouling properties of uncoated ZnO nanopillars may be compromised when bacteria cells accumulate and cover the surface, reducing the bactericidal effectiveness through direct bacteria-surface contact. (42) In comparison, a discernible decrease in the bacterial presence was observed on the PDMS-coated nanopillar surface, although a coexistence of live and dead bacteria persisted. Nonetheless, the coverage of bacteria was less on the superhydrophobic ZnO nanopillars, likely due to the low adhesion, than on the bare zinc and untreated ZnO nanopillars. SEM images of *S. aureus* on the bare zinc, ZnO nanopillars, and PDMS-coated nanopillars are shown in Figure 4d–f. It is evident that *S. aureus* initiated the formation of biofilm on the bare zinc surface following an 18 h incubation. Bacterial remnants that were deformed/dehydrated were observed on the ZnO nanopillars. This is consistent with the confocal microscopy analysis that showed the nonviability of the bacterial population of *S. aureus* on the uncoated ZnO nanopillars. By contrast, there was an apparent absence of large bacterial populations of *S. aureus* on the superhydrophobic ZnO nanopillars. From the SEM study, there were sparsely distributed bacteria of *S. aureus* on the PDMS-coated ZnO nanopillars, similar to the confocal microscopy result. A closer observation (Figure 4f) indicates that some of the bacteria appeared to be structurally deformed after being exposed to the PDMS-coated ZnO nanopillars.

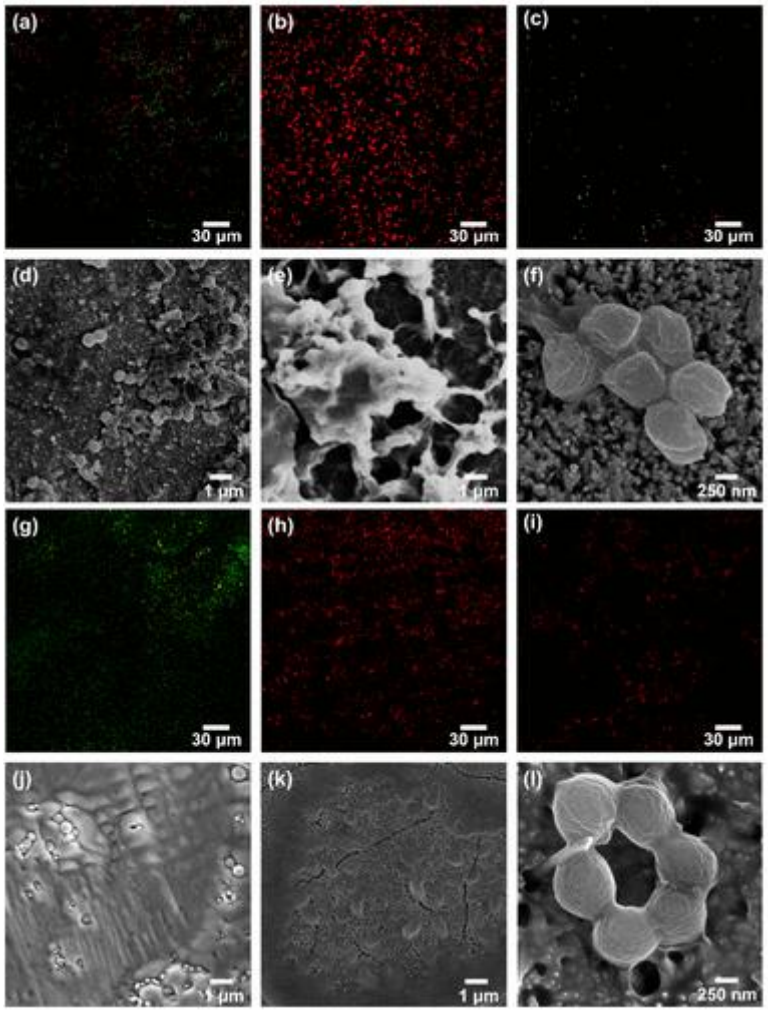


Figure 4. (a–c, g–i) Confocal microscopy and (d–f, j–l) SEM images of *S. aureus* after (a–f) 18 and (g–l) 72 h of incubation on different surfaces: (a, d, g, j) bare zinc, (b, e, h, k) ZnO nanopillars, and (c, f, i, l) PDMS-coated nanopillars.

Tests were also conducted with an incubation time of 72 h to examine whether the antibiofouling effect could be sustained on the surfaces for longer durations. The confocal microscopy and SEM images reveal that on the bare zinc surface, *S. aureus* cells were still able to survive and form biofilms (Figure 4g,j). In contrast, the ZnO nanopillars continued to exhibit similar trends to the 18 h incubation, with an extensive coverage of dead bacteria, as shown in Figure 4h,k. On the superhydrophobic ZnO nanopillars coated with PDMS, the longer incubation of 72 h allowed the accumulation of *S. aureus* to moderately increase, as shown in Figure 4i,l, in comparison with the 18 h incubation. Nevertheless, the coverage of bacteria after 72 h of incubation on the superhydrophobic PDMS-coated ZnO surface was still less than on the uncoated ZnO surface. Also, the bacteria that were residual on the superhydrophobic surface appeared to be largely dead (Figure 4i). This is attributed to the extended exposure to the photocatalytic activities of ZnO underneath the surface that caused the bacteria to be structurally deformed (Figure 4l).

Furthermore, the confocal microscopy images (Figure 5a–c) show stained *E. coli* bacterial suspensions incubated for 18 h on different surfaces: the bare zinc, ZnO nanopillars, and PDMS-coated nanopillars. Similar to the findings with *S. aureus*, most bacteria of *E. coli* were green stained on the bare zinc surface, whereas nearly all bacterial populations appeared red

stained on the ZnO nanopillars. However, on PDMS-coated nanopillars, the stained *E. coli* emitted red signals indicative of dead cells. This is attributed to the disparities in the bacterial morphology and inner structure between *S. aureus* and *E. coli*. Generally, *S. aureus* is usually spherically shaped, with a diameter of approximately 0.5–1.0 μm and a thicker peptidoglycan layer than *E. coli*. In contrast, *E. coli* is typically rod-shaped, with a width of 0.5 μm and a length of 1.5 μm. (43−45) The differences in structural morphology between the bacteria may have had an effect on their viability on nanopillar-based structures. The shape of the *E. coli* bacteria could have had greater surface contact with the nanopillar structures than that of *S. aureus*, even in the presence of the PDMS layer. This would impose a stressful stimulus on bacterial cell walls, causing irreparable cell wall rupture and bacterial death. (46) Indeed, SEM images (Figure 5d–f) further illustrate that bacteria of *E. coli* with disfigured appearances were observed on both the uncoated ZnO nanopillars (Figure 5e) and the PDMS-coated ZnO nanopillars (Figure 5f). This was more notable on the uncoated ZnO nanopillar structure, which could cause the bacteria to be punctured as adhesive forces pulled them toward the surface due to its superhydrophilicity. (24) Nevertheless, the PDMS-coated ZnO nanopillars, because of the low interfacial adhesion associated with the superhydrophobicity, reduced the attachment of *E. coli* on the surface.

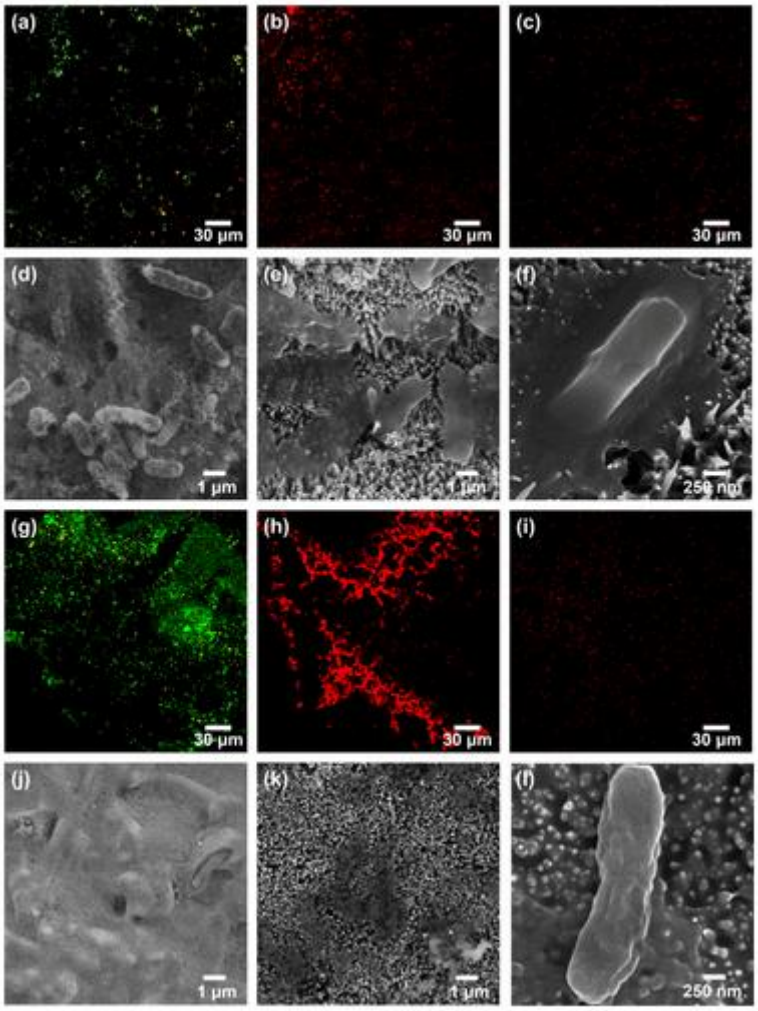


Figure 5. (a–c, g–i) Confocal microscopy and (d–f, j–l) SEM images of *E. coli* after (a–f) 18 and (g–l) 72 h of incubation on different surfaces: (a, d, g, j) bare zinc, (b, e, h, k) ZnO nanopillars, and (c, f, i, l) PDMS-coated nanopillars.

The 72 h incubation test was also performed for *E. coli*, with confocal microscopy and SEM images collected to analyze the behavior of *E. coli* on different surfaces. Bacterial cells on bare zinc still exhibited green signals and displayed a tendency to form large-area biofilms (Figure 5g). SEM observations confirmed the presence of some large-area biofilms on the surface, as shown in Figure 5j. In contrast, the trend observed after the 72 h incubation of the uncoated ZnO nanopillars and the superhydrophobic ZnO nanopillars remained essentially consistent with that observed after the 18 h incubation. It is worth noting that in addition to the results of the above three kinds of surfaces, confocal microscopy and SEM images of the control group, glass, and pure PDMS were also collected at different incubation times (18 and 72 h), as shown in Figures S15–S17. We note that the term "control" in this work refers to tests wherein the bacteria are exposed to conditions without any specific surface material. From the results, it can be observed that bacteria could proliferate in the control group and remained active. Similarly, as neither glass nor PDMS possessed inherent antibiofouling properties, they also allowed substantial proliferation and biofilm formation to take place. Therefore, bacteria on the surfaces of ZnO nanopillars with excessive PDMS coatings did not exhibit any noticeable deformation (Figures S16 and S17).

The coverage percentage of bacteria populations on various surfaces was calculated based on the confocal microscopy images, as shown in Figure 6a,c corresponding to the 18 h and 72 h of incubation, respectively. (47) A consistent trend is observed, where the bacterial coverage on superhydrophobic PDMS-coated nanopillars is significantly reduced. This is attributed to the low liquid–solid adhesion associated with the superhydrophobicity of the surfaces that were characterized by the small contact angle hysteresis and tilting angle. Additionally, the antimicrobial properties of the surfaces are quantitatively illustrated in Figure 6b,d, using colony-forming units (CFU). Notably, there was very few CFU that could be detected from the samples, which had been exposed to the superhydrophilic ZnO nanopillars in both the cases of 18 h and 72 h incubations. This is consistent with recent studies that nanostructures of ZnO can exhibit antimicrobial activities through bacterial cell wall damage. (48,49) In particular, a recent study used a similar approach to the development of ZnO nanopillars coated with PDMS for antibacterial applications. (50) It is noteworthy that in our case, the ZnO nanopillars exhibited more uniform upright morphologies, which had been preserved even in the presence of PDMS coatings (Figure 1d). This makes it possible to enhance the antimicrobial properties of the surfaces through a combination of the two following complementary mechanisms: (a) direct bacterial membrane puncture and (b) photocatalytic activities of ZnO. However, there is a possibility that PDMS layers exceeding a certain thickness, typically several nanometres, could impede or slow down the photocatalytic activity. (34,51) Thicker PDMS layers also obscure the nanopillar structure, hindering the mechanical stress of the pillars against the bacteria. This will affect the surface's antibiofouling behaviors, as shown in Figures S16, S17, and S19.

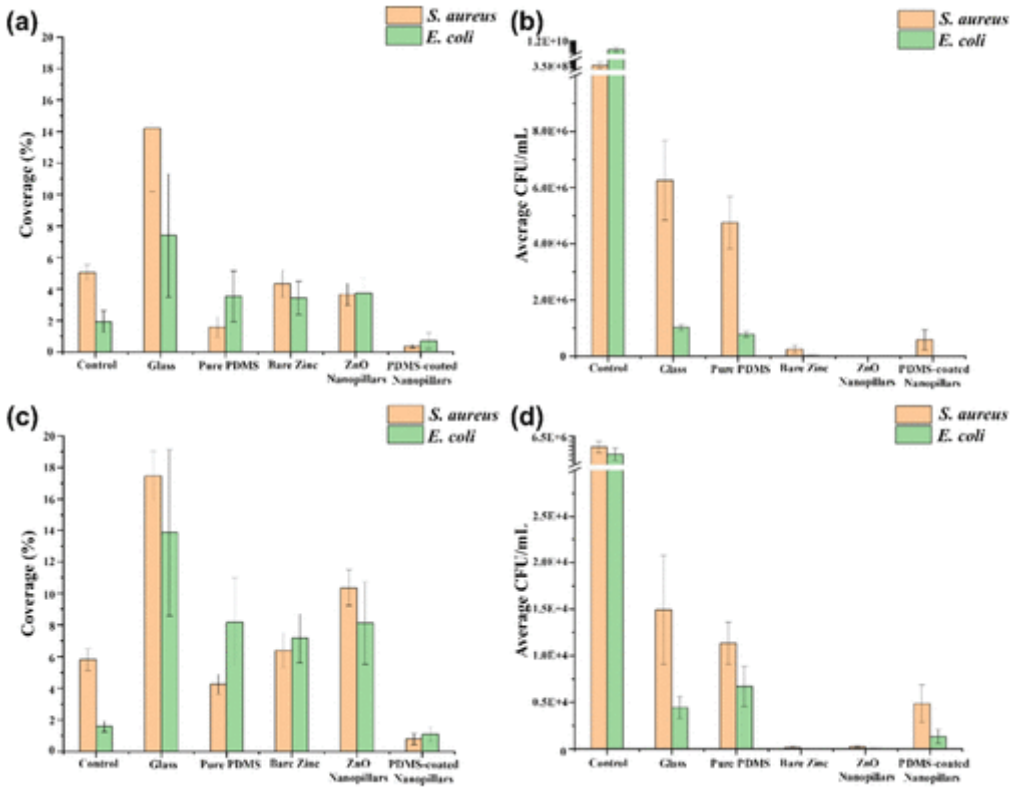


Figure 6. Coverage percentage of bacteria population after (a) 18 and (c) 72 h incubation. The number of colony forming units (CFU)/mL on each surface sample after (b) 18 and (d) 72 h incubation.

On the other hand, the number of CFU on ZnO nanopillars is significantly lower than those on glass and pure PDMS. Further, we note that the low intensity of the CFU of the bare zinc surface is ascribed to the arbitrary presence of an oxide layer on the zinc surface, which could lead to antibiofouling behaviors. However, given that live bacteria signals can be widely found on the zinc surfaces under confocal microscopy, they are not considered to be resistant to biofouling. Furthermore, to evaluate the efficacy of superinfection prevention, multicycle tests were implemented (Figures S20 and S21). The antibacterial response and behavior of each sample type over the multiple cycles of testing aligned consistently with the trends observed in the initial antibiofouling efficacy testing. In addition, the relevant surfaces showed no signs of cytotoxicity against mammalian cells (Figure S22), indicating good biocompatibility.

Conclusions

In conclusion, ZnO nanopillars were coated with PDMS to form superhydrophobic surfaces with antibiofouling properties. Droplets of water on these superhydrophobic surfaces exhibited large apparent contact angles and low contact angle hysteresis of within 3°. In addition, such surfaces showed low droplet adhesion, characterized by a low tilting angle of 1°. The liquid repellence of the surfaces was further demonstrated by droplet impingement tests, where impinging droplets bounced off over a range of Weber numbers (8–46). Notably, the PDMS-coated ZnO nanopillars exhibited effective antibiofouling behaviors under ambient illumination due to the intrinsic photocatalytic activities of ZnO nanomaterials. Therefore, the superhydrophobic PDMS-coated ZnO surfaces integrated a low interfacial adhesion and bactericidal effect. This synergy, without requiring additional UV illumination or antimicrobial agents, makes the PDMS-coated ZnO nanopillar surfaces a promising material for antibiofouling applications.

References

1. van Kleef, E.; Robotham, J. V.; Jit, M.; Deeny, S. R.; Edmunds, W. J. Modelling the transmission of healthcare associated infections: a systematic review. *BMC Infect Dis* **2013**, *13*, 294, DOI: 10.1186/1471-2334-13-294
2. Percival, S. L.; Suleman, L.; Vuotto, C.; Donelli, G. Healthcare-associated infections, medical devices and biofilms: risk, tolerance and control. *J. Med. Microbiol.* **2015**, *64*, 323– 334, DOI: 10.1099/jmm.0.000032
3. Dadi, N. C. T.; Radochova, B.; Vargova, J.; Bujdakova, H. Impact of Healthcare-Associated Infections Connected to Medical Devices-An Update. *Microorganisms* **2021**, *9* (11), 2332, DOI: 10.3390/microorganisms9112332
4. Kollef, M. H.; Torres, A.; Shorr, A. F.; Martin-Loeches, I.; Micek, S. T. Nosocomial Infection. *Crit Care Med* **2021**, *49* (2), 169– 187, DOI: 10.1097/CCM.0000000000004783
5. Monegro, A. F.; Muppidi, V.; Regunath, H. *Hospital Acquired Infections*; StatPearls Publishing: Treasure Island (FL), 2022.
6. van den Broek, P. J.; Daha, T. J.; Mouton, R. P. Bladder irrigation with povidone-iodine in prevention of urinary-tract infections associated with intermittent urethral catheterisation. *Lancet* **1985**, *1* (8428), 563– 565, DOI: 10.1016/s0140-6736(85)91217-6

7. Heal, J. S.; Blom, A. W.; Titcomb, D.; Taylor, A.; Bowker, K.; Hardy, J. R. Bacterial contamination of surgical gloves by water droplets spilt after scrubbing. *J Hosp Infect* **2003**, *53* (2), 136– 139, DOI: 10.1053/jhin.2002.1352
8. Ranjbaran, M.; Datta, A. K. Retention and infiltration of bacteria on a plant leaf driven by surface water evaporation. *Phys. Fluids* **2019**, *31* (11), 112106, DOI: 10.1063/1.5126127
9. Pishbin, E.; Kazemzadeh, A.; Chimerad, M.; Asiaei, S.; Navidbakhsh, M.; Russom, A. Frequency dependent multiphase flows on centrifugal microfluidics. *Lab Chip* **2020**, *20* (3), 514– 524, DOI: 10.1039/C9LC00924H
10. Hizal, F.; Rungraeng, N.; Lee, J.; Jun, S.; Busscher, H. J.; van der Mei, H. C.; Choi, C. H. Nanoengineered Superhydrophobic Surfaces of Aluminum with Extremely Low Bacterial Adhesivity. *ACS Appl Mater Interfaces* **2017**, *9* (13), 12118– 12129, DOI: 10.1021/acsami.7b01322
11. Ware, C. S.; Smith-Palmer, T.; Peppou-Chapman, S.; Scarratt, L. R. J.; Humphries, E. M.; Balzer, D.; Neto, C. Marine Antifouling Behavior of Lubricant-Infused Nanowrinkled Polymeric Surfaces. *ACS Appl Mater Interfaces* **2018**, *10* (4), 4173– 4182, DOI: 10.1021/acsami.7b14736
12. Agbe, H.; Sarkar, D. K.; Chen, X. G.; Faucheux, N.; Soucy, G.; Bernier, J. L. Silver-Polymethylhydrosiloxane Nanocomposite Coating on Anodized Aluminum with Superhydrophobic and Antibacterial Properties. *ACS Appl Bio Mater* **2020**, *3* (7), 4062– 4073, DOI: 10.1021/acsabm.0c00159
13. Encinas, N.; Yang, C. Y.; Geyer, F.; Kaltbeitzel, A.; Baumli, P.; Reinholz, J.; Mailander, V.; Butt, H. J.; Vollmer, D. Submicrometer-Sized Roughness Suppresses Bacteria Adhesion. *ACS Appl Mater Interfaces* **2020**, *12* (19), 21192– 21200, DOI: 10.1021/acsami.9b22621
14. Yan, Y. Y.; Gao, N.; Barthlott, W. Mimicking natural superhydrophobic surfaces and grasping the wetting process: a review on recent progress in preparing superhydrophobic surfaces. *Adv. Colloid Interface Sci.* **2011**, *169* (2), 80– 105, DOI: 10.1016/j.cis.2011.08.005
15. Cassie, A. B. D.; Baxter, S. Wettability of porous surfaces. *Trans. Faraday Soc.* **1944**, *40*, 546, DOI: 10.1039/tf9444000546
16. Roach, P.; Shirtcliffe, N. J.; Newton, M. I. Progess in superhydrophobic surface development. *Soft Matter* **2008**, *4* (2), 224– 240, DOI: 10.1039/B712575P
17. Bonn, D.; Eggers, J.; Indekeu, J.; Meunier, J.; Rolley, E. Wetting and spreading. *Rev. Mod. Phys.* **2009**, *81* (2), 739– 805, DOI: 10.1103/RevModPhys.81.739
18. Singh, N. S.; Zhang, J.; Stafford, J.; Anthony, C.; Gao, N. Implementing Superhydrophobic Surfaces within Various Condensation Environments: A Review. *Adv. Mater. Interfaces* **2021**, *8* (2), 2001442, DOI: 10.1002/admi.202001442
19. Vasudevan, R.; Kennedy, A. J.; Merritt, M.; Crocker, F. H.; Baney, R. H. Microscale patterned surfaces reduce bacterial fouling-microscopic and theoretical analysis. *Colloids Surf B Biointerfaces* **2014**, *117*, 225– 232, DOI: 10.1016/j.colsurfb.2014.02.037
20. Ayazi, M.; Golshan Ebrahimi, N.; Jafari Nodoushan, E. Bacterial adhesion reduction on the surface with a simulated pattern: An insight into extrand model. *International Journal of Adhesion and Adhesives* **2019**, *88*, 66– 73, DOI: 10.1016/j.ijadhadh.2018.10.017
21. Manoj, T. P.; Rasitha, T. P.; Vanithakumari, S. C.; Anandkumar, B.; George, R. P.; Philip, J. A simple, rapid and single step method for fabricating superhydrophobic titanium surfaces with improved water bouncing and self cleaning properties. *Appl. Surf. Sci.* **2020**, *512*, 145636 DOI: 10.1016/j.apsusc.2020.145636

22. Ivanova, E. P.; Linklater, D. P.; Aburto-Medina, A.; Le, P.; Baulin, V. A.; Khuong Duy Nguyen, H.; Curtain, R.; Hanssen, E.; Gervinskas, G.; Hock Ng, S.Antifungal versus antibacterial defence of insect wings. *J. Colloid Interface Sci.* **2021**, *603*, 886– 897, DOI: 10.1016/j.jcis.2021.06.093
23. Oh, J.; Dana, C. E.; Hong, S.; Roman, J. K.; Jo, K. D.; Hong, J. W.; Nguyen, J.; Cropek, D. M.; Alleyne, M.; Miljkovic, N. Exploring the Role of Habitat on the Wettability of Cicada Wings. *ACS Appl Mater Interfaces* **2017**, *9* (32), 27173– 27184, DOI: 10.1021/acsami.7b07060
24. Román-Kustas, J.; Hoffman, J. B.; Reed, J. H.; Gonsalves, A. E.; Oh, J.; Li, L.; Hong, S.; Jo, K. D.; Dana, C. E.; Miljkovic, N.Molecular and Topographical Organization: Influence on Cicada Wing Wettability and Bactericidal Properties. *Adv. Mater. Interfaces* **2020**, *7* (10), 202000112, DOI: 10.1002/admi.202000112
25. Ruben, B.; Elisa, M.; Leandro, L.; Victor, M.; Gloria, G.; Marina, S.; Mian, K. S.; Pandiyan, R.; Nadhira, L. Oxygen plasma treatments of polydimethylsiloxane surfaces: effect of the atomic oxygen on capillary flow in the microchannels. *Micro Nano Lett.* **2017**, *12* (10), 754– 757, DOI: 10.1049/mnl.2017.0230
26. Trantidou, T.; Elani, Y.; Parsons, E.; Ces, O. Hydrophilic surface modification of PDMS for droplet microfluidics using a simple, quick, and robust method via PVA deposition. *Microsyst Nanoeng* **2017**, *3*, 16091, DOI: 10.1038/micronano.2016.91
27. Mata, A.; Fleischman, A. J.; Roy, S. Characterization of polydimethylsiloxane (PDMS) properties for biomedical micro/nanosystems. *Biomed Microdevices* **2005**, *7* (4), 281– 293, DOI: 10.1007/s10544-005-6070-2
28. van Poll, M. L.; Zhou, F.; Ramstedt, M.; Hu, L.; Huck, W. T. A self-assembly approach to chemical micropatterning of poly(dimethylsiloxane). *Angew. Chem., Int. Ed. Engl.* **2007**, *46* (35), 6634– 6637, DOI: 10.1002/anie.200702286
29. Zhou, J.; Ellis, A. V.; Voelcker, N. H. Recent developments in PDMS surface modification for microfluidic devices. *Electrophoresis* **2010**, *31* (1), 2– 16, DOI: 10.1002/elps.200900475
30. van den Berg, D.; Asker, D.; Awad, T. S.; Lavielle, N.; Hatton, B. D. Mechanical deformation of elastomer medical devices can enable microbial surface colonization. *Sci Rep* **2023**, *13* (1), 7691, DOI: 10.1038/s41598-023-34217-5
31. Adams, L. K.; Lyon, D. Y.; Alvarez, P. J. Comparative eco-toxicity of nanoscale TiO2, SiO2, and ZnO water suspensions. *Water Res.* **2006**, *40* (19), 3527– 3532, DOI: 10.1016/j.watres.2006.08.004
32. Jones, N.; Ray, B.; Ranjit, K. T.; Manna, A. C. Antibacterial activity of ZnO nanoparticle suspensions on a broad spectrum of microorganisms. *FEMS Microbiol Lett* **2008**, *279* (1), 71– 76, DOI: 10.1111/j.1574-6968.2007.01012.x
33. Leung, Y. H.; Chan, C. M.; Ng, A. M.; Chan, H. T.; Chiang, M. W.; Djurisic, A. B.; Ng, Y. H.; Jim, W. Y.; Guo, M. Y.; Leung, F. C.Antibacterial activity of ZnO nanoparticles with a modified surface under ambient illumination. *Nanotechnology* **2012**, *23* (47), 475703 DOI: 10.1088/0957-4484/23/47/475703
34. Wooh, S.; Encinas, N.; Vollmer, D.; Butt, H. J. Stable Hydrophobic Metal-Oxide Photocatalysts via Grafting Polydimethylsiloxane Brush. *Adv. Mater.* **2017**, *29* (16), 1604637, DOI: 10.1002/adma.201604637
35. He, G.; Wan, M.; Wang, Z.; Zhou, X.; Zhao, Y.; Sun, L. A simple surface modification method to prepare versatile PVDF electrospun nanofibrous felts for separation, sterilization and degradation. *Prog. Org. Coat.* **2023**, *182*, 107664 DOI: 10.1016/j.porgcoat.2023.107664

36. Pettinari, C.; Pettinari, R.; Nicola, C. D.; Tombesi, A.; Scuri, S.; Marchetti, F. Antimicrobial MOFs. *Coord. Chem. Rev.* **2021**, *446*, 214121 DOI: 10.1016/j.ccr.2021.214121
37. Wu, X.; Bai, H.; Li, C.; Lu, G.; Shi, G. Controlled one-step fabrication of highly oriented ZnO nanoneedle/nanorods arrays at near room temperature. *Chem. Commun.* **2006**, *15*, 1655, DOI: 10.1039/b516497d
38. Watson, R.; Maxwell, M.; Dunn, S.; Brooks, A.; Jiang, L.; Hill, H. J.; Williams, G.; Kotowska, A.; Nikoi, N. D.; Stamataki, Z.Development of biocide coated polymers and their antimicrobial efficacy. *Nano Select* **2023**, *4* (7), 442– 453, DOI: 10.1002/nano.202300005
39. Chan, S.; Pullerits, K.; Keucken, A.; Persson, K. M.; Paul, C. J.; Radstrom, P. Bacterial release from pipe biofilm in a full-scale drinking water distribution system. *NPJ Biofilms Microbiomes* **2019**, *5* (1), 9, DOI: 10.1038/s41522-019-0082-9
40. Maes, S.; Vackier, T.; Nguyen Huu, S.; Heyndrickx, M.; Steenackers, H.; Sampers, I.; Raes, K.; Verplaetse, A.; De Reu, K. Occurrence and characterisation of biofilms in drinking water systems of broiler houses. *BMC Microbiol* **2019**, *19* (1), 77, DOI: 10.1186/s12866-019-1451-5
41. Mahapatra, A.; Padhi, N.; Mahapatra, D.; Bhatt, M.; Sahoo, D.; Jena, S.; Dash, D.; Chayani, N. Study of biofilm in bacteria from water pipelines. *J. Clin. Diagn. Res.* **2015**, *9* (3), DC09– DC11, DOI: 10.7860/JCDR/2015/12415.5715
42. Uneputty, A.; Dávila-Lezama, A.; Garibo, D.; Oknianska, A.; Bogdanchikova, N.; Hernández-Sánchez, J. F.; Susarrey-Arce, A. Strategies applied to modify structured and smooth surfaces: A step closer to reduce bacterial adhesion and biofilm formation. *Colloids Interface. Sci Commun* **2022**, *46*, 100560 DOI: 10.1016/j.colcom.2021.100560
43. Wang, M.; Buist, G.; van Dijl, J. M. Staphylococcus aureus cell wall maintenance – the multifaceted roles of peptidoglycan hydrolases in bacterial growth, fitness, and virulence. *FEMS Microbiol. Rev.* **2022**, *46* (5), fuac025, DOI: 10.1093/femsre/fuac025
44. Shiomi, D.; Sakai, M.; Niki, H. Determination of bacterial rod shape by a novel cytoskeletal membrane protein. *EMBO J.* **2008**, *27* (23), 3081– 3091, DOI: 10.1038/emboj.2008.234
45. Monteiro, J. M.; Fernandes, P. B.; Vaz, F.; Pereira, A. R.; Tavares, A. C.; Ferreira, M. T.; Pereira, P. M.; Veiga, H.; Kuru, E.; VanNieuwenhze, M. S.Cell shape dynamics during the staphylococcal cell cycle. *Nat Commun* **2015**, *6*, 8055, DOI: 10.1038/ncomms9055
46. Luan, Y.; Liu, S.; Pihl, M.; van der Mei, H. C.; Liu, J.; Hizal, F.; Choi, C.-H.; Chen, H.; Ren, Y.; Busscher, H. J. Bacterial interactions with nanostructured surfaces. *Curr. Opin. Colloid Interface Sci.* **2018**, *38*, 170– 189, DOI: 10.1016/j.cocis.2018.10.007
47. Jitniyom, T.; Gaddam, A.; Williams, G.; Churm, J.; Dearn, K.; Banzhaf, M.; de Cogan, F.; Dimov, S.; Gao, N. Biofouling resistant materials based on micro-structuredsurfaces with liquid-repellent properties. *Nano Select* **2024**, *5*, 2300158, DOI: 10.1002/nano.202300158
48. Yi, G.; Yuan, Y.; Li, X.; Zhang, Y. ZnO Nanopillar Coated Surfaces with Substrate-Dependent Superbactericidal Property. *Small* **2018**, *14* (14), 1703159, DOI: 10.1002/smll.201703159
49. Alves, M. M.; Bouchami, O.; Tavares, A.; Cordoba, L.; Santos, C. F.; Miragaia, M.; de Fatima Montemor, M. New Insights into Antibiofilm Effect of a Nanosized ZnO Coating against the Pathogenic Methicillin Resistant Staphylococcus aureus. *ACS Appl Mater Interfaces* **2017**, *9* (34), 28157– 28167, DOI: 10.1021/acsami.7b02320

50. Tang, Y.; Sun, H.; Qin, Z.; Yin, S.; Tian, L.; Liu, Z. Bioinspired photocatalytic ZnO/Au nanopillar-modified surface for enhanced antibacterial and antiadhesive property. *J. Chem. Eng.* **2020**, *398*, 125575 DOI: 10.1016/j.cej.2020.125575
51. Liu, J.; Ye, L.; Wooh, S.; Kappl, M.; Steffen, W.; Butt, H. J. Optimizing Hydrophobicity and Photocatalytic Activity of PDMS-Coated Titanium Dioxide. *ACS Appl Mater Interfaces* **2019**, *11* (30), 27422– 27425, DOI: 10.1021/acsami.9b07490

Supplementary Results

S1 Formation mechanism of ZnO nanopillars

The formation of ZnO pillars on bare zinc substrate in an alkaline zincate solution (NaOH + Zn(NO3)2·6H2O) can be described by the following reactions:

$$Zn + 2H2O + 2OH^- \rightarrow Zn(OH)4\ 2^- + H2\uparrow$$

$$Zn(OH)4\ 2^- = ZnO\downarrow + H2O + 2OH^-$$

Throughout the process of ZnO nanopillar growth, zinc atoms dissolve into the solution, leading to an increased concentration gradient of zincate ions near the bare zinc substrate. Consequently, the growth rate along the z-axis (i.e., the (001) direction according to the XRD results shown in Section S4) gradually decreases from the root to the top of the nanostructure, ultimately resulting in the formation of nanopillars.

S2 Agar plates preparation and anti-biofouling efficacy testing

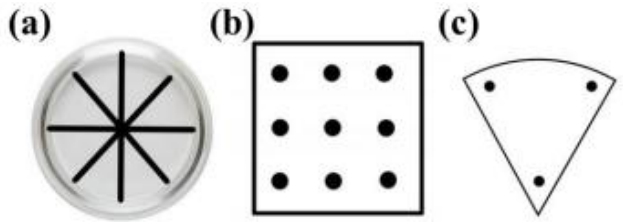


Figure S1. Schematic diagram of agar plates preparation and anti-biofouling efficacy testing: (a) Agar plate with divided areas. (b) Bacterial culture spots on surface. (c) Bacterial drops on an individual section of the agar plate.

S3 Surface morphology

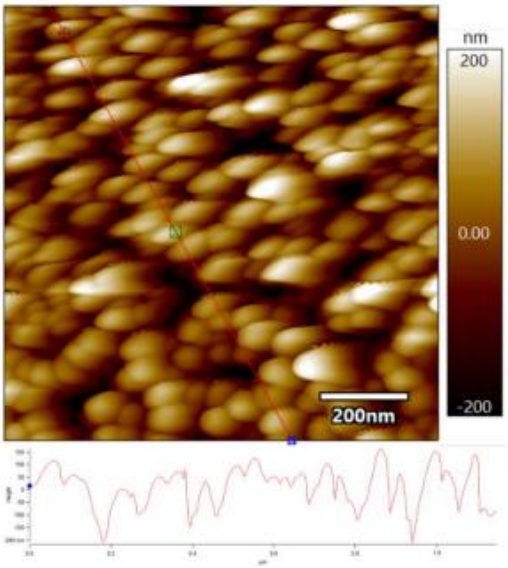


Figure S2. AFM image of ZnO nanopillars.

Table S1. Surface roughness of plain surfaces

Ra (nm)	Bare zinc	Glass	Pure PDMS
1st	7.19	2.08	0.97
2nd	8.69	3.01	0.90
3rd	11.12	4.54	1.43
Average	9.00 ± 1.98	3.21 ± 1.24	1.10 ± 0.29
Rq (nm)	Bare zinc	Glass	Pure PDMS
1st	9.07	2.72	1.13
2nd	10.72	3.74	1.07
3rd	14.14	6.21	1.70
Average	11.31 ± 2.59	4.22 ± 1.79	1.30 ± 0.35

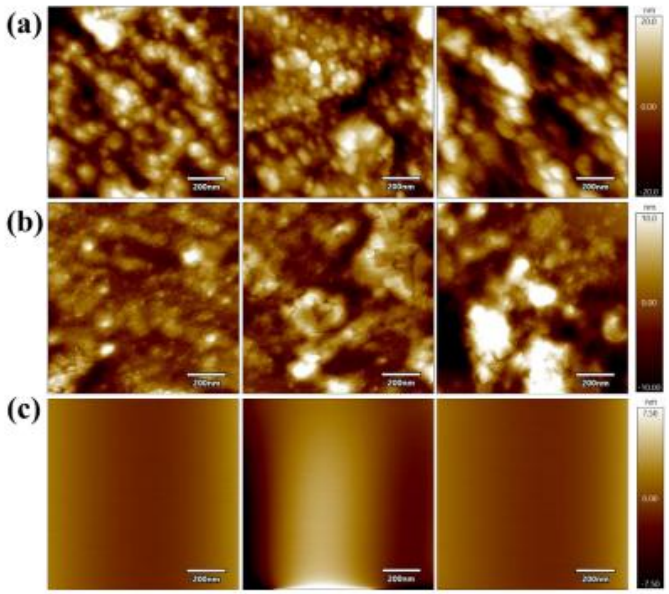


Figure S3. AFM images of the plain surfaces used in roughness calculation: (a) Bare zinc, (b) Glass and (c) Pure PDMS

Table S2. Surface roughness of nanopillar-based surfaces

Ra (nm)	ZnO nanopillars	PDMS-coated nanopillars
1st	64.47	17.08
2nd	65.05	15.95
3rd	56.30	12.89
4th	67.61	72.68
5th	56.16	60.95
6th	43.65	60.04
Average	58.87 ± 8.85	39.93 ± 27.38
Rq (nm)	ZnO nanopillars	PDMS-coated nanopillars
1st	80.67	21.33
2nd	82.42	21.45
3rd	70.80	16.64
4th	84.06	88.82
5th	70.26	76.08
6th	54.95	74.73
Average	73.86 ± 10.99	49.84 ± 33.31

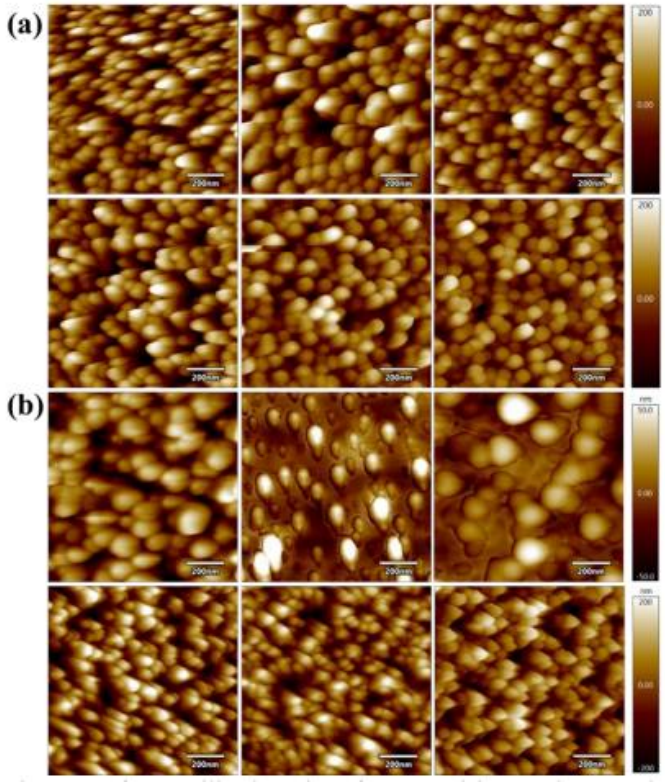


Figure S4. AFM images of nanopillar-based surfaces used in roughness calculation: (a) ZnO nanopillars and (b) PDMS-coated ZnO nanopillars.

S4 X-ray diffraction (XRD) analysis

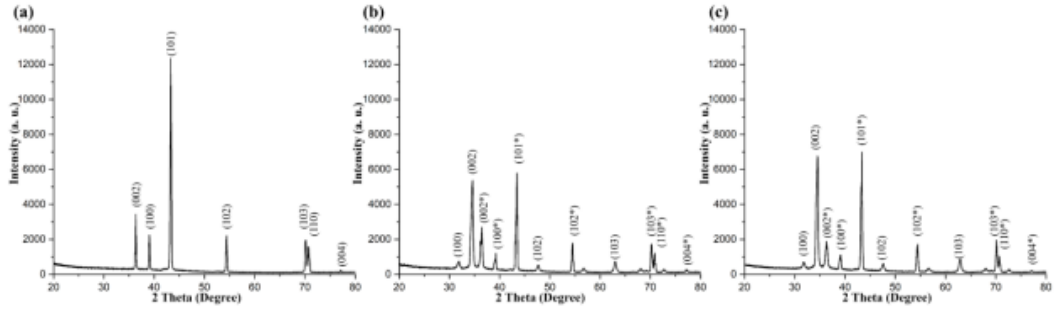


Figure S5. (a) Bare zinc, (b) ZnO nanopillars and (c) PDMS-coated nanopillars. Peaks marked with asterisks (*) are attributed to the zinc substrate.

S5 Fourier-transform infrared (FTIR) spectroscopy

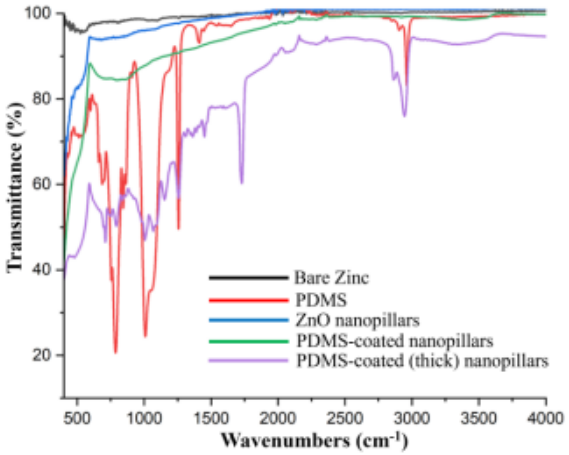


Figure S6. The FTIR spectra of samples.

S6 Photocatalysis

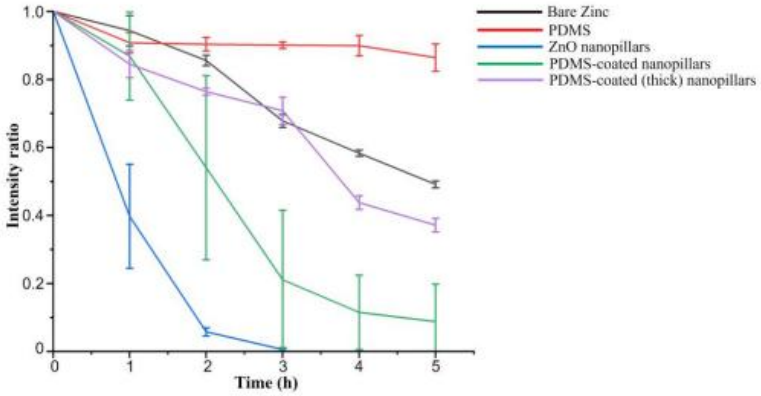


Figure S7. Fluorescence intensity changes of CF633 measured by UV-visible spectroscopy.

S7 Wetting properties

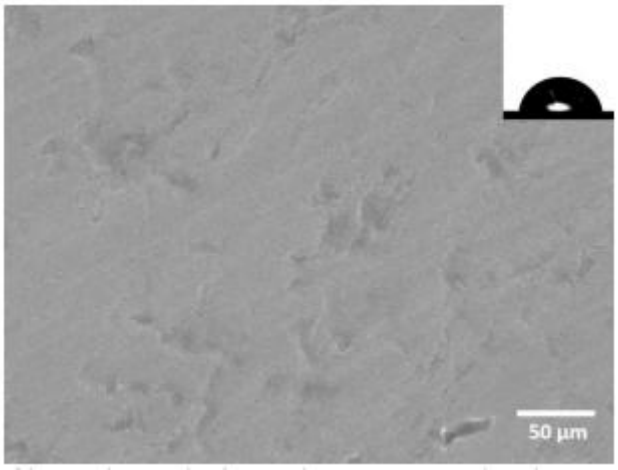


Figure S8. SEM image of bare zinc. The inset shows a water droplet on the bare zinc, with a static contact angle of around 77.8 ± 0.6°.

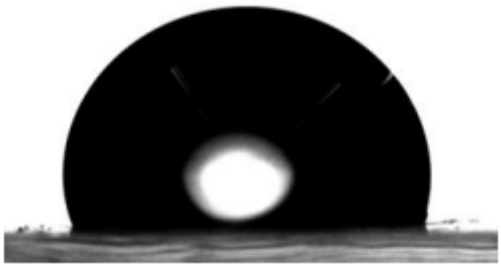


Figure S9. Water droplet on pure PDMS, with a static contact angle of around 106.1 ± 1.7°.

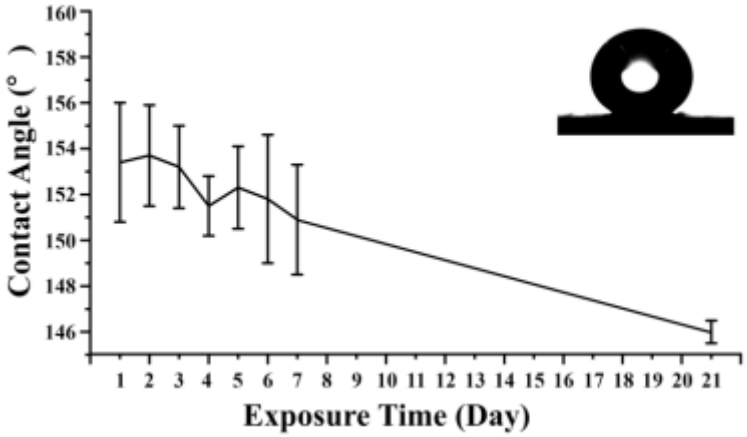


Figure S10. Droplet contact angle as a function of time. The inset shows that the water contact angle was around 146 ± 0.5° even after 21 days.

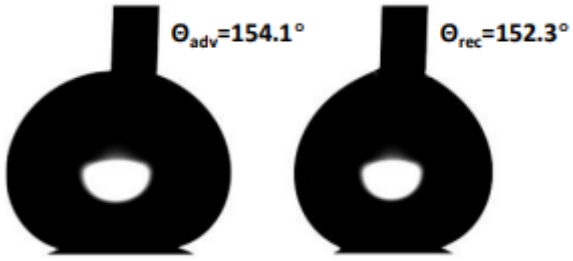


Figure S11. Measurement of dynamic contact angles of water on PDMS-coated ZnO nanopillars.

Table S3. Dynamic contact angles of PDMS-coated nanopillars

Frame No.	Advancing contact angle (°)	Receding contact angle(°)
1	153.9	153.3
2	153.8	153.3
3	154.3	153.3
4	154.3	153.1
5	154.3	152.7
6	154.3	152.2
7	154.1	151.7
8	154.0	151.4
9	153.9	151.5
10	153.8	151.2
Average	154.1 ± 0.2	152.3 ± 0.9

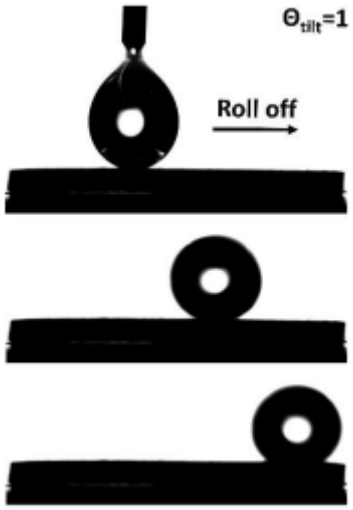


Figure S12. Water droplet rolling off.

S8 Weber number calculation

Weber number is calculated using the below formula:

$$We = \frac{D_o \rho U^2}{\sigma}$$

D_o is the diameter of the droplet, ρ is the density of the liquid (ρ = 998 kg/m3 for water), U is the velocity of the droplet and σ is the interfacial tension (σ = 0.072 N/m for water).

The dimension calibration, as shown in Figure S13(a) and Table S4, has been used to calculate the diameter of the droplet and the velocity. The size and pixel numbers are compared in Table S4, using the black screw in the image left as a reference system. Calculation details for Weber numbers are listed in Table S5. We perform calculations using the data from a single frame captured just before the droplet hits the surface (-1 ms). Figure S13(b) and (c) also show the full bouncing series and velocity change of droplet impact on PDMS-coated superhydrophobic surfaces.

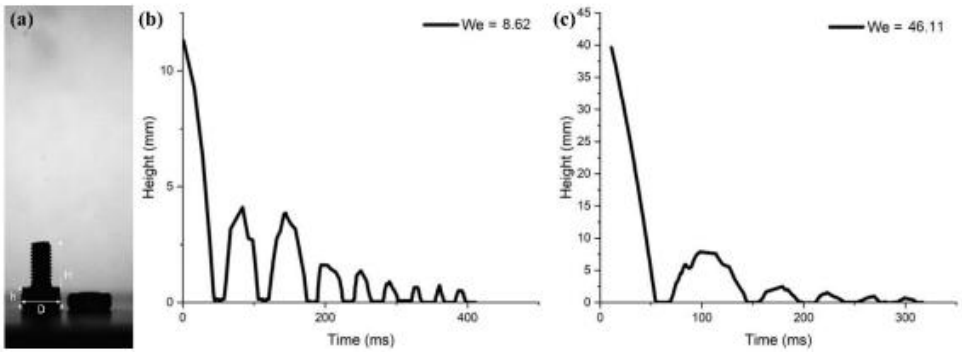


Figure S13. (a) Dimension calibration: 1 pixel in the image should be equal to 0.037 mm. Full bouncing series and velocity change of a water droplet (Do = 2.7 mm) on superhydrophobic PDMS-coated nanopillars with (b) We = 8.62 and (c) We = 46.11.

Table S4. Dimension calibration.

	Screw total height (H)	Screw head diameter (D)	Screw head thickness (h)
Real size (mm)	9	5.45	3
Pixels	250	148	79
Converting ratio	0.036 mm/pixel	0.037 mm/pixel	0.038 mm/pixel
The converting ratio used in the calculation = 0.037 ± 0.001 mm/pixel (average)			

Table S5. Weber number calculation.

	Impact time (Frame)	Impact distance (Pixel)	Converted impact time (ms)	Converted impact distance (mm)	Impact velocity calculation (m/s)	Weber number
Impact 1	1	13	1	0.48	0.48	8.62
Impact 2	1	30	1	1.11	1.11	46.11

S9 Droplet impact

The droplet impact images of the superhydrophilic ZnO nanopillars and pure PDMS surfaces are shown in Figure S14.

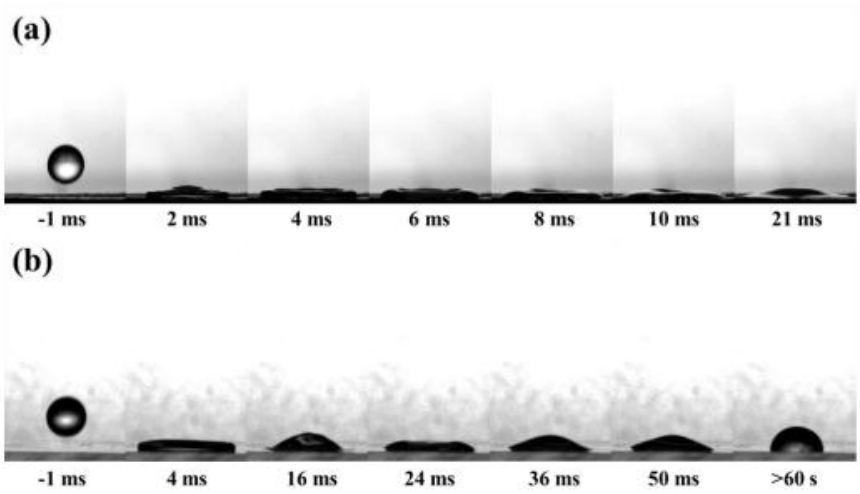


Figure S14. Water droplet impacting on (a) uncoated ZnO nanopillar surfaces and (b) pure PDMS surface with We = 46.11.

S10 Anti-biofouling properties

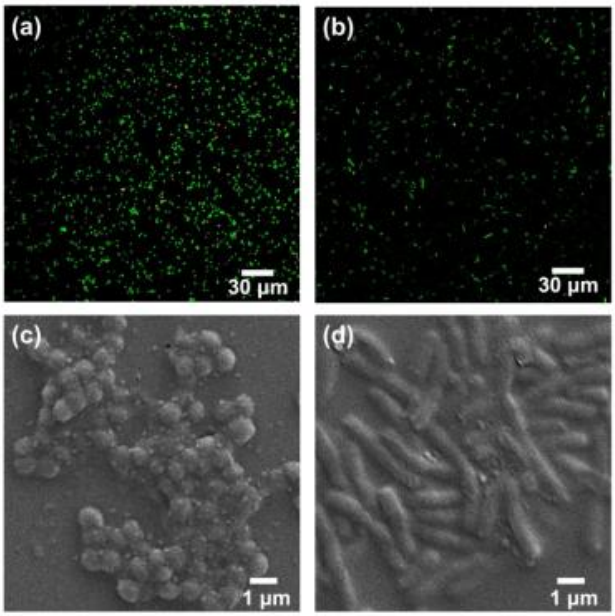


Figure S15. Confocal microscopy (a, b) and SEM (c, d) images of bacteria from the "no surface" control group: S. aureus (a, c) and E. coli (b, d).

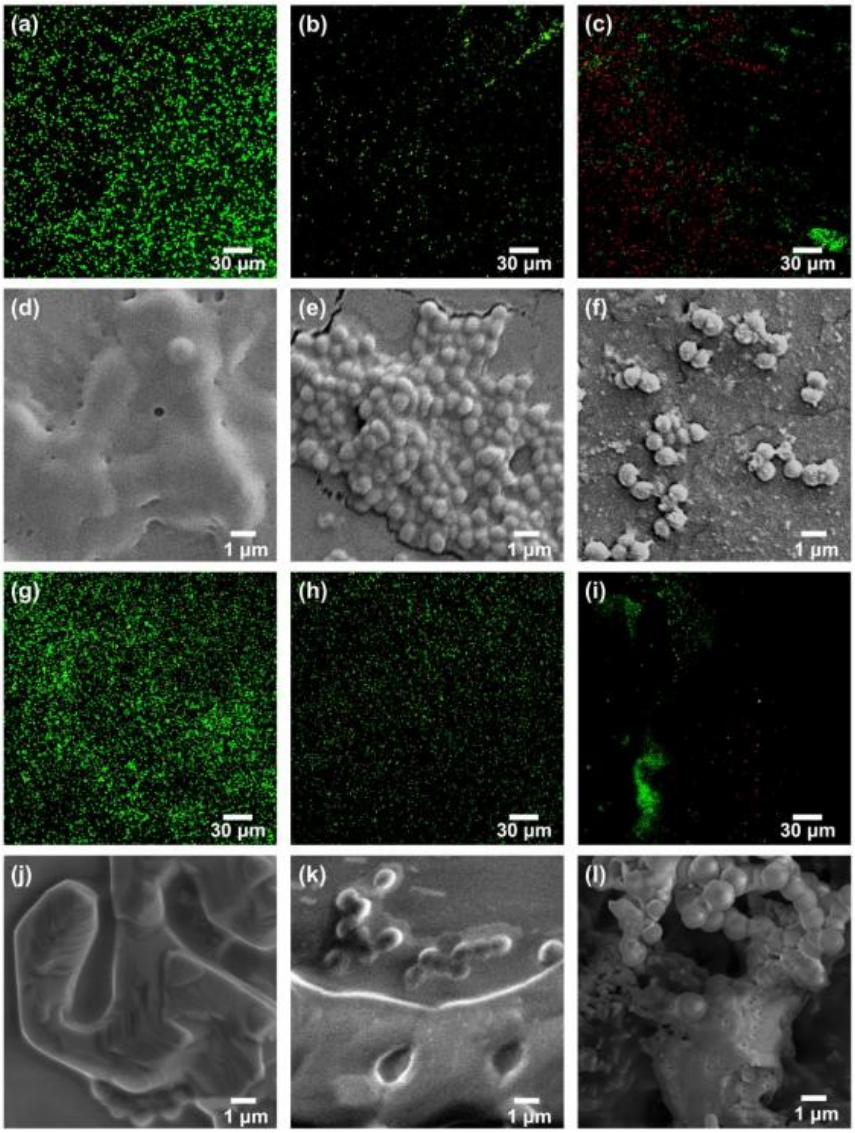


Figure S16. Confocal microscopy (a-c and g-i) and SEM (d-f and j-l) images of S. aureus after 18 (a-f) and 72 (g-l) hours of incubation, respectively, on different surfaces: glass (a, d, g, j), pure PDMS (b, e, h, k) and thick PDMS-coated nanopillars (c, f, i, l).

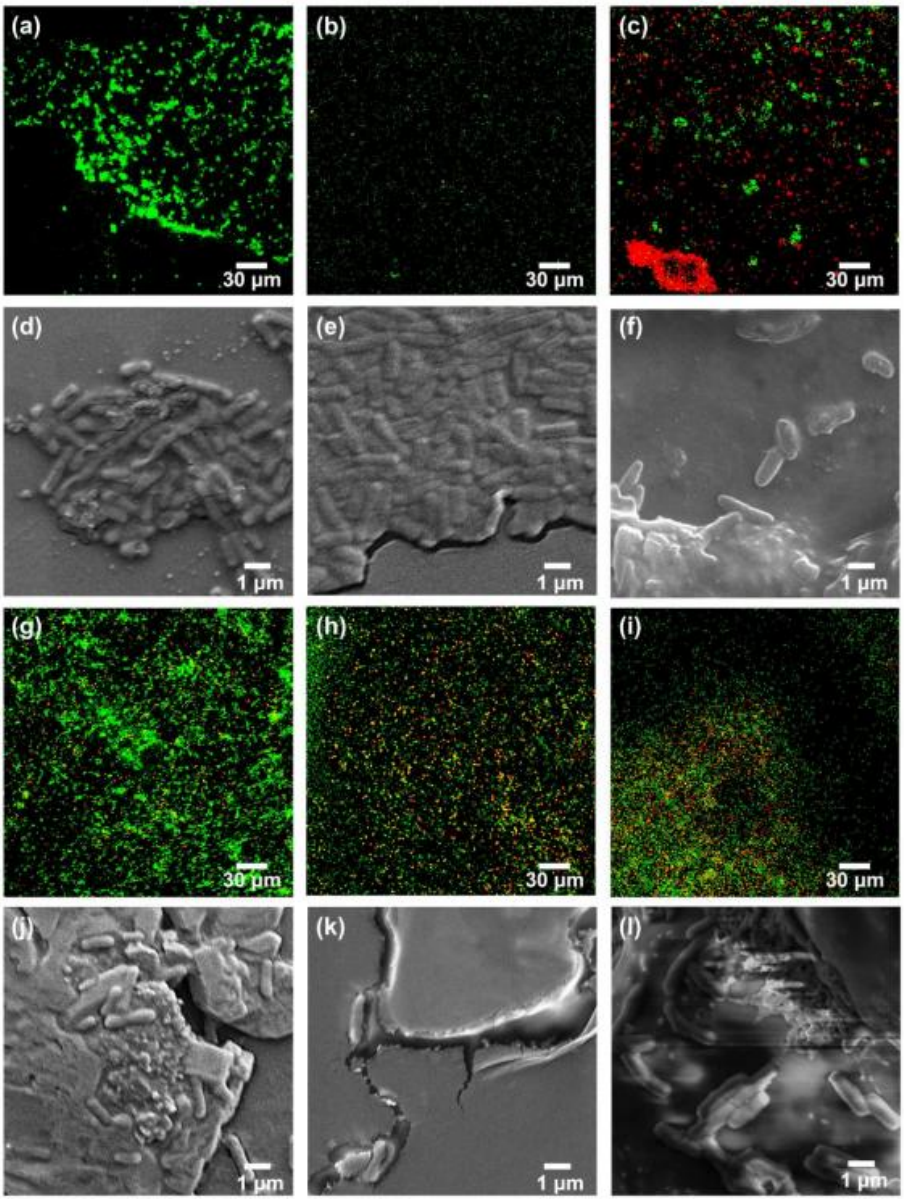


Figure S17. Confocal microscopy (a-c and g-i) and SEM (d-f and j-l) images of E. coli after 18 (a-f) and 72 (g-l) hours of incubation, respectively, on different surfaces: glass (a, d, g, j), pure PDMS (b, e, h, k) and thick PDMS-coated nanopillars (c, f, i, l).

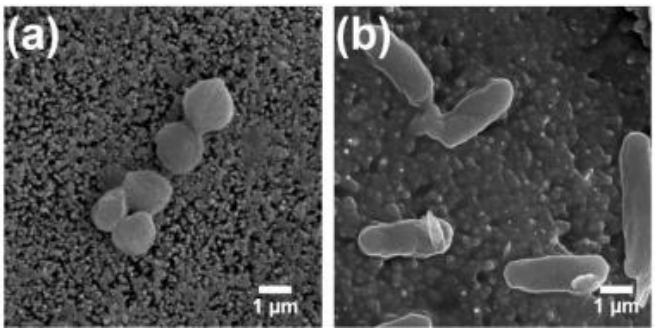


Figure S18. SEM image of (a) S. aureus and (b) E.coli on PDMS-coated nanopillars.

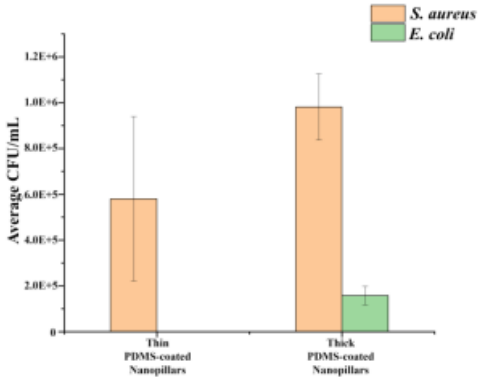


Figure S19. The number of colony forming units (CFU)/mL on different PDMS-coated nanopillar surfaces after 18-hour incubation.

S11 Multi-cycle tests

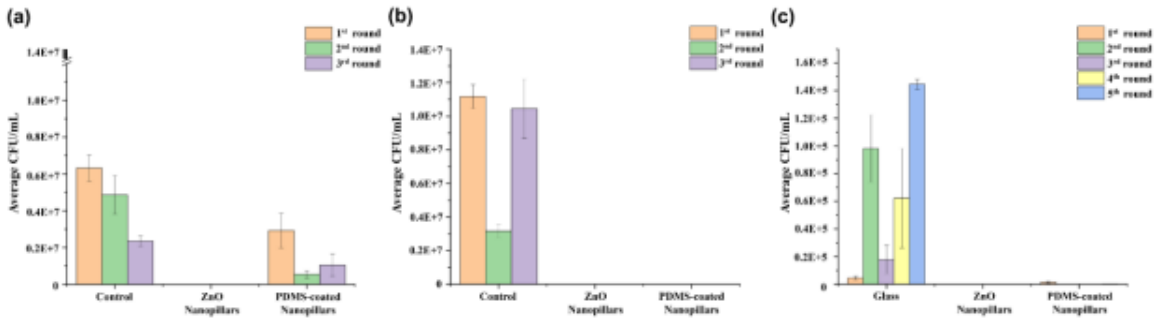


Figure S20. The number of colony forming units (CFU)/mL on the ZnO nanopillar-based surfaces of (a) S. aureus after three rounds of 18-hour incubation and E. coli after (b) three rounds and (c) five rounds of 18-hour incubation.

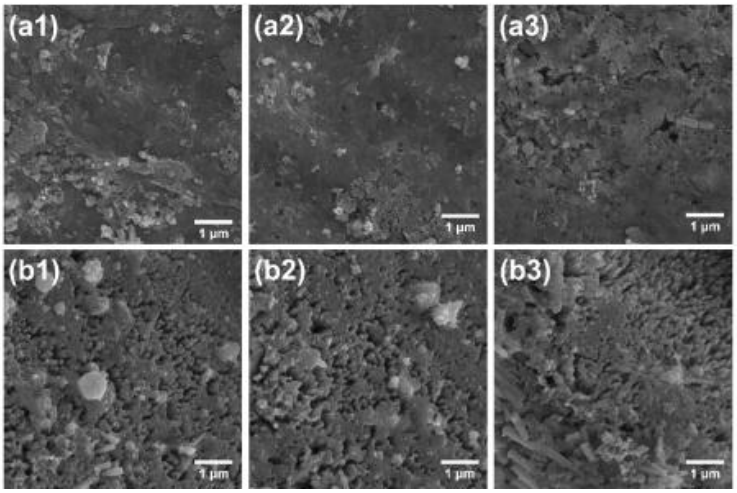


Figure S21. SEM images of surface morphology after multi-cycle tests: (a) ZnO nanopillars and (b) PDMS-coated ZnO nanopillars.

S12 Cytotoxicity tests

After the anti-biofouling efficacy tests, a cytotoxicity test was conducted to probe the safety and biocompatibility of the relevant surfaces. The results indicated no statistical significance ($p=0.247$) in the absorbance at 570 nm between the cell culture media and the relevant surfaces, as shown in Figure S22. This implies that the metabolism of resazurin in the Alamar blue solution was not significantly different, and consequently, the viability of the 3T3 fibroblast cells remained unaffected. The treated surfaces exhibited no indication of cytotoxicity against our mammalian cells.

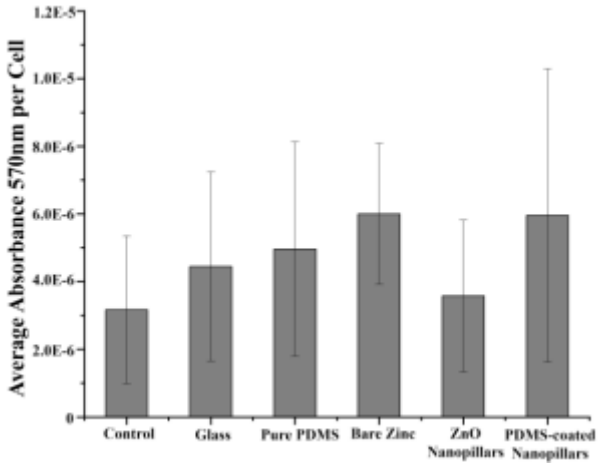


Figure S22. Cytotoxicity results from different surfaces.

S13 Bacterial coverage

The bacterial coverage on surfaces was characterised utilizing FIJI (ImageJ). In this process, confocal microscopy images were imported into FIJI and subsequently converted to 8-bit images. The pixel intensity distribution in this process was visualized, enabling the identification of selected pixels or regions of interest, which were highlighted in white/grey. Subsequent image analysis included the determination of bacteria count, total area, average size, and coverage area. Figure S23 provides an illustrative example of FIJI's capability in detecting bacteria attached to sample surfaces from confocal microscopy images. Tables S6 and S7 present coverage data derived from the confocal microscopy images. The confocal microscopy images utilized for this analytical process are displayed in Figures S24-27.

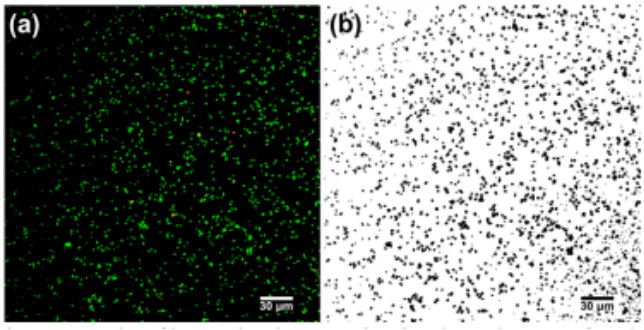


Figure S23. Illustrative example of bacteria characterisation based on confocal microscopy images: (a) Original confocal microscopy image and (b) FIJI converted image.

Table S6. Bacterial coverage (18-hour incubation).

***S. aureus* (%)**	Image 1	Image 2	Image 3	Image 4	Image 5	Average
Control	4.23	5.16	5.42	5.40	5.02	5.05±0.49
Glass	15.75	10.75	20.56	11.83	12.08	14.19±4.03
Pure PDMS	2.08	0.91	2.03	0.81	2.06	1.58±0.66
Bare zinc	3.72	3.73	4.68	5.75	3.83	4.34±0.88
ZnO nanopillars	4.87	3.50	3.44	3.36	3.11	3.66±0.69
PDMS-coated nanopillars	0.36	0.18	0.42	0.37	0.50	0.37±0.12
***E. coli* (%)**	Image 1	Image 2	Image 3	Image 4	Image 5	Average
Control	1.69	1.72	1.26	3.08	1.87	1.92±0.68
Glass	9.06	10.53	11.03	3.08	3.27	7.39±3.92
Pure PDMS	2.75	3.98	2.68	6.14	2.11	3.53±1.61
Bare zinc	1.97	2.79	4.35	3.51	4.49	3.42±1.06
ZnO nanopillars	2.49	4.29	5.05	3.40	3.37	3.72±0.98
PDMS-coated nanopillars	1.09	0.24	1.30	0.21	0.68	0.70±0.49

Table S7. Bacterial coverage (72-hour incubation).

***S. aureus* (%)**	Image 1	Image 2	Image 3	Image 4	Image 5	Average
Control	3.97	5.18	4.08	4.49	6.33	5.81±0.69
Glass	16.26	16.06	18.69	19.53	16.73	17.45±1.56
Pure PDMS	5.30	4.11	3.74	3.79	4.33	4.25±0.63
Bare zinc	5.38	5.97	5.84	8.21	6.57	6.39±1.10
ZnO nanopillars	11.86	11.91	11.12	11.85	11.02	10.35±1.13
PDMS-coated nanopillars	1.19	0.40	1.04	0.49	0.80	0.78±0.34
***E. coli* (%)**	Image 1	Image 2	Image 3	Image 4	Image 5	Average
Control	1.71	1.51	1.61	1.08	2.01	1.58±0.34
Glass	18.18	11.91	9.98	20.59	8.55	13.84±5.27
Pure PDMS	12.25	9.86	5.80	7.24	5.69	8.17±2.83
Bare zinc	6.57	5.66	7.60	9.62	6.35	7.16±1.54
ZnO nanopillars	9.19	9.78	5.48	5.23	10.92	8.12±2.60
PDMS-coated nanopillars	1.22	0.80	1.44	0.42	1.59	1.09±0.48

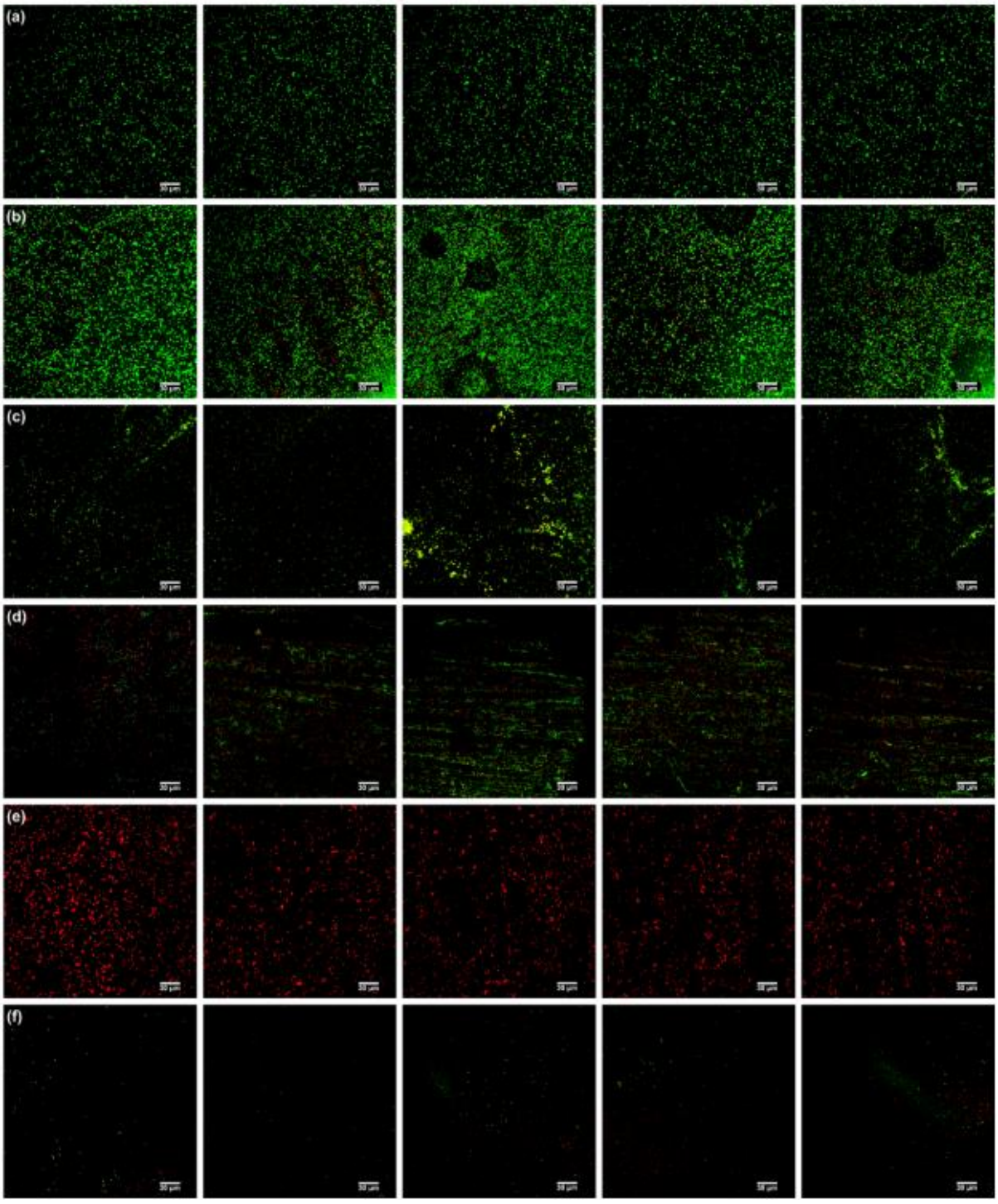


Figure S24. Confocal microscopy images of S. aureus after 18 hours of incubation on (a) control, (b) glass, (c) pure PDMS, (d) bare zinc, (e) ZnO nanopillars, (f) PDMS-coated nanopillars.

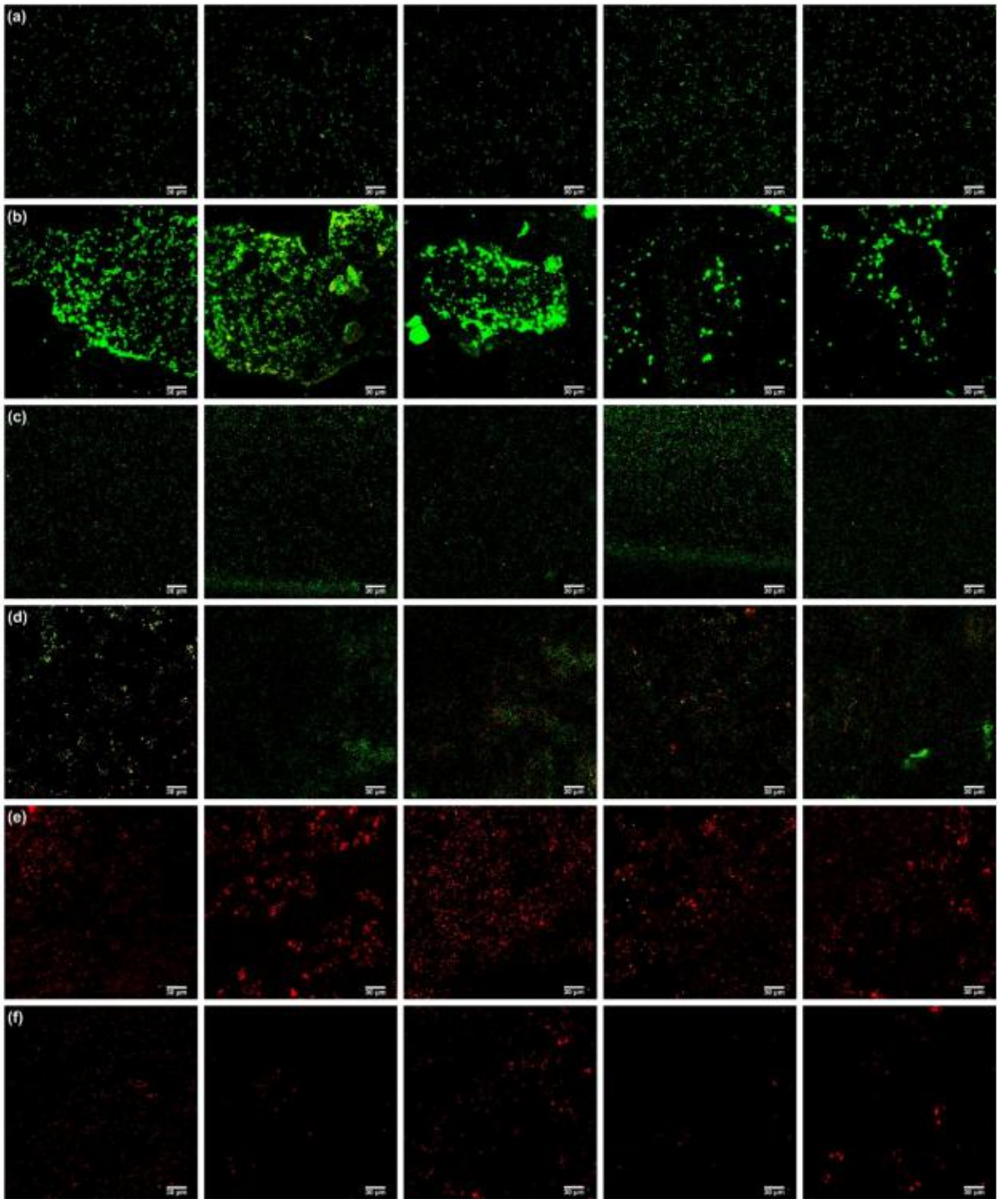


Figure S25. Confocal microscopy images of E. coli after 18 hours of incubation on (a) control, (b) glass, (c) pure PDMS, (d) bare zinc, (e) ZnO nanopillars, (f) PDMS-coated nanopillars.

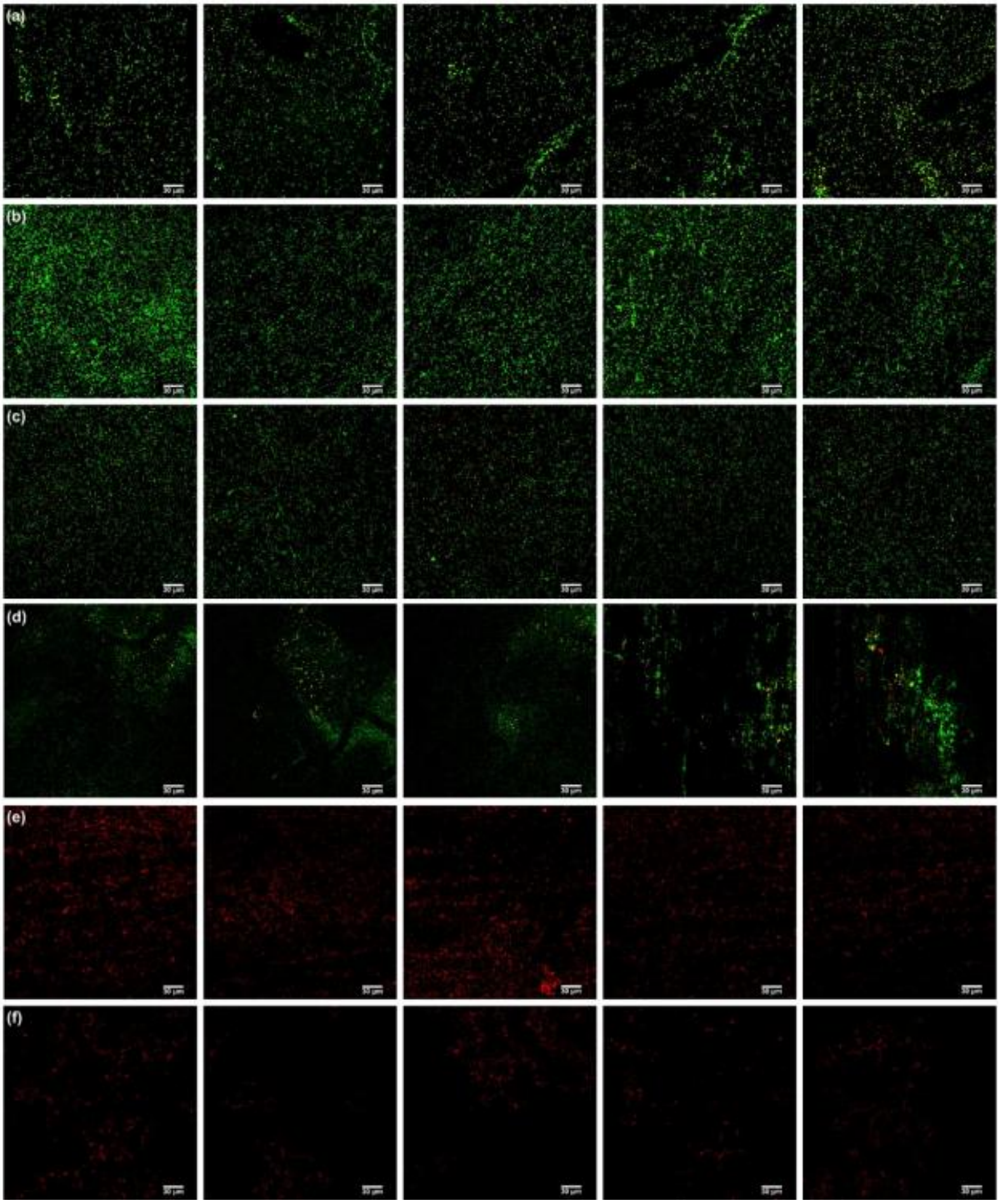


Figure S26. Confocal microscopy images of S. aureus after 72 hours of incubation on (a) control, (b) glass, (c) pure PDMS, (d) bare zinc, (e) ZnO nanopillars, (f) PDMS-coated nanopillars.

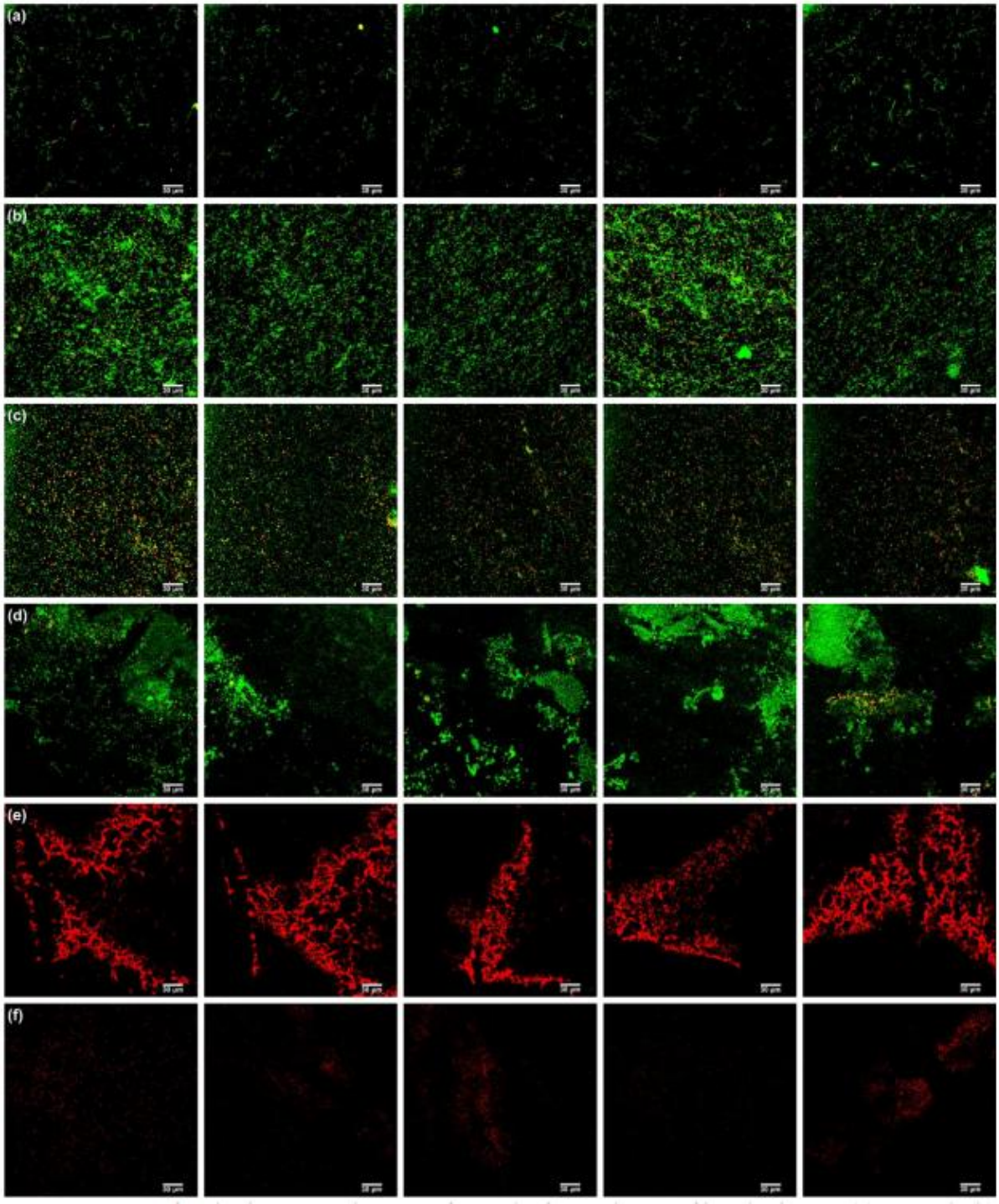


Figure S27. Confocal microscopy images of E. coli after 72 hours of incubation on (a) control, (b) glass, (c) pure PDMS, (d) bare zinc, (e) ZnO nanopillars, (f)